

PIXEL-BASED DUST-EXTINCTION MAPPING IN NEARBY GALAXIES:
A NEW APPROACH TO LIFTING THE VEIL OF DUST

by

Kazuyuki Tamura

A Dissertation Presented in Partial Fulfillment
of the Requirements for the Degree
Doctor of Philosophy

ARIZONA STATE UNIVERSITY

December 2009

© 2009 Kazuyuki Tamura
All Rights Reserved

PIXEL-BASED DUST-EXTINCTION MAPPING IN NEARBY GALAXIES:
A NEW APPROACH TO LIFTING THE VEIL OF DUST

by

Kazuyuki Tamura

has been approved

November 2009

Graduate Supervisory Committee:

Rogier A. Windhorst, Chair

Rolf A. Jansen

Sangeeta Malhotra

Steven Desch

Timothy Newman

ACCEPTED BY THE GRADUATE COLLEGE

ABSTRACT

In the first part of this dissertation, I explore a new approach to mapping dust extinction in galaxies, using the observed and estimated dust-free flux-ratios of optical V -band and mid-IR 3.6 micro-meter emission. Inferred missing V -band flux is then converted into an estimate of dust extinction. While dust features are not clearly evident in the observed ground-based images of NGC 0959, the target of my pilot study, the dust-map created with this method clearly traces the distribution of dust seen in higher resolution *Hubble* images. Stellar populations are then analyzed through various pixel Color-Magnitude Diagrams and pixel Color-Color Diagrams (pCCDs), both before and after extinction correction. The $(B - 3.6 \text{ microns})$ versus $(\text{far-UV} - U)$ pCCD proves particularly powerful to distinguish pixels that are dominated by different types of or mixtures of stellar populations. Mapping these pixel-groups onto a pixel-coordinate map shows that they are not distributed randomly, but follow genuine galactic structures, such as a previously unrecognized bar. I show that selecting pixel-groups is not meaningful when using uncorrected colors, and that pixel-based extinction correction is crucial to reveal the true spatial variations in stellar populations. This method is then applied to a sample of late-type galaxies to study the distribution of dust and stellar population as a function of their morphological type and absolute magnitude. In each galaxy, I find that dust extinction is not simply decreasing radially, but that is concentrated in localized clumps throughout a galaxy. I also find some cases where star-formation regions are not associated with dust.

In the second part, I describe the application of astronomical image analysis tools for medical purposes. In particular, Source Extractor is used to detect nerve

fibers in the basement membrane images of human skin-biopsies of obese subjects. While more development and testing is necessary for this kind of work, I show that computerized detection methods significantly increase the repeatability and reliability of the results. A patent on this work is pending.

This dissertation is dedicated to my wife, Kyoko, and my son, Soya, and to my parents for their unconditional love and support.

ACKNOWLEDGMENTS

In the past years, many people have helped and guide me through my doctoral study at the Department of Physics and School of Earth and Space Exploration (SESE) at Arizona State University (ASU).

I would like to express my wholehearted gratitude to my advisors Drs. Rolf Jansen and Rogier Windhorst for their financial support, helpful instructions, suggestions, and advice, and especially continuous encouragement during the hard times of my study. They provided me with many ideas which resulted in many proposals and various research topics. I also thank Drs. Seth Cohen and Nimish Hathi for their help, discussion, and encouragement during the course of my doctoral study. They helped me tremendously in my learning research techniques and how to approach scientific problems. I also thank my whole Dissertation committee for doing their part to help my research and advices. They are Professors Rogier Windhorst, Rolf Jansen, Sangeeta Malhotra, Steven Desch, and Timothy Newman.

I gratefully thank my fellow ASU graduate students who shared my experience and supported me emotionally. Discussions with them enhanced my learning of research skills and critical thinking. In no particular order, they are Erik DeSimone, Jake Russell, Jon Rohbach, Russell Ryan, Amber Straughn, Mike Lesniak, Todd Veach, Hwi Hyun Kim, Katie Kaleida, Michael Rutkowski, Teresa Ashcraft, and Matt Mechtley. In addition to those already mentioned, I would like to express my thanks to Drs. Paul Eskridge, Norman Grogin, and Michael Corbin for helping my research, and many intriguing suggestions and discussions.

I also thank all the rest of the faculty and staff of ASU Department of Physics and SESE, and especially to Ms. Sunny Thompson for help and support to accomplish my study.

Financial support during my research at ASU has come from various sources. First, I thank ASU, the Department of Physics and SESE for giving me Teaching Assistantships during the earlier years of my graduate studies. I also thank the Palms Clinic and Hospital Corporation Foundation, ASU College of Liberal Arts and Science, ASU Department of Physics, the ASU Department of Bioengineering, and the Arizona State University Vice President for Research for funding the interdisciplinary study between astronomy and medical field. And I would like to thank the NASA/ADP program and NASA/*JWST* for various research grants that helped me during my thesis work, which are NASA grants NNX07AH50G and NAG5-12460.

Finally, but most importantly, I would like to thank my wife, son, and parents for their continuous support and encouragement. I especially thank my parents for their understanding, and for letting me pursue my dreams in astronomy.

TABLE OF CONTENTS

	Page
LIST OF TABLES	xiii
LIST OF FIGURES	xiv
CHAPTER 1 INTRODUCTION	1
1.1 Background	1
1.2 Currently Popular Extinction Measurement Methods	2
1.3 Pixel-Based Analysis	5
1.4 New Approach to Estimating Dust Extinction	5
1.5 Application to Future Work	7
1.6 Interdisciplinary Study: Medical Image Analysis	8
1.7 Outline	9
CHAPTER 2 MAPPING THE SPATIAL DISTRIBUTION OF DUST EXTINC-	
TION IN NGC 0959	11
2.1 Overview	11
2.2 Concept	12
2.2.1 Simple Stellar Population Models	12
2.2.2 Optimal Filter Selection	13
2.2.3 Theoretical V -to- $3.6\ \mu\text{m}$ Flux Ratio Map	16
2.2.4 Estimating the V -Band Dust Extinction, A_V	19
2.3 Data Analysis	22
2.3.1 Datasets	22

CHAPTER	Page
2.3.1.1	<i>GALEX</i> Images 23
2.3.1.2	Ground-Based Images 23
2.3.1.3	<i>Spitzer</i> /IRAC Images 24
2.3.2	Pixel-Based Analysis 24
2.3.3	Assumptions about the Dust Distribution 25
2.3.4	Separating Younger and Older Stellar Populations 28
2.3.5	Selecting the Theoretical V -to- $3.6\ \mu\text{m}$ Flux Ratio 34
2.3.6	Calculating the Flux Difference 39
2.3.7	Measuring the Dust Extinction 44
2.3.7.1	Impact of the Uncertainty in $\beta_{V,0}$ 45
2.3.7.2	Analysis at Higher Spatial Resolution as Confirmation 48
2.3.7.3	Interesting Regions 50
2.3.7.4	Correcting for Dust Extinction 53
2.4	Application to Other Filters 54
2.4.1	Extinction Curves 54
2.4.2	A Dust-Free View of NGC 0959 60
2.5	Discussion 66
2.5.1	Radial Dust Extinction Profile, $A_V(R)$ 66
2.5.2	Summary 69
2.5.3	Future Application 70
2.6	Conclusions 72

CHAPTER	Page
CHAPTER 3 SIGNIFICANCE OF PIXEL-BASED EXTINCTION CORRECTION	75
3.1 Overview	75
3.2 Recapitulation of Pixel-Based Dust-Extinction Measurements	75
3.3 Lifting the Veil of Dust from NGC 0959	77
3.3.1 Color Composite Images	77
3.3.2 A $(B - 3.6 \mu\text{m})$ versus $(FUV - U)$ pCCD	81
3.3.3 Definition of Pixel Groups	82
3.3.4 Effect of Pixel-Based Extinction Correction	86
3.3.5 Is NGC 0959 Unique? Application to Other Galaxies	88
3.3.6 A Pixel Coordinate Map of Stellar Populations within NGC 0959	90
3.4 Summary and Conclusions	94
CHAPTER 4 MAPPING THE DISTRIBUTIONS OF DUST-EXTINCTION AND STELLAR CONTENT OF 27 NEARBY LATE-TYPE GALAXIES	97
4.1 Recapitulation of the Pixel-Based Extinction Measurement and its Effect	97
4.2 Application to 26 Other Late-Type Galaxies	99
4.2.1 Sample Selection	99
4.2.2 Analysis of 26 Galaxies	103
4.2.3 Comments on Individual Galaxies	132
4.3 Discussion of the Pixel-based Dust Extinction Measurement	145
4.4 Dust Distribution Pattern and Galaxy Parameters	149
4.4.1 The Dust Distribution in Spiral Galaxies	149

CHAPTER	Page
4.4.2 The Dust Distribution in Irregular Galaxies	155
4.4.3 The Dust Distribution as a Function of Absolute Magnitude: All Galaxies	159
4.4.4 The Dust Distribution as a Function of Absolute Magnitude: Spirals	161
4.4.5 The Dust Distribution as a Function of Absolute Magnitude: Irregulars	166
4.5 Summary and Conclusion	169
CHAPTER 5 CONCLUSION	173
5.1 Summary of Current Work	173
5.2 Future Work	178
CHAPTER 6 APPLICATION OF ASTRONOMICAL IMAGE ANALYSIS TOOLS: DETECTION OF SMALL SENSORY NERVE FIBERS IN TYPE-II DIA- BETES DIAGNOSIS	182
6.1 Overview	182
6.2 Background	182
6.3 Materials and Methods	185
6.3.1 Sample Preparation	186
6.3.1.1 Biopsy Technique	186
6.3.1.2 Sectioning and Staining	186
6.3.1.3 Visualization and Image Acquisition	187
6.3.1.4 Intraepidermal Nerve Fiber Density Quantification	187

CHAPTER	Page
6.3.2 Data and Tools	189
6.3.2.1 Definition and Terminology	189
6.3.2.2 Steps of Computerized Detection Method	190
6.3.2.3 Astronomical Tools	190
6.3.3 Post-Digitized Image Preparation	192
6.3.3.1 Image Format Conversion	192
6.3.3.2 Stacking Layer-Images and Smoothing the Basement Membrane Image	193
6.3.3.3 Preparation of the SSNF Images	196
6.3.4 Analysis	198
6.3.4.1 Determining the Basement Membrane	198
6.3.4.2 Detecting SSNF Segments	201
6.3.4.3 Calculating the SExtractor Detection Rate	202
6.4 Results	206
6.4.1 Visual Classification Results	206
6.4.2 Normalization of the CDM Results	208
6.4.3 Comparison to the Visual Densities	210
6.5 Discussion	212
6.6 Conclusion	214
REFERENCES	217

LIST OF TABLES

Table		Page
1	Dust Extinction Based on Different $\beta_{V,0}$ Values	48
2	Dust Extinction in Different Filters, (A_{filter}/A_V)	59
3	Selection Criteria for the Pixel-Groups in pCCD	84
4	Target Galaxies	101
5	Galaxy Data	105
6	Apparent and Absolute Magnitudes	160

LIST OF FIGURES

Figure	Page
1. Theoretical SEDs	14
2. Theoretical β_V Map	18
3. Theoretical μ_V vs. ($U-3.6\ \mu\text{m}$) Color-Magnitude Diagram	30
4. Selection of Pixels Dominated by Younger Stellar Populations	31
5. Color Composite Images of NGC 0959	35
6. Histograms of Observed V -to- $3.6\ \mu\text{m}$ Flux Ratio, β_V	37
7. Histogram of the Difference between Observed and Theoretical Flux, Δf_V	40
8. Pixel-Map of the Flux Difference, Δf_V	42
9. Comparison of Δf_V , with $\beta_{V,0,OB}$ and $\beta_{V,0}$ for Younger Pixels	43
10. Spatial Distribution of Visual Dust Extinction, A_V	47
11. A_V Map at <i>Spitzer</i> /IRAC Resolution	49
12. <i>HST</i> /WFPC2 Color Composite Image of NGC 0959	52
13. Observed vs. Extinction-Corrected V -Band Images and IRAC 3.6 & 4.5 μm Images	55
14. Extinction Curves	57
15. Observed and Extinction-Corrected FUV and NUV Images	62
16. Observed and Extinction-Corrected U - and B -Band Images	63
17. Observed and Extinction-Corrected R -Band Images	64
18. Radial Dust Extinction Profile, $A_V(R)$	68
19. Spatial Distribution of Pixel-Averaged Visual Dust Extinction	76

Figure	Page
20. Color Composite Images of NGC 0959 at <i>GALEX</i> Resolution	78
21. Color Composite Image of NGC 0959 at VATT Resolution	80
22. $(B - 3.6 \mu\text{m})$ vs. $(FUV - U)$ pCCDs for NGC 0959	83
23. $(B - 3.6 \mu\text{m})$ vs. $(FUV - U)$ pCCDs for NGC 7320 and UGC 10445	89
24. Pixel Coordinate Map of Pixel-Groups for NGC 0959	91
25. NGC 0959	100
26. UGC 01104	107
27. NGC 1156	108
28. UGC 04459	109
29. UGC 04483	110
30. NGC 2623	111
31. NGC 2719/2719A	112
32. UGC 04998	113
33. UGC 05101	114
34. UGC 05189	115
35. UGC 05340	116
36. NGC 3079	117
37. UGC 05423	118
38. NGC 3239	119
39. NGC 3274	120
40. NGC 3353	121
41. NGC 3445	122

Figure	Page
42. UGC 06541	123
43. NGC 3729	124
44. NGC 3738	125
45. NGC 3741	126
46. NGC 4299	127
47. NGC 5668	128
48. NGC 5996	129
49. UGC 10445	130
50. NGC 7320	131
51. Radial A_V Profile for Spiral Galaxies, as a Function of Morphological Type	150
51. Radial A_V Profile for Spiral Galaxies, as a Function of Morphological Type (Continued)	151
52. Comparison of Stellar and AGN SEDs	154
53. Radial A_V Profile for Irregular Galaxies, as a Function of Morphological Type	157
53. Radial A_V Profile for Irregular Galaxies, as a Function of Morphological Type (Continued)	158
54. Radial A_V Profile of All Galaxies as a Function of M_V	162
54. Radial A_V Profile of All Galaxies as a Function of M_V (Continued)	163
54. Radial A_V Profile of All Galaxies as a Function of M_V (Continued)	164
55. Radial A_V Profile of Spiral Galaxies as a Function of M_V	165

Figure	Page
55. Radial A_V Profile of Spiral Galaxies as a Function of M_V (Continued)	166
56. Radial A_V Profile for Irregular Galaxies as a Function of M_V	167
56. Radial A_V Profile for Irregular Galaxies as a Function of M_V (Continued)	168
57. A Diagrammatical Illustration of Image Preparation at Different Stages	188
58. Zoomed-in Images of Basement Membrane	194
59. Zoomed-in Images of SSNF	197
60. Final Set of Basement Membrane and SSNF Images	200
61. Pre-Normalized CDM Results	204
62. Comparisons of the CDM and Visual Classification Results	207

CHAPTER 1

INTRODUCTION

1.1. Background

Analyzing stellar populations in nearby galaxies, especially in spiral, irregular, and peculiar galaxies, and in galaxies at different stages of the merging process, is important to understand their structure, as well as the formation and evolution of galaxies in general. These galaxies may contain a moderate to large amount of dust, which can affect the observed light from the underlying stellar populations significantly. Measuring and correcting for dust extinction in individual galaxies is important to understand the true nature of their stellar populations, especially when one aims to study small-scale structures such as H II regions of spiral galaxies, which tend to be particularly dusty (e.g., Petersen & Gammelgaard 1997; Scoville et al. 2001; Calzetti et al. 2005). However, correcting for dust extinction, especially in extragalactic objects, has remained a problem for nearly a century (e.g., Trumpler 1930; Mathis et al. 1977; Viallefond et al. 1982; Caplan & Deharveng 1985; Witt et al. 1992; Roussel et al. 2005; Driver et al. 2008). Dust is distributed neither uniformly nor symmetrically within our own Galaxy, and in extragalactic objects. Instead, it is distributed in complicated patterns and structures, that roughly follow the star-forming structure of galaxies (e.g., Waller et al. 1992; Deo et al. 2006). Furthermore, Elmegreen (1980), Walterbos & Kennicutt (1988), and Calzetti et al. (1994) showed that the dust extinction depends on the geometry of the dust-distribution. The amount of light absorbed and scattered by dust depends on the amount, the geometrical distribution, as well as the physical and chemical properties of the dust (e.g., Witt et al. 1992; Whittet et al. 2001, 2004). Without correcting for—or taking into account—the effects of

dust extinction, stellar population analysis may lead to incorrect interpretations, and a biased understanding of the formation and evolution of galaxies.

1.2. Currently Popular Extinction Measurement Methods

Many different methods are used to estimate dust extinction within target galaxies. Some common measures of dust extinction are: (1) the ratios of Hydrogen recombination-line fluxes (e.g., Rudy 1984; Caplan & Deharveng 1985, 1986; Héraudeau & Simien 1996; Petersen & Gammelgaard 1997; Scoville et al. 2001; Maíz-Apellániz et al. 2004; Calzetti et al. 2005, 2007; Roussel et al. 2005; Relaño et al. 2006; Kennicutt et al. 2009); (2) the ratio of far-IR (FIR) and UV fluxes (e.g., Buat & Xu 1996; Calzetti et al. 2000; Charlot & Fall 2000; Witt & Gordon 2000; Bell et al. 2002b; Panuzzo et al. 2003; Boissier et al. 2004, 2005); (3) the UV spectral slope (e.g., Calzetti et al. 1994; Meurer et al. 1999; Bell 2002a; Kong et al. 2004); and (4) the CO column density from (sub-)millimeter observations of, e.g., $^{12}\text{CO}(J=1-0)$ line and $J=1-0$ and $J=2-1$ transitions of ^{13}CO and C^{18}O (Encrenaz et al. 1975; Dickman 1978; Frerking et al. 1982; Harjunpää & Mattila 1996; Hayakawa et al. 1999, 2001; Harjunpää et al. 2004).

Even though all these methods measure a galaxy's dust extinction in some way, each has its limitations. The method using Hydrogen recombination-lines is constrained to the lines of sight toward H II regions (e.g., Héraudeau & Simien 1996; Scoville et al. 2001; Calzetti et al. 2005). These H II regions can be distributed all over a galaxy, but cover only a small fraction of an entire galaxy disk. This method also requires moderate-resolution spectrophotometry (Petersen & Gammelgaard 1997;

Boissier et al. 2004). The methods using the FIR-to-UV flux ratio and UV spectral slope can be used throughout a galaxy. However, these methods are heavily affected not only by dust, but also by the age-metallicity degeneracy at UV wavelengths (e.g., Worthey 1994; Kaviraj et al. 2007a; Li & Han 2007, 2008), which introduces another complication in the dust-extinction correction process. Until recently, FIR telescopes (e.g., the *Infrared Astronomical Satellite* (IRAS; Neugebauer et al. 1984), the *Midcourse Space Experiment* (MSX; Mill et al. 1994), and the *Spitzer*/Multiband Imaging Photometer for SIRTIF (MIPS; Rieke et al. 2004; Werner et al. 2004) had very coarse spatial resolution of full width at half maximum (FWHM) $\gtrsim 20''$ – $100''$, or even larger (e.g., Xu & Helou 1996; Price et al. 2002; Rieke et al. 2004; Boissier et al. 2004), and were thus not suitable to study small-scale dust structures. The newly launched *Herschel Space Observatory* (Pilbratt 2004) improves the FIR resolution significantly, yet still has FWHM $\simeq 18$ – $36''$ at 250 – $500 \mu\text{m}$ (Griffin et al. 2007).

Finally, sub-millimeter and millimeter observations are used to measure the column density of CO molecules directly, and hence—under certain assumptions—that of molecular hydrogen, H_2 . The CO (and hydrogen) column density is converted to extinction using the correlation found between CO and dust-extinction in nearby galaxies (e.g., Dickman 1978; Bachiller & Cernicharo 1986; Komugi et al. 2005). The typical resolution at millimeter wavelengths is poor (FWHM $\simeq 20''$ – $2'6$; Encrenaz et al. 1975; Dickman 1978; Frerking et al. 1982; Harjunpää & Mattila 1996; Hayakawa et al. 1999, 2001; Harjunpää et al. 2004), although the Atacama Large Millimeter Array (ALMA; Brown et al. 2004) will soon greatly improve upon this. Studies such as that

of Boissier et al. (2007) also show that the relationship between the dust column-density and the amount of extinction is complicated.

A two-dimensional measurement of dust extinction is therefore limited to the closest galaxies, where individual galaxy features of interest are still sufficiently resolved. For more distant galaxies, dust extinction is still commonly treated as a single, averaged value across the entire galaxy.

Regan (2000) investigated the dust extinction using the radiative transfer modeling with input colors from images observed in the ground-based optical *BVRI* and near-IR (NIR) *JHK* filters. The advantage of using optical–NIR filters is that the extinction measurement is independent of the dust temperature (Regan 2000), and that the images can have much higher spatial resolution at these wavelengths than at FIR wavelengths (e.g., Regan & Mulchaey 1999). Combining theoretical models and color maps from optical–NIR images, the spatial dust distribution can then be derived. Figure 7 of Regan (2000) shows that this method can reconstruct extinction-free galaxy images. However, as Regan (2000) points out, there are several issues with this particular method. The first is that all of the passbands involved are affected by the dust to some degree: no single optical–NIR filter directly maps the distribution of either stars or dust by itself. The second issue is that, while the intrinsic colors of the underlying stellar populations are well known for older stellar populations, the colors of younger stellar populations in star-formation (SF) regions vary, depending on their specific properties and environment. Since he treated all stellar populations as old stellar populations, Regan (2000) points out that his extinction measurements

for stellar populations in SF regions are less accurate, and should be treated with care.

1.3. Pixel-Based Analysis

In recent years, a pixel-based analysis of stellar populations in nearby galaxies has become increasingly popular. This method was introduced by Bothun (1986), who used pixel Color-Magnitude Diagrams (pCMDs) to study the stellar populations and structure of NGC 4449. Since then, this technique has become an important tool to analyze the properties of stellar populations and their distribution within galaxies (e.g., Abraham et al. 1999; Eskridge et al. 2003; Lanyon-Foster et al. 2007; Welikala et al. 2008). This technique allows a full two-dimensional analysis throughout a galaxy, or any part of a galaxy, without any overlap or gaps as would be created in regular aperture photometry (see figures by, e.g., Scoville et al. 2001; Calzetti et al. 2005, 2007). To perform a pixel-based stellar population analysis properly, dust extinction has to be measured and corrected for each pixel individually.

1.4. New Approach to Estimating Dust Extinction

In this dissertation, I explore the possibility of a new approach to the problem of dust extinction. In the past decades, many galaxies have been observed from both ground and space in a wide range of wavelengths (from X-ray to Radio). These data are now readily available for large samples of galaxies through publicly available archives. Among all available wavelengths, I am focusing on data spanning the *Galaxy Evolution Explorer* (*GALEX*; Martin et al. 2005) far-UV (FUV; $\lambda_{\text{eff,FUV}} = 1516 \text{ \AA}$) and near-UV (NUV; $\lambda_{\text{eff,NUV}} = 2267 \text{ \AA}$) passbands, the ground-based optical *UBVR*

filters, the Two Micron All Sky Survey (2MASS; Skrutskie et al. 2006) NIR JHK_s filters, and the *Spitzer*/Infrared Array Camera (IRAC; Fazio et al. 2004) 3.6, 4.5, 5.8, and 8.0 μm mid-IR (MIR) channels. Especially, MIR wavelengths images observed by *Spitzer*/IRAC—which have become increasingly available in recent years—make this thesis work possible, and unique.

The *Spitzer* Space Telescope was launched in August 2003, and has been in scientific operation since December 2003. Whereas images observed through NIR filters are treated as *relatively* free of extinction, dust extinction is *non-zero* in these filters (e.g., Trewella 1998). Analyzing dust extinction combining NIR filters and other (usually optical $UBVR$) filters therefore requires careful theoretical (e.g., radiative transfer) modeling. While the longer wavelengths (5.8 and 8.0 μm) of IRAC channels are sensitive to dust emission due to polycyclic aromatic hydrocarbon (PAH; e.g., Leger & Puget 1984), the advantage of *Spitzer*/IRAC MIR channels is that the IRAC 3.6 and 4.5 μm channels are treated as free of dust extinction and dust emission (e.g., Fazio et al. 2004; Willner et al. 2004). The IRAC 3.6 and 4.5 μm images are therefore used as tracers of the stellar mass distribution (e.g., Kennicutt et al. 2003; Helou et al. 2004). The success of *Spitzer* in the past few years made it possible to explore a new approach to the problem of dust extinction.

While the dust extinction is due to the dust along the line-of-sight toward stellar populations, dust in a galaxy is intermixed with stellar populations both as thin layers and dense clumps. Also, while there are some effects of light scattering due to dust (e.g., Witt et al. 1992; Byun 1992), I assume that the effect of dust absorption

is much larger. A detailed description of the assumption about the dust geometry, and its effects, is given in Chapter 2 (Section 2.3.3).

1.5. Application to Future Work

Even though this dissertation is focused on dust-extinction measurements in just 27 nearby late-type galaxies, two-dimensional extinction mapping has a wide range of applications. This new method—based on optical V and IRAC $3.6\mu\text{m}$ passbands—does not require observations at wavelengths shorter than 4000 \AA . Such (near) UV light is mostly emitted by young stellar populations. Therefore, this method is not restricted to galaxies (or any object) that host such young stellar populations. Elliptical galaxies, for example, do not have much young stellar populations or star-formation (SF) activity, but may contain non-negligible amounts of dust (e.g., Goudfrooij et al. 1994a,b; Van Dokkum & Franx 1995; Kaviraj et al. 2007a; Oosterloo et al. 2007a,b; Emonts et al. 2008). While other extinction measurement methods that use UV wavelengths or emission-line ratios are not suitable, this new method can be used to study the two-dimensional dust distribution even in elliptical galaxies.

Another application of this new technique is to measure the two-dimensional dust extinction in galaxies at higher redshifts ($0.5 \lesssim z \lesssim 2.0$), that will be observed with *Hubble Space Telescope* (*HST*)/WFC3 and the *James Webb Space Telescope*. The galaxy merger rate is known to increase as the redshift increases (e.g., Zepf & Koo 1989; Burkey et al. 1994; Conselice 2006), and peaks at $z \simeq 1.3 \pm 0.4$ (Ryan et al. 2008). While studying these mergers is crucial to understand the mechanism

of galaxy formation and evolution, a single averaged value of dust extinction is commonly used to correct for an entire galaxy. Combining the superb spatial resolution of *HST*/WFC3 and *JWST* with this new pixel-based method to map the dust-extinction, the stellar populations and hence the evolution, of these galaxies can be studied in much more detail.

1.6. Interdisciplinary Study: Medical Image Analysis

In addition to the pixel-based analysis of nearby galaxies, I describe and demonstrate the use of some well known astronomical image analysis tools (e.g., Source Extractor and Smithsonian Astrophysical Observatory Image DS9) in a field other than astronomy. In particular, these astronomical tools are applied to diagnose the presence and severity of Type-II diabetes.

Damage to the peripheral nervous system can be idiopathic, or can occur as a result of known causes, such as pre- and post-diabetic disorder (e.g., Lacomis 2002; Smith & Singleton 2006). This damage can be characterized by pathology of Small Sensory Nerve Fibers (SSNFs: e.g., Dyck et al. 1981; Periquet et al. 1999; Verghese et al. 2001; Sumner et al. 2003; Malik et al. 2005; Smith & Singleton 2006). The difficulty in diagnosing an SSNF neuropathy has led to the development of histological analysis of skin-punch biopsy tissue, utilizing morphological surrogate markers and confocal, or conventional microscopy (e.g., Dalsgaard et al. 1989; Karanth et al. 1991; Kennedy & Wendelschafer-Crabb 1993). A basis for such diagnostic procedure is that these biopsy tissues are rich in SSNFs, that can be labeled by immunostaining with a pan-neuronal marker (e.g., Protein Gene-Product (PGP) 9.5; Dalsgaard et al. 1989;

Karanth et al. 1991), and quantified as density values (e.g., fibers mm^{-1}) of epidermal length—or as in this presentation—of basement membrane length, where fibers are counted in the basement membrane.

Under normal clinical conditions, the key issue in visually measuring the density of SSNFs is the reliability of the fiber counts. Since these immunostained nerve fibers appear narrow, and sometimes fragmented into multiple short segments in scanned biopsy images, visual detection methods have a limited repeatability, and hence in some cases, reliability. To improve the reliability, a number of computerized programs have been adopted (e.g., Kennedy et al. 1996). Since the 1960's, astronomers have developed many techniques for detection of tiny objects, such as stars and faint and small galaxies at distant Universe. I therefore employ the rich expertise of astronomical image analysis software and tools to detect SSNFs in the basement membrane of skin punch biopsies of volunteer subjects.

1.7. Outline

In Chapter 2, I explore the best combination of filters and theoretical feasibility of a new method to measure dust extinction using the spectra energy distribution (SED) library created by Anders & Fritze-von Alvensleben (2003), and then describe each step of the pixel-based dust-extinction correction method using the galaxy NGC 0959 as a case study.

In Chapter 3, using pCMD and pixel Color-Color Diagrams (pCCDs), I examine the effect of a pixel-based dust-extinction correction on the stellar population

analysis of NGC 0959. This work shows that a detailed pixel-based extinction correction is essential to reveal the nature and distribution of stellar populations in galaxies.

In Chapter 4, I apply this pixel-based dust-extinction correction to a total of 27 nearby galaxies, to study any pattern or correlation between the two-dimensional distribution of dust within these galaxies and their morphological type.

In Chapter 5, I summarize this new method to estimate the pixel-based two-dimensional dust extinction, and present the findings of the dust distribution patterns as a function of galaxy morphological types and other galaxy properties (i.e., absolute magnitude).

At the time of this writing, the contents of Chapter 2 have been published in the *Astronomical Journal* as Tamura, K., et al. 2009, *AJ*, 138, 1634 (the December 2009 issue of the *Astronomical Journal*). The results presented in Chapter 3 have been submitted to the *Astronomical Journal*, and the work presented in Chapter 4 is in preparation for submission to the *Astrophysical Journal Supplement Series*. The interdisciplinary work presented in Chapter 6 is accepted for publication in the *Journal of Neuroscience Methods*.

CHAPTER 2

MAPPING THE SPATIAL DISTRIBUTION OF DUST EXTINCTION IN NGC 0959

2.1. Overview

In this chapter, we present a method to estimate and map the two-dimensional distribution of dust extinction in the late-type spiral galaxy NGC 0959 from the theoretical and observed flux ratio of optical V and mid-IR (MIR) $3.6\ \mu\text{m}$ images. Our method is applicable to both young and old stellar populations for a range of metallicities, and is not restricted to lines-of-sight toward star-formation (SF) regions. We explore this method using a pixel-based analysis on images of NGC 0959 obtained in the V -band at the Vatican Advanced Technology Telescope (VATT) and at $3.6\ \mu\text{m}$ (L -band) with *Spitzer*/Infrared Array Camera (IRAC). We present the original and extinction corrected *Galaxy Evolution Explorer* (*GALEX*) far-UV (FUV) and near-UV (NUV) images, as well as optical $UBVR$ images of NGC 0959. While the dust lanes are not clearly evident at *GALEX* resolution, our dust map clearly traces the dust that can be seen silhouetted against the galaxy's disk in the high-resolution *Hubble Space Telescope* (*HST*) images of NGC 0959. The advantages of our method are: (1) it only depends on two relatively common broadband images in the optical V -band and in the MIR at $3.6\ \mu\text{m}$ (but adding a near-UV band improves its fidelity); and (2) it is able to map the two-dimensional spatial distribution of dust within a galaxy. This powerful tool could be used to measure the detailed distribution of dust extinction within higher redshift galaxies to be observed with, e.g., the *HST*/Wide Field Camera 3 (WFC3; optical–near-IR) and *James Webb Space Telescope* (*JWST*; mid-IR), and to distinguish properties of dust within galaxy bulges, spiral arms, and inter-arm regions.

2.2. Concept

Before we analyze any observed images, we first evaluate theoretical spectral energy distribution (SED) models for single stellar populations (SSPs) at different ages and metallicities. In this section, we describe the SED library that we used in our study, and then select the optimal filters for the subsequent SED analysis. Once the filters are selected, we describe how to estimate the dust extinction, using the theoretical SEDs and observed images, through flux ratios of an optimal set of filters.

2.2.1. *Simple Stellar Population Models*

Among published SSP SED libraries (e.g., AF03; Bruzual & Charlot 2003; Maraston 2005; Kotulla et al. 2009), we elected to use the SED library by AF03. While other SED libraries do not contain information about emission lines, this library includes both spectral and gaseous emission for young stellar populations. AF03 has created multiple sets of SED libraries¹ of SSPs, using the Padova (Bertelli et al. 1994) and Geneva (Lejeune & Schaerer 2001) isochrone models with Scalo (1986), Salpeter (1955), and Kroupa (2002) Initial Mass Functions (IMFs). These SED libraries contain models for metallicities of $Z = 0.0004, 0.004, 0.008, 0.02$ (Solar), and 0.04. Both isochrone models include the thermally pulsing asymptotic giant branch (TP-AGB) phase and model atmosphere spectra from Lejeune et al. (1997). The main difference between the two libraries with different isochrone models is the time resolution, Δt . While the library with the Padova isochrones have an age coverage

¹Since the publication of Anders & Fritze-von Alvensleben (2003), there have been several updates and additions to their models, resulting in slightly different combinations of IMFs and metallicities from the original description. We used the version dated 28 October, 2007: <http://www.galev.org/>

from 4 Myr to 14 Gyr with $\Delta t = 4$ Myr up to an age of 2.35 Gyr, and $\Delta t = 20$ Myr for older ages, the library with the Geneva isochrones have variable time steps. Among the available models, we will focus on the ones computed with Padova isochrones and the Scalo IMF—adopting an upper mass limit of $\sim 50 M_{\odot}$ for super-solar metallicity, and $\sim 70 M_{\odot}$ for all other metallicities. We refer the reader to AF03 and references therein for a detailed description of this library. The SEDs of SSPs change rapidly at all wavelengths, but especially so in the UV for ages younger than ~ 100 Myr (see Figure 1). Once a stellar population reaches the age of ~ 500 Myr, the rate of change in SED diminishes with increasing age. As a practical subset for our analysis, we consider 10 different ages ($t = 4, 8, 12, 52, 100, 500$ Myr, 1, 5, 10, and 13.5 Gyr) for each metallicity, resulting in a model grid of 50 different SEDs. In the main panel of Figure 1, we plot the SEDs for six ages and two metallicities that span the full range of our adopted model grid.

2.2.2. Optimal Filter Selection

The bottom panel of Figure 1 shows the total throughput curves, $T(\lambda)$, for various FUV–MIR filters considered in this study, as well as in the subsequent multi-wavelength studies on NGC 0959 (Chapter 3) and on a sample of 27 galaxies (Chapter 4). Total throughput curves for the *GALEX* filters—published in Morrissey et al. (2005) and on the *GALEX* web page²—are multiplied by a factor of 10 for better visibility. The throughput curves for the VATT filters are the total responses of the

²Goddard Space Flight Center, the *GALEX* Post Launch Response Curve Data:
<http://galexgi.gsfc.nasa.gov/docs/galex/Documents/PostLaunchResponseCurveData.html>

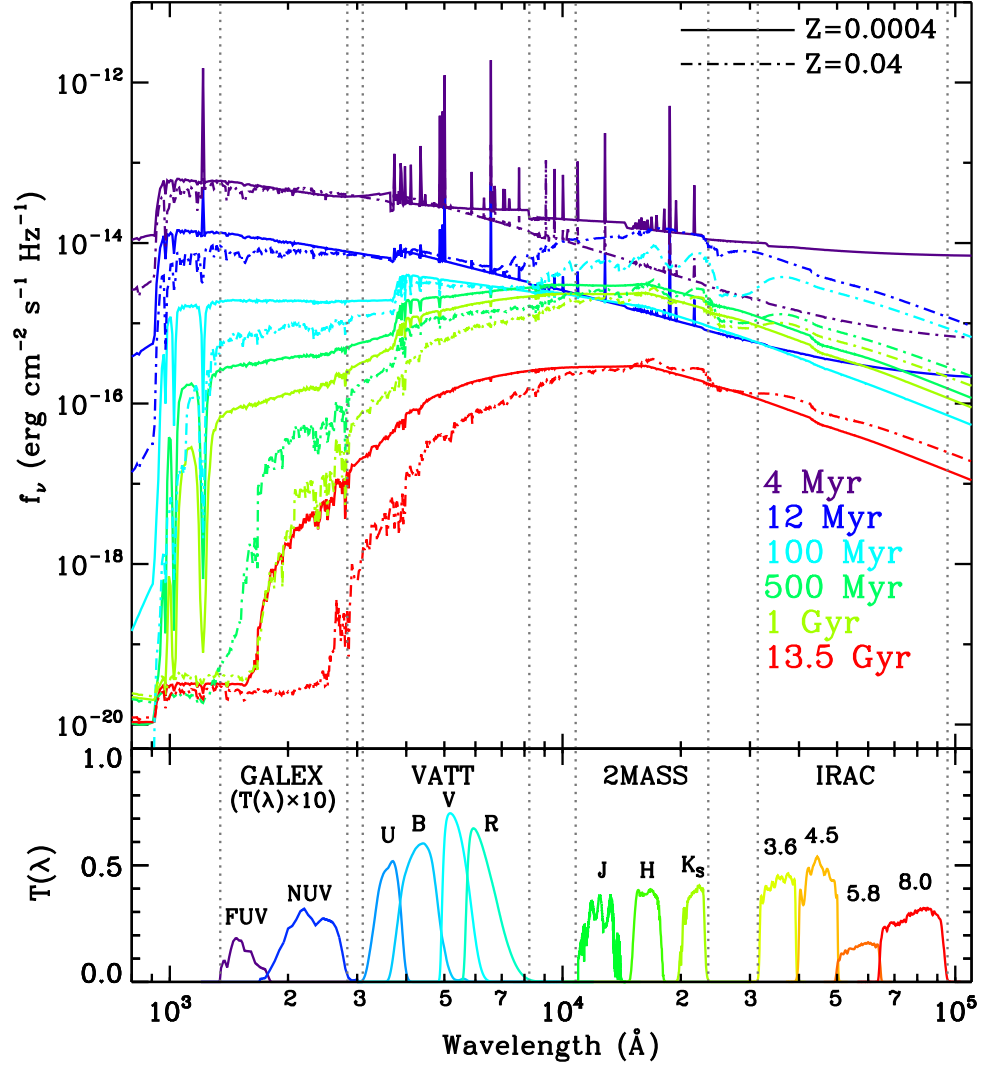


Figure 1. Top panel: theoretical SEDs from the library of Anders & Fritze-von Alvensleben (2003). Among the different sets of isochrones and IMFs, SEDs for Padova isochrones assume a Scalo IMF with metallicity of 0.0004 (solid curves) and 0.04 (dash-dotted curves) at six different ages as indicated. The age-metallicity degeneracy is clearly visible for wavelengths shortward of 4000 \AA . On the other hand, SEDs at $\lambda \gtrsim 6000 \text{ \AA}$ are less affected by metallicity, except for extremely young ($t \lesssim 100 \text{ Myr}$) stellar populations. Bottom panel: total throughput curves, $T(\lambda)$, for different telescope-filter combinations. Throughput for the *GALEX* filters are scaled up by a factor of 10 for better visibility. Vertical dotted lines indicate the wavelength coverage for each telescope-filter combination.

filters, CCD, and telescope³. The throughput curves for the Two Micron All Sky Survey (2MASS; Skrutskie et al. 2006) JHK_s filters are the total responses of the filters, CCD, telescope, and atmosphere⁴. Finally, for the *Spitzer*/IRAC filters, the total throughput curves are calculated using all components of the *Spitzer* instrument⁵. The vertical dotted lines in Figure 1 indicate the wavelength ranges covered by different telescopes and instruments.

The largest change in SEDs with the increase in age is the reduction of flux for wavelengths shortward of 4000 Å. Especially the UV flux—as measured by, e.g., the *GALEX* FUV and NUV filters—decreases by up to ~ 6 dex relative to the maximum flux level, as an SSP ages from 4 Myr to 13.5 Gyr. SEDs are also significantly affected by metallicity. For SSPs older than 100 Myr, the metallicity mainly affects the wavelengths $\lesssim 4000$ Å, where the flux decreases by up to ~ 2 dex from $Z = 0.0004$ to $Z = 0.04$. Since our primary goal is to measure dust extinction and to map its spatial distribution, filters covering wavelengths shorter than 4000 Å should be avoided to minimize effects from the age-dust-metallicity degeneracy.

According to AF03, the model SEDs become uncertain longward of $\sim 5 \mu\text{m}$. Also, the observed stellar continuum at MIR wavelengths redward of $\sim 5 \mu\text{m}$ is contaminated by emission from polycyclic aromatic hydrocarbons (PAHs; Leger & Puget 1984) and silicates (Willner et al. 2004). We thus exclude *Spitzer*/IRAC 4.5, 5.8, and

³Instrumentation for VATT (VATT 2k CCD):

<http://vaticanobservatory.org/vattinst.html>

⁴2MASS All-Sky Data Release Explanatory Supplement Facilities and Operations:

http://www.ipac.caltech.edu/2mass/releases/allsky/doc/sec3_1b1.html

⁵Spitzer Science Center: IRAC: Spectral Response:

http://ssc.spitzer.caltech.edu/irac/spectral_response.html

8.0 μm filters. On the other hand, the effects from dust extinction and emission by PAHs and silicates reach a minimum near 3.5 μm (L -band; e.g., Fazio et al. 2004; Willner et al. 2004). The IRAC 3.6 μm filter therefore provides the most reliable stellar population tracer (see, e.g., Kennicutt et al. 2003; Helou et al. 2004).

From the filters with $0.4 \lesssim \lambda \lesssim 3.5 \mu\text{m}$ —optical VR and NIR JHK_s in our study—we need to select (at least) one more filter to trace dust extinction. Since dust extinction is much smaller in the NIR than in the optical V - and R -bands (e.g., van Houten 1961; Cardelli et al. 1989; Calzetti et al. 1994; Gordon et al. 2003), NIR filters are not optimal for this purpose. Another reason to avoid ground-based NIR observations is absorption due to atmospheric water vapor. The amount and uncertainty due to this absorption depend on atmospheric conditions, as well as the location of the observations (e.g., Nitschelm 1988; Cohen et al. 2003). Dust extinction is stronger in the V -band (e.g., Calzetti et al. 1994; Gordon et al. 2003), while the metallicity effects are slightly weaker (see Figure 1). We therefore choose the V and 3.6 μm filters to globally trace the dust extinction. In the following section, we will explore the theoretical V -to-3.6 μm flux ratio in detail, and explain how we can use this ratio to estimate dust extinction. For other studies, in general, it should be noted that filters like SDSS g , HST F555W, F550M, and F606W would be adequate substitutes for V -band after calibration of the theoretical flux ratios.

2.2.3. *Theoretical V-to-3.6 μm Flux Ratio Map*

Given the SEDs from the AF03 library and the throughput curves of the optical V and IRAC 3.6 μm filters (see Figure 1), we explore the range in the theoret-

ical flux ratio, $\beta_V = f_V/f_{3.6\mu\text{m}}$, as a function of age and metallicity. The resulting flux ratio map in age-metallicity space is shown in Figure 2. From the input of 50 SEDs described above, both age and metallicity are resampled logarithmically using 100 steps with Spline interpolation to map the variation in β_V values over the full parameter ranges. The minimum ratio, $\beta_{V,\text{min}} = 0.39$, occurs for the most metal-rich ($Z = 0.04 = 2Z_\odot$) and oldest ($t = 13.5$ Gyr) SSP, while the maximum ratio, $\beta_{V,\text{max}} = 17.4$, is found for the most metal-rich and the youngest ($t = 4$ Myr) SSP. Contours for $\beta_V = 0.5$ (white solid curves) and 2.0 (white dashed curve) are drawn in Figure 2. A band of orange dots—also included as an orange band in the color bar—indicates the region where the V -to- $3.6\mu\text{m}$ flux ratio spans the range $0.75 \leq \beta_V \leq 1.50$.

For stellar populations older than 500 Myr, or $\log(t_{\text{Myr}}) \gtrsim 2.70$, the theoretical flux ratio changes little as a function of age and metallicity. Figure 2 shows that β_V ranges mostly between ~ 0.5 and ~ 2.0 . On the other hand, for stellar populations younger than 500 Myr, β_V changes more dramatically, depending on their age and metallicity. Especially for SSPs with super-solar metallicity, β_V changes from ~ 17 (red) for the youngest SSPs to $\lesssim 0.5$ (dark purple/black) in a matter of only a few 100 Myr. For the young SSPs with sub-solar metallicities, the value of β_V is more stable, but still changes much more rapidly than for SSPs older than 500 Myr. Among these young sub-solar metallicity SSPs, Figure 2 shows two distinctive ranges of β_V values: (1) a band color-coded in green ($9 \lesssim \beta_V \lesssim 13$) for SSPs younger than 10–100 Myr; and (2) a band coded in blue ($4 \lesssim \beta_V \lesssim 7$) for SSPs up to ~ 500 Myr.

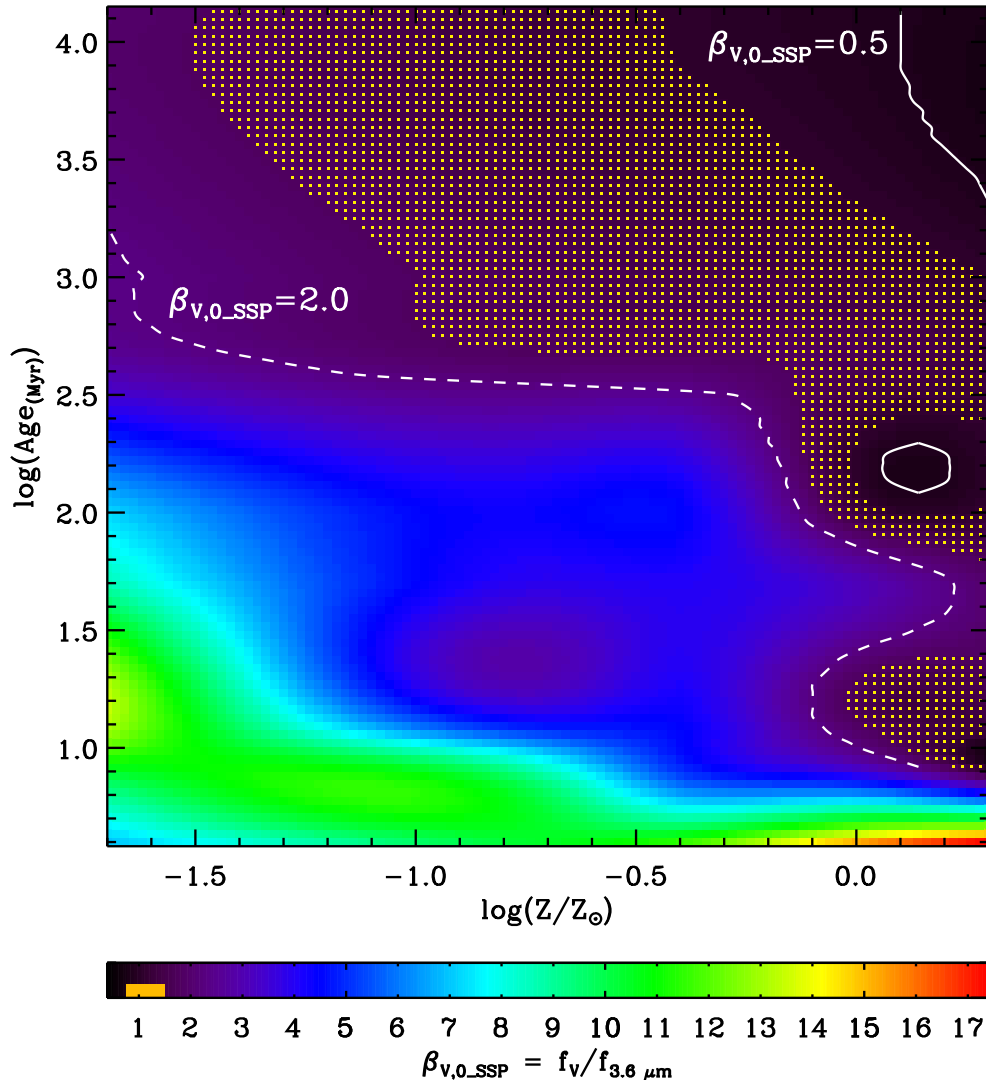


Figure 2. Map of the theoretical V -to- $3.6 \mu\text{m}$ flux ratio, β_V , calculated from an SSP library of Anders & Fritze-von Alvensleben (2003) for varying age and metallicity. Contours are plotted at $\beta_V = 0.5$ (solid curves) and 2.0 (dashed curve). The orange stippled region (and the orange band in the color bar) indicates the regions in the metallicity-age space where the flux ratio is $0.75 \leq \beta_V \leq 1.50$. While β_V varies rapidly for young— $t \lesssim 500 \text{ Myr}$ or $\log(t_{\text{Myr}}) \lesssim 2.7$ —stellar populations, it is relatively stable and insensitive to age and metallicity for older stellar populations.

The distribution of β_V values in Figure 2 confirms the assumption of, e.g., Regan (2000): that old stellar populations have relatively constant color, while young stellar populations change their colors more rapidly depending on their properties and environments. An important corollary of the former is that a mixture of SSPs with ages larger than 500 Myr will have a β_V value that is very similar to that of a single SSP at those ages. Our analysis of the theoretical V -to- $3.6\ \mu\text{m}$ flux ratios furthermore shows that—at least for young stellar populations with sub-solar metallicities—the theoretical flux ratio can be approximated as being constant for stellar populations in either of the two age ranges ($t \lesssim 10\text{--}100$ Myr or $10\text{--}100 \lesssim t \lesssim 500$ Myr) described above. In the following section, we will derive a method for using these theoretical and observed V -to- $3.6\ \mu\text{m}$ flux ratios to estimate the amount and spatial distribution of dust extinction in the V -band.

2.2.4. *Estimating the V-Band Dust Extinction, A_V*

To estimate the dust extinction for an observed stellar population, we first have to determine its approximate age and metallicity. The appearance of horizontal bands of different β_V values in Figure 2 indicates that an age determination is more important than the determination of metallicity. Based on the β_V values and corresponding age range for different metallicities as described above, the accuracy required in determining age is ~ 0.5 dex for extremely metal poor stellar populations, and ~ 1 dex for sub-solar to solar metallicity and older ($t \gtrsim 500$ Myr) stellar populations. For stellar populations with super-solar metallicities, the accuracy required is also $\sim 0.5\text{--}1$ dex for most ages, unless they are extremely young ($t \lesssim 10$ Myr). The

use of color-magnitude diagrams (CMDs) and color-color diagrams, therefore, should suffice to estimate the age of a stellar population and select a theoretical β_V value from Figure 2. By comparing the theoretical and observed flux ratios, we can infer the amount of flux missing in the V -band observation due to dust. The missing flux is a very robust property of the dust distribution, independent of the geometry and fine structure of obscuration. The amount of extinction by dust along the line-of-sight that this stellar population suffers can then be estimated from this missing V -band flux.

The dust extinction, A_V , is defined as

$$A_V = (m_V - m_{V,0}), \quad (2.1)$$

where m_V and $m_{V,0}$ denote the observed and intrinsic (extinction-free) V -band magnitudes, respectively. Even though the extinction-free magnitude is not known for an observed stellar population, we can use the selected β_V value and observed $3.6 \mu\text{m}$ flux to estimate the predicted $m_{V,0}$. Since we assume that the observed $3.6 \mu\text{m}$ flux is unaffected by dust extinction (e.g., Fazio et al. 2004; Willner et al. 2004), we can estimate the extinction-free V -band flux by multiplying the selected theoretical β_V value with the observed $3.6 \mu\text{m}$ flux:

$$f_{V,0} = \beta_V \times f_{3.6 \mu\text{m}}. \quad (2.2)$$

Therefore, Equation 2.1 can be rewritten as

$$A_V = m_V - [-2.5 \log(\beta_V \times f_{3.6 \mu\text{m}}) - V_{\text{zp}}], \quad (2.3)$$

where V_{zp} is the zero-point magnitude for the V -band. Compared to popular methods such as the UV spectral slopes (e.g., Bell 2002a; Kong et al. 2004) and the FIR-to-UV flux ratio (e.g., Dale et al. 2001; Buat et al. 2005), this method is much simpler.

Even though our prescription is simple, there remain many possible sources of error. In addition to the usual uncertainties due to observational measurements, there are several sources of uncertainty in the selected theoretical β_V value. Only when the age and metallicity are known for a resolved stellar population can we determine β_V for this stellar population with minimal error. For unresolved stellar populations, determining the age and metallicity becomes much harder as a result of light blending from intermixed and superposed stellar populations. As we have shown above, the metallicity dependency is not as strong as the age dependence in determining the likely β_V value. We therefore are still able to estimate the β_V value, if an approximate age of the stellar populations can be determined. Even though stellar population composites span a range in age, their luminosity tends to be dominated by their younger components at most wavelengths (see Figure 1). From the distribution of β_V values in Figure 2, we find a typical uncertainty in the determination of β_V for a stellar population of a factor of ~ 1.4 (e.g., assuming a theoretical $\beta_V = 1.1$, an old stellar population may actually show a range of $0.75 \lesssim \beta_V \lesssim 1.5$). This corresponds to an error in dust extinction, σ_{A_V} , of up to $\sim \pm 0.37$ mag, or mag arcsec^{-2} in the case of surface brightness. If this stellar population is either extremely metal-poor or metal-rich, the uncertainty is a factor of ~ 2 , or $\sigma_{A_V} \simeq \pm 0.75$ mag. On the other hand, if an extremely young (old) stellar population is treated as an old (extremely

young) stellar population, the error in the estimated theoretical β_V value will become a factor of ~ 5 or larger. This corresponds to a significant error in estimating the dust extinction, with $\sigma_{A_V} \gtrsim \pm 1.75$ mag. Since the extremely young and old stellar populations usually have distinct characteristics in the CMDs and color-color diagrams, it is highly unlikely that one would mistake a young stellar population for an old one. In Section 2.3.4 below, we will use U -band observations to robustly separate pixels dominated by the light of younger and older stellar populations.

2.3. Data Analysis

In this section, we apply the above method to the observational data. Before applying it to a large sample of galaxies, we assess its reliability in this chapter for one galaxy: NGC 0959. In the following chapters, we reconstruct and analyze the extinction-corrected images of NGC 0959 (Chapter 3) and a sample of 27 galaxies (Chapter 4), spanning a wide range of spiral and irregular galaxies, with *GALEX* FUV and NUV, optical *UBVR*, and *Spitzer*/IRAC images using the present method.

2.3.1. Datasets

The galaxy we will use for our proof of concept, NGC 0959, is a nearby late-type spiral galaxy classified as Sdm in the Third Reference Catalog of Bright Galaxies (RC3; de Vaucouleurs et al. 1991), at a distance of 9.9 ± 0.7 Mpc⁶ (Mould et al. 2000), with an inclination of 50° (Esipov et al. 1991). This galaxy has been observed with *GALEX* (Martin et al. 2005; Morrissey et al. 2007) in the FUV and near-UV (NUV), with the Vatican Advanced Technology Telescope (VATT) in *UBVR* from the ground

⁶This value is based on its recession velocity including the influence of the Virgo cluster, the Great Attractor, and the Shapley supercluster, and taken from the NASA/IPAC Extragalactic Database (NED) as of September 24, 2008

(Taylor et al. 2005), and with *Spitzer*/IRAC in the 3.6, 4.5, 5.8, and 8.0 μm filters (Fazio et al. 2004). Near-IR JHK_s images are also available from the 2MASS archive, but these images are too shallow for our purpose, and therefore excluded from the analysis. All displayed images and pixel-maps are rotated such that North is up and East is to the left. The surface brightness and colors are in units of mag arcsec^{-2} and mag, respectively, and are on the AB magnitude system (Oke 1974; Oke & Gunn 1983).

2.3.1.1. GALEX Images

The *GALEX* FUV and NUV images are obtained from the Multi-Mission Archive at the Space Telescope Science Institute⁷ (MAST). NGC 0959 was observed in the *GALEX* All-sky Imaging Survey (AIS; Martin et al. 2005) and the *GALEX* Nearby Galaxy Survey (NGS; Gil de Paz et al. 2007). Since the galaxy is barely visible in the AIS images, we will use the deeper (~ 1695 sec) NGS data for our analysis, focusing only on a 7.5×7.5 image section centered on NGC 0959.

2.3.1.2. Ground-Based Images

Ground-based *UBVR* images were obtained by Taylor et al. (2005) with the direct imager at the VATT at Mt. Graham International Observatory (MGIO) in Arizona. These images are available through the NASA/IPAC Extragalactic Database⁸ (NED). A detailed description of this data-set is provided by Taylor et al. (2005), and references therein. The effective exposure times in *UBVR* are 1200, 600, 480, and 360 sec, respectively.

⁷Galaxy Evolution Explorer, GR4 Data Release (as of May 1, 2009): <http://galex.stsci.edu/GR4/>

⁸NASA/IPAC Extragalactic Database: <http://nedwww.ipac.caltech.edu/>

2.3.1.3. *Spitzer/IRAC Images*

The *Spitzer*/IRAC 3.6–8.0 μm pipeline-product images were obtained from the *Spitzer* Archive⁹ via *Leopard*. For each filter, the mosaiced image was created with an effective exposure time of 26.8 sec.

2.3.2. *Pixel-Based Analysis*

In this study, we use a pixel-based analysis, first introduced by Bothun (1986) in the form of pixel Color-Magnitude Diagrams (pCMDs). This has recently become a popular technique to study stellar populations in nearby galaxies (e.g., Abraham et al. 1999; Eskridge et al. 2003; Lanyon-Foster et al. 2007; Welikala et al. 2008). This technique is performed in the same way as regular aperture photometry, but simply with an individual pixel as a source of flux. The advantage of using a pixel-based analysis is that this technique allows a two-dimensional analysis throughout a galaxy, or any part of a galaxy, without any object overlap or gaps as would be created in regular aperture photometry (see figures by, e.g., Scoville et al. 2001; Calzetti et al. 2005, 2007).

To perform this pixel-based analysis on images from different telescopes and instruments, we first have to resample the pixel scales and convolve all the images to a matching resolution. IDL¹⁰ and IRAF¹¹ routines were used to match the pixel scales and point spread functions (PSFs) of all images to the $1''.5 \text{ pixel}^{-1}$ and $\sim 5''.3$ FWHM

⁹*Spitzer* Science Center (SCC): Data Archives/Analysis:
<http://ssc.spitzer.caltech.edu/archanaly>

¹⁰IDL is distributed by ITT Visual Information Solutions (Research System Inc.), Boulder, Colorado: <http://rsinc.com/idl/>

¹¹IRAF is distributed by National Optical Astronomy Observatory (NOAO), which is operated by the Association of Universities for Research in Astronomy, Inc., under cooperative agreement with the National Science Foundation (NSF): <http://iraf.net>

of the *GALEX* NUV image, because these have the coarsest pixel scale and PSF among the filters considered for further panchromatic (FUV–MIR) studies. At the distance of NGC 0959 ($D = 9.9 \pm 0.7$ Mpc), each $1''.5$ pixel spans 72 pc. As a result, the light from different stellar populations is mixed together within a single pixel, and the observed flux ratios cannot be compared directly to the SSP-derived β_V values in Figure 2. While the pixels with most of the light coming from older stellar populations are not affected as much, the pixels with light from younger stellar populations will be affected significantly. Even though the light is smoothed over a much larger area than the area covered by a single pixel, the peak of the light distribution stays at the same pixel coordinate as before the smoothing. In the following, we therefore statistically analyze the observed images to estimate the intrinsic, dust-free flux ratios for both younger and older stellar populations, instead of a direct comparison to SSP models in the previous section. We will only use pixels with signal-to-noise ratio of $S/N \geq S/N_{\min} = 3.0$ in all FUV–MIR filters used.

2.3.3. *Assumptions about the Dust Distribution*

The dust is not uniformly distributed across an entire galaxy. Instead, it is distributed in complicated patterns of wisps, lanes, and bands of thin and filamentary structures, as well as in small clumps (e.g., Waller et al. 1992; Deo et al. 2006). Using stellar radiative transfer models, Elmegreen (1980) and Witt et al. (1992) showed that depending on different spatial distributions of the dust, e.g., a cloud or a slab, the effect of dust extinction—including both absorption and scattering—varies along different lines-of-sight. Walterbos & Kennicutt (1988) estimated the variations in ex-

extinction values calculated from the “symmetry argument” (e.g., Lindblad 1941; Elvius 1956). Calzetti et al. (1994) compared models of five different dust distributions to the observational data: (1) a uniform dust screen; (2) a clumpy dust screen; (3) a uniform scattering slab; (4) a clumpy scattering slab; and (5) an internal dust model (see their Fig. 8). The importance of these models is that the resulting extinction is different for each model although the amount of dust is same. Even though Calzetti et al. (1994) could not find satisfactory agreement between the observed data and these models using Large Magellanic Cloud (LMC) or Milky Way (MW) dust-extinction curves, models 2 and 4 with clumpy dust distributions show in general a better fit to the data than the other models. We will assume that the dust affecting the observed light is distributed in wisps and clumps, and is mostly in front of the observed stellar populations—with a much larger effect of absorption than light scattering (Byun 1992)—following the observations of, e.g., Waller et al. (1992) and Deo et al. (2006). The true distribution of the dust would be more complex, but representable by a combination of different types of simple geometrical distributions, with the dust distributed not only in front, but also intermixed with stellar populations. Dust located mostly behind the stars would not be detected at the wavelengths considered here.

Another important issue is the filling factor of dust within a pixel. While each pixel subtends $1''.5$, the dust features can span either a larger or smaller area. Given a single average value of the dust extinction in each pixel, there are two extreme possibilities for the dust distribution within that pixel: (1) an extended distribution of a relatively thin layer of dust; and (2) small high-density clumps of dust covering

only a fraction of the area in that pixel. Since the light observed in a single pixel is a mixture of light from different stellar populations, the effect that we observe is a weighted average of the light from those stellar populations. For the former type of dust distribution, the dust is affecting the light of all stellar populations contributing to a single pixel equally. For the latter case, the dust is only affecting a small fraction of the total light in that pixel. While the light from stellar populations behind a dust clump is reduced, the light from unextincted stellar populations is observed at its full strength, reducing the average effect of dust extinction within a pixel. If the intrinsic V -band flux is estimated from the observed NIR-flux—which is still affected by dust extinction to some degree—this partial coverage of any dust extinction might cause a large uncertainty. Our method, on the other hand, estimates the intrinsic V -band flux from the observed MIR ($3.6\ \mu\text{m}$) flux, which is usually considered as extinction free (e.g., Fazio et al. 2004; Willner et al. 2004). The observed $3.6\ \mu\text{m}$ flux is therefore the *total* light from all stellar populations along the line-of-sight, ranging from the front to the far side of a galaxy. Since the intrinsic V -band flux is estimated based on this $3.6\ \mu\text{m}$ flux, our method estimates the *total* amount of missing V -band flux. Hence, even though the “exact” effect of dust extinction depends on the true dust geometry, the *total* missing V -band flux and the corresponding dust extinction should not be affected by the dust geometry, unless the extinction in individual knots or filaments is $\gg 1.0$ mag, thereby also affecting the observed MIR flux, and preferentially affecting only young and highly concentrated (on scales $\ll 72$ pc) stellar populations. In retrospect, this does not appear to be the case (see

e.g., Figure 11), although one has to be careful that this does not become a circular argument.

2.3.4. *Separating Younger and Older Stellar Populations*

Even though the effect of light blending is significant in NGC 0959, some pixels are still dominated by the light from younger stellar populations. Therefore, the first step in our data analysis is to separate these pixels from pixels whose light mostly comes from older stellar populations. Figure 3 shows theoretical tracks of μ_V versus $(U-3.6\ \mu\text{m})$ using 52 Myr and 10 Gyr SSP SED models with a metallicity of $Z = 0.008$. These metallicity and ages are selected because: (1) $Z = 0.008$ is the central metallicity among five metallicities available for the SED library by AF03; (2) $t = 10$ Gyr represents an old stellar population; and (3) $t = 52$ Myr represents a young, but not an extremely young ($t \lesssim 10$ Myr) stellar population (see Figure 2). Since the U -band light is sensitive to younger stellar populations and $3.6\ \mu\text{m}$ light traces older stellar populations, the $(U-3.6\ \mu\text{m})$ color indicates the luminosity-weighted average age of stellar populations within a given pixel. The solid curve shows a track of the surface brightness and color as the fraction of light from the young stellar population increases. The fraction indicated in the figure is the mass fraction of stellar populations, i.e., “100%” indicates that the mass ratio between young and old stellar populations is one-to-one. A reddening vector corresponding to a visual extinction of $A_V = 1.0$ mag arcsec⁻² is drawn in the lower left of Figure 3, and is applied to selected data-points. Even though this is an extreme case, Figure 3 shows that, once the young stellar population dominates, the color of mixed stellar populations tend to

an asymptotic value of $(U-3.6\ \mu\text{m}) \simeq -1.0$ mag. In a real situation, younger stellar populations are known to associate with a larger amount of dust (e.g. van Houten 1961; Knapen et al. 1991; Regan et al. 2004; Barmby et al. 2006), and the observed color will therefore most likely shift away from the no-extinction track to redder colors.

Figure 4(a) shows a pCMD of μ_V versus $(U-3.6\ \mu\text{m})$ of the observed images at *GALEX* resolution. The photometric uncertainties plotted along the right side of the figure are calculated using data points within a horizontal slice of $\mu_V \pm 0.1$ mag arcsec⁻² at each point. A reddening vector corresponding to $A_V = 0.5$ mag arcsec⁻² and assuming the LMC extinction curve is drawn at the lower left. The stellar populations in NGC 0959 are unresolved due to a combination of its distance, the coarse pixel scale, and a large PSF. As a result, Figure 4(a) does not show clear separations among different stellar populations, as are seen for partially resolved stellar populations (e.g., Eskridge et al. 2003). Nevertheless, some branches and grouping features in this pCMD are still recognizable. For simplicity, in the following sections, we will refer to *pixels in which the flux is dominated by light from younger stellar populations* as “younger pixels”, and *pixels dominated by light from older stellar populations* as “older pixels”. Visual inspection of Figure 4(a) (in particular, different slopes for groups of branching pixels on left and right sides of the distribution and groups of pixels forming a “shoulder-like” distributions at $\mu_V \simeq 21$ mag arcsec⁻² in the pCMD) suggests an empirical division between the “younger” and “older” pixels at $(U-3.6\ \mu\text{m}) = 0.72$ mag—close to the color indicated by a dash-dotted line at $(U-3.6\ \mu\text{m}) = 0.76$ mag in Figure 3, where young stellar populations start dominat-

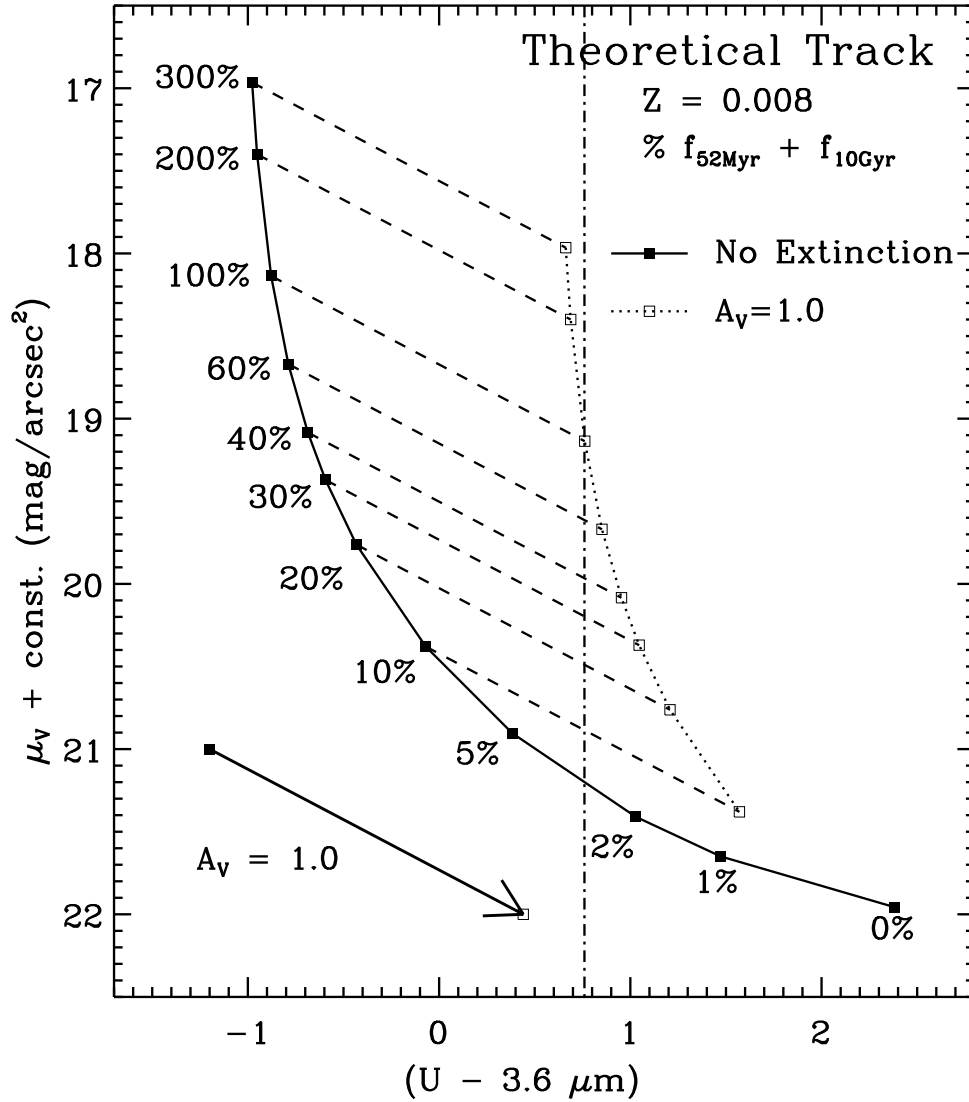


Figure 3. Theoretical μ_V vs. $(U-3.6 \mu\text{m})$ CMD. The solid curve is the theoretical track produced by adding different fractions of a young (52 Myr) SSP SED to an old (10 Gyr) SSP SED: the “100%” indicates a mass ratio between young and old SSPs of 1, and “200%” means the mass ratio is two-to-one. The effect of an average visual extinction of $1.0 \text{ mag arcsec}^{-2}$ is shown as a reddening vector in the lower left, and by dashed lines for selected data points. The dotted curve traces a theoretical track for the color and surface brightness if the entire pixel (with a filling factor of 100%) is affected by this reddening. The vertical dot-dashed line at $(U-3.6 \mu\text{m}) = 0.76 \text{ mag}$ represents the color where the mass-weighted SEDs of young and old SSPs are contributing equally, and are both affected by a dust extinction of $A_V = 1.0 \text{ mag arcsec}^{-2}$.

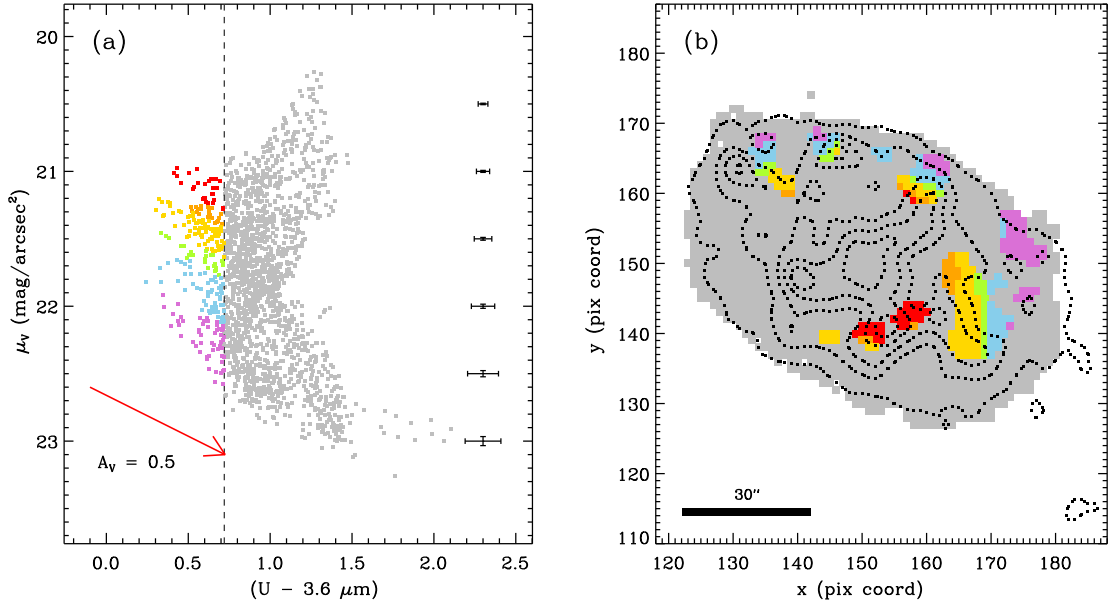


Figure 4. (a) pCMD of μ_V vs. $(U - 3.6 \mu\text{m})$ for observed images. The pixels dominated by the light from younger stellar populations (“younger pixels”) with $(U - 3.6 \mu\text{m}) \lesssim 0.72 \text{ mag}$ are plotted in different colors according to the branch-like feature (see the text) that they appear to be part of. The average uncertainty as a function of magnitude is indicated by the error bars along the right side of this panel. A reddening vector with $A_V = 0.5 \text{ mag arcsec}^{-2}$ is plotted at the lower left. (b) Spatial distribution of the color-coded and light gray pixels selected in panel (a). Dotted contours trace the *Spitzer* $8.0 \mu\text{m}$ PAH emission. The younger pixels form *contiguous* regions; they are *not* randomly distributed. Different branch-like features in panel (a) correspond to regions at both systematically different galactocentric radius and with systematically different PAH emission. The younger pixels on the red-coded branch correspond to regions with strong PAH emission, and likely significant A_V , that are also relatively close-in; the purple pixels are faint at $8.0 \mu\text{m}$, suffer little extinction, and are found at larger distances from the center.

ing the mass fraction of a mixed stellar population within a resolution element and suffering a total extinction of $A_V = 1.0 \text{ mag arcsec}^{-2}$.

Before we proceed, we first perform several visual checks to ensure this separation of younger and older pixels is indeed acceptable. At colors bluer than $(U - 3.6 \mu\text{m}) = 0.72 \text{ mag}$, groups of pixels—or “branch-like features”—seem to have similar slopes as the reddening vector, suggesting that they represent young stellar populations affected by dust. This agrees with the notion (e.g., van Houten 1961; Knapen et al. 1991; Regan et al. 2004; Barmby et al. 2006) that dust is strongly associated with active and recent SF regions. On the redder side of the pCMD, the brighter pixels ($\mu_V \lesssim 21.9 \text{ mag arcsec}^{-2}$) form a distribution with a positive slope (i.e., perpendicular to the reddening vector), indicating that a mechanism other than dust extinction might affect the fluxes in these pixels. Since the younger stellar populations tend to be much brighter than the older stellar populations (see Figure 1), for the lower surface brightness (μ_V) pixels, the fraction of light from younger stellar populations as well as its corresponding dust extinction would be smaller. The theoretical tracks in Figure 3 suggest this would result in a pile-up of points along a fairly vertical line, e.g., the dash-dotted line at $(FUV - 3.6 \mu\text{m}) = 0.76 \text{ mag}$. We therefore conclude that our separation of younger and older pixels is reasonable, at least to first order. We will perform several more checks to confirm that this separation is appropriate (see below). At this point and at the present resolution, we do not see any special features indicating possible pixels dominated by the light from “extremely” young stellar populations (i.e., $t \lesssim 10\text{--}100 \text{ Myr}$, see Figure 2). Considering the effect of light

blending, the light from extremely young stellar populations would most likely be diluted, and hence the separation of pixels simply into younger and older pixels seems to be sufficient for this galaxy (and galaxies viewed at similar linear resolution).

Figure 4(b) shows the spatial distribution of the younger and older pixels selected in Figure 4(a). The *Spitzer*/IRAC 8.0 μm PAH emission—an indicator of nearby SF-activity (e.g., Helou et al. 2004; Calzetti et al. 2005, 2007)—is overplotted in dotted contours. The distributions of younger pixels and 8.0 μm PAH emission do not exactly overlap, but are shifted slightly with respect to one another. Since the directions of these shifts are not constant, they are not the result of astrometric error in the World Coordinate System (WCS) of the images, but are genuine features, as shown by Calzetti et al. (2005). The most important result obtained from Figure 4(b) is that—while no coordinate information is used to select the younger pixels in Figure 4(a)—the selected pixels are grouped together into cohesive regions that coincide, or are close to peaks in the IRAC 8.0 μm emission. Moreover, different branch-like features in Figure 4(a) turn out to correspond to regions at both systematically different distances from the galaxy center and systematically different PAH surface brightness. The younger pixels that form the high-surface brightness (μ_V) feature that is color-coded red in Figure 4(a) originate mostly from two regions that are located near one of the strongest peaks in the 8.0 μm emission and likely suffer significant extinction. Their high surface brightness appears mostly due to the relatively small distance from the galaxy center and exponential decline in surface brightness of the disk of NGC 0959 (e.g., Héraudeau & Simien 1996; Taylor et al. 2005). Younger

pixels on progressively lower surface brightness features (color-coded in order: orange, gold, green, blue and purple) correspond to regions with progressively larger distance from the center and fainter PAH emission (smaller A_V).

To further confirm that our selection of the younger pixels is *not* a random result, we also visually compare Figure 4b to color composite images of NGC 0959. Figure 5 shows *UVR* color composites at two different spatial resolutions. Both are composed from the same *U*-, *V*-, and *R*-band images observed at the VATT (Taylor et al. 2005). Figure 5(a) is presented at the original pixel scale of $0''.37 \text{ pixel}^{-1}$, with the PSFs in all images matched to $\sim 1''.3$ FWHM. In Figure 5(b), the pixel scale and resolution were matched to that of the *GALEX* NUV image, i.e., $1''.5 \text{ pixel}^{-1}$ and $5''.3$ FWHM. *Spitzer*/IRAC $8.0 \mu\text{m}$ contours (green) are overlaid in the latter image for a comparison to the pixel-map (Figure 4(b)). We find that the spatial distribution of the selected *younger* pixels clearly follows that of *bluer* regions in NGC 0959.

2.3.5. *Selecting the Theoretical V-to-3.6 μm Flux Ratio*

Having separated the “younger” and “older” pixels, we now want to estimate the theoretical extinction-free flux ratio for each pixel. As mentioned above, however, the theoretical β_V value cannot be simply selected from Figure 2, due to the smoothing over stellar populations and subsequent blending of light. For pixels dominated by the light from older stellar populations, this should not be a major problem, since their theoretical flux ratios do not change much with age (see Figure 2). The problem is the effect on pixels dominated by younger stellar populations. While a young SSP has a theoretical flux ratio of ~ 5 (or up to ~ 11 for an extremely young stellar population),

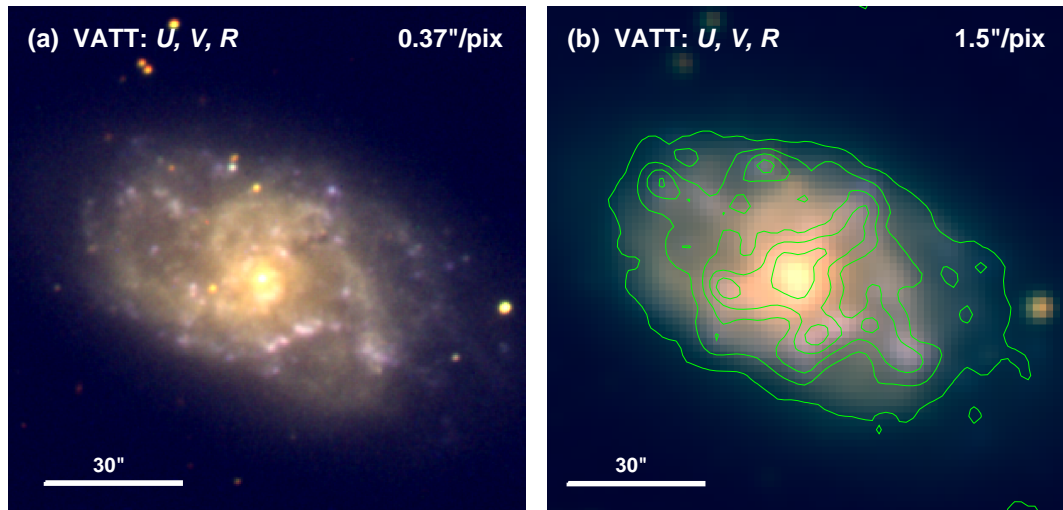


Figure 5. *UVR* color composite images of NGC 0959 at two different spatial resolutions. (a) A color composite image constructed at the original pixel scale of the VATT CCD, $0''.37 \text{ pixel}^{-1}$ with a seeing of $1''.3$ FWHM. Dust lanes and stellar populations with different color are readily discernable in this image. (b) A color composite image constructed from images that are resampled to the *GALEX* pixel scale of $1''.5 \text{ pixel}^{-1}$, and convolved to the *GALEX* PSF of $\sim 5''.3$ FWHM. IRAC $8.0 \mu\text{m}$ emission is indicated by green contours. Compared to the higher resolution image, dust lanes and stellar populations in this lower resolution image are not as evident. However, the blue young stellar populations remain clearly visible in the lower resolution image.

the extinction-free β_V value for mixed stellar populations depends strongly on how large a fraction of the light originates from underlying and neighboring older stellar populations. Since we cannot measure the exact fractions of light from younger and older stellar populations, we have to find another way to estimate theoretical β_V values.

We first calculate the flux ratio of the observed V and $3.6\ \mu\text{m}$ images for each pixel to characterize the effects of light blending. The result is plotted in Figure 6, where the white-colored histogram represents the distribution of β_V values for the pixels dominated by the light from older stellar populations (“older” pixels), and the gray-colored histogram for those dominated by the light from younger stellar populations (“younger” pixels). The older pixels have a peak around $\beta_V \simeq 1.0$ with a secondary peak, or a shoulder, at $\beta_V \simeq 1.25$. This confirms our assumption that light blending has only a minor effect on older pixels. The younger pixels display a peak at $\beta_V \simeq 1.32$, which is much lower than the theoretical ratio ($4 \lesssim \beta_V \lesssim 7$, see Figure 2). This indicates that younger pixels are significantly affected by the light from underlying and neighboring older stellar populations. An important feature of the distribution for the younger pixels is that the observed range of β_V values is narrow and concentrated within $0.9 \lesssim \beta_V \lesssim 1.6$. This implies the effect of light blending is rather uniform and consistent for these pixels. Stated differently, the contaminating older stellar population is distributed much more smoothly than the younger stellar population (see Figure 5, Figure 13, and Figures 15–17).

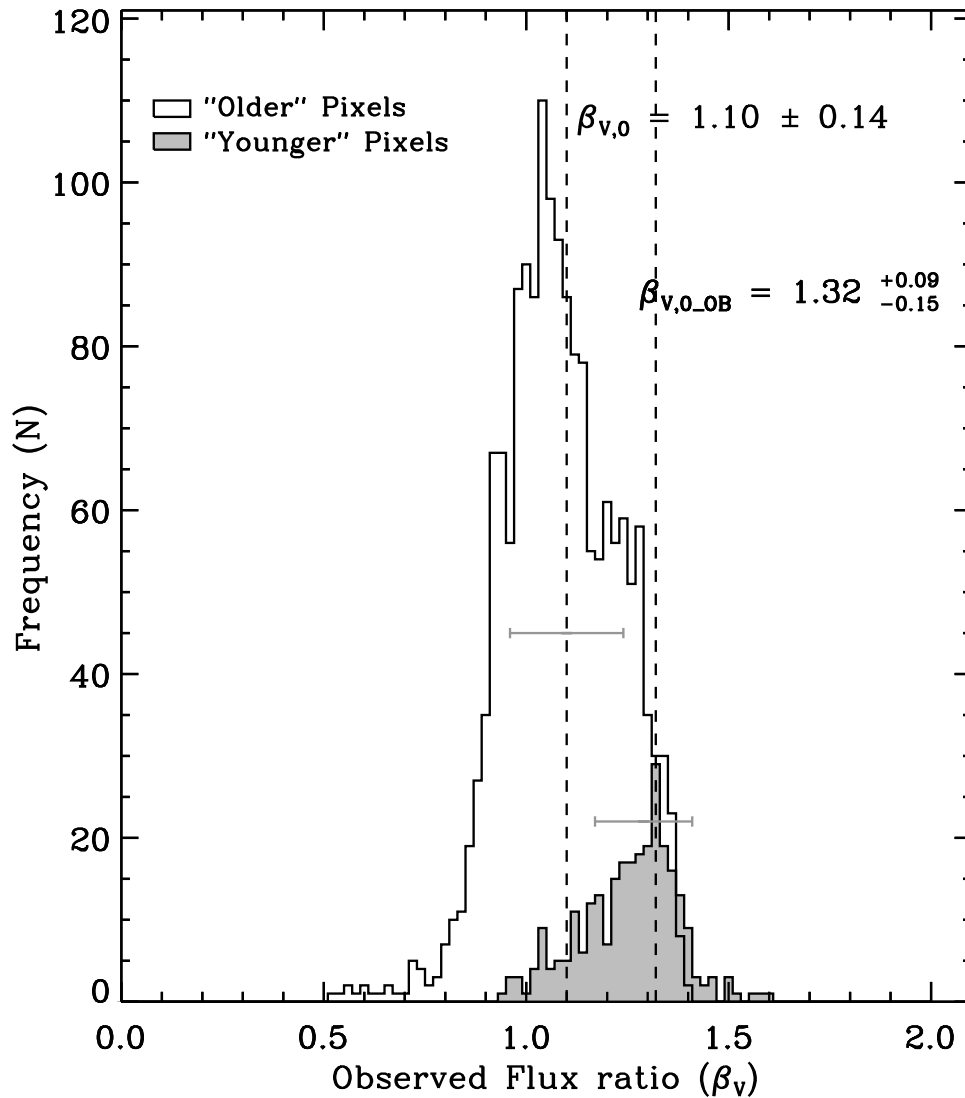


Figure 6. Histograms of observed V -to- $3.6\ \mu\text{m}$ flux ratio, β_V , for individual pixels dominated by the light from older stellar populations (“older pixels”) and younger stellar populations (“younger pixels”), as selected in Figure 4. For both populations, the low-ratio tail of the distribution—presumably due to dust extinction—is more extended than the tail on the high-ratio side. We adopt an extinction-free flux ratio, $\beta_{V,0}$, of 1.10 ± 0.14 for the older pixels and of $1.32^{+0.09}_{-0.15}$ for the younger pixels. Once 2σ clipped mean and peak values are selected for older and younger pixels, respectively, corresponding uncertainties are determined from the FWHM of β_V distributions. Because of light blending from different populations contributing to the flux in a given pixel, the β_V values for the young stellar population are significantly reduced compared to those calculated for SSP models in Figure 2.

Another important feature of Figure 6 is that the tail of the distribution toward lower β_V values is larger than the tail toward higher values. Since dust extinction is the primary cause for the reduction of the V -band flux, the pixels with anomalously low β_V values are most likely located in the high-extinction regions within the galaxy. While both groups of pixels have low- β_V tails, the relative size of the tail, compared to the size of the main distribution, is much larger for the younger pixels. This indicates that dust extinction is more significant for the younger pixels.

Because interstellar dust is usually concentrated in relatively small regions (e.g., Deo et al. 2006)—while most other regions suffer minimal dust extinction—we should be able to estimate the intrinsic dust-free V -to- $3.6\ \mu\text{m}$ flux ratio, $\beta_{V,0}$, for both stellar populations from Figure 6. While the peak of the distribution for the older pixels is at $\beta_V = 1.04$, this value occurs toward the lower end of the distribution. A statistical analysis with 2σ clipping shows that the mean is at $\beta_{V,0} = 1.10$ with a standard deviation of 0.14. Even though the exact value of the intrinsic flux ratio varies from pixel-to-pixel due to the different stellar population components in each pixel, we adopt this value of $\beta_{V,0} = 1.10 \pm 0.14$ as the dust-free flux ratio for the older pixels. Unlike the older pixels, the β_V distribution of the younger pixels is more asymmetric, with a much larger tail toward lower β_V values. After 1σ clipping, the statistical mean is $\beta_V = 1.29$, which is smaller than the peak value of $\beta_V = 1.32$. Because younger stellar populations are more affected by dust than older stellar populations, which is also apparent from the much larger and wider lower- β_V tail, we elected to use $\beta_{V,0_OB} = 1.32^{+0.09}_{-0.15}$ (the peak β_V value) as the extinction-free flux ratio

for the younger pixels. The added subscript, OB, indicates that the value is for the pixels dominated by the light from younger stellar populations, but does not imply that such pixels have no light contributed by older stellar populations.

2.3.6. Calculating the Flux Difference

Having determined appropriate extinction-free flux ratios, the next step is to calculate the V -band flux difference, Δf_V , for each pixel. Using the theoretical flux defined in Equation 2.2, the flux difference is calculated as

$$\Delta f_V = [f_V - (\beta_{V,0} \times f_{3.6\mu\text{m}})], \quad (2.4)$$

where, f_V and $f_{3.6\mu\text{m}}$ are the observed pixel fluxes in the optical V and IRAC 3.6 μm bands, and $\beta_{V,0}$ is the estimated extinction-free flux ratio. The distribution of Δf_V values is shown in Figure 7 for both younger and older pixels. The solid histograms are for the Δf_V values calculated from our adopted values for $\beta_{V,0}$, while the dashed (dotted) histograms are computed for $\beta_{V,0}$ values at the upper (lower) bound of the quoted 1σ uncertainty range in Figure 6. While Figure 6 shows simply the level of the V -band flux relative to the flux in 3.6 μm filter, Figure 7 shows the *absolute* difference between the observed and estimated theoretical V -band pixel-fluxes. Regardless of the selection of $\beta_{V,0}$, both histograms—for both younger and older pixels—show that the number of pixels with positive Δf_V goes to zero quickly, and that there are distinct tails extending to large negative values of Δf_V . For the younger pixels, the effect of the uncertainty in the selection of $\beta_{V,0}$ is small (i.e., the three histograms show similar distribution in Figure 7(b)). The older pixels, however, are affected more (Figure 7(a)). Since older stellar populations tend to have less dust intermixed, and

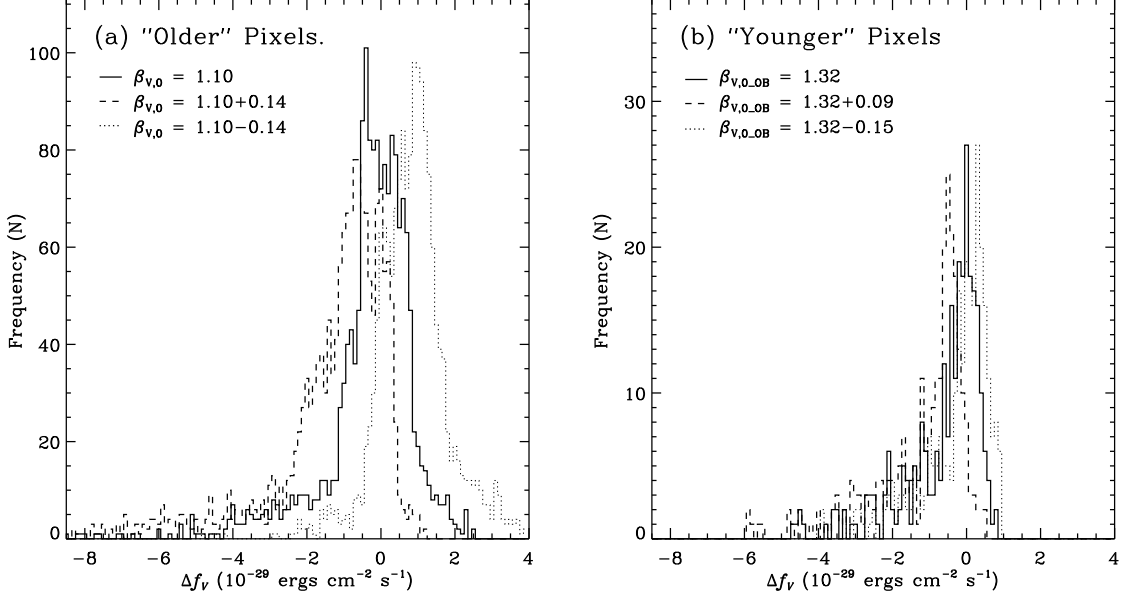


Figure 7. Histograms of Δf_V , the difference between the observed and theoretical V -band flux for selected pixels with light dominated by (a) older and (b) younger stellar populations. In each panel, the solid histogram is for the adopted value of $\beta_{V,0}$, while the dashed (dotted) histogram assumes a value for $\beta_{V,0}$ that corresponds to the upper (lower) bound of the uncertainty range determined in Figure 6.

hence suffer less extinction, the dashed histogram for the larger value of $\beta_{V,0}$ produce an excess of pixels with large values of A_V . On the other hand, the dotted histogram for the smaller value of $\beta_{V,0}$ will produce many pixels with an unphysical excess of visual flux, indicating that this value must be a robust lower bound on $\beta_{V,0}$. This confirms that $\beta_{V,0} = 1.10$ is a reasonable and appropriate value for the older pixels.

Next, we check the spatial distribution of the calculated Δf_V values. If the distribution of negative Δf_V follows genuine galactic features, such as SF regions, spiral arms, and PAH emission, then this strengthens our argument that our method largely traces the dust extinction. The spatial distribution of Δf_V is shown as a pixel-coordinate map in Figure 8, with the IRAC $8.0 \mu\text{m}$ emission overlaid as dotted

contours. This map demonstrates that the distribution of Δf_V values is not random at all, but closely associated with genuine galactic structures. Visual comparison of this map to the color composite image in Figure 5*b* confirms that pixels with a large deficiency of observed V -band flux are not simply corresponding to pixels appearing darker (lower surface brightness). Instead, pixels with $\Delta f_V < 0$ are distributed around the regions that appear bluer, as well as near the center of the galaxy. The higher resolution image of Figure 5*a* shows that some pixels with larger negative values of Δf_V (darker gray in Figure 8) trace the visible dust lanes, seen in silhouette, and the bluer SF regions. This demonstrates that even though some of the dust is not visually conspicuous (as in the lower resolution image in Figure 5(b)), our method is capable of estimating dust extinction and its spatial distribution from observations in only two broadband filters—with a third filter (U -band) serving only to robustly separate younger pixels from older pixels (Figures 3 and 4). Since regions with visible or plausible dust content are recovered well by our method, this gives us confidence that regions for which this method indicates a low dust content could also be real.

Before we proceed to estimate the amount of dust extinction in each pixel, there is one more check that we must perform to support our separate treatment of the younger pixels. The main panel of Figure 9 shows a map of Δf_V for the younger pixels for our adopted value of $\beta_{V,0_{OB}} = 1.32$, while the inset shows the result when these pixels are treated as older pixels with $\beta_{V,0_{OB}} = \beta_{V,0} = 1.10$. The lighter shade of gray of the pixels in the inset panel indicates that most of them have positive Δf_V , suggesting that the observed V -band flux is equal to or larger than expected from

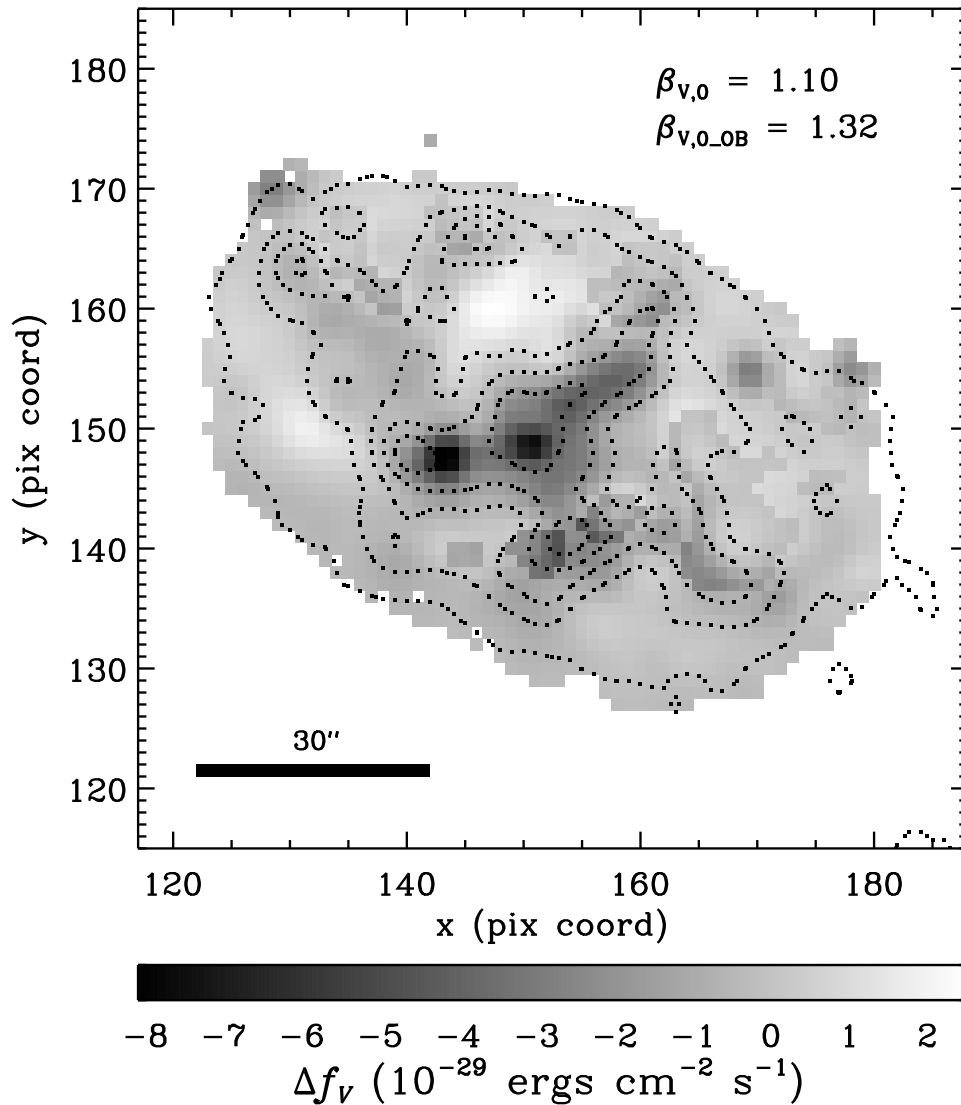


Figure 8. Pixel map of the flux difference, Δf_V , rendered at the resampled pixel scale of 1.5 pixel^{-1} . Darker gray-scale levels indicate a larger deficiency of observed V -band flux compared to the modeled intrinsic flux. Black dotted contours trace the IRAC $8.0 \mu\text{m}$ PAH emission. While it is hard to visually trace the distribution of dust in Figure 5(b), the locations of the dust lanes in Figure 5(a) generally agree with the distribution of the flux-deficient pixels in the present figure.

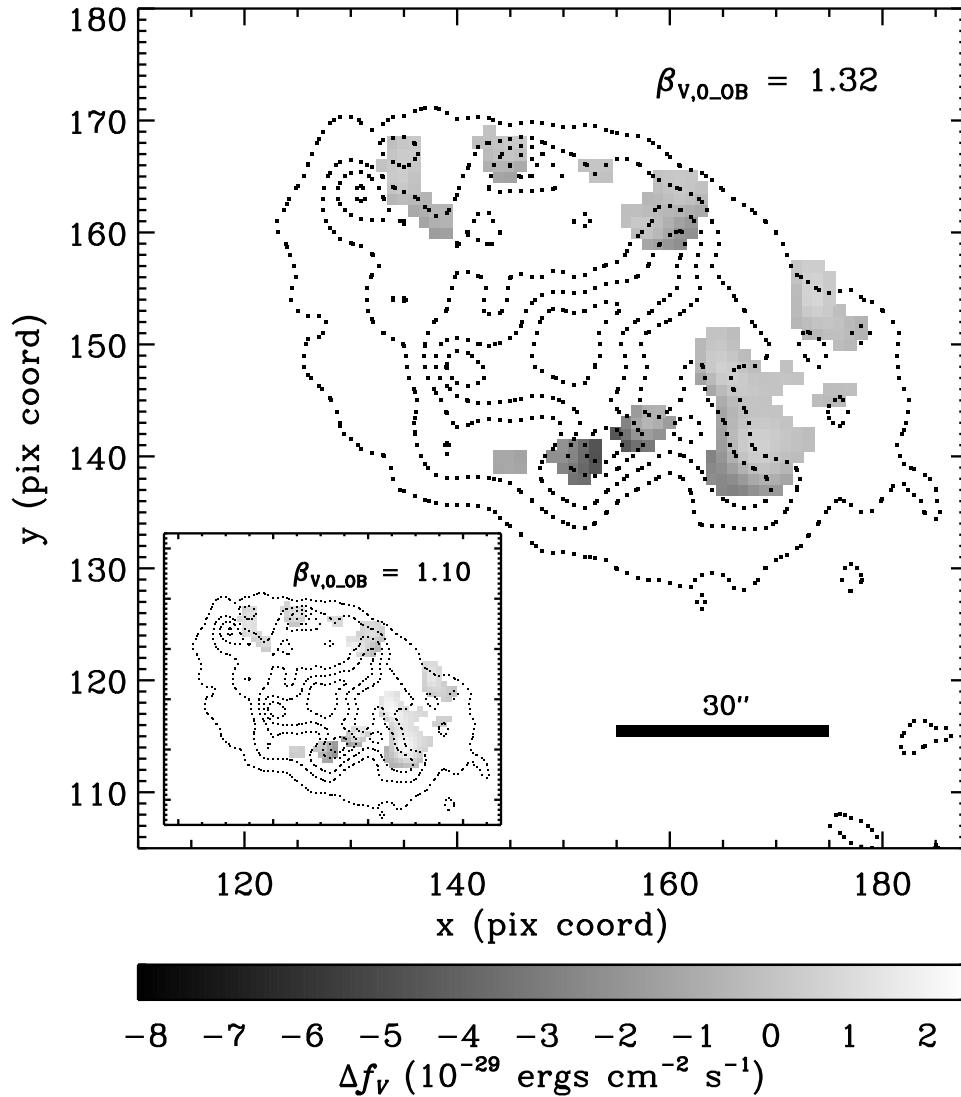


Figure 9. Comparison of the flux difference, Δf_V , inferred for pixels dominated by younger stellar populations. The main panel shows the result when the younger pixels are treated separately, adopting $\beta_{V,0,OB} = 1.32$. Here, most pixels show that they are missing the V-band flux, as expected. The inset panel shows the result for no such special treatment (i.e., assuming $\beta_{V,0,OB} = \beta_{V,0} = 1.10$, as for pixels dominated by old stellar populations). Here, most of the younger pixels show an unphysical *excess* of the observed V-band flux. Black dotted contours trace $8.0 \mu\text{m}$ PAH emission.

the $3.6\ \mu\text{m}$ data, i.e., that the younger pixels miss either no V -band flux or show an unphysical *excess* of the observed V -band flux. Since young stellar populations are usually associated with relatively large amounts of dust (e.g., van Houten 1961; Knapen et al. 1991; Regan et al. 2004; Barmby et al. 2006), a value of $\beta_{V,0} = 1.10$ is clearly too small for the younger pixels. Our separate treatment of the younger pixels, adopting $\beta_{V,0\text{-OB}} = 1.32^{+0.09}_{-0.15}$ as outlined above, is therefore appropriate. For that larger value of $\beta_{V,0}$, the younger pixels are found to suffer small-to-moderate amounts of extinction by dust, consistent with the known presence of dust at or near these regions of recent star formation and producing consistent results with previous studies.

2.3.7. Measuring the Dust Extinction

We can now estimate the most likely amount of dust extinction in each pixel. With $\beta_{V,0} = 1.10$ (and $\beta_{V,0\text{-OB}} = 1.32$) and AB-magnitude zeropoint, $V_{\text{zp,AB}} = 48.59$ mag, Equation 2.3 becomes

$$A_V = m_V - [-2.5 \log(\beta_{V,0} \times f_{3.6\ \mu\text{m}}) - V_{\text{zp,AB}}]. \quad (2.5)$$

We cannot simply apply Equation 2.5 to all pixels, however, since some pixels have $\beta_V > \beta_{V,0}$ (see Figure 6) and $\Delta f_V > 0$ (see Figure 7), i.e., seemingly implying an unphysical negative dust extinction. Because the $\beta_{V,0}$ value is the *estimated* extinction-free flux ratio, rather than the true dust-free ratio, it is possible that some pixels have an observed β_V value that is larger than $\beta_{V,0}$. We therefore have to be careful how we treat these pixels in our analysis.

As mentioned above, the pixels with positive Δf_V (Figure 8) appear darker than neighboring regions in the color composites of Figure 5. Considering also that the $8.0\ \mu\text{m}$ PAH emission is weak in these regions (i.e., these pixels are surrounded by outer $8.0\ \mu\text{m}$ contours with large spacing between neighboring contours), these positive Δf_V pixels are not caused by SF-activity, but are most likely the result of underestimating the intrinsic $\beta_{V,0}$ value. The actual amount of dust extinction might also be minimal or zero ($A_V \simeq 0$) for these pixels. We adopted a single $\beta_{V,0}$ for younger and for older pixels, yet the intrinsic flux ratio for each pixel will vary slightly based on different factors. As a result, some pixels with positive Δf_V are expected, even in the absence of noise. For our adopted $\beta_{V,0}$ of 1.10 (1.32) for older (younger) pixels, most pixels with excess flux have $\Delta f_V \lesssim 1.0 \times 10^{-29}\ \text{erg cm}^{-2}\ \text{s}^{-1}$, and only a very small fraction has an excess as large as $\sim 2.0 \times 10^{-29}\ \text{erg cm}^{-2}\ \text{s}^{-1}$ (see Figure 7). In the following, we will therefore assume that these pixels suffer no measurable extinction, i.e., that $A_V = 0\ \text{mag arcsec}^{-2}$.

2.3.7.1. *Impact of the Uncertainty in $\beta_{V,0}$*

Since neither the relationship between A_V and Δf_V nor the relationship between Δf_V and β_V is linear, the 1σ errors in the estimated extinction-free flux ratios ($\sigma_{\beta_{V,0}} = \pm 0.14$ and $\sigma_{\beta_{V,0,\text{OB}}} = +0.09$ and -0.15) cannot be simply converted to the corresponding σ_{A_V} values. Instead, we will assess *how* the distribution and values of A_V change, as we vary the estimated dust-free flux ratio from the adopted value of $\beta_{V,0}$ to $\beta_{V,0} \pm \sigma_{\beta_{V,0}}$.

Figure 10 shows the spatial distribution of the estimated dust extinction, A_V , for each pixel in NGC 0959, for two sets of theoretical extinction-free flux ratios. Figure 10(a) shows the distribution of A_V inferred for our adopted $\beta_{V,0}$ values of 1.10 and 1.32 for older and younger pixels, while Figure 10(b) shows the result for $\beta_{V,0}$ values set at the higher end of the uncertainty range (i.e., $\beta_{V,0} = 1.24$ and 1.41, respectively). The mean and maximum dust extinction for all pixels in Figure 10(a) (Figure 10(b)) are $\overline{A_V} = 0.064$ (0.15) and $A_{V,\max} = 0.80$ (0.93) mag arcsec⁻². As expected, the dust-extinction map for the lower limit, $\beta_{V,0} - \sigma_{\beta_{V,0}}$ (not shown here), is covered mostly by $A_V = 0$ pixels. These results are summarized in Table 1, where the last column indicates the fraction of pixels with $A_V = 0$ mag arcsec⁻² in the image.

Even though the estimated $\beta_{V,0}$ value changes, Figure 10 shows that the distribution of dust extinction follows the structures of the galaxy and the 8.0 μm contours. Figure 10 and Table 1 also show that the effect of varying the theoretical $\beta_{V,0}$ value is not equal to simply adding or subtracting a constant value ΔA_V to the dust-extinction values calculated for our adopted value of $\beta_{V,0}$. As $\beta_{V,0}$ change from 1.10 and 1.32 (Figure 10(a)) to 1.24 and 1.41 (Figure 10(b)), some pixels near pixels with $A_V \gtrsim 0$ mag arcsec⁻², which originally were deemed extinction-free, now suffer a slight amount of dust extinction. Other pixels that are further away, e.g., pixels in areas that are faint at 8.0 μm , stay at $A_V = 0$ mag arcsec⁻². This confirms our assumption that these pixels have minimal or no dust extinction.

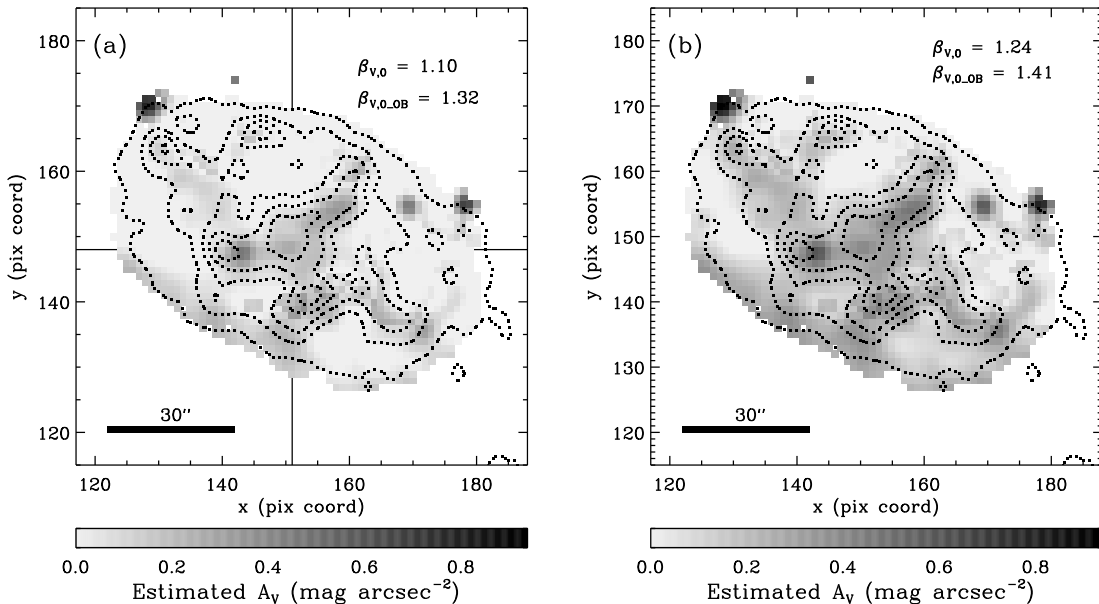


Figure 10. Spatial distribution of A_V , inferred for $\beta_{V,0}$ values of (a) 1.10 and 1.32 (mean), and (b) 1.24 and 1.41 (upper limit), for older and younger pixels, respectively. The same gray-scale is used for both (a) and (b). The pixels with the lightest shade of gray have no detectable extinction ($A_V = 0 \text{ mag arcsec}^{-2}$). The darkest pixels have a visual extinction $A_V \simeq 0.8 \text{ mag arcsec}^{-2}$ in (a) and $\simeq 0.93 \text{ mag arcsec}^{-2}$ in (b). Dotted contours trace the $8.0 \mu\text{m}$ PAH emission. These extinction maps indicate that the higher extinction coincides with SF-regions that appear blue in the color composite images (see Figure 5), as well as with several dust features visible in Figure 5(a).

Table 1
Dust Extinction Based on Different $\beta_{V,0}$ Values

Selected $\beta_{V,0}$ level	$\beta_{V,0}$	$\beta_{V,0,OB}$	$\overline{A_V}$ (mag arcsec $^{-2}$)	$A_{V,max}$ (mag arcsec $^{-2}$)	% of pixels with $A_V = 0$
Estimated $\beta_{V,0}$	1.10	1.32	0.064	0.80	45.0%
Upper (+ σ)	1.24	1.41	0.15	0.93	16.4%
Lower ($-\sigma$)	0.96	1.27	0.015	0.63	83.1%

2.3.7.2. Analysis at Higher Spatial Resolution as Confirmation

While individual dust features usually are small-scale structures, our initial analysis was performed at the low spatial resolution of the *GALEX* NUV image. To determine if our result is a true measure of dust extinction or not, we repeat the same analysis with *higher* spatial resolution images, using only *U*, *V*, and IRAC 3.6 μm images. Since the 3.6 μm image has the coarsest pixel scale of 1''.2 pixel $^{-1}$ and a PSF with $\sim 2''.2$ FWHM, the ground-based *U*- and *V*-band images are registered, resampled, and convolved to match the orientation, pixel scale, and resolution of the 3.6 μm image. Figure 11 shows the distribution of estimated A_V values at this higher spatial resolution. The 8.0 μm contours are overplotted at the native IRAC resolution of $\sim 2''.3$ FWHM.

An important difference between the two spatial resolutions is that, while the maximum dust extinction is $A_{V,max} \simeq 0.8$ mag arcsec $^{-2}$ in Figure 10(a), $A_{V,max}$ in Figure 11 reaches ~ 2.3 mag arcsec $^{-2}$. This jump in A_V value is expected, since the coarser *GALEX* PSF smoothes out the effect of dust extinction and reduces the averaged A_V for each pixel. Since the ratio of the effective areas of the *GALEX* NUV

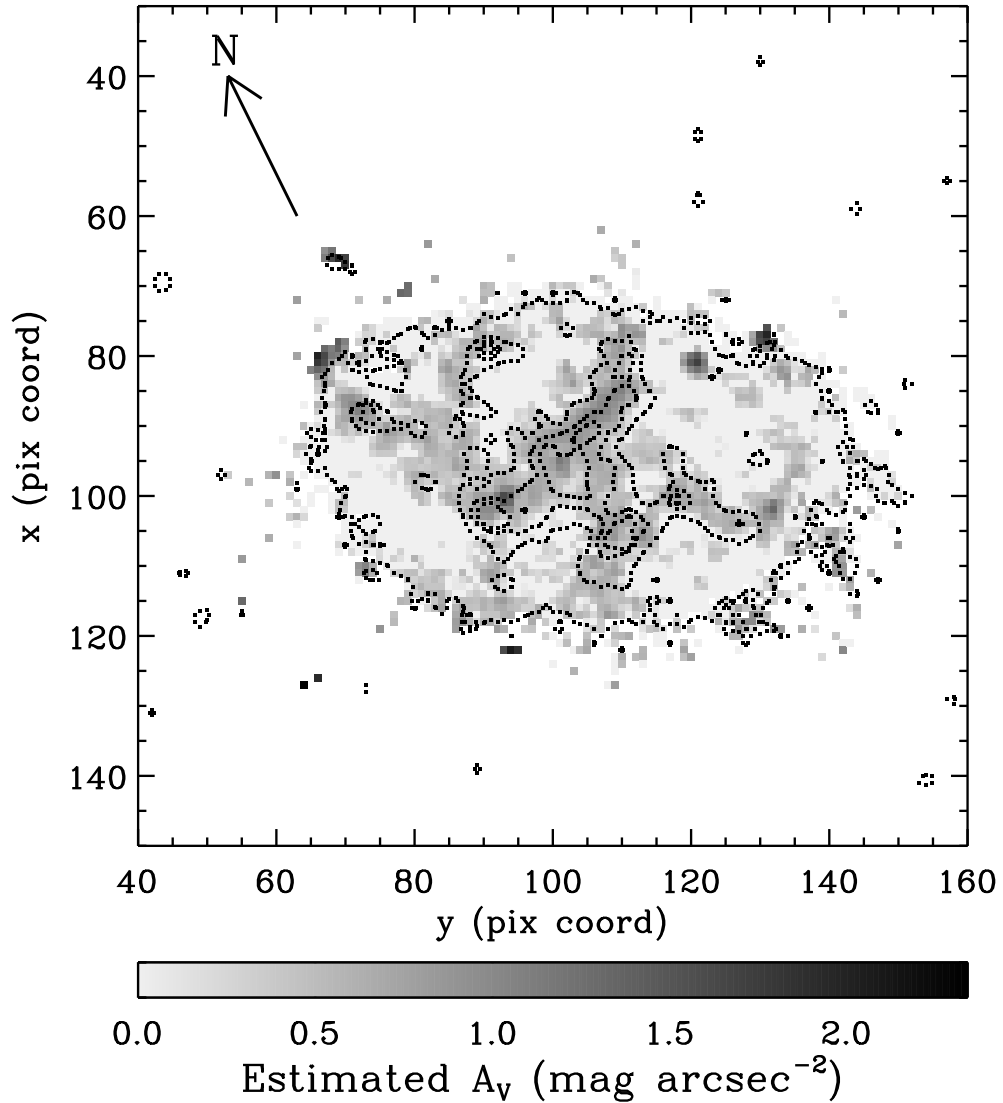


Figure 11. Distribution of dust extinction at the (higher) spatial resolution of the *Spitzer*/IRAC $3.6\ \mu\text{m}$ image ($1''.2\ \text{pixel}^{-1}$ and $\sim 2''.2$ FWHM). The dotted contours trace $8.0\ \mu\text{m}$ PAH emission at a native resolution of $\sim 2''.3$ FWHM. This map is presented in the instrument coordinate system, oriented as indicated at the upper left.

and *Spitzer* $3.6\ \mu\text{m}$ PSFs is $(5''3/2''2)^2 \simeq 6$, the typical extinction per pixel should change, to first order, by $\sim 1.9\ \text{mag arcsec}^{-2}$. Other factors, such as uncertainties in estimating $\beta_{V,0}$ and blending of light from structures that are unresolved with the coarser while resolved with the smaller PSF, also play a role. The observed shift in A_V of $\Delta A_V \simeq 1.5\ \text{mag arcsec}^{-2}$ is therefore broadly consistent, while the $0.4\ \text{mag arcsec}^{-2}$ difference illustrates the effects of the clumpiness of stars and dust on scales of $2''2$ – $5''3$ (~ 110 – 250 pc at the distance of NGC 0959). The higher spatial resolution images are better at tracing smaller dust features and their higher extinction values within a single pixel. Nonetheless, the overall distribution of dust extinction is similar in Figures 10 and 11. While the fine details of the measurable dust extinction and its spatial distribution depend on the resolution, both extinction maps trace the $8.0\ \mu\text{m}$ PAH emission and trace genuine galactic structures.

In conclusion, from the series of tests described above, we find that the two-dimensional distribution of dust extinction can, indeed, be reliably estimated by our pixel-based method and the observed V -to- $3.6\ \mu\text{m}$ flux ratio.

2.3.7.3. *Interesting Regions*

Having produced the spatial distribution maps of dust extinction in NGC 0959, we now discuss some of the most interesting dust features in Figure 10 (and Figure 11). While the distribution of regions with larger A_V closely traces the SF regions, a not previously identified bar, and arm-like structures, there are several regions that draw our attention. These are: (1) a compact region at the northeast edge (NE; upper-left) of NGC 0959 that appears to suffer very high extinction; (2) another such

high-extinction region at the northwest edge (NW; upper-right); and (3) an extended area of moderate dust extinction along the southeast (SE; bottom), rim of the galaxy. Since all of these features are also visible in Figure 11, these must be real features. To visually confirm small-scale dust features in NGC 0959, and check their interpretation as genuine galactic features as opposed to chance superpositions of unrelated objects, we created another color composite from Archival *HST*/WFPC2 F450W, F606W, and F814W images, shown in Figure 12. The two circles in this image mark regions (1) and (2).

The NE high- A_V region, region (1), is centered around pixel coordinates $[x, y] \simeq [128, 169]$ in Figure 10. Even though nothing conspicuous is visible in the low-resolution color composite (Figure 5a), the *HST* image (Figure 12) reveals a compact, bright red source at the center of the marked region. Without morphological indicators, multi-filter photometry, or spectroscopic information for this particular object, it is hard to decide whether this is a reddened stellar population within NGC 0959's disk, or a background (foreground) object that is visible through (against) the disk. We do note, however, that the color of this object is very similar to that of the edge-on background galaxy that is visible at the bottom left of Figure 12. Region (2) is located in the NW corner of the galaxy around $[x, y] \simeq [178, 155]$. There is no F606W coverage for this region in Figure 12, but there is no object discernable in the other two *HST* filters. At present, we lack sufficient information to establish if these regions are truly associated with NGC 0959. Until further evidence is obtained, we will treat these regions as a part of the galaxy.

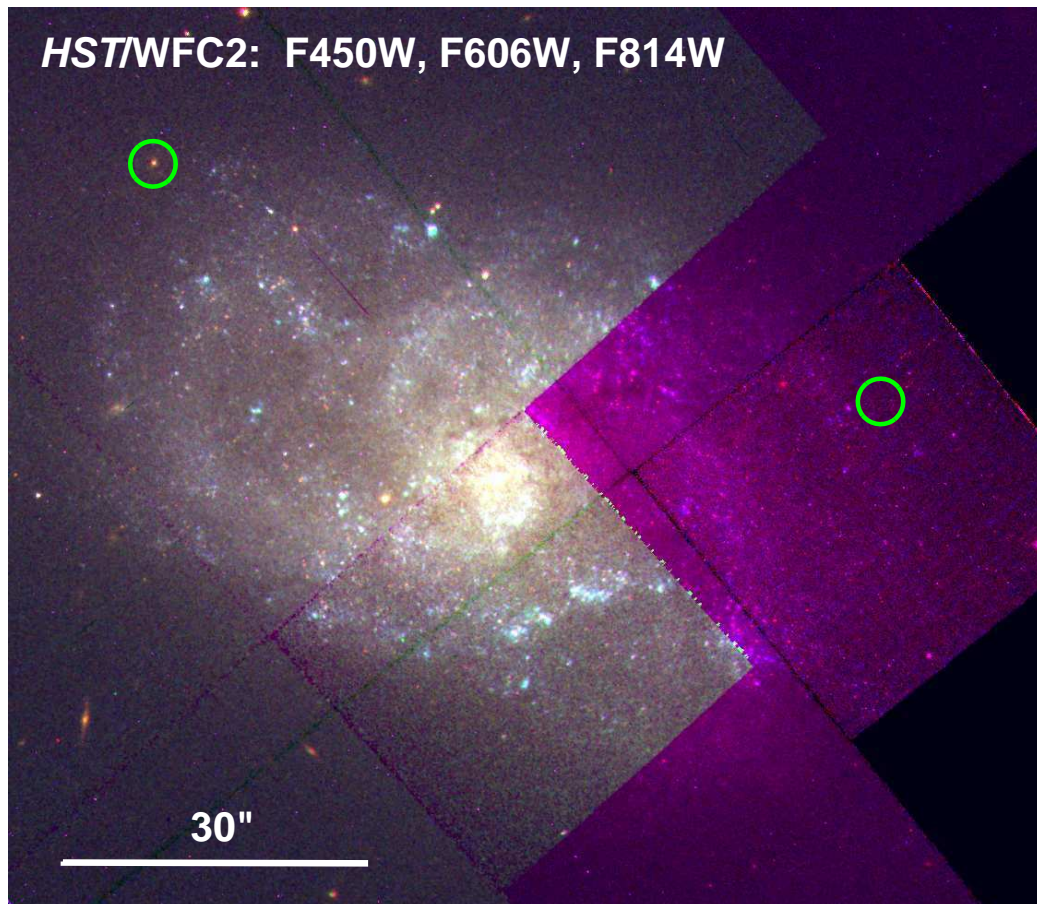


Figure 12. Color composite of Archival *HST*/WFPC2 F450W, F606W, and F814W images. The green circles indicate the two regions with high apparent A_V in Figure 10. While there is no object evident within the right green circle, the circle in the upper left corner contains a red object. Along the southern rim of NGC 0959, a faint dust lane is discernable that appears to trace an outer arm. The typical extinction along this dust feature is $A_V \simeq 0.3\text{--}0.4 \text{ mag arcsec}^{-2}$ in Figure 10.

The pixels comprising feature (3), the moderate-extinction region running along the SE rim of the galaxy disk, initially did not show up as having particularly large-negative Δf_V values (see Figure 8). Once the dust extinction is calculated, these pixels do stand out with low–moderate A_V values, indicating the presence of an extended dust structure. The higher-resolution dust extinction map (Figure 11) also shows that the pixels in this region suffer higher dust extinction than inferred for the opposite (NW) rim of the galaxy. Visual comparison to Figure 12 confirms that a faint dust lane runs along the SE rim, apparently tracing an outer spiral arm or armlet. This shows that our dust extinction measurement using the V -to- $3.6\ \mu\text{m}$ flux ratio is sensitive to even low amounts of dust extinction per resolution element, whether inherently smoothly distributed or resulting from a small filling factor.

2.3.7.4. *Correcting for Dust Extinction*

Finally, using the calculated A_V values for each pixel, we correct the observed V -band image of NGC 0959 to reveal the true underlying stellar populations. The observed (uncorrected) and extinction-corrected images are shown at *GALEX* resolution in the top panels of Figure 13, using the *same* gray-scale lookup table. The surface brightness distribution before extinction correction (Figure 13(a)) has lower contrast overall and fewer high-contrast features. Most conspicuous after applying our dust correction (Figure 13(b)) is that bluer regions in the color composite of Figure 5(b) become much more prominent, while other galactic structures (particularly the central bulge) also become better defined. Especially for areas SE (centered on $[x, y] \simeq [142, 148]$) and NW ($[x, y] \simeq [159, 155]$) of the galaxy center, the V -band sur-

face brightness becomes much brighter in areas where dust lanes are evident in the color composites (Figure 5(a) and Figure 12). The bottom two panels show the observed *Spitzer*/IRAC 3.6 μm and 4.5 μm images (Figures 13(c) and (d)), which trace the distribution of the underlying older stellar populations (e.g., Regan et al. 2004; Willner et al. 2004). These MIR images and the *extinction-corrected* *V*-band surface brightness distribution show excellent qualitative agreement. Therefore, as Regan (2000) did with optical–NIR images and radiative transfer modeling, we successfully corrected the dust extinction with images in only two filters (*V* and 3.6 μm)—with a *U*-band image serving only to robustly separate pixels dominated by the flux from younger stellar populations from those dominated by older stellar populations.

2.4. Application to Other Filters

Given the amount of visual dust extinction, A_V , in each pixel, we can calculate the extinction in any other filter. The extinction in a given filter depends on its throughput as a function of wavelength, as well as on the metallicity of the stellar populations of the galaxy of interest through the adopted extinction curve (e.g., Seaton 1979; Koornneef & Code 1981; Howarth 1983; Cardelli et al. 1989; Calzetti et al. 1994; Gordon et al. 2003). In the following chapter (Chapter 3), we will use UV–MIR multi-filter dust-corrected surface photometry for a detailed analysis of the stellar populations within NGC 0959.

2.4.1. *Extinction Curves*

In general, dust extinction increases toward shorter wavelengths. For metal-poor stellar populations—such as those in the Small Magellanic Cloud (SMC)—the

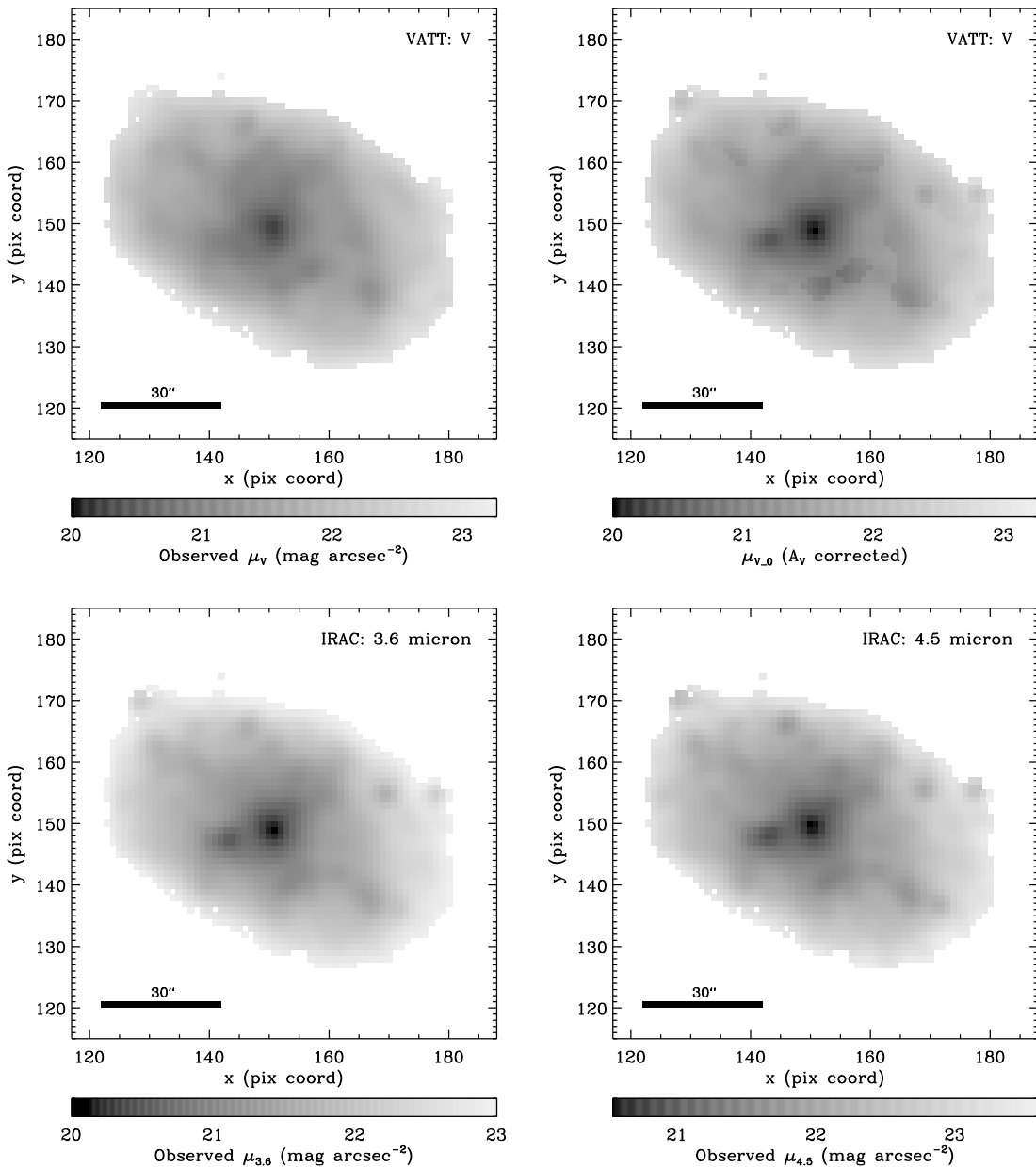


Figure 13. Comparison of observed (top left) and extinction-corrected (top right) V -band images and the observed *Spitzer*/IRAC 3.6 and 4.5 μm images (bottom) of NGC 0959 at *GALEX* resolution. The MIR images are good tracers of the underlying stellar distribution. The extinction-corrected image in V displays more brighter (darker shade) pixels around blue SF regions (see Figure 5) and better resembles the MIR images than does the observed V -band image.

dust-extinction curve is largely monotonic as a function of wavelength. The shape of the extinction curve becomes more complicated for metal-rich stellar populations. Especially the extinction at shorter wavelengths ($\lambda \lesssim 2200 \text{ \AA}$) may be significantly affected by the 2175 \AA interstellar dust feature and the increased steepness of the UV extinction (e.g., Calzetti et al. 1994; Gordon et al. 2003, see also Figure 14 here).

Gordon et al. (2003) compared the observations of many stars to calibrate the extinction curves—the wavelength dependent extinction relative to that at $0.55 \mu\text{m}$ —for SMC, LMC, and MW type dust. Based on Table 4 (and Fig. 10) of Gordon et al. (2003), we interpolated the published extinction curves on a finer wavelength grid. In the NIR, Gordon et al. (2003) have only one data-point for each of the 2MASS JHK_s filters, and the SMC extinction curve in particular appears quite uncertain. To cover longer wavelengths up to the *Spitzer*/IRAC filters, in the NIR and MIR, we adopted the Galactic extinction curve of Fitzpatrick (1999), rescaled for $R = A_V/E(B - V) = 3.1$. The adopted extinction curves for SMC, LMC, and MW metallicities are plotted in Figure 14. For wavelengths shorter than the 2175 \AA interstellar dust feature, the SMC and MW type extinctions differ by ~ 2 mag. The bottom panel of Figure 14 shows the relevant filter throughput curves for comparison. The amount of dust extinction in each filter, A_{filter} , is calculated as a ratio to the extinction in V :

$$A_{\text{filter}}/A_V = \frac{\int_{\lambda} T_{\text{filter}}(\lambda) [A(\lambda)/A_V] d\lambda}{\int_{\lambda} T_{\text{filter}}(\lambda) d\lambda}, \quad (2.6)$$

where, $T_{\text{filter}}(\lambda)$ is the throughput curve for each filter, and $[A(\lambda)/A_V]$ denotes an extinction curve (Figure 14). Table 2 summarizes the computed dust extinction

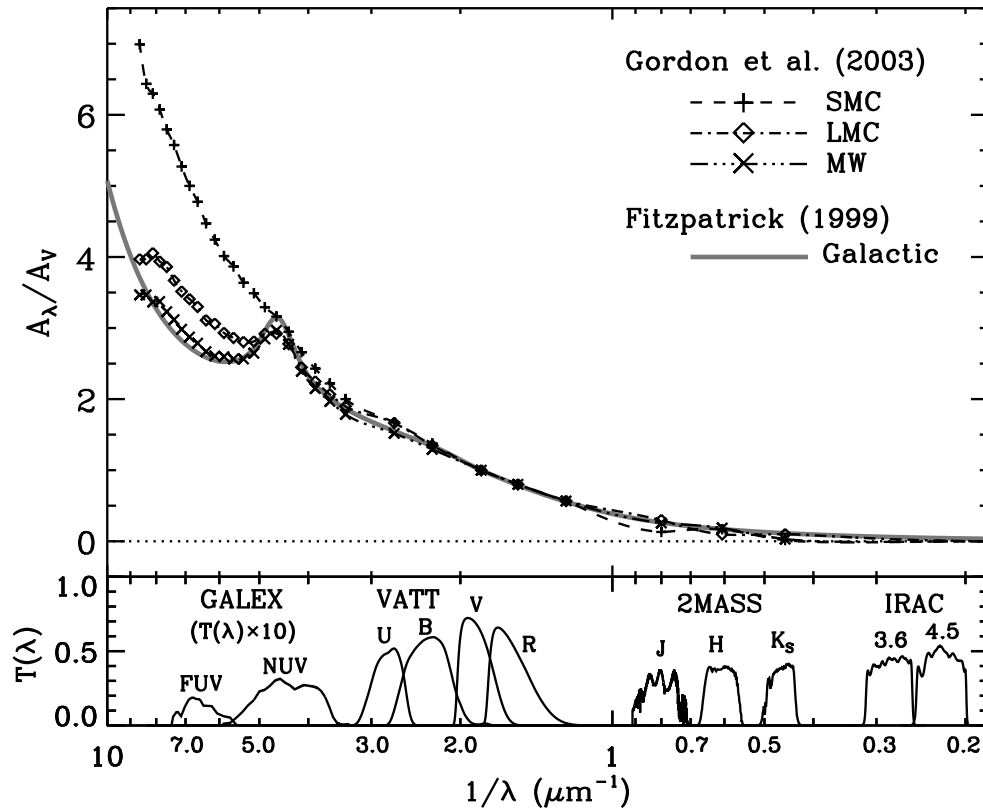


Figure 14. Top panel: extinction curves for SMC (pluses), LMC (open diamonds), and MW (crosses) metallicity from FUV to MIR wavelengths. The smooth extinction curves were interpolated from the data points of Gordon et al. (2003). Also shown is the Galactic extinction curve from Fitzpatrick (1999), which we adopt for the NIR and MIR filters. Bottom panel: total throughput curves, $T(\lambda)$, for different telescope-filter combinations (see also Figure 1). The *GALEX* filter curves were scaled up by a factor of 10 for better visibility.

for the different extinction curves. For the 2MASS JHK_s filters, the extinction calculated from the SMC, LMC, and MW extinction curves of Gordon et al. (2003) differs significantly (indicated with asterisks in Table 2). Since the extinction at longer wavelengths is progressively insensitive to metallicity, we conclude that these values must be highly uncertain. Instead, we use the extinction curve of Fitzpatrick (1999) to provide an upper limit to the dust extinction in the filters longward of $1\ \mu\text{m}$ (parenthesized values in Table 2). Since the extinction is small ($A_{\text{filter}}/A_V < 0.1$), following previous studies (e.g., Fazio et al. 2004; Regan et al. 2004), we assume that there is no measurable dust extinction in the IRAC filters.

An important assumption for the extinction curves described above is that the dust is distributed in the form of a “diffuse-ISM” or in a diffuse-screen geometry, which is applicable only for nearby stars and star clusters *within* our own Galaxy. In extragalactic objects, the dust appears to be distributed in smaller clumps of much higher density (e.g., Deo et al. 2006) intermixed with the stars. Even though the effect of dust extinction is averaged (or smoothed out) within an aperture or a resolution element—a single pixel in our pixel-based analysis—the properties of dust extinction (e.g., the $2175\ \text{\AA}$ feature and the steepness of the UV-extinction curve) are governed by the actual geometry of the dust distribution within a galaxy. This means that two regions with the same *average* visual extinction A_V can have different amounts of extinction A_λ at another wavelength, either because of differences in *metallicity* or because of different *dust geometries*.

Table 2
Dust Extinction in Different Filters, (A_{filter}/A_V)

Instrument & Filter	λ_{center} (μm)	x (μm^{-1})	SMC	LMC	MW (Galactic)
GALEX FUV	0.153	6.536	4.56	3.16	2.70
GALEX NUV	0.227	4.405	2.91	2.59	2.53
VATT U	0.360	2.778	1.65	1.64	1.50
VATT B	0.437	2.288	1.37	1.35	1.29
VATT V	0.542	1.845	1.00	1.00	1.00
VATT R	0.642	1.558	0.81	0.81	0.81
2MASS J	1.235	0.810	0.14*	0.29*	0.36* (≤ 0.26)
2MASS H	1.662	0.602	0.15*	0.10*	0.18* (≤ 0.17)
2MASS K_S	2.159	0.463	0.03*	0.09*	0.04* (≤ 0.11)
IRAC 3.6 μm	3.550	0.282	(≤ 0.06)
IRAC 4.5 μm	4.493	0.223	(≤ 0.04)
IRAC 5.8 μm	5.791	0.173	(≤ 0.03)
IRAC 8.0 μm	7.872	0.127	(≤ 0.02)

Notes. An asterisk indicates that the uncertainty is significant compared to actual extinction values. The values in parenthesis are calculated using the Galactic extinction curve from Fitzpatrick (1999).

Two extreme cases of dust geometry are: (1) a uniform thin slab (i.e., commonly referred to as a “diffuse ISM”); and (2) dense clumps covering a small fraction of a resolution element. While we would like to perform a detailed study of the dust geometry and its effect on the extinction curve for extragalactic objects, this is beyond the scope of this thesis. Here, we briefly discuss the effects of the different dust geometries studied by Whittet et al. (2001, 2004). Whittet et al. (2001) studied a total of 27 sight-lines (stars) toward the dark clouds in the Taurus region. One of the results from their study is that $R_V = A_V/E(B-V)$ changes from a “normal” to a

“dense cloud” regime once the extinction exceeds a threshold value of $A_{\text{th}} \simeq 3.2$ mag. Whittet et al. (2004) subsequently studied the effect of dust geometries in detail, which included a thin “diffuse screen” and a diffuse screen with an embedded “dense cloud” (see their Fig. 1). For a detailed analysis and discussion, we refer the reader to their papers. The main effect of the “dense cloud” geometry on the extinction curve is to weaken or remove the 2175 Å extinction bump (see Fig. 5 of Whittet et al. 2004) while having little effect on the extinction curve at other wavelengths, which remains at the same level as for the mean “diffuse ISM” (Fig. 2 of Whittet et al. 2004). The extinction curves recreated from Gordon et al. (2003) and Fitzpatrick (1999), and the calculated extinction values A_{filter}/A_V (Figure 14 and Table 2) are therefore treated as the upper limit to the dust extinction from different dust geometries. Since the 2175 Å feature is covered only by the *GALEX* NUV filter, the uncertainty associated with different dust geometries is assumed to be minimal in all filters except the *GALEX* NUV. Since the *GALEX* NUV filter is not used in our method, we will defer further analysis of the NUV filter to future analysis.

2.4.2. A Dust-Free View of NGC 0959

Since NGC 0959 is classified as an Sdm galaxy in the RC3, we assume that it has an average metallicity between the SMC and the MW value. We therefore adopt the LMC extinction curve to estimate the extinction in filters other than V . Using the LMC extinction ratios A_{filter}/A_V from Table 2, we scale the V -band extinction for each pixel as

$$A_{\text{filter}} = A_V \times (A_{\text{filter}}/A_V), \quad (2.7)$$

where, A_V was computed using Equation 2.5. Figures 15–17 show the *uncorrected* (left panels) and the *extinction-corrected* images (right panels) for NGC 0959 from the FUV to R at *GALEX* NUV resolution. In all filters, the SF-regions become more clearly visible in the extinction corrected images. Compared to the optical V -band and the MIR 3.6 and $4.5\ \mu\text{m}$ images (Figure 13), in which the highest surface brightness is reached in the galaxy center, the brightest regions in the extinction-corrected *GALEX* FUV and NUV images are distributed all over the galactic disk. Since these FUV and NUV filters are especially sensitive to young stellar populations (see Figure 1), this indicates that most of the recent star formation occurred in the galaxy disk, and *not* in its nuclear region. The color composites of Figure 5 and Figure 12 show that the extinction-corrected FUV and NUV images are clearly tracing stellar populations that appear bluer than other regions. The images in U , B , and R (Figures 16 and 17) show the transition of the dominant emission from young stellar populations in the SF regions to older stellar populations in the bulge and center of the galaxy (Figure 5(a)). While the extinction corrected image in U is still sensitive mostly to young stellar populations, the R -band image shows that the older stellar populations in the small bulge of NGC 0959 become the dominant light source at redder wavelengths, as expected.

Among the FUV– R filters, the largest morphological change as a result of the dust-extinction correction occurs in the optical images, especially in the B -band image. In the FUV, NUV, and U , the light from the younger stellar populations dominates even without applying our dust-extinction correction. Correcting for dust

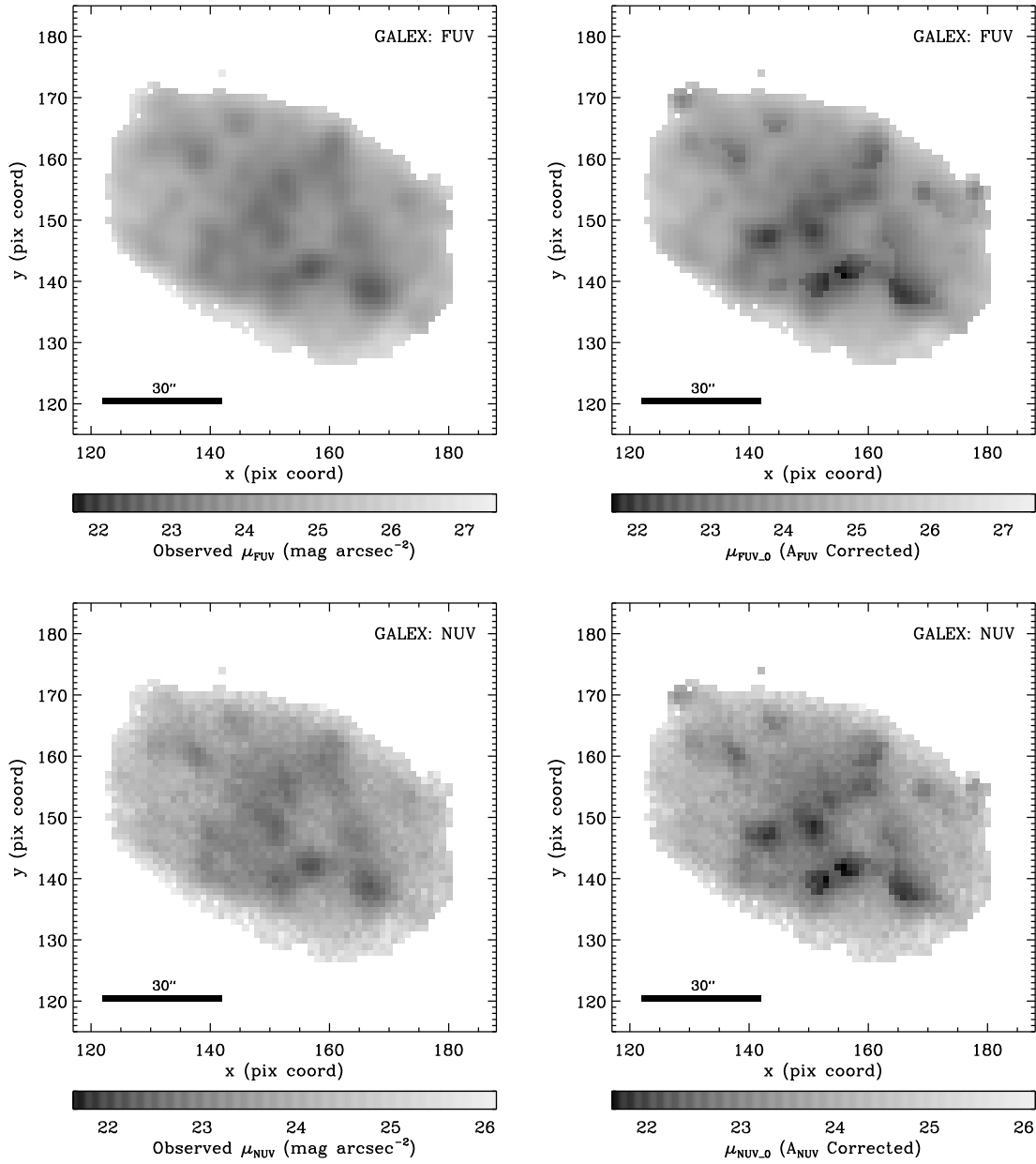


Figure 15. Comparison of observed (left) and extinction-corrected (right) images in the *GALEX* FUV (top) and NUV (bottom) filters.

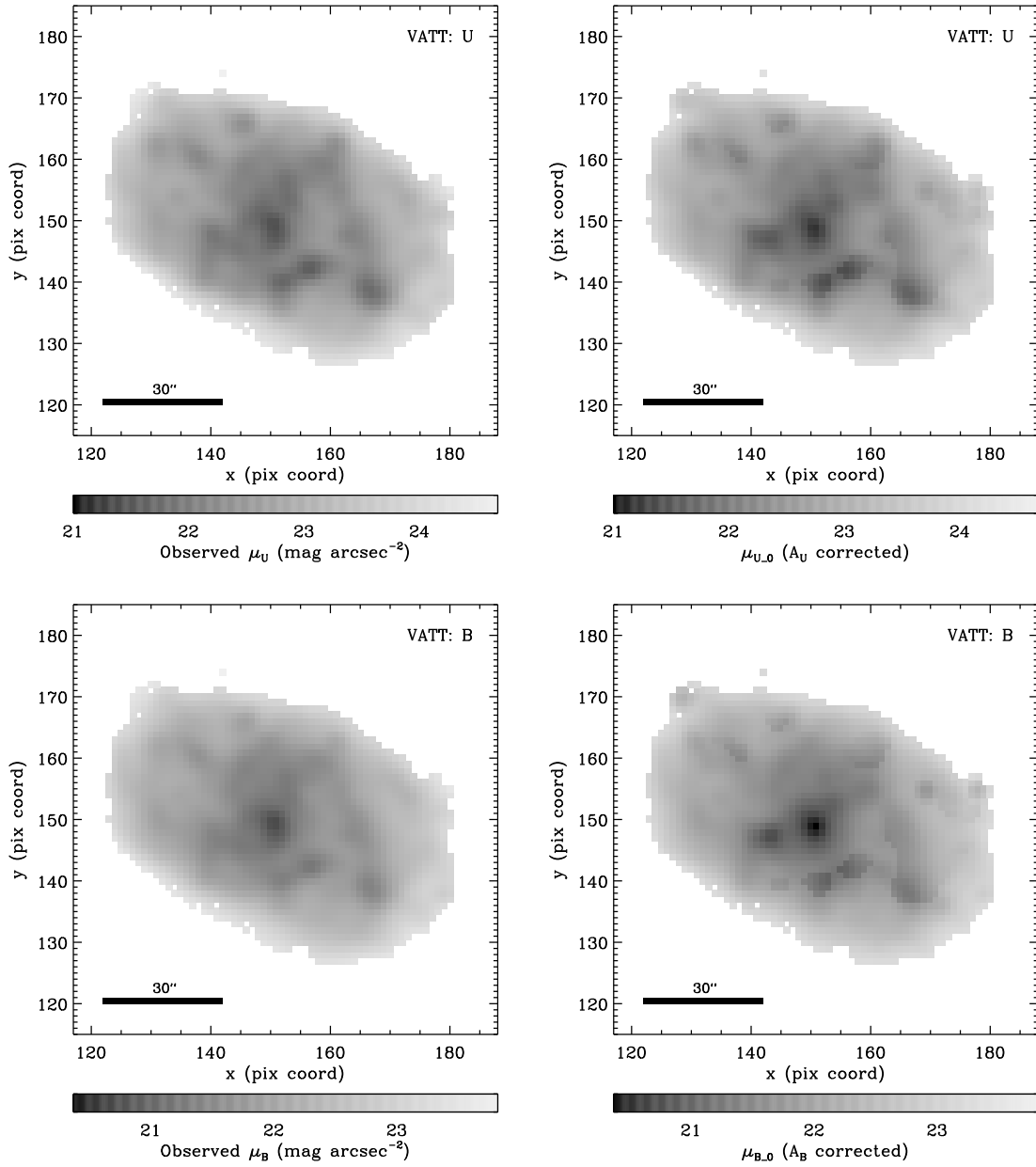


Figure 16. Comparison of observed (left) and extinction-corrected (right) images in the VATT U (top) and B (bottom) filters at $GALEX$ resolution.

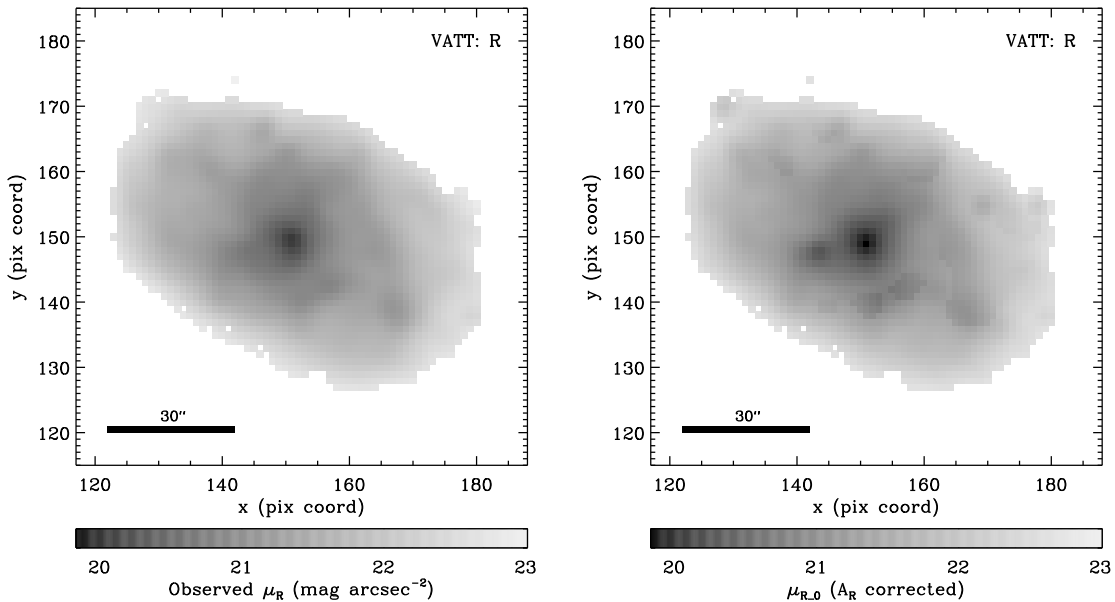


Figure 17. Comparison of observed (left) and extinction-corrected (right) images in the VATT R filter at *GALEX* resolution.

extinction therefore strengthens already discernable galactic structures, but does not dramatically change the apparent morphology (cf., Windhorst et al. 2002). The R -band image, on the other hand, is dominated by light from older stellar populations and suffers to a lesser degree from the effects of dust. The B -band samples both younger and older stellar populations (see Figure 1) and suffers a larger dust extinction than V (see Figure 14 and Table 2). After the extinction correction, light from younger stellar populations that is initially largely hidden behind the dust becomes visible, causing the galaxy morphology to change relatively more in B than in other filters.

Previous studies have compared the morphological appearance in B - and NIR H - or K_s -bands (e.g., Block & Puerari 1999; Elmegreen et al. 1999; Block et al. 2001; Buta & Block 2001; Eskridge et al. 2002; Block et al. 2004; Seigar et al. 2005). Eskridge et al. (2002) compared the morphological classifications in B and H for

~ 200 spiral galaxies from the Ohio State University (OSU) Bright Spiral Galaxy Survey. They found a relatively good correlation between the classifications in the optical and NIR (see their Fig. 2 and Table 2). On average, the H -band classification was found to be ~ 1 T-type earlier than the optical one. Other studies, however, found no correlation between optical Hubble type (Hubble 1926) and dust-penetrated morphological classes for smaller samples of 14–36 galaxies observed in K_s (e.g., Block & Puerari 1999; Elmegreen et al. 1999; Block et al. 2001; Buta & Block 2001; Block et al. 2004; Seigar et al. 2005). Since the Hubble types are based on blue photographic plates, the Hubble classification can be significantly affected by dust extinction (e.g., Windhorst et al. 2002). K_s -band images suffer only 10% of the extinction in V (Figure 14 and, e.g., Martin & Whittet 1990) and therefore show the stellar distribution with much smaller effects from dust. Therefore, if the amount of dust in (and in front of) a galaxy is significant, the optical B -band is affected accordingly, possibly resulting in drastically different morphology than suggested by the NIR classification. As this was seen in only a small subset of the OSU Bright Spiral Galaxy Survey samples (Eskridge et al. 2002), the galaxy samples used in the K_s -band studies by, e.g., Block & Puerari (1999) may have selected dustier galaxies.

The apparent B -band morphology of NGC 0959 before and after extinction correction (bottom panels of Figure 16) does not differ as drastically as the optical versus K_s morphologies reported in the above studies. But some regions, such as the SE side of the bulge at $[x, y] \simeq [142, 148]$, become much more prominent after extinction correction and the distribution of light becomes similar to that seen at 3.6

and $4.5\ \mu\text{m}$ (see bottom panels of Figure 13). This means that if a galaxy contains a large amount of dust along major structures, such as a bar or spiral arms, it is possible that the B -band morphology can change significantly after correction for dust.

2.5. Discussion

2.5.1. *Radial Dust Extinction Profile, $A_V(R)$*

At this point, we would have liked to compare our results for NGC 0959 with extinction measurements from other methods. While Esipov et al. (1991) and Taylor et al. (2005) have studied this galaxy, they did not analyze the internal dust extinction, so we cannot directly compare our results to prior work. However, radial extinction profiles have been analyzed in other galaxies (e.g., Jansen et al. 1994; Boissier et al. 2004, 2005; Calzetti et al. 2005; Holwerda et al. 2005, 2009). Jansen et al. (1994) used the special geometry offered by a nearly edge-on disk and a large bulge to demonstrate that the maximum extinction in the dust lanes of two galaxies (UGC 03214 and UGC 03065) decreased outward with distance from the minor axis. Boissier et al. (2004) used the azimuthally averaged FIR/UV flux ratio to measure radial extinction profiles for six nearby late-type spiral galaxies. Their results are reproduced in Figure 18(a), where radius is expressed in units of R_{25} , the major axis radius at the $m_B = 25.0$ mag arcsec $^{-2}$ isophote as listed in the RC3. Each galaxy shows a general trend of decreasing extinction from the center to the outer regions of the galaxy. Boissier et al. (2005) studied the radial profiles of extinction in M 83 using different methods—the Total-IR/FUV luminosity ratio, the UV spectral slope, and the Balmer decrement. Their Fig. 2 of shows that all three methods give simi-

lar results: a general decrease of extinction with radius, with a small upturn at the outer edge of M 83’s disk. Calzetti et al. (2005) measured the $H\alpha/Pa\alpha$ ratio in H II regions to study the distribution of dust extinction in M 51. Their Fig. 14 shows the distribution of individual extinction measurements as a function of radial distance from the center of M 51. While there are some relatively highly extinguished H II regions at outer radii—corresponding to the bump at $R/R_{25} \sim 0.8$ in the profile for M 51 in our Figure 18(a)—the distribution does follow the general decreasing trend with increasing radius. On the other hand, Holwerda et al. (2009) used an occulting galaxy pair to measure the distribution and amount of dust via the optical depth against the background galaxy, providing measurements that extend beyond the optically visible disk of the foreground galaxy (see their Fig. 2). They showed that large amounts of dust can exist even in the outermost parts of spiral galaxies, where these dust features are usually undetectable by other means (see their Figures 11 and 12).

If we see a similar radial trend for our estimated dust extinction in NGC 0959 as in the studies above, it would lend additional credence to the reliability of our method. Figure 18(b) shows the radial distribution of A_V for each pixel in NGC 0959. The galaxy center is located at $[x, y] = [151, 148]$, and the radius is expressed in units of R_{25} . Also indicated are mean extinction values computed within 0.1 kpc bins in radius, with (asterisks) and without (open diamonds) pixels with $A_V = 0 \text{ mag arcsec}^{-2}$. The error bars represent standard deviations for the distribution of A_V values in each such bin. While A_V for individual pixels spans a wide range at each radius, the azimuthally averaged extinction, $\overline{A_V}(R)$, clearly decreases from the center outward. At

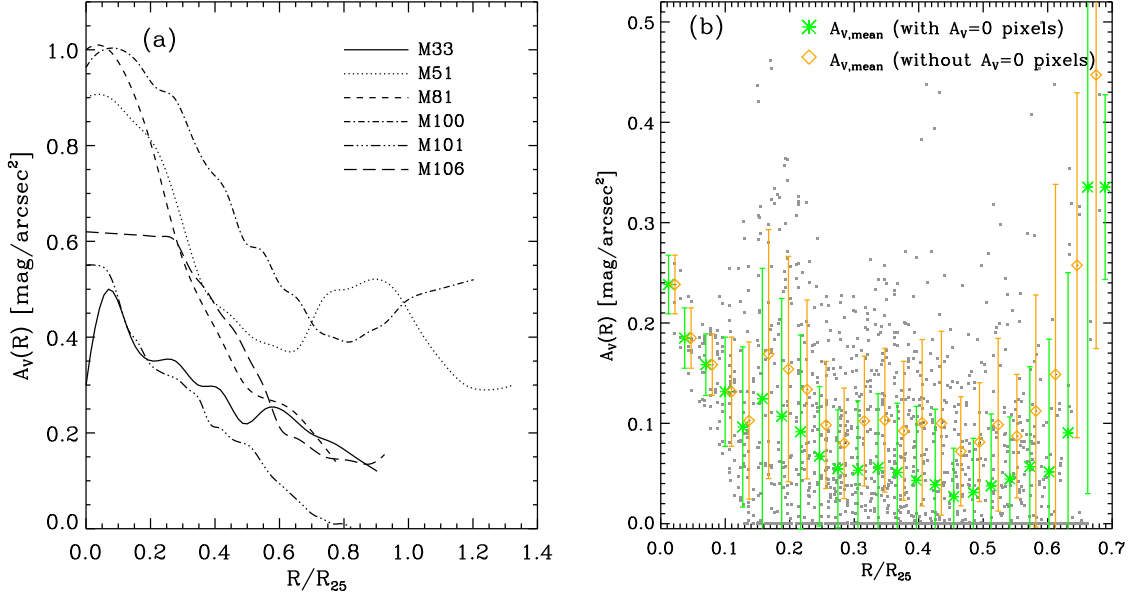


Figure 18. (a) Radial extinction profiles for the six nearby spiral galaxies from Boissier et al. (2004), with distances expressed in units of R_{25} . While some galaxies show a bump or an upturn in the outermost regions of their disk, the extinction generally decreases from the center of a galaxy outward. (b) Visual extinction, A_V , as a function of distance from the center of NGC 0959. Each dot represents the extinction measured in a single pixel. Averages within 0.1 kpc annuli are plotted as asterisks (green) when including pixels with $A_V = 0$ mag arcsec⁻², and as open diamonds (orange) when excluding such pixels. The error bars represent the standard deviation within each annulus. Twelve pixels with $A_V \gtrsim 0.5$ mag arcsec⁻² and $R \gtrsim 1.3$ kpc ($R \gtrsim 0.6 R_{25}$) are not shown here. Note that the very outskirts of NGC 0959 may suffer from the light blending from pixels with $S/N \lesssim 3$ in one or more of the filters, hence rendering the A_V measurements more uncertain.

the outermost radial bin, however, the average extinction shoots up to $\overline{A_V}(R) > 0.3$. This is caused mostly by the pixels with high A_V within the “interesting regions” discussed in Section 2.3.7.3 (see also Figure 10), which may or may not be associated with NGC 0959. The larger uncertainties for the outermost bins also reflect the fact that these pixels only marginally exceed our minimum S/N criterion in one or more of the filters, hence possibly affecting the reliability of β_V and A_V . Yet, some pixels with relatively high A_V ($0.2 \lesssim A_V \lesssim 0.5$ mag arcsec⁻²) indicate the existence of dust in the outermost regions of NGC 0959, perhaps analogous to the findings of Holwerda et al. (2009). The extensive tests described in previous sections, as well as the general agreement with results from other studies—although they involved different galaxies—give us confidence that our method produces reliable measurements of the spatial distribution of extinction by dust within a galaxy.

2.5.2. Summary

An important lesson from the application of our method to NGC 0959 is that we are able to map the two-dimensional distribution of dust extinction even from the low-resolution images, which show *no* conspicuous dust features silhouetted against the stars in Figure 5(b). Our initial expectation was that the extinction map created with our method might be relatively featureless, with specific dust features smoothed out. Instead, a map with a complicated pattern that follows the galactic structure emerged (see Figure 10). A similar, but more detailed dust distribution is recovered when the analysis is repeated on images at the higher IRAC 3.6 μm resolution (Figure 11). Pixels with large A_V in Figures 10 and 11 clearly trace the location

of silhouetted dust features in the higher resolution VATT (Figure 5(a)) or *HST* (Figure 12) color composites of NGC 0959. These results stress that the contrast between regions with high and relatively low extinction can be large within a galaxy disk. At resolutions of $2''.2$ (*Spitzer/IRAC*) and $5''.3$ (*GALEX*) or $\sim 110\text{--}250$ pc at the distance of NGC 0959, our method is able to reliably and meaningfully generate a two-dimensional distribution of the dust extinction. Such modest resolutions are accessible and our method will be applicable in galaxies well beyond the Local Group, where the individual dust features may no longer necessarily be spatially resolved.

2.5.3. Future Application

Our method will also be useful to study dust extinction in galaxies at much larger distances. Once *HST/WFC3* and *JWST* are in operation, galaxies at $z \simeq 0.3\text{--}0.4$ will be easily accessible for such studies, and galaxies at even larger redshifts might be reachable. WFC3¹² has two imaging channels: Ultraviolet and Visual (UVIS) channel covers $0.2\text{--}1.0\ \mu\text{m}$ with a pixel scale of $0''.04\ \text{pixel}^{-1}$, while NIR covers $0.9\text{--}1.7\ \mu\text{m}$ at $0''.13\ \text{pixel}^{-1}$. *JWST*¹³ will also have two imaging cameras: Near Infrared Camera (NIRCam), covering $0.6\text{--}5\ \mu\text{m}$ at $0''.032$ or $0''.065\ \text{pixel}^{-1}$ (short versus long wavelength channel), and Mid-Infrared Instrument (MIRI), which covers $5\text{--}27\ \mu\text{m}$ at $\sim 0''.11\ \text{pixel}^{-1}$. At $z \gtrsim 0.3$, the rest-frame V and $3.6\ \mu\text{m}$ bands shift progressively further into the near- to mid-IR regime covered by *HST/WFC3* and *JWST*, allowing one to apply our method to large numbers of intermediate redshift galaxies. The only limiting factor is the apparent size of the galaxy at these redshifts. Up to $z \simeq 1.6$,

¹²Space Telescope Science Institute (STScI), Wide Field Camera 3:
<http://www.stsci.edu/hst/wfc3>

¹³NASA, The *James Web Space Telescope*: <http://www.jwst.nasa.gov>

the angular scale becomes smaller (Wright 2006) and each pixel samples a larger surface area within a galaxy. At $z \simeq 0.4$, the central wavelengths of the V and $3.6 \mu\text{m}$ bands shift to $0.77 \mu\text{m}$ and $5.04 \mu\text{m}$, where UVIS and MIRI are expected to deliver resolutions of $\text{FWHM} \simeq 0''.08$ and $0''.195$, respectively. This corresponds to $\sim 420 \text{ pc}$ and $\sim 1 \text{ kpc}$, where the latter sets the relevant resolution for our method. While dust lanes will certainly not be visible, we expect our method to still produce meaningful maps of the variations in extinction on scales of $\sim 1 \text{ kpc}$, as long as a galaxy is at least several kpc in diameter.

Another application of our method is to investigate the result of Taylor et al. (2005) that the color in the outer regions becomes redder in the majority of late-type spiral and irregular galaxies. This reddening may be caused either by a change in stellar populations or be due to the presence of dust, which is usually only apparent in higher resolution images when silhouetted against a relatively bright stellar background (as in, e.g., Holwerda et al. 2009). In NGC 0959, a nearly face-on late-type spiral galaxy, we found evidence for the existence of a moderate amount of extinction in the outermost regions of its disk (Figure 10). Our method will also be useful to study the dust content of elliptical and lenticular galaxies. In recent years, large amounts of dust were discovered to exist in elliptical and lenticular galaxies, as well as in the halo of spiral galaxies (e.g., Kaviraj et al. 2007b; Oosterloo et al. 2007a,b; Emonts et al. 2008). Since very little SF-activity is ongoing in these galaxies, methods based on the FIR/UV flux ratio or on Hydrogen recombination lines are not as useful as they are for actively star-forming galaxies. Our method, which only depends on

images in V and $3.6\ \mu\text{m}$ filters, is well-suited for a study of the distribution of dust within early-type galaxies. We will present a more detailed study of dust distribution in spiral and irregular galaxies—a total of 27 galaxies—in a subsequent Chapter 4, and planning to expand our study to elliptical and lenticular galaxies in a future.

A potential future use of our method is to estimate the distribution of dust in simulated galaxy models (e.g., Croton et al. 2006). A detailed two-dimensional analysis of the dust extinction in a large number of galaxies would help understand the properties of dust for different types of galaxies or galactic structures, such as SF regions, bars, spiral arms, and inter-arm regions. Current simulations are able to model the extinction-free SEDs for many galaxies, while the treatment of internal dust extinction is still broad-stroke. For such models, it will be useful to construct a database of galaxies of different morphological type and mass, to constrain age, metallicity, and the amount and spatial distribution of the dust.

2.6. Conclusions

In this chapter, we presented a new method for estimating the extinction by dust within galaxies by comparing the observed V -to- $3.6\ \mu\text{m}$ flux ratio, β_V , to theoretical SED models. Using a pixel-based analysis, our method is able to estimate the two-dimensional distribution of dust extinction within a galaxy. As a proof of concept, we applied this method to NGC 0959, a nearby late-type spiral galaxy. From a pCMD, constructed using an additional U -band image, we robustly selected pixels dominated either by the light from younger stellar populations, or from older ones. Since their intrinsic V -to- $3.6\ \mu\text{m}$ flux ratios differ, they were treated separately

in our analysis. We presented a two-dimensional map of the visual extinction, A_V , that closely resembles the observed distribution of SF regions and underlying galactic structures (including a newly identified bar), and which traces the distribution of $8.0\ \mu\text{m}$ PAH emission. Although dust features are inevitably smoothed out to some extent due to light blending and the low spatial resolution of the images, we were able to construct a two-dimensional extinction map with sufficient detail to delineate the structure of dust features within the disk of NGC 0959. We then presented original and extinction-corrected views of NGC 0959 from the FUV through MIR. Through a series of tests, we demonstrated the validity of our results and method.

Our method has several advantages over other methods based on, e.g., the FIR/UV flux ratio, UV spectral slope, or Hydrogen recombination line ratios. At its core, our method only depends on images in two relatively common broadband filters, V and $3.6\ \mu\text{m}$ (L -band), and is therefore applicable continuously across the face of a galaxy. We exploit the fact that the wavelength-dependent extinction by interstellar dust reaches a minimum near $3.6\ \mu\text{m}$ while it increases toward shorter wavelengths. In the V -band, we are sensitive to dust extinction, but fairly insensitive to age and metallicity effects compared to UV-blue filters. We demonstrated that the intrinsic V -to- $3.6\ \mu\text{m}$ flux ratio, $\beta_{V,0}$, is well-behaved over a wide range in stellar age and metallicity. While $\beta_{V,0}$ depends on age more strongly than on metallicity, this ratio stays relatively constant for older ($t \gtrsim 500$ Myr) stellar populations, and occupies a relatively narrow range for younger stellar populations. As a result, we can simply compare the observed and intrinsic V -to- $3.6\ \mu\text{m}$ flux ratios (after taking

mixing or superposition of stellar populations into account) to estimate the amount of dust extinction, A_V , in each pixel. To translate A_V to bluer filters, knowledge of the metallicity becomes more important (or, alternatively, the uncertainty increases) due to the metallicity-dependence of the extinction curve. This simplicity allows our method—which is mostly automated with only a few manual parameter settings for each galaxy—to be applied to a large number of galaxies in a very short time.

Since our method does not require visual confirmation or identification of individual dust features, it is applicable to any galaxy beyond the Local Groups, if rest-frame V and $3.6\ \mu\text{m}$ images are available with at least several resolution elements across that galaxy. This offers the possibility of applying our method to *HST*/Advanced Camera for Surveys (ACS), *HST*/WFC3, and *JWST* NIRCam and MIRI images to study the two-dimensional distribution of dust not only in the local universe, but also for higher redshift galaxies.

CHAPTER 3

SIGNIFICANCE OF PIXEL-BASED EXTINCTION CORRECTION

3.1. Overview

In this chapter, we present the results of a study of the late-type spiral galaxy NGC 0959, before and after application of the pixel-based dust extinction correction. *Galaxy Evolution Explorer* (*GALEX*) far-UV (FUV) and near-UV (NUV), ground-based Vatican Advanced Technology Telescope (VATT) *UBVR*, and *Spitzer*/Infrared Array Camera (IRAC) 3.6, 4.5, 5.8, and $8.0\ \mu\text{m}$ images are studied through pixel Color-Magnitude Diagrams (pCMDs) and pixel Color-Color Diagrams (pCCDs). We define groups of pixels based on their distribution in a pCCD of $(B - 3.6\ \mu\text{m})$ versus $(\text{FUV} - U)$ colors after extinction correction. In the same pCCD, we trace the locations of these groups of pixels before the extinction correction was applied. This shows that selecting pixel groups is not meaningful when using uncorrected colors. We also trace their spatial distribution on a pixel coordinate map of the galaxy. We find that the pixel-based (two-dimensional) extinction correction is crucial to reveal the spatial variations in the dominant stellar population, averaged over each resolution element. Different types and mixtures of stellar populations, and galaxy structures such as a *previously unrecognized* bar, become readily discernible in the extinction-corrected pCCD and as coherent spatial structures in the pixel coordinate map.

3.2. Recapitulation of Pixel-Based Dust-Extinction Measurements

In Chapter 2, we estimated the visual dust extinction (A_V in mag arcsec^{-2}) measured over each $1''.5 \times 1''.5 \simeq 72 \times 72\ \text{pc}^2$ pixel for NGC 0959. We reproduce our extinction map in Figure 19, where darker grayscales correspond to higher values of A_V . The grayscales saturate for $A_V \geq 0.4\ \text{mag arcsec}^{-2}$ (indicated by the white

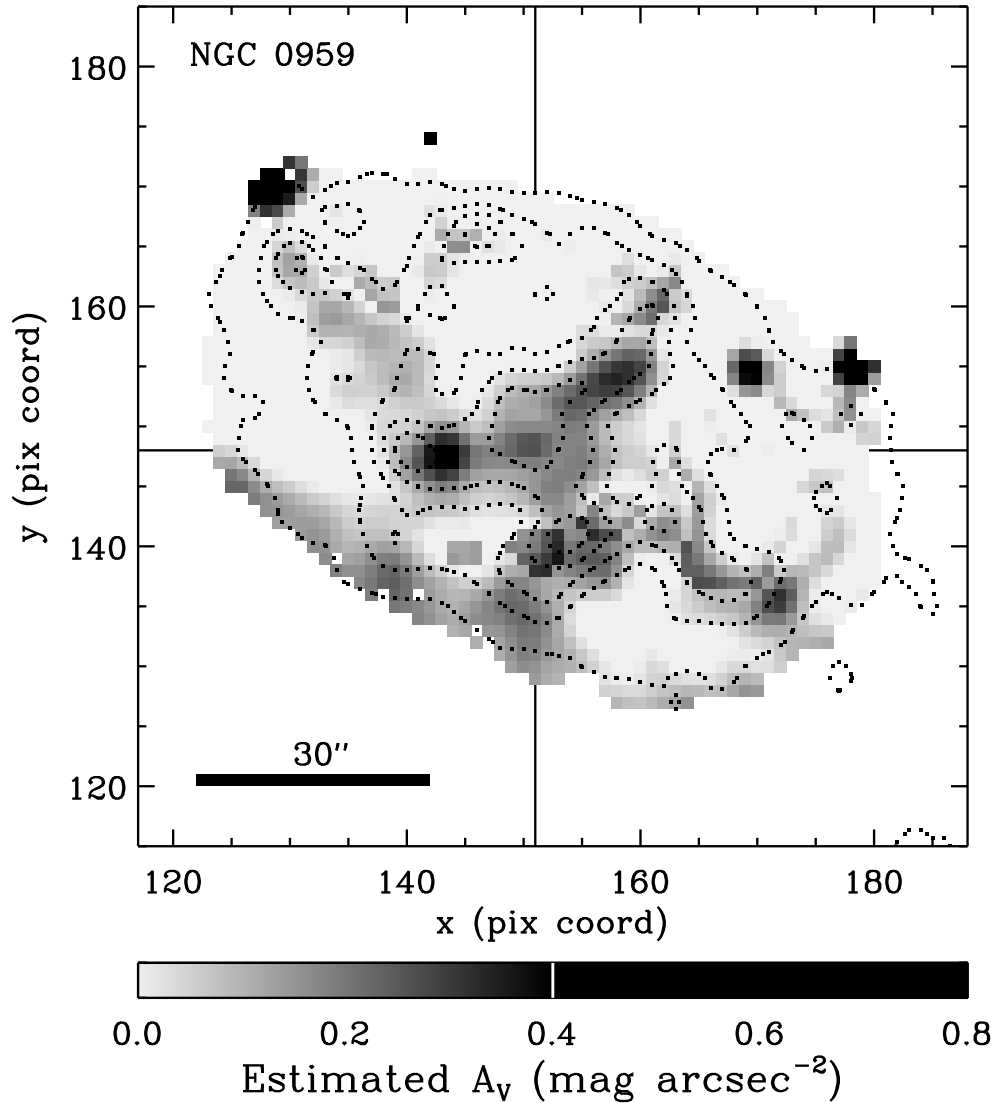


Figure 19. Spatial distribution of the pixel-averaged visual dust extinction, A_V , from Chapter 2. Extinction values map onto a grayscale from light-gray ($A_V = 0$) to black ($A_V = 0.4 \text{ mag arcsec}^{-2}$; indicated by a white vertical line in the color bar). The few pixels with $0.4 \leq A_V \leq 0.8 \text{ mag arcsec}^{-2}$ are also rendered as black. Dotted contours trace the *Spitzer*/IRAC $8.0 \mu\text{m}$ polycyclic aromatic hydrocarbon (PAH) emission and show good agreement with the visual extinction estimates, which were inferred from the observed V -band and $3.6 \mu\text{m}$ fluxes only. North is up, and east is to the left.

vertical line in the color bar) to enhance the visibility of the lower A_V values in the galaxy. The maximum extinction measured in this galaxy, averaged over a pixel, is $A_{V,\max} \simeq 0.8 \text{ mag arcsec}^{-2}$. Using histograms of the observed visual to $3.6 \mu\text{m}$ flux ratio ($f_V/f_{3.6\mu\text{m}}$) in each pixel, we estimated the intrinsic extinction-free flux ratios ($\beta_{V,0}$) for two groups of pixels — pixels apparently dominated by the light from either younger or older stellar populations — which are separated based on their distribution pattern and $(\text{FUV} - U)$ color in a pCMD of μ_V versus $(\text{FUV} - U)$ *before* the extinction correction was applied. Since the mid-IR $3.6 \mu\text{m}$ flux is assumed to be minimally affected by the dust, and hence usually treated as extinction-free (e.g., Fazio et al. 2004; Willner et al. 2004), A_V in each pixel is calculated from the difference between the amount of *observed* ($f_{V,\text{obs}}$) and *estimated* extinction-free (i.e., $f_{V,0} = \beta_{V,0} \times f_{3.6\mu\text{m},\text{obs}}$) V -band fluxes. The extinctions in other passbands (*GALEX* NUV and FUV, and optical U , B , and R bands) are scaled from A_V , adopting the Large Magellanic Cloud (LMC) extinction curve of Gordon et al. (2003).

3.3. Lifting the Veil of Dust from NGC 0959

3.3.1. Color Composite Images

To visually (qualitatively) investigate the effect of our pixel-based extinction correction on an image of NGC 0959, we first construct two color composites of the galaxy, composed of the *Spitzer*/IRAC $3.6 \mu\text{m}$ (red channel), the ground-based V (green channel), and the *GALEX* FUV (blue channel) images. Figures 20(a) and 20(b) show the color composites *before* and *after* extinction correction. The image resolutions are matched to that of the *GALEX* NUV image. For easy comparison,

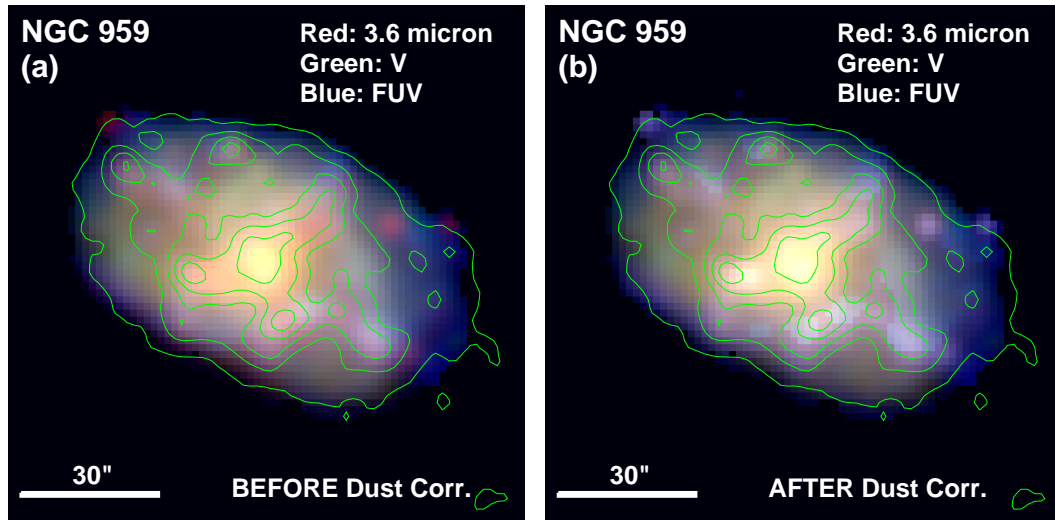


Figure 20. Color composite images of NGC 0959 using images from *Spitzer*/IRAC 3.6 μm (red), VATT *V* (green), and *GALEX* FUV (blue) at *GALEX* resolution (a) *before* and (b) *after* application of our pixel-based dust-extinction correction (Chapter 2). The *Spitzer*/IRAC 8.0 μm emission is over-plotted as green contours. Both color composites are created using the same color stretch. Regions corresponding to high A_V values in Figure 19 clearly become much bluer after extinction correction (panel (b)). This is especially clear in the blue star-forming knots which generally coincide with peaks in the *Spitzer* 8.0 μm emission.

both images were created using the *same* color stretch, and with the IRAC 8.0 μm contours over-plotted.

In Figure 20(a), there are several regions in the galaxy that appear much redder than other parts of the galaxy. These regions include: (a) the southern half of the galaxy, especially along the southern “edge” of the galaxy disk (as defined by our $S/N_{\text{min}} = 3.0$ requirement in each of the filters); (b) the strong 8.0 μm emission region that is running from NW to SE of the galaxy through its center, appearing especially redder at its northern end point; and (c) some localized regions at the northwestern and eastern edge of the galaxy disk. Since dust features are not resolved at *GALEX* resolution, we cannot tell whether these pixels in Figure 20(a) are red due

to extinction, or are dominated by intrinsically red stellar populations. From the distribution of the estimated visual dust extinction A_V in Figure 19, however, we infer that these red pixels are indeed red due to intervening dust at these locations.

After applying our extinction correction, Figure 20(b) shows that many of the strikingly red pixels in Figure 20(a) indeed have become bluer. Especially regions (b) and (c) have become much bluer than before, while some of the regions (a) still seem to have relatively red colors compared to other parts of NGC 0959's disk. There are some other regions which have become much bluer as well — mostly located in the SW region and northern regions of the galaxy. These regions already had a relatively blue hue in Figure 20(a) but become much bluer and brighter after extinction correction. They likely are actively star-forming regions.

To see whether these red and blue regions in Figure 20 actually correspond to dust features and SF regions, we created a third color composite image with a higher spatial resolution from the ground-based UVR images at their native resolution and pixel scale of full width at half maximum (FWHM) $\simeq 1''.3$ (matched across UVR) and $0''.37 \text{ pixel}^{-1}$. Figure 21 shows that the blue regions that become bluer and brighter are indeed likely SF regions. It also shows that the redder pixels in region (b) described above seem to be caused by thick dust lanes running from the NW to SE in the galaxy. It is hard to see whether regions (a) and (c) are caused by a dust lane or not, but regions (a) seems to be distributed around bluer clumps in Figure 21. The localized regions (c) do not appear to be unrelated background or foreground objects. Such objects usually have colors sufficiently different from those of the genuine galaxy

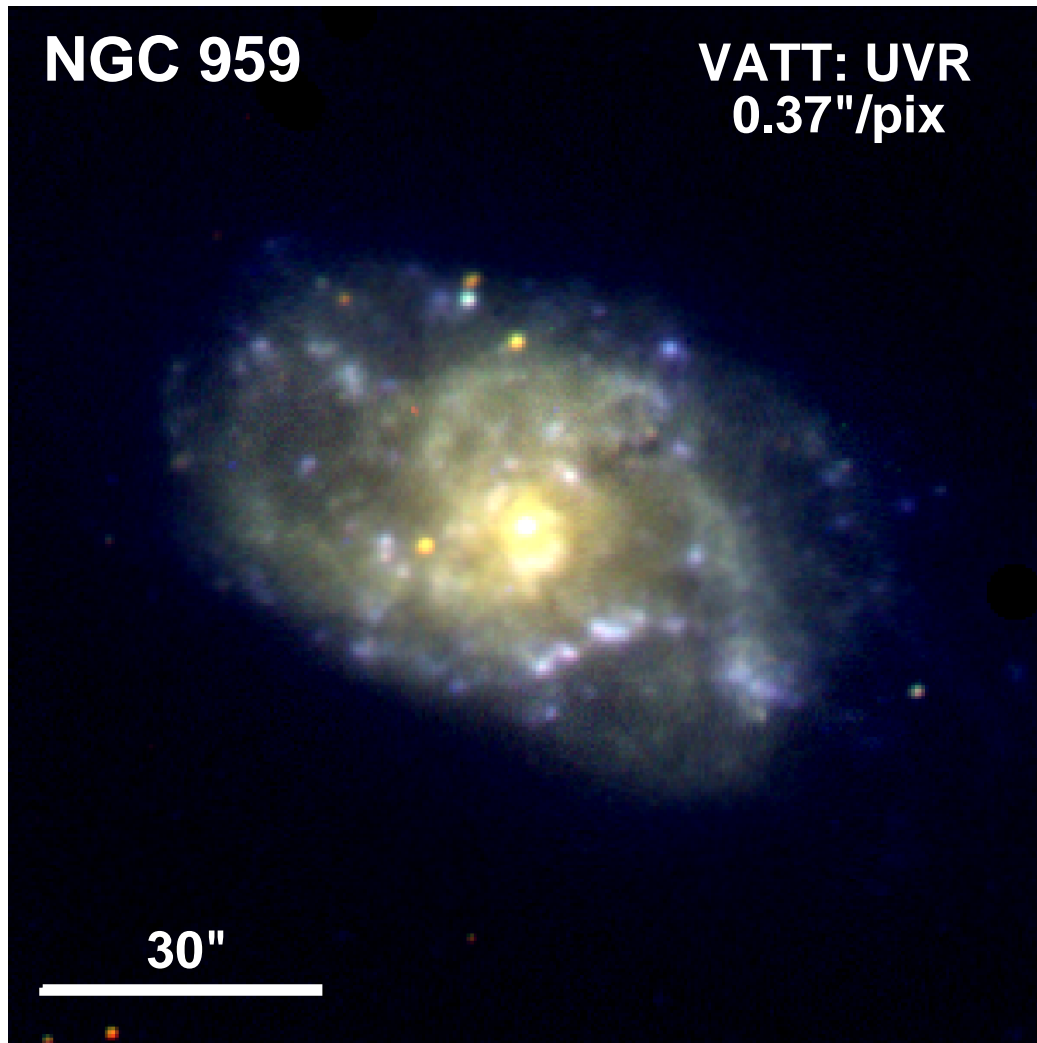


Figure 21. Color composite image of NGC 0959 using VATT U , V , and R images at their native ground-based resolution (full width at half maximum (FWHM) $\simeq 1''.3$) and pixel scale ($0''.37 \text{ pixel}^{-1}$), and *without* any extinction correction. Some dust features and blue star forming regions are readily discernible.

pixels, that they would appear as a distinct and separate branch or grouping of pixels in pCMDs and pCCDs. Since we found no such feature in the examined pCMDs and pCCDs for NGC 0959 (e.g., Figure 22), we treat these regions as parts of the galaxy.

3.3.2. A $(B - 3.6 \mu\text{m})$ versus $(FUV - U)$ pCCD

To study the effect of our pixel-based extinction correction in a more quantitative way, we examined pCMDs and pCCDs using various combinations of images from FUV through $8.0 \mu\text{m}$ for significant features or groupings in the pixel-distribution. A distinct grouping of pixels in these diagrams should indicate that those pixels are dominated by the same or similar mix of stellar populations. Among different diagrams plotted (not shown here), a pCCD of $(B - 3.6 \mu\text{m})$ versus $(FUV - U)$ color *after* extinction correction (Figure 22(a)) was selected, because it clearly shows distinct tracks and groupings of pixels. In particular, distinct red and blue sequences can be identified.

The uncertainties in the colors at the 25th and 75th percentiles are ~ 0.01 and ~ 0.02 mag in $(FUV - U)$, and ~ 0.05 and ~ 0.08 mag in $(B - 3.6 \mu\text{m})$, respectively. Since the gap of ~ 0.2 mag at the bluer end of $(FUV - U)$ color between the two sequences in Figure 22(a) is much larger than the photometric uncertainties in the colors, this separation of pixels is not a random effect. The sequences are also not the result of differences in residual reddening, as can be seen by comparing the directions of the sequences with that of the reddening vector drawn in Figure 22(a). The red and blue sequences are connected in the $1.15 \lesssim (FUV - U) \lesssim 1.65$ mag color range by pixels with intermediate colors. At colors redder than $(FUV - U) \simeq 1.65$ mag, the

pixels again somewhat separate into sequences with redder and bluer ($B - 3.6 \mu\text{m}$) colors.

As can be seen in various spectral energy distribution (SED) models (e.g., Anders & Fritze-von Alvensleben 2003; Bruzual & Charlot 2003; Maraston 2005; Kotulla et al. 2009), the $(\text{FUV} - U)$ color is very sensitive to age for the youngest stellar populations. Since most of the FUV flux is emitted by young, massive OB-stars, combining a *GALEX* and an optical broad-band filter provides strong age constraints (e.g., Kaviraj et al. 2007a). The $(B - 3.6 \mu\text{m})$ color was selected empirically, while examining different combinations of colors. The IRAC $3.6 \mu\text{m}$ passband is commonly used as a stellar mass distribution tracer (e.g., Willner et al. 2004), because it is associated more with the distribution of redder and older stars. Since the optical B -band is generally sensitive to younger stars, the $(B - 3.6 \mu\text{m})$ color can be used to distinguish mixtures of stellar populations with and without significant recent high-mass star formation. The combination of $(\text{FUV} - U)$ and $(B - 3.6 \mu\text{m})$ colors in Figure 22(a), therefore, provides a powerful diagnostic of the recent star formation history averaged over a pixel.

3.3.3. *Definition of Pixel Groups*

Based on the distinct red and blue sequences, as well as transition regions identified in Figure 22(a), we separated pixels into six different groups (color-coded in Figure 22(a)). The group boundaries (selection criteria) are summarized in Table 3. The exact location of the boundaries between some of these pixel groups is somewhat arbitrary, but is motivated by the following considerations.

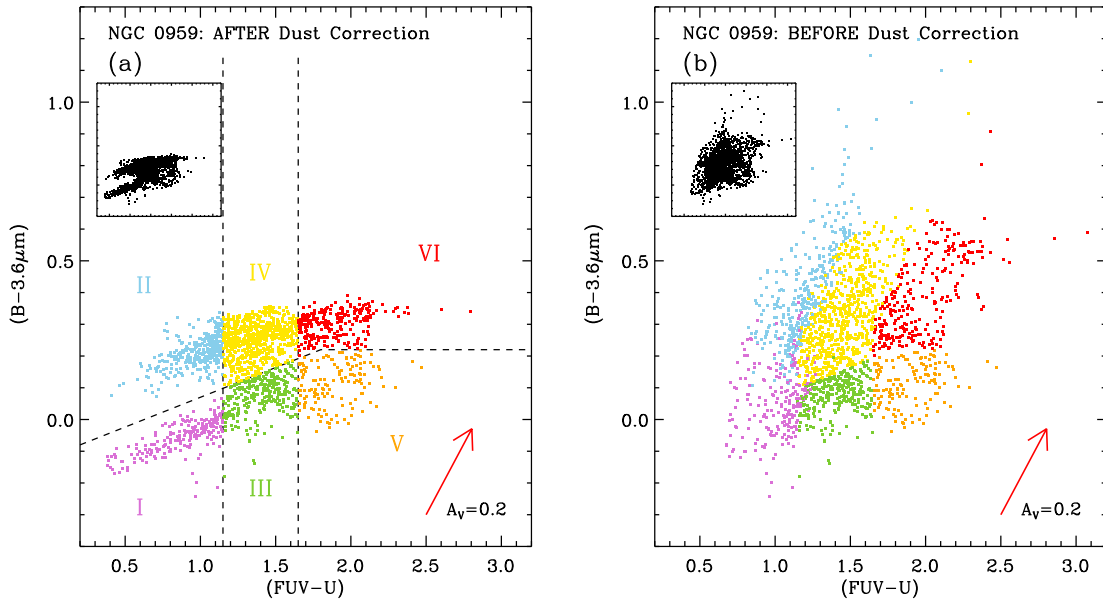


Figure 22. Pixel Color-Color Diagrams (pCCDs) of $(B - 3.6 \mu\text{m})$ versus $(FUV - U)$ color for NGC 0959. Panel (a) shows the pCCD *after* our extinction correction (see Chapter 2) has been applied, while panel (b) shows the pCCD using the *observed* pixel colors. The 25th and 75th percentile uncertainties in color are ~ 0.05 and ~ 0.08 mag in $(B - 3.6 \mu\text{m})$, and ~ 0.01 and ~ 0.02 mag in $(FUV - U)$, respectively. Reddening vectors corresponding to $A_V = 0.2$ mag arcsec⁻² are drawn in the bottom right corners. Pixel groups were selected in panel (a) and retain their group assignment and color-coding in panel (b). Small insets show the pCCDs, plotted over the same color ranges as the main panels, but omitting the color coding that might guide the reader’s eye. While the pCCD before extinction correction shows no prominent well-separated features in color-color space, distinct sequences and pixel groupings appear *after* application of our extinction correction (panel (a)).

Table 3
Selection Criteria for the Pixel-Groups in pCCD

Pixel Group	Color Code	Group Boundary Definition (mag)
Group I	Purple	$(FUV - U) < 1.15$ $(B - 3.6 \mu\text{m}) < 0.188 \cdot (FUV - U) - 0.118$
Group II	Blue	$(FUV - U) < 1.15$ $(B - 3.6 \mu\text{m}) \geq 0.188 \cdot (FUV - U) - 0.118$
Group III	Green	$1.15 \leq (FUV - U) < 1.65$ $(B - 3.6 \mu\text{m}) < 0.188 \cdot (FUV - U) - 0.118$
Group IV	Yellow	$1.15 \leq (FUV - U) < 1.65$ $(B - 3.6 \mu\text{m}) \geq 0.188 \cdot (FUV - U) - 0.118$
Group V	Orange	$(FUV - U) \geq 1.65$ $(B - 3.6 \mu\text{m}) < 0.22$ and $(B - 3.6 \mu\text{m}) < 0.188 \cdot (FUV - U) - 0.118$
Group VI	Red	$(FUV - U) \geq 1.65$ $(B - 3.6 \mu\text{m}) \geq 0.22$ or $(B - 3.6 \mu\text{m}) \geq 0.188 \cdot (FUV - U) - 0.118$

The Group I pixels (color-coded purple) reside on the blue part of the blue sequence, and have blue colors in both $(B - 3.6 \mu\text{m})$ and $(\text{FUV} - U)$. The dominant stellar populations are very young and massive OB-stars, while older stellar populations contribute little to the total flux in these pixels. The $(B - 3.6 \mu\text{m})$ and $(\text{FUV} - U)$ colors become redder as these young stellar populations age and the number of remaining OB-stars decreases.

On the other extreme, the Group VI pixels (color-coded red) have red colors in both $(B - 3.6 \mu\text{m})$ and $(\text{FUV} - U)$. These pixels are therefore dominated by old, quiescent, “red-and-dead” stellar populations and do not contain a detectable fraction of young, massive stars.

The Group II pixels (color-coded blue) have the same blue $(\text{FUV} - U)$ color range as Group I, but redder $(B - 3.6 \mu\text{m})$ colors. The blue $(\text{FUV} - U)$ color implies the presence of OB-stars. The redder $(B - 3.6 \mu\text{m})$ color indicates that Group II pixels have a non-negligible contribution to the total light from older (underlying or superposed along the line-of-sight) stellar populations.

Group V pixels (color-coded orange) cover the same, red, $(\text{FUV} - U)$ color range as Group VI, indicating that they too lack a detectable fraction of young, massive OB-stars. Yet, their bluer $(B - 3.6 \mu\text{m})$ color suggests that the flux in these pixels is dominated by light from intermediate age stellar populations.

The Group III and Group IV pixels (color-coded green and yellow, respectively) are located between these extreme cases. The light in these pixels is likely dominated by stellar populations in transition between the extreme groups along either blue or

red sequences, or between the blue and the red sequence, or represents a mixture of stellar populations (from unresolved adjacent regions or regions superposed along the line of sight) with different star formation histories.

3.3.4. *Effect of Pixel-Based Extinction Correction*

Figure 22(b) shows the pCCD of $(B - 3.6 \mu\text{m})$ versus $(\text{FUV} - U)$ color *before* the application of the extinction correction. For each pixel, the color coding was preserved from that in Figure 22(a). This allows us to track the effect of applying the extinction correction in this color–color space. Interestingly, as shown in the inset of Figure 22(b), once the color coding is removed, obvious features like the blue and red sequences of Figure 22(a) are no longer discernible. The Group I and II pixels, for example, which were clearly separated in Figure 22(a), have blended to form a continuous distribution in Figure 22(b). The main difference between Groups I and II, which both are characterized by the presence of OB-stars, is the fraction of light contributed by older stellar populations. Group III and IV pixels, defined as having $1.15 \leq (\text{FUV} - U) < 1.65$ mag *after* extinction correction, are affected differently by the extinction correction (as a comparison of Figures 22(a) and 22(b) shows). Like Group I and II pixels, Group IV pixels are found scattered out to much redder $(B - 3.6 \mu\text{m})$ colors *before* extinction correction. Most of the Group III pixels, on the other hand, can be located in the same color–color space in both panels of Figure 22. The same difference is seen between pixel groups V and VI. This indicates that Group III and V pixels have almost no measurable dust extinction, while Group IV and VI pixels are significantly obscured by dust. As a side note, the re-

duction of the scatter going from the observed to the extinction-corrected version of the $(B - 3.6 \mu\text{m})$ vs. $(\text{FUV} - U)$ pCCD is only possible if the extinction correction applied to each individual pixel was appropriate, at least to first order.

As shown in Figure 19, the pixel-averaged dust extinction estimated by our method in NGC 0959 indeed varies from $A_V = 0.0$ to $A_V \simeq 0.8 \text{ mag arcsec}^{-2}$. In Chapter 2, we also measured the average visual dust extinction across the entire galaxy, $\overline{A_V} = 0.064^{+0.086}_{-0.049} \text{ mag arcsec}^{-2}$, and the azimuthally averaged radial extinction profile, $A_V(R)$, which has a central value of $A_V(R = 0) \simeq 0.25 \text{ mag arcsec}^{-2}$, but quickly drops to below $A_V = 0.1 \text{ mag arcsec}^{-2}$ beyond a radius of $\sim 0.2 R_{25}$, where R_{25} denotes the major axis radius at the $\mu_B = 25.0 \text{ mag arcsec}^{-2}$ isophote (RC3; de Vaucouleurs et al. 1991). These average A_V values are much smaller than the peak pixel-based A_V estimate. Also, while the $\overline{A_V}$ and radial profile do not become zero at any radius, with our method (see Chapter 2) about $\sim 55\%$ of the analyzed pixels in NGC 0959 have $A_V = 0.0 \text{ mag arcsec}^{-2}$ to within the photometric uncertainties.

Before we proceed to the next section, let us consider what might cause the difference in dust extinction between Groups I and III on the blue sequence. Dust and gas are easily removed by starburst heating (e.g., Mihos & Hernquist 1994, 1996) and stellar winds (e.g, Murray et al. 2005), and both mechanisms become stronger as the size of an OB-association becomes larger. Therefore, if the dominant stellar populations in Group III pixels are indeed evolved Group I populations wherein OB-stars have died off, we would *expect* them to suffer less extinction, unless some mechanism for rapid reformation and pervasive distribution of dust were at play. Figures 22(a)

and 22(b) show that, once dust-free, these populations do *not* become significantly dustier evolving from Group III to Group V, apparently ruling out such rapid reformation. Since we do not observe a similar strong drop in extinction going from Group II to Group IV, we conclude that most of the extinction in those pixels is not physically associated with the OB-associations themselves, although they could still represent star formation “blisters” on the far side of large molecular cloud complexes.

3.3.5. *Is NGC 0959 Unique? Application to Other Galaxies*

To determine whether our pixel-based extinction correction can be used as a general method, or whether NGC 0959 is a special case, we applied the same method to NGC 7320 (SA(s)d at $D = 14.0 \pm 1.0$ Mpc, sampling $102 \times 102 \text{ pc}^2 \text{ pixel}^{-1}$) and UGC 10445 (SBc at $D = 20.0 \pm 1.4$ Mpc, $146 \times 146 \text{ pc}^2 \text{ pixel}^{-1}$), which, although more distant, are selected from our larger sample of 27 galaxies with FUV through mid-IR imagery as relatively close analogs. A more detailed analysis of the distribution of extinction and the intrinsic stellar populations of these galaxies will be performed in Chapter 4. Here we simply compare their $(B - 3.6 \mu\text{m})$ versus $(\text{FUV} - U)$ pCCDs before and after the application of our pixel-based extinction correction, to help validate the results for NGC 0959.

Figure 23 shows the distribution of the pixels of NGC 7320 and UGC 10445 that meet our S/N criteria in the same color-color space as Figure 22. The main panels show the distributions *after*, the insets show the distributions *before* extinction correction. For each galaxy, both the main panel and inset show the *same* ranges in colors. The vertical dotted lines in the insets represent $(\text{FUV} - U) = 0.0$ mag.

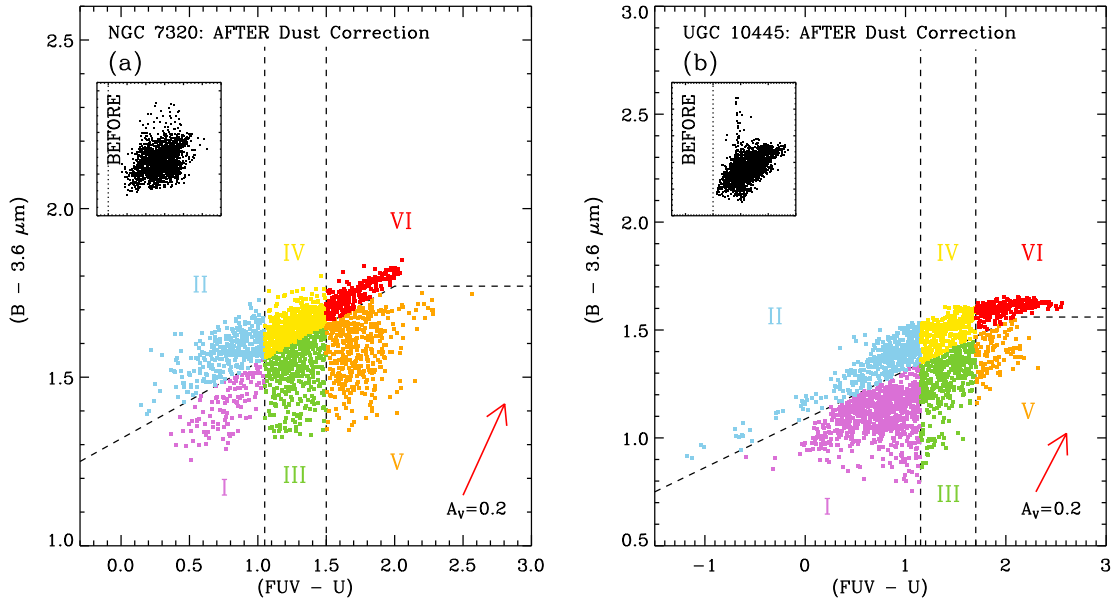


Figure 23. Extinction corrected pCCDs for (a) NGC 7320 (SA(s)d, $D = 14.0 \pm 1.0$ Mpc) and (b) UGC 10445 (SBc, $D = 20.0 \pm 1.4$ Mpc), two more distant analogs of NGC 0959 ($D = 9.9 \pm 0.7$ Mpc). Since the area subtended by a single pixel is (much) larger in these galaxies, the effects of light blending are more severe, resulting in smaller and fuzzier separations of red and blue sequences than for NGC 0959. Of course, their star formation histories may also differ. Yet, groupings of pixels that are qualitatively similar to those in NGC 0959 are recognizable in both pCCDs. The insets, plotted over the same color ranges as the main panels for each galaxy, show the distribution of pixels before dust correction. The vertical dotted lines in the inset panels indicate the locations of $(FUV - U) = 0.0$ mag, for comparison with the main panels.

Reddening vectors corresponding to $A_V = 0.2$ mag arcsec $^{-2}$ are drawn in the lower right corners of the main panels. Since the area subtended by a single pixel is larger than was the case for NGC 0959, the blending of light from distinct stellar populations within a single pixel becomes more significant, resulting in less clear separation of blue and red sequences. Yet, different groupings of pixels, analogous to those defined in Figure 22(a) for NGC 0959, are still recognizable in Figure 23 for both galaxies.

3.3.6. A Pixel Coordinate Map of Stellar Populations within NGC 0959

Having shown that application of our pixel-based extinction correction (Chapter 2) reveals significant groupings of pixels — dominated by different types or mixtures of stellar populations—in the $(B - 3.6 \mu\text{m})$ versus $(FUV - U)$ pCCD, our next question becomes whether the spatial distribution of pixels belonging to these pixel groups will reveal meaningful large- and small-scale physical structures within NGC 0959. To address this question and study how each pixel group relates to the visual and physical properties of stellar populations, we plot the pixel groups defined in Figure 22(a) (and Table 3) onto a two-dimensional pixel coordinate map as shown in Figure 24. Each square in this figure represents a $1''.5 \times 1''.5$ pixel, color-coded according to the pixel group it is a member of. Black dotted contours again trace the *Spitzer*/IRAC $8.0 \mu\text{m}$ polycyclic aromatic hydrocarbon (PAH) emission. We emphasize that each pixel group was defined *without* using any pixel coordinate information. In other words, this is the *first time* that the spatial distribution of pixels belonging to each of the selected pixel groups is revealed.

First and foremost, Figure 24 demonstrates that the different pixels groups are *not* distributed randomly across the face of NGC 0959's galactic disk, but cluster in well-defined regions. No systematics in the data processing and process of defining the pixel groups would be expected to result in spatial artifacts larger than 3×3 pixels. Since most regions cover much larger contiguous areas, we therefore conclude that the smallest spatial groupings must also be genuine. Since defining the different pixel groups was possible only in the extinction corrected $(B - 3.6 \mu\text{m})$ versus

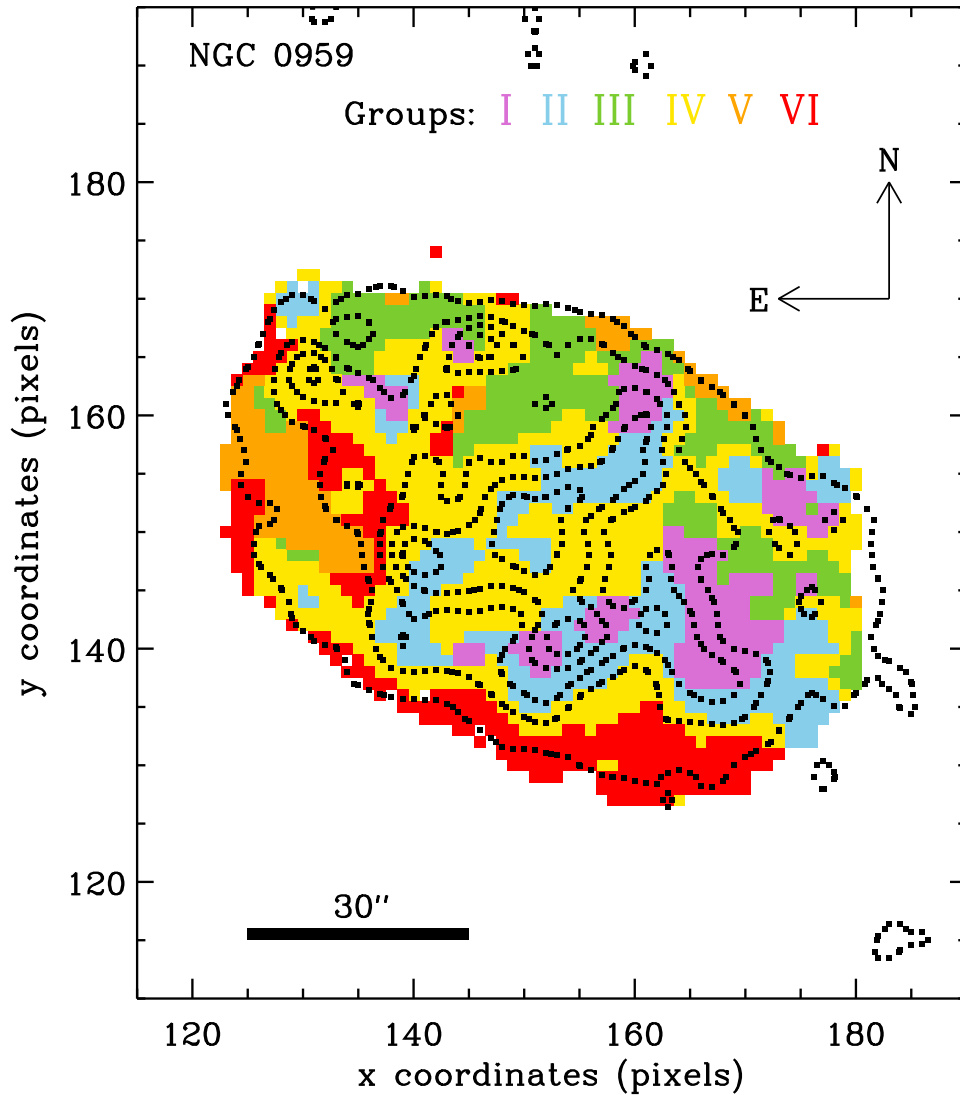


Figure 24. Pixel coordinate map of NGC0959, showing the spatial distribution of pixels belonging to the different pixel groups selected in Figure 22(a), i.e., *after* application of our pixel-based extinction correction. Each square represents a single $1''.5 \times 1''.5$ pixel. The black dotted contours trace the *Spitzer*/IRAC $8.0 \mu\text{m}$ emission. Group I (purple) and Group II (blue) pixels appear to define some large-scale structure in the galactic disk, highlighted by OB-associations. Especially, Group II pixels reveal a *previously unrecognized* bar-like structure, running from NW to SE across the galaxy center.

($FUV - U$) pCCD, a (pixel-based) two-dimensional extinction correction is crucial to reveal regions with systematically different star-formation histories.

Group I pixels (purple) are found in and around some of the bluest regions in the extinction-corrected color composite of FUV , V , and $3.6\mu\text{m}$ images (Figure 20(b)), most of which are recognizable as such in the uncorrected, higher resolution, ground-based UVR color composite (Figure 21) as well. Since the stellar populations dominating these pixels are much brighter than those in other regions (Figure 21), these regions must indeed be vigorously star-forming.

Group II pixels (blue) are generally distributed in regions adjacent to the Group I pixels. Each of the regions (b) and (c) of Section 3.3.1 is found to belong to this pixel group, as well. In particular, much of a more or less linear structure that runs from the NW to SE of the galaxy through its center, with high $8.0\mu\text{m}$ surface brightness (due to PAH emission) and signs of higher than average obscuration (Figures 19 and 21), consists of pixels that belong to Group II. These regions have the blue ($FUV - U$) colors—characteristic of OB-associations—but are redder in ($B - 3.6\mu\text{m}$) colors, because a larger fraction of the light is contributed by older stellar populations than Group I pixels. These observations are consistent with the presence of a stellar bar. Although NGC 0959 has been studied before (e.g., Esipov et al. 1991; Taylor et al. 2005), to our knowledge this bar has not previously been reported. The extinction-corrected color composite in Figure 20(b) also suggests that NGC 0959 has a non-negligible bulge or central condensation that is partially obscured by dust in Figures 20(a) and 21. We suggest, therefore, that its morphological classification be

changed from Sdm (RC3; de Vaucouleurs et al. 1991) or Sc/Irr (UGC; Nilson 1973) to SBcd.

An interesting contrast in average stellar population age is revealed by comparing the spatial distributions of Group III (green), Group IV (yellow), and Group V and VI (orange and red) pixels. Whereas Group III pixels are mostly found in the northwestern half of the galaxy, Group V and VI pixels are distributed predominantly toward the eastern and southeastern periphery of the galaxy (although a smaller region of Group V pixels appears along the northern rim). The regions occupied by Group III pixels appear neither particularly blue (actively star-forming) nor red (quiescent) in Figure 20(b), consistent with the idea that intermediate age (a few 100 Myr) stellar populations are the dominant contributors to the flux in these pixels. The extinction map of Figure 19 shows that these pixels suffer no, or at most minimal extinction by dust. The Group V regions correspond to regions that have a smooth appearance without abrupt changes in surface brightness in Figures 20 and 21, and lacking any signatures of dust (Figures 19 and 21). Their red ($FUV - U$) colors and neutral ($B - 3.6 \mu\text{m}$) colors indicate that these must be regions with intermediate age ($\sim 1\text{--}2$ Gyr), largely unattenuated stellar populations in the outskirts of the galaxy. The Group VI pixels (red) in the southern half of the galaxy disk suffer some extinction (Figure 19), but the low surface brightness in these regions does not allow one to easily discern dust features in Figures 20 and 21. Even though these regions suffer some extinction, Figure 22(a) demonstrates that these pixels are red mostly because the light is dominated by older (likely older than a few Gyr) stellar

populations. The Group IV pixels are distributed throughout the galaxy between the other populations, but perhaps mostly surrounding the Group II pixels. Like Group III, their $(FUV - U)$ colors indicate the presence of relatively young stars and absence of OB-stars, but the redder $(B - 3.6 \mu\text{m})$ colors of Group IV pixels show that a larger fraction of the flux is contributed by older populations. Figure 19 shows that these pixels tend to suffer somewhat less attenuation than Group I and II pixels. The overall impression is that of a large-scale past star formation episode that started in the south or southeast and propagated toward the northwest, and that is unrelated to the ongoing massive star formation traced by Group I and II pixels, which presently is concentrated more toward the western half of NGC 0959.

The apparent ridge of somewhat higher extinction along the southeastern edge (as defined by our $S/N \geq 3$ criterion) of NGC 0959, so striking in Figure 19, might hint at the presence of either a warp in the galactic disk or an outer spiral arm delineated by a dust lane. In either case, no significant star formation must have been associated with that portion of the galactic disk for the past few Gyr.

3.4. Summary and Conclusions

in this chapter, we have presented the results of a study of NGC 0959 using color composite images, a pCCD, and a pixel coordinate map, and demonstrated the importance and potential of a pixel-based extinction correction. Our study combined ground- and space-based surface photometry, ranging in wavelength from the far-UV (*GALEX*) through mid-IR (*Spitzer/IRAC*). Among the possible combinations of color-magnitude and color-color diagrams examined, we found that the $(B - 3.6 \mu\text{m})$

versus $(FUV - U)$ pCCD proved the most powerful diagnostic of differences in the stellar populations contributing to the flux in a pixel. After applying the pixel-based, two-dimensional extinction correction described in Chapter 2, we defined six different pixel groups in this diagnostic diagram, ranging from pixels for which both $(FUV - U)$ and $(B - 3.6 \mu\text{m})$ colors indicate that their fluxes are dominated by very young, massive stellar populations, to pixels that appear to sample only light from evolved stellar populations. We demonstrated that it was not possible to meaningfully define such pixel groups before extinction correction. We then showed that pixels that belong to a given pixel group form well-defined, contiguous regions in a pixel coordinate map, revealing systematic spatial variations in the dominant stellar populations that would not be readily discernible without a two-dimensional correction for extinction. We were able to report the presence of a previously unrecognized stellar bar, for example.

Our pixel-based two-dimensional method to correct for extinction, based on only $3.6 \mu\text{m}$ and V -band images (adding U improves fidelity), has the advantage that it is applicable to any galaxy that is significantly resolved at rest-frame $\sim 3.6 \mu\text{m}$ and that it is not restricted to a few individual sightlines within a galaxy, nor to the very nearest galaxies. Although seemingly simple and crude, we have demonstrated that application of this method allowed us to uncover relatively detailed spatial information on the nature of stellar populations and on the star formation history within NGC 0959, despite significant spatial variations in the attenuation by intervening dust.

While the spatial resolution in the present study was limited by the *GALEX* NUV PSF of $5''.3$ (FWHM) to linear scales of ~ 250 pc, in the near future, combination of *Hubble Space Telescope* (*HST*)/Wide Field Camera 3 (WFC3) and *James Webb Space Telescope* (*JWST*) would provide much higher resolution (FWHM $\simeq 0''.06$ – $0''.11$) at rest-frame UV through mid-IR wavelengths. These instruments will thus allow us to study the distribution of dust extinction and the underlying stellar populations at high fidelity and at much finer spatial resolution within nearby galaxies, as well as at similar scales of a few hundred pc within more distant galaxies. Since galaxies at $z \gtrsim 1$ are important building blocks of the galaxies that we see today at $z = 0$, studying these higher redshift objects with proper two-dimensional extinction estimates will be of significant importance to reveal the nature of galaxy assembly, and to better understand any effects that cosmology may have had on these processes.

CHAPTER 4

MAPPING THE DISTRIBUTIONS OF DUST-EXTINCTION AND STELLAR CONTENT OF 27 NEARBY LATE-TYPE GALAXIES

4.1. Recapitulation of the Pixel-Based Extinction Measurement and its Effect

In previous chapters, we have introduced a new pixel-based method of estimating the two-dimensional distribution of dust extinction in the late-type spiral galaxy NGC 0959, using only the optical V and the mid-IR $3.6\ \mu\text{m}$ passbands (Chapter 2). Using these images before and after the application of our extinction correction, we demonstrated how important it is to unveil the true nature of stellar populations hidden underneath the complicated distribution of dust extinction (Chapter 3). The results of Chapters 2 and 3 are recreated as a single page summary in Figure 25, where the most relevant figures from both these chapters are gathered together.

In the top row of Figure 25, panels (a)–(c) are the color composites of NGC 0959 (Figure 21 with Vatican Advanced Technology Telescope (VATT) UVR at their original resolution, and two panels of Figure 20 with the *Spitzer*/Infrared Array Camera (IRAC) $3.6\ \mu\text{m}$, VATT V , and *Galaxy Evolution Explorer* (*GALEX*) far-UV (FUV) at *GALEX* near-UV (NUV)-band resolution) from Chapter 3. To facilitate comparison, the color stretches used for panels (b) and (c) are identical. Red contours trace the IRAC $8.0\ \mu\text{m}$ PAH emission in the galaxy. To distinguish from contours that trace the FUV emission (blue colored contours) for some galaxies in Figures 26–50, the color of these $8.0\ \mu\text{m}$ contour lines has been changed from previous chapters. In the middle row, the main panel and inset of panel (d) consist of Figure 6 and Figure 4(a) from Chapter 2, respectively. The color scheme has been changed from the original to simply represent the dominant age groupings: older pixels as red and

younger pixels as blue, and some pixels dominated by extremely young stellar populations (if applicable) are colored purple in Figures 26–50. Panel (e) is the same figure as Figure 19 in Chapter 3. The crosshairs, which are drawn behind the galaxy, indicate the coordinates of the galaxy center. For the NGC 0959, the full range of gray scales is reserved for the dust extinction values $0.0 \leq A_V \leq 0.4 \text{ mag arcsec}^{-2}$, and pixels with $A_V > 0.4 \text{ mag arcsec}^{-2}$ are saturated in black, to enhance the visibility of the dust distribution. Dotted contours trace the IRAC $8.0 \mu\text{m}$ emission. Panel (f) is the radial dust-extinction profile of Figure 18(b) in Chapter 2. The averaged radial extinction profiles, $\overline{A_V}(R)$, are calculated within (A_V -weighted) $0.1 R_{25}$ bins, rather than within a 0.1 kpc bin as in Figure 18. This normalization from 0.1 kpc to $0.1 R_{25}$ bin allows for a more straightforward comparison of the 27 galaxies studied in this chapter. Panel (g) consists of the pixel Color-Color Diagrams (pCCDs) from Figure 22 of Chapter 3. The main panel and inset show the pCCD *after* and *before* the application of our dust-extinction correction, respectively. Both the main panel and inset are plotted over the same ranges of colors. The dotted horizontal line (and dotted vertical line for some galaxies in Figures 26–50) in the inset indicates a color $(B - 3.6 \mu\text{m}) = 0.0 \text{ mag}$ (and $(\text{FUV} - U) = 0.0 \text{ mag}$). The color coding is the same as that used in Figure 22 of Chapter 3. Panel (h) is the same figure as Figure 24 in Chapter 3. As in the panel (g), color coding is the same as before, and the black dotted contours trace the *Spitzer*/IRAC $8.0 \mu\text{m}$ emission. In Figures 26–50, contours in panels (e) and (h) are tracing the same IRAC $8.0 \mu\text{m}$ (red) or *GALEX* FUV (blue) contours used in panels (b) and (c) for each galaxy. All color-composite images and

pixel-coordinate maps in Figures 26–50 are oriented so that the north is up and east is to the left.

4.2. Application to 26 Other Late-Type Galaxies

4.2.1. *Sample Selection*

As we briefly mentioned in Section 3.3.5 (see Figure 23 of Chapter 3), our method works not only for NGC 0959, but also for other galaxies. To study the distribution of dust extinction in different types of galaxies, we selected a total of 27 galaxies (including NGC 0959) spanning a wide range of spiral, irregular, and merging galaxies. These galaxies are selected from a sample of 199 galaxies studied by Taylor-Mager et al. (2007), which includes mostly late-type spirals, irregulars, and mergers. This was done for the specific purpose of the study of galaxy types that dominate the faint galaxy counts at large redshifts. Studying these nearby galaxy samples prepare us for comparisons to high redshift galaxies observed with *Hubble Space Telescope* (*HST*)/Wide Field Camera 3 (WFC3) and *James Webb Space Telescope* (*JWST*) in future. Of the 199, 143 galaxies are observed with the direct imager at the VATT in the ground-based *UBVR* filters. A detailed description of these galaxies and observations is provided by Taylor et al. (2005) and Taylor-Mager et al. (2007). From these 143 galaxies, we selected 27 galaxies that also have images in the *GALEX* FUV and NUV passbands, as well as in the *Spitzer*/IRAC 3.6, 4.5, 5.8, and 8.0 μm channels, or at least with IRAC 3.6 μm images deep enough for the application of our method (see Chapter 2). A list of these target galaxies are summarized in Table 4.

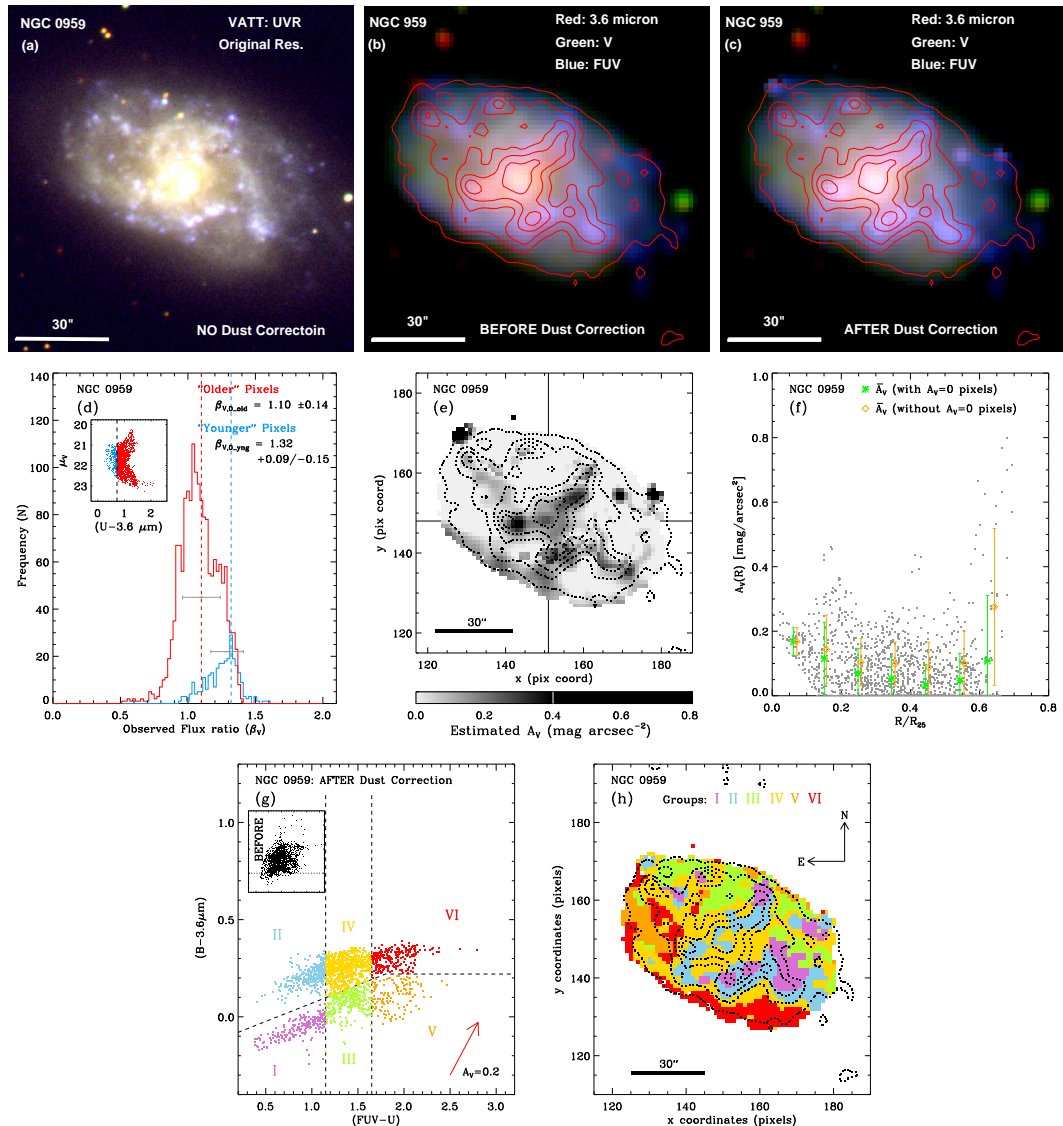


Figure 25. Color composite using (a) VATT *UVR* images at their original resolution, and using IRAC 3.6 μm (Red), VATT V (Green), and GALEX FUV (Blue) at GALEX NUV resolution (b) *before* and (c) *after* extinction correction. Red contours in (b) and (c) and black contours in (e) and (h) traces the IRAC 8.0 μm emission. (d) Histogram of observed *V*-to-3.6 μm flux ratio, β_V (main panel), and a selection of younger and older pixels (inset). (e) Spatial distribution of A_V . The crosshairs converge on the galaxy center. (f) Radial profiles of dust extinction. (g) A pCCD of $(B - 3.6 \mu\text{m})$ versus $(FUV - U)$ color after (main panel) and before (inset) correction for extinction. (h) A coordinate map of the spatial distribution of the various pixel groups. In this and all following figures, north is up and east is to the left in all images and maps.

Table 4
Target Galaxies

ID	Galaxy	R.A. ^a (h m s)	Decl. ^a (° ′ ″)	<i>l</i> ^b (deg)	<i>b</i> ^b (deg)	<i>A</i> _{V,Galactic} ^c (mag)	Distance ^d (Mpc)	Scale ^d (kpc/(″))	Morphology Type ^e	Comments ^f
1	UGC 01104	01 32 42.5	18 10 01.6	136.48	-43.47	0.150	10.4 ± 0.7	0.050	Im	H II
2	NGC 0959	02 32 33.9	35 29 40.7	145.09	-23.00	0.179	9.9 ± 0.7	0.048	Sdm	SBcd ^g
3	NGC 1156	02 59 42.2	25 14 14.2	156.31	-29.20	0.621	6.5 ± 0.5	0.032	IB(s)m	
4	UGC 04459	08 34 07.2	66 10 54.0	149.30	34.95	0.099	2.5 ± 0.2	0.012	Im ^h	
5	UGC 04483	08 37 03.0	69 46 31.0	144.97	34.38	0.109	5.1 ± 0.4	0.025	BlueCG	
6	NGC 2623	08 38 24.1	25 45 16.6	198.84	33.97	0.102	79.4 ± 5.6	0.385	Pec ^h	LINER, LIRG, Sy2
7	NGC 2719 ⁱ	09 00 15.5	35 43 39.5	187.79	40.64	0.081	46.4 ± 3.3	0.225	Im ^h	pec?
8	NGC 2719A ⁱ	09 00 15.9	35 43 12.5	187.80	40.64	0.081	47.0 ± 3.3	0.228	Im ^h	pec
9	UGC 04998	09 25 11.0	68 22 58.9	144.69	38.88	0.157	13.1 ± 1.0	0.063	Im	
10	UGC 05101	09 35 51.7	61 21 11.3	152.48	42.90	0.093	164.3 ± 11.5	0.797	S?	LINER, LIRG, Sy1.5
11	UGC 05189	09 42 54.7	09 29 01.4	225.36	42.25	0.061	48.9 ± 3.4	0.237	Im? ^h	
12	UGC 05340	09 56 45.7	28 49 35.0	199.89	51.61	0.042	6.9 ± 0.5	0.033	Im/BCD	
13	NGC 3079	10 01 57.8	55 40 47.3	157.81	48.36	0.019	20.7 ± 1.5	0.100	SB(s)c	LINER, Sy2
14	UGC 05423	10 05 30.6	70 21 52.0	140.03	40.81	0.200	8.6 ± 0.6	0.042	Im	
15	NGC 3239	10 25 04.9	17 09 48.9	221.63	54.82	0.095	9.8 ± 0.7	0.048	IB(s)m ^h	pec
16	NGC 3274	10 32 17.3	27 40 07.6	203.76	59.21	0.059	6.8 ± 0.5	0.033	SABd?	
17	NGC 3353	10 45 22.4	55 57 37.4	152.30	53.37	0.012	18.5 ± 1.3	0.090	BCD/Irr ^h	H II
18	NGC 3445	10 54 35.5	56 59 26.5	149.59	53.66	0.013	34.3 ± 2.4	0.166	SAB(s)m ^h	
19	UGC 06541	11 33 28.9	49 14 14.0	151.90	63.28	0.030	4.6 ± 0.3	0.022	Irr + Comp	H II
20	NGC 3729	11 33 49.3	53 07 32.0	146.64	60.28	0.019	20.8 ± 1.5	0.101	SB(r)a	Sb? pec
21	NGC 3738	11 35 48.8	54 31 26.0	144.55	59.31	0.017	4.9 ± 0.4	0.024	Irr	H II
22	NGC 3741	11 36 06.2	45 17 01.1	157.57	66.45	0.043	3.8 ± 0.3	0.018	ImIII/BCD	
23	NGC 4299	12 21 40.9	11 30 12.2	277.40	72.88	0.062	1.3 ± 0.1	0.006	SAB(s)dm	H II
24	NGC 5668	14 33 24.3	04 27 01.7	354.43	56.75	0.080	27.6 ± 1.9	0.134	SA(s)d	
25	NGC 5996	15 46 58.9	17 53 03.1	29.51	48.63	0.079	53.4 ± 3.7	0.259	SBC ^h	Starburst

Continued on next page...

Table 4
(Continued)

ID	Galaxy	R.A. ^a (h m s)	Decl. ^a (° ′ ″)	<i>l</i> ^b (deg)	<i>b</i> ^b (deg)	$A_{V,\text{Galactic}}^c$ (mag)	Distance ^d (Mpc)	Scale ^d (kpc/″)	Morphology Type ^e	Comments ^f
26	UGC 10445	16 33 47.6	28 59 05.2	48.85	41.37	0.072	20.0 ± 1.4	0.097	SBc	Starburst
27	NGC 7320	22 36 03.4	33 56 53.2	93.27	-21.01	0.256	14.0 ± 1.0	0.068	SA(s)d	H II

Notes.

^a Coordinates in J2000.

^b Galactic longitude and latitude.

^c Galactic *V*-band foreground extinction. Calculated as the average A_B values of Burstein & Heiles (1982) and Schlegel et al. (1998) as given by NED and converted to A_V using $A_B/A_V = 1.324$ (Rieke & Lebofsky 1985).

^d Distances and pixel-scale corrected for “Virgo + Great Attractor + Shapley” gravitational infall (Mould et al. 2000) as given by NED.

^e Classifications listed in NED.

^f Comments on the galaxy classification or properties, from NED.

^g New classification assigned as a result of Chapter 3.

^h Classified as major mergers by Taylor et al. (2005).

ⁱ NGC 2791 and 2719A appear in the same field-of-view, and are treated as a single object.

4.2.2. Analysis of 26 Galaxies

Following Chapters 2 and 3, we analyzed the remaining 26 galaxies in the sample, and plotted the results in Figures 26–50 with the format explained above and in Figure 25 for NGC 0959. Since the parameters (e.g., the number of pixels analyzed, the range of visual dust-extinction, as well as galaxy radius, colors, and surface brightness) varies for different galaxies, the plotting ranges and areas in Figures 26–50 are adjusted for each individual galaxy to show the full range of parameters covered by that galaxy. Plotting the panels using a common parameter range across the entire galaxy sample would be ideal for object comparison. However, a matched range that covers some galaxies become too large or too wide for other galaxies, so that the plotted information becomes unreadable. The only common range used for all galaxies in Figures 25–50 is the range of the observed flux ratio, β_V , in each panel (d), which is fixed to $0.0 \leq \beta_V \leq 2.1$.

Our sample of galaxies spans a rather wide range in distance and morphology. Especially, the distance to these galaxies ranges from ~ 1.3 Mpc for NGC 4299 to ~ 165 Mpc for UGC 05101. The physical area covered by a single *GALEX* pixel of $1''.5 \times 1''.5$ therefore varies from $\sim 9 \times 9$ pc² to $\sim 1200 \times 1200$ pc² in this galaxy sample. This wide range in physical area coverage, combined with the different degree of light blending due to the large PSFs, results in slight shifts in the distribution of pixels in the pCMDs and pCCDs for different galaxies. As a result, the age and pixel-group separations in panels (d) and (g) have to be adjusted for each galaxy. In other words, the group separation is somewhat arbitrary for each galaxy, but is based

only on the visual selection in the color-magnitude and color-color distributions of pixels in the pCMDs and pCCDs. Also, since the depth of some of the *Spitzer*/IRAC 8.0 μm images is insufficient, contours overplotted for some of the sample galaxies are tracing the *GALEX* FUV emission instead of the IRAC 8.0 μm polycyclic aromatic hydrocarbon (PAH; Leger & Puget 1984) emission. In Figures 26–50, contours tracing IRAC 8.0 μm emission are colored red, while those tracing *GALEX* FUV light are colored blue in panels (b) and (c). The black dotted contours in panels (e) and (h) are always identical to those shown in panels (b) and (c) for each galaxy. The exposure times, the passbands represented by the contours, and the minimum S/N ratio used for the selection of pixels are summarized in Table 5.

Table 5
Galaxy Data

ID	Galaxy	Exposure Times			Contours	S/N _{min} ^d
		<i>GALEX</i> ^a FUV/NUV (sec)	VATT ^b <i>UBVR</i> (sec)	<i>Spitzer/IRAC</i> ^{a,c} 3.6/4.5/5.8/8.0 μm (sec)		
1	UGC 01104	1168/2864	1200/600/480/360	26.8/26.8/26.8/26.8	8.0 μm	2.0
2	NGC 0959	1694/1694	1200/600/480/360	26.8/26.8/26.8/26.8	8.0 μm	3.0
3	NGC 1156	1423/1423	1200/600/480/360	26.8/26.8/26.8/26.8	8.0 μm	3.0
4	UGC 04459	9561/9561	2400/1200/960/720	26.8/. . ./. . ./. . .	FUV	3.0
5	UGC 04483	1393/1393	2400/1200/960/720	26.8/. . ./. . ./. . .	FUV	3.0
6	NGC 2623	1696/4026	1200/600/480/360	10.4/10.4/. . ./. . .	FUV	2.5
7/8	NGC 2719/2719A	2693/2693	1200/600/480/360	10.4/10.4/10.4/10.4	FUV	1.5
9	UGC 04998	1948/1948	2400/1200/1440/720	26.8/26.8/. . ./26.8	8.0 μm	2.0
10	UGC 05101	1687/1687	1200/300/240/180	10.4/10.4/. . ./. . .	FUV	3.0
11	UGC 05189	1471/2704	1200/600/480/360	96.8/96.8/96.8/46.8	FUV	3.0
12	UGC 05340	1439/1439	2400/1200/960/720	26.8/. . ./. . ./. . .	FUV	3.0
13	NGC 3079	1680/1680	1200/600/480/360	10.4/10.4/10.4/10.4	FUV	3.0
14	UGC 05423	1698/1698	1200/600/480/360	26.8/26.8/. . ./. . .	FUV	3.0
15	NGC 3239	1766/1766	1200/600/480/360	26.8/26.8/. . ./. . .	FUV	4.0
16	NGC 3274	1661/1661	1200/600/480/360	26.8/26.8/. . ./. . .	FUV	3.0
17	NGC 3353	16601/36808	1200/600/480/360	1.2/1.2/1.2/1.2	FUV	3.0
18	NGC 3445	28080/85021	1200/600/480/360	10.4/10.4/. . ./10.4	FUV	2.0
19	UGC 06541	1648/1648	1200/600/480/600	26.8/26.8/. . ./. . .	FUV	2.5

Continued on next page...

Table 5
(Continued)

ID	Galaxy	Exposure Times			Contour	S/N _{min}
		<i>GALEX</i> ^a FUV/NUV (sec)	VATT ^b <i>UBVR</i> (sec)	<i>Spitzer/IRAC</i> ^{a,c} 3.6/4.5/5.8/8.0 μm (sec)		
20	NGC 3729	1618/1618	1200/600/480/360	10.4/10.4/10.4/10.4	8.0 μm	3.0
21	NGC 3738	1620/1620	1200/600/480/360	26.8/26.8/26.8/26.8	8.0 μm	3.0
22	NGC 3741	1663/3231	2400/1200/960/720	26.8/26.8/26.8/26.8	FUV	3.0
23	NGC 4299	1691/3280	1200/600/480/360	26.8/26.8/26.8/26.8	8.0 μm	3.0
24	NGC 5668	1698/1698	1200/600/480/360	26.8/26.8/. . ./26.8	8.0 μm	3.0
25	NGC 5996	2609/4899	120000/600/480/360	10.4/10.4/. . ./ . . .	FUV	2.5
26	UGC 10445	4281/4281	1200/600/480/360	26.8/26.8/. . ./26.8	8.0 μm	3.0
27	NGC 7320	7646/12239	1200/600/480/360	10.4/10.4/. . ./10.4	8.0 μm	2.5

Notes.

^a Exposure time recorded in the header of the final pipeline product images.

^b Total exposure time (from Taylor et al. 2005).

^c “. . .” means that the image was not deep enough for our analysis. This is (by selection) only true for some of the IRAC4.5, 5.8, and 8.0 μm images, but not the IRAC 3.6 μm image.

^d Minimum S/N for some galaxies are adjusted from 3.0 so that enough pixels are selected in FUV images.

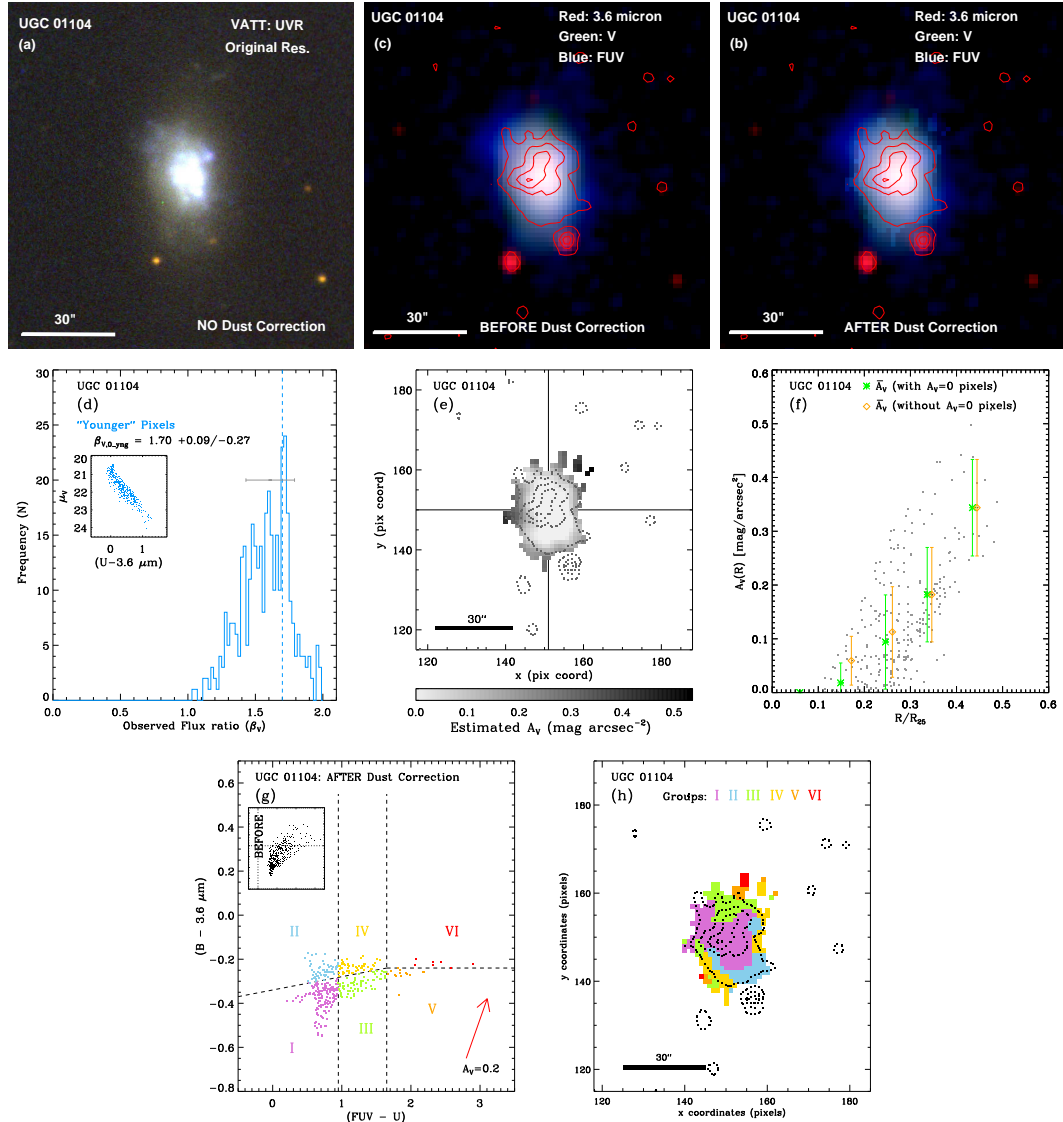


Figure 26. Analysis of UGC01104, as Figure 25. Red contours in panels (b) and (c) trace the IRAC $8.0 \mu\text{m}$ emission, which are plotted as black dotted curves in all panels (e) and (h). (d) All pixels are treated as younger pixels for this galaxy. (e) Dust extinction is mapped using the full range of gray-scales. The crosshairs in panel (e) indicates the x - and y -coordinates of the galaxy center (same is true for Figures 27–50). (f) Radial A_V profile for this galaxy shows the extinction is steeply increasing as radius increases. (g) Pixels in pCCD of $(B - 3.6 \mu\text{m})$ versus $(\text{FUV} - U)$ color are separated into six pixel-groups based on visual distribution pattern. (h) The selected pixel-groups are mapped onto a pixel coordinate map. Distribution of Group I pixels at the center indicates the SF-activity is strongest at the center of galaxy. The color coding used in panels (g) and (h) (and in Figures 27–50) is the same as for NGC 0959 (Figure 25).

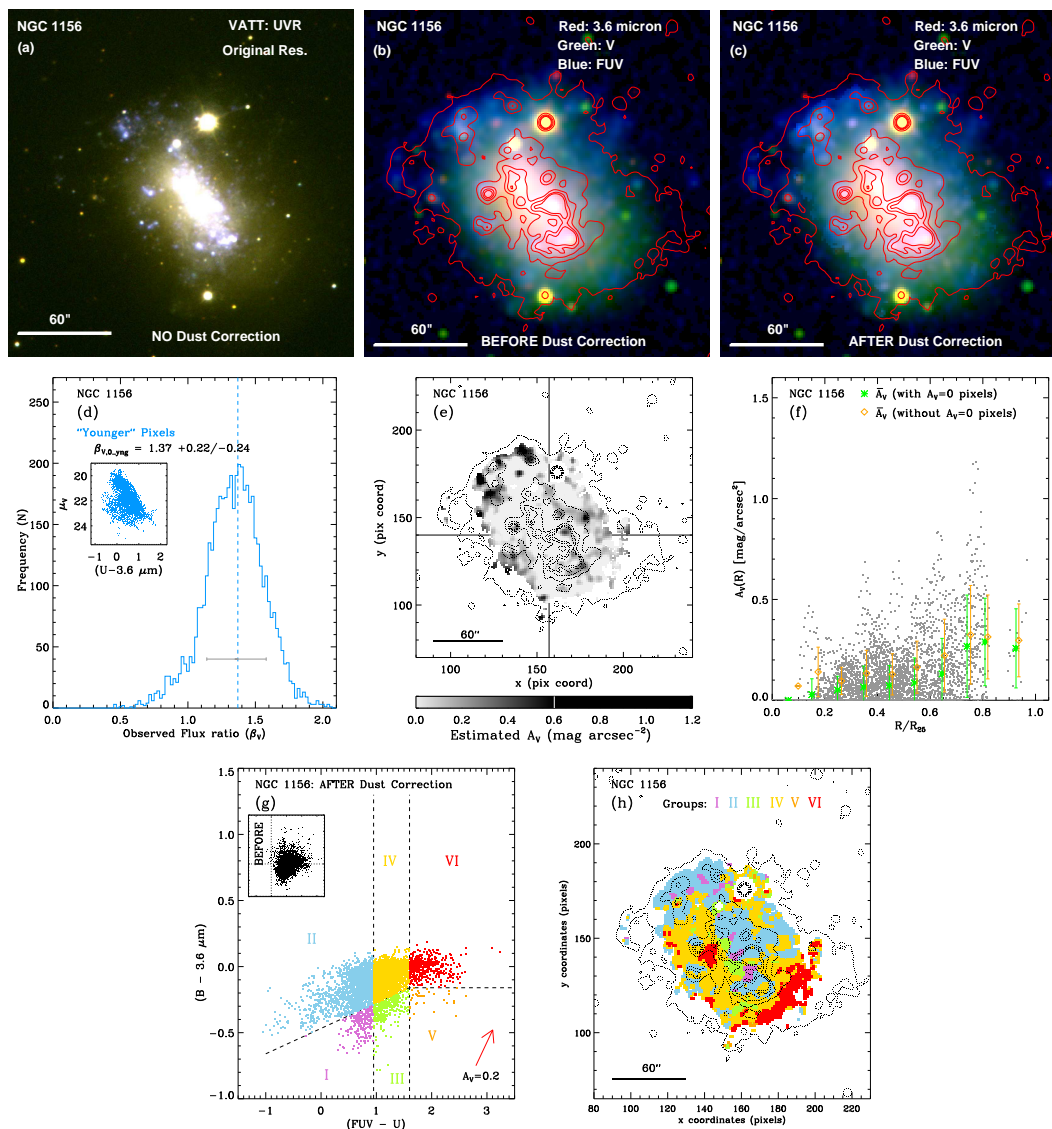


Figure 27. As Figure 25, for NGC 1156. Red contours in panels (b) and (c) trace the IRAC $8.0 \mu\text{m}$ emission. (d) All pixels are treated as the younger pixels for this galaxy. (e) Dust extinction is mapped using the full range of gray-scales for $A_V \leq 0.6 \text{ mag arcsec}^{-2}$, as indicated by the vertical white line in the gray-scale bar. Unless indicated otherwise, panels (f), (g), and (h) are as described for Figures 25 and 26.

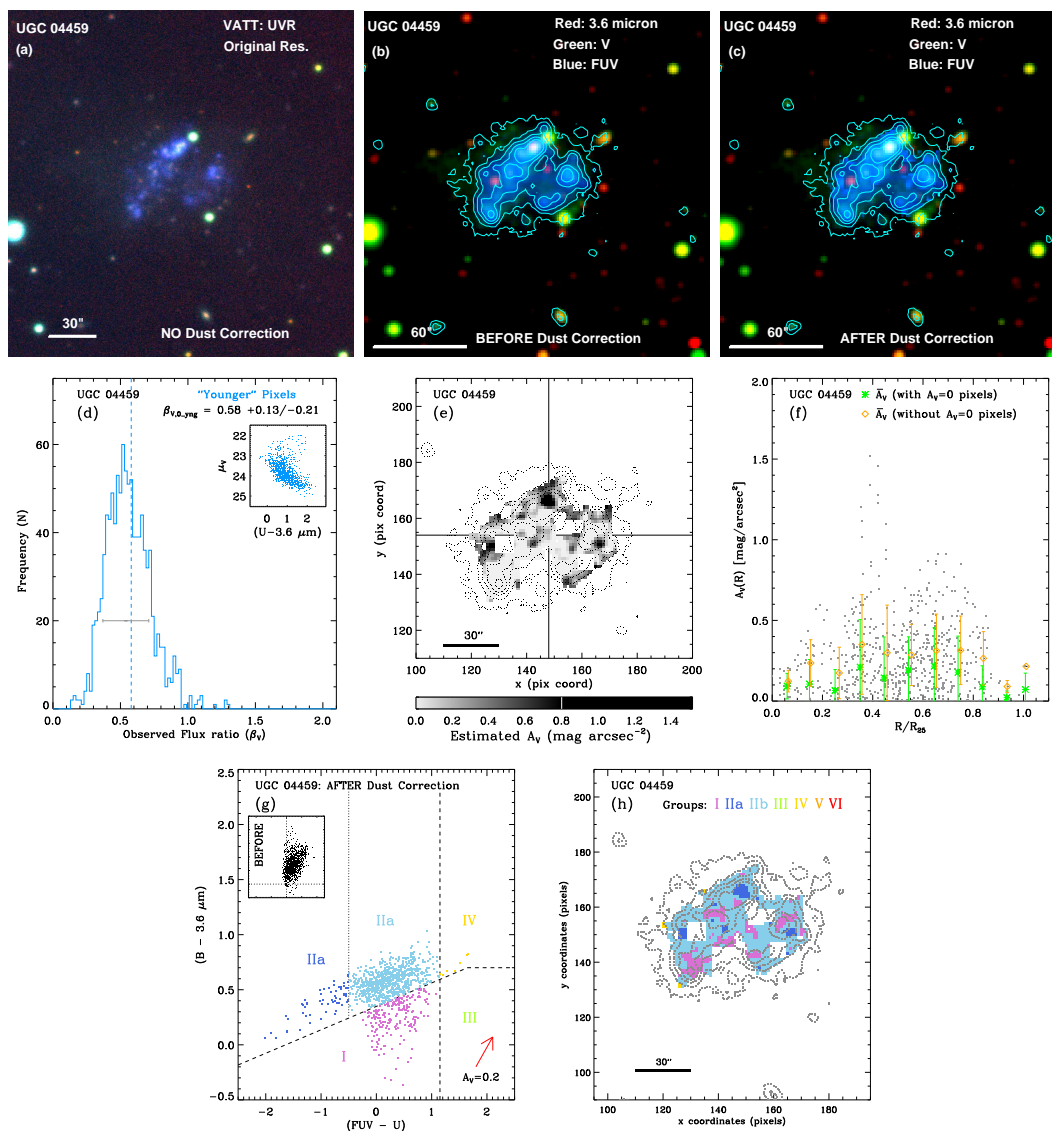


Figure 28. As Figure 25, for UGC 04459. Blue contours in panels (b) and (c), and black dotted contours in panels (e) and (h) trace the *GALEX* FUV emission. (d) All pixels are treated as younger pixels for this galaxy. (e) Dust extinction is mapped using the full range of gray-scales for $A_V \leq 0.8 \text{ mag arcsec}^{-2}$. (g) Group II pixels are separated into IIa and IIb, and no Group III, V, and VI pixels are selected for this very young galaxy.

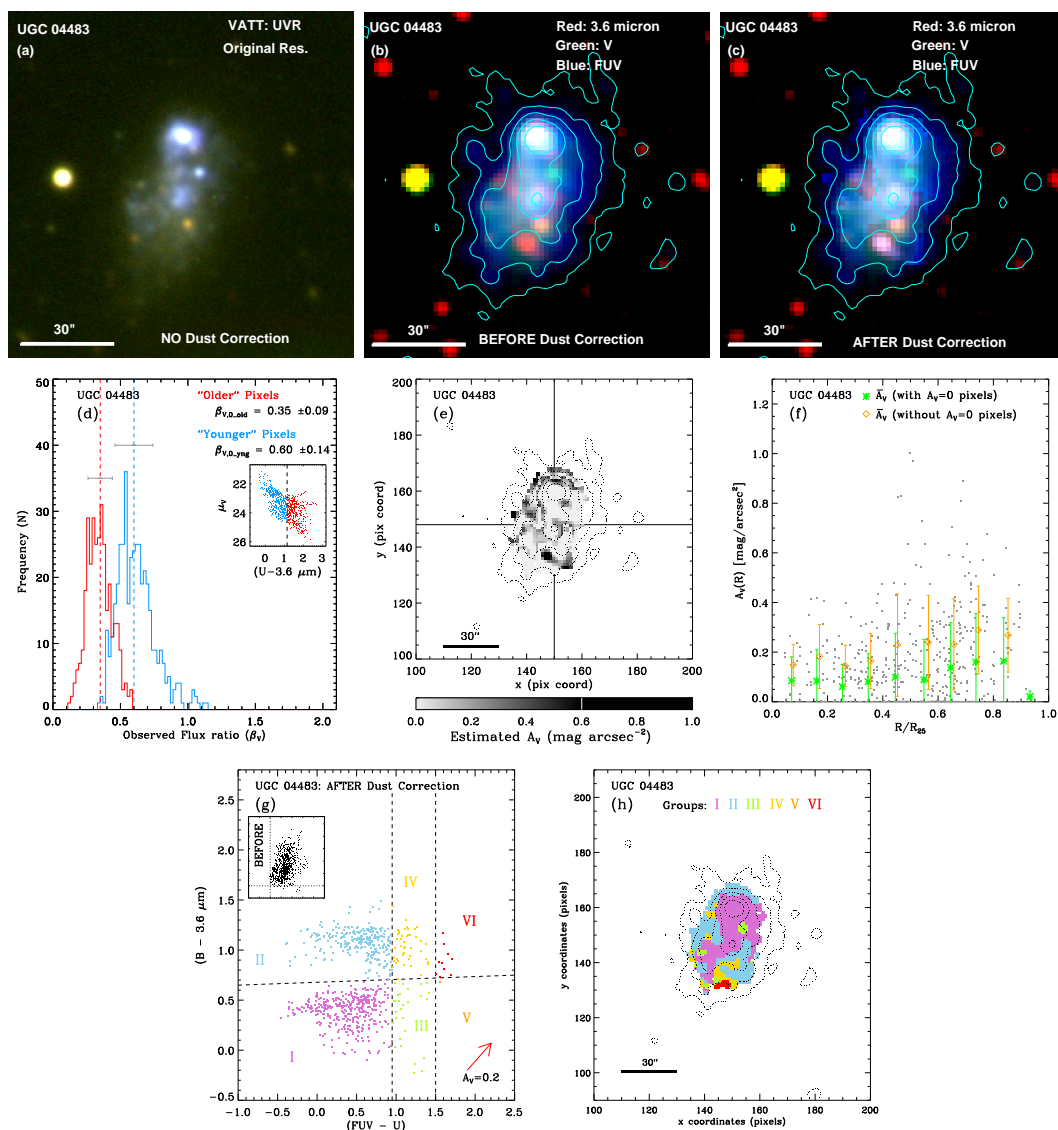


Figure 29. As Figure 25, for UGC04483. Blue contours in panels (b) and (c) trace the *GALEX* FUV emission. (e) Dust extinction is mapped using the full range of gray-scales for $A_V \leq 0.6 \text{ mag arcsec}^{-2}$. Panels (f), (g), and (h) are as described for Figures 25 and 26.

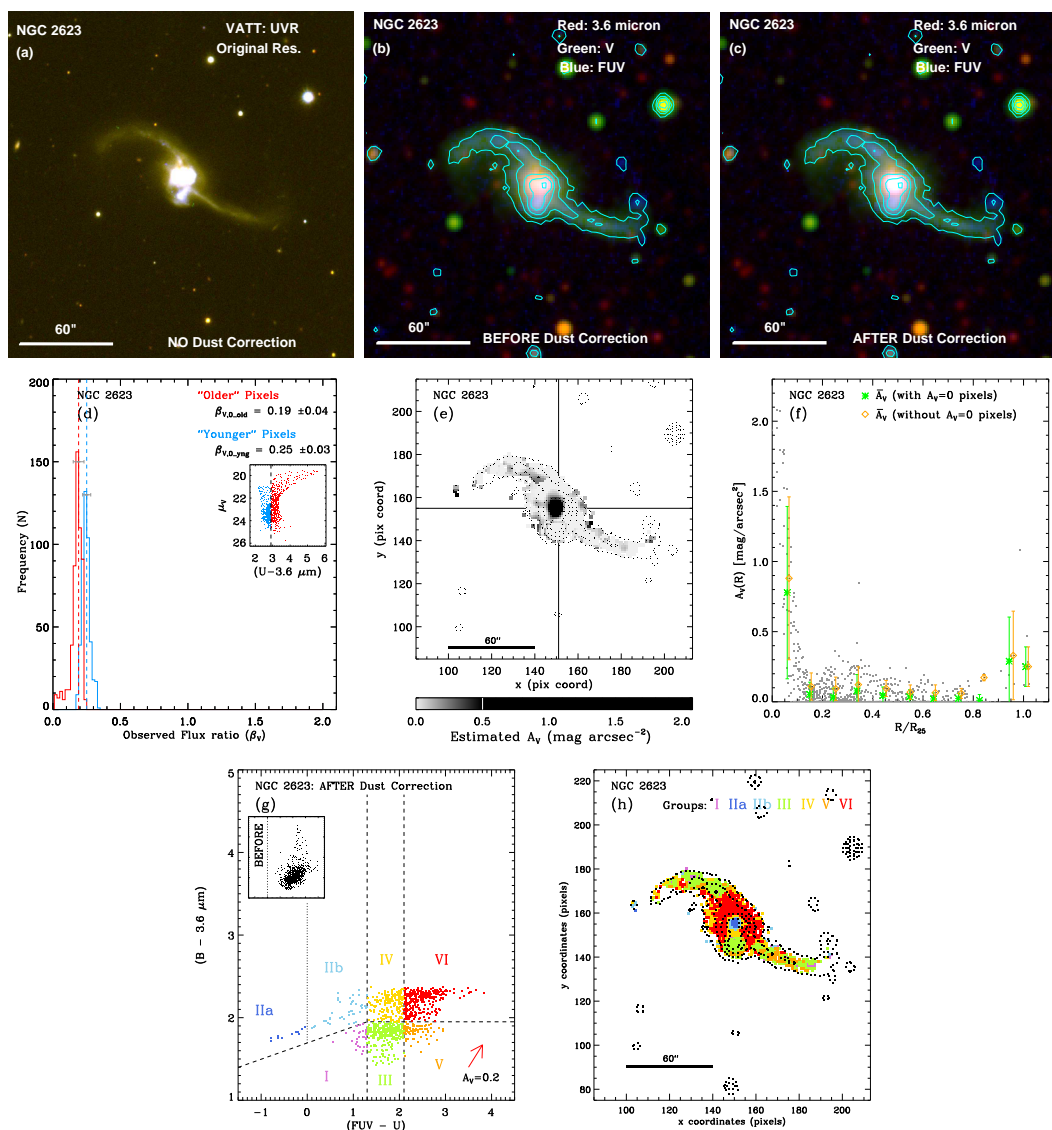


Figure 30. As Figure 25, for NGC 2623. Blue contours in panels (b) and (c) trace the *GALEX* FUV emission. (e) Dust extinction is mapped using the full range of gray-scales for $A_V \leq 0.5$ mag arcsec $^{-2}$. (g) Group II pixels are separated into IIa and IIb, and Group IIb pixels only occur in the galaxy center.

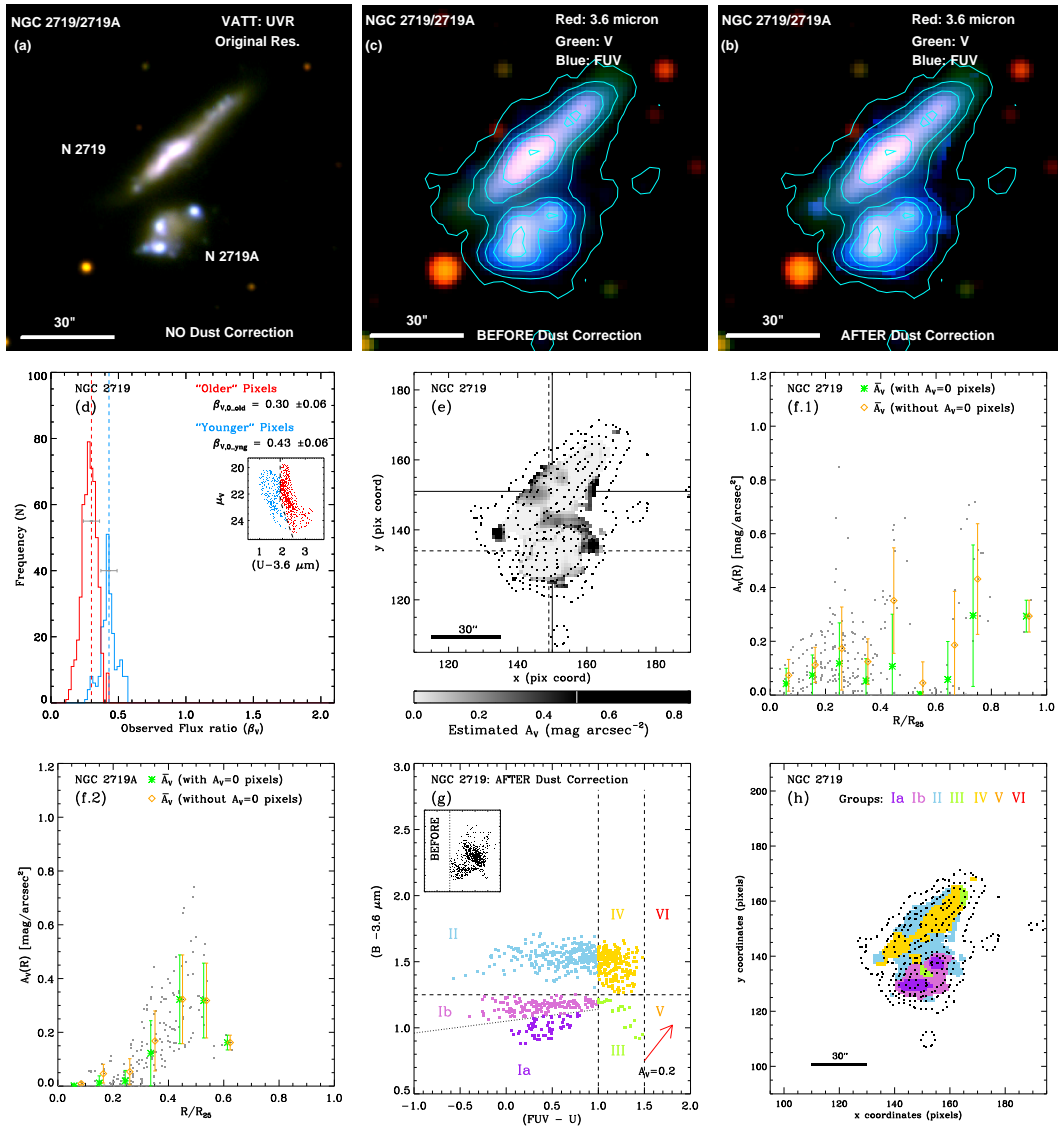


Figure 31. As Figure 25, for NGC 2719/2719A. Blue contours in panels (b) and (c) trace the *GALEX* FUV emission. (e) Dust extinction is mapped using the full range of gray-scales for $A_V \leq 0.5 \text{ mag arcsec}^{-2}$. (f) The radial A_V profile is split into two panels for NGC 2719 (f.1) and NGC 2719A (f.2), respectively. (g) Group I pixels are separated into Ia and Ib due to a slight gap in distribution between them, which corresponds to clearly distinct regions in NGC 2719A.

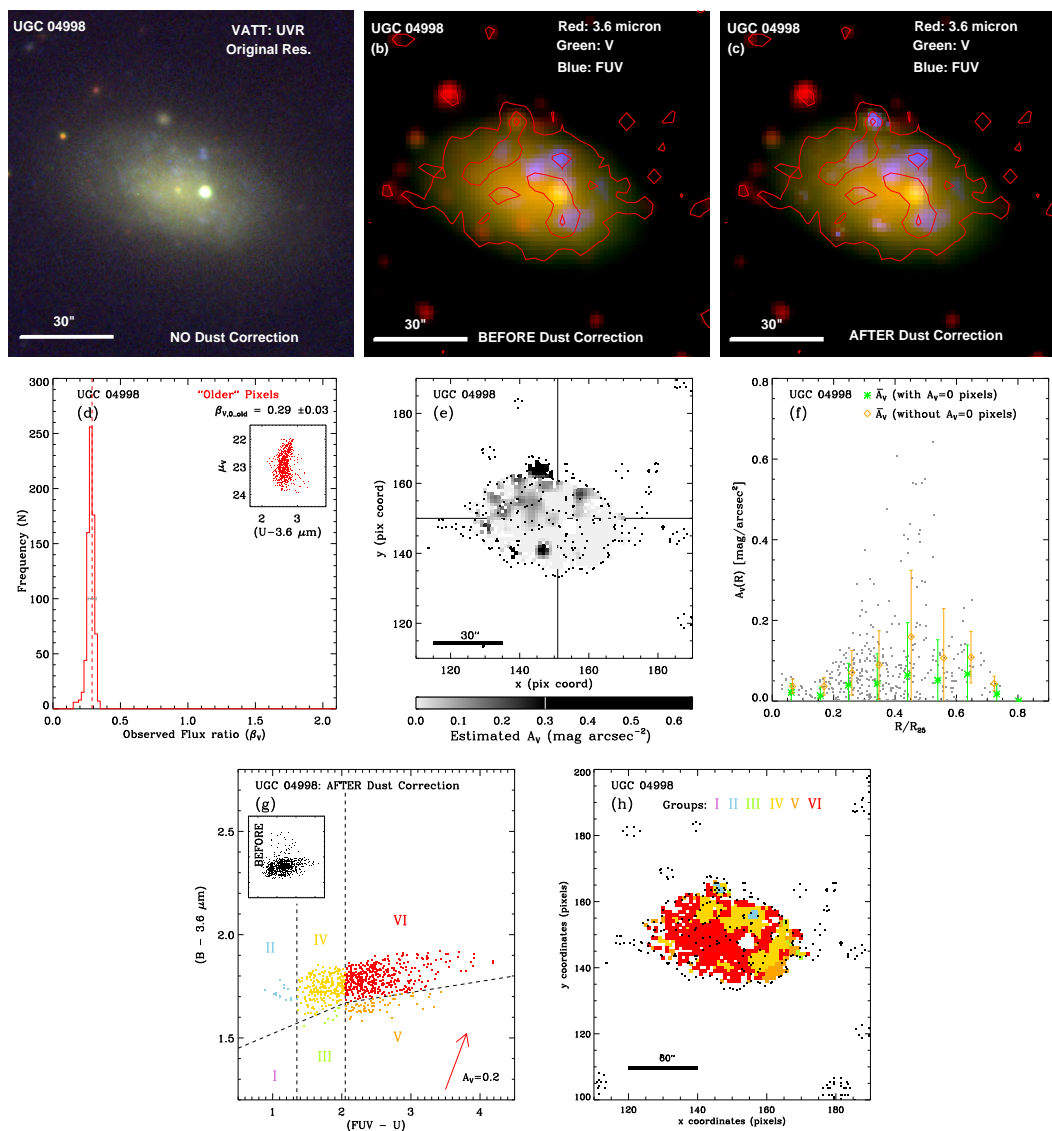


Figure 32. As Figure 25, for UGC04998. Red contours in panels (b) and (c) trace the IRAC $8.0 \mu\text{m}$ emission. (d) All pixels are treated as older pixels for this galaxy. (e) Dust extinction is mapped using the full range of gray-scales for $A_V \leq 0.3 \text{ mag arcsec}^{-2}$. (g) This panel shows clearly most of pixels in UGC04998 is dominated by older stellar populations (Group VI pixels). No Group I pixels are selected in this rather old galaxy.

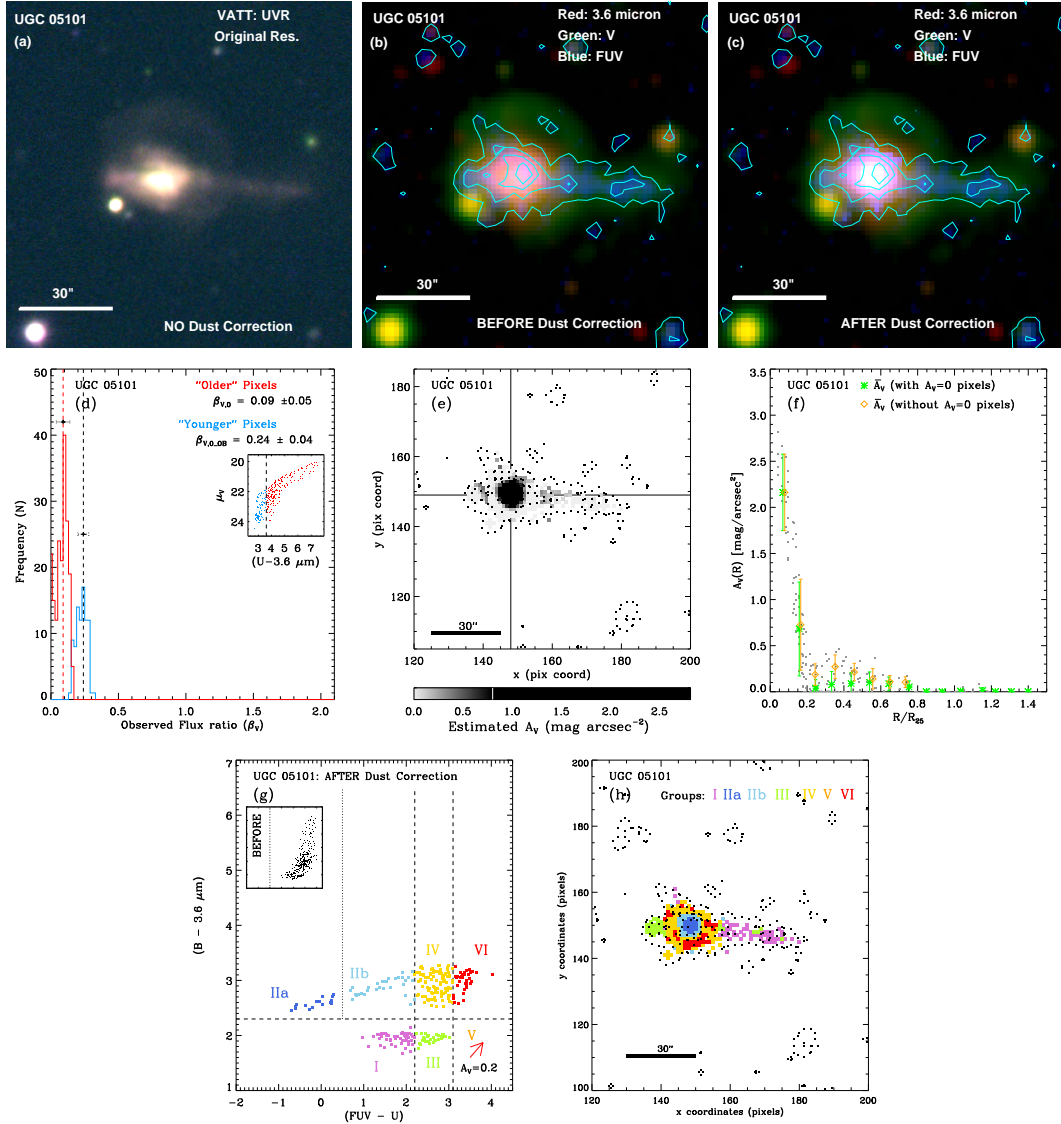


Figure 33. As Figure 25, for UGC 05101. Blue contours in panels (b) and (c) trace the *GALEX* FUV emission. Panels (b) and (c) show that there is a faint disk surrounding the galaxy center, yet these regions are not analyzed due to low S/N not satisfying our minimum criteria in some filters. (d) While the main panel shows a two-peak distribution, the shape of the pixel-distribution in the inset pCMD does not show two different populations or any branches. Since UGC 05101 is at $D \simeq 164$ Mpc, a single pixel covers physically a large area, resulting in significant light blending. Therefore, all pixels are treated older pixels for this galaxy. (e) Dust extinction is mapped using the full range of gray-scales for $A_V \leq 0.8 \text{ mag arcsec}^{-2}$. (g) Group II pixels are separated into IIa and IIb, and Group IIa pixels are only located in the galaxy center.

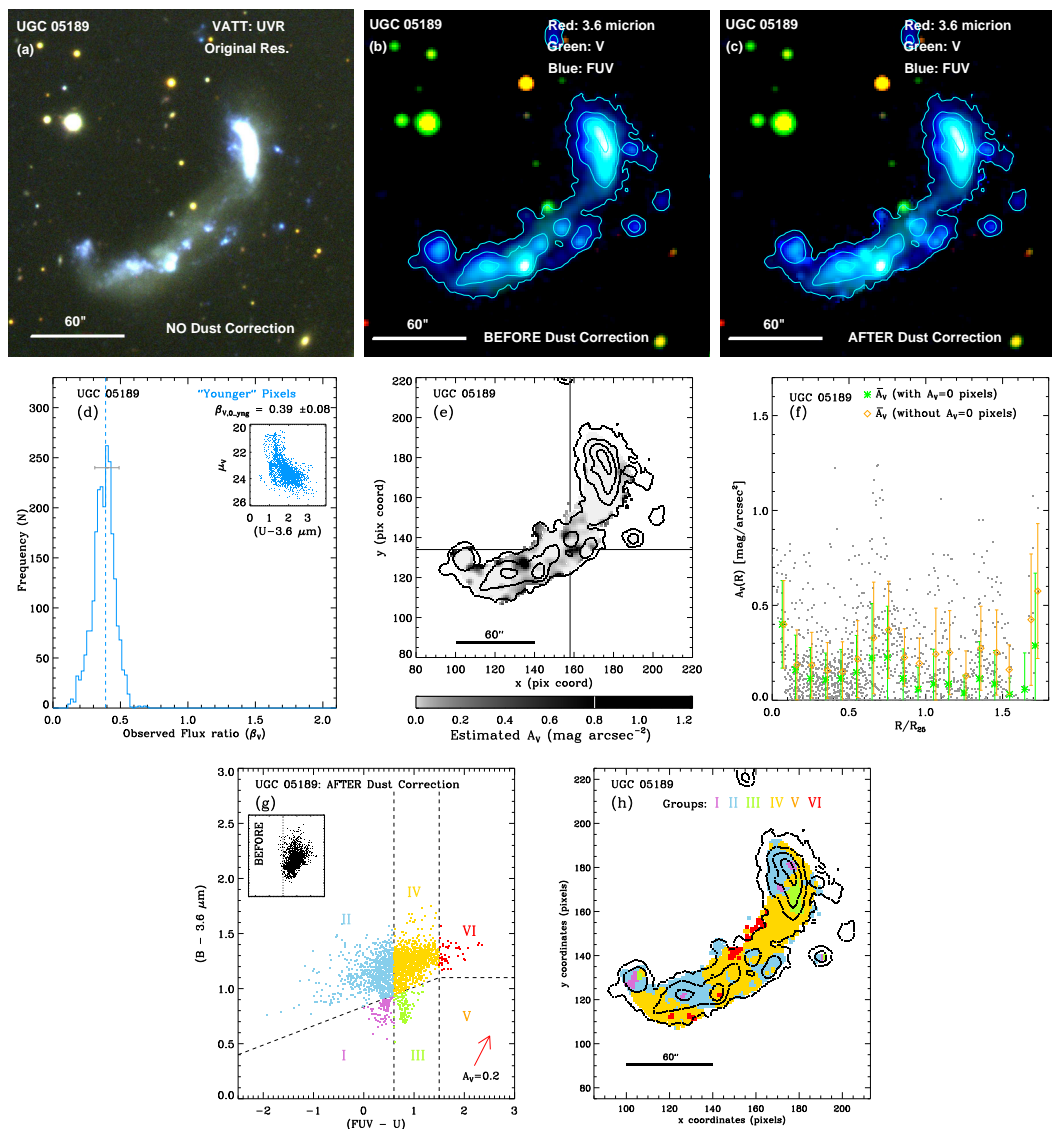


Figure 34. As Figure 25, for UGC05189. Blue contours trace the *GALEX* FUV emission. There is no apparent structure to this galaxy, and bright SF regions are distributed throughout (see panels (a)–(c)). (d) All pixels are treated as younger pixels for this galaxy. (e) Dust extinction is mapped using the full range of gray-scales for $A_V \leq 0.8 \text{ mag arcsec}^{-2}$. Panels (f), (g), and (h) are as described in Figures 25 and 26.

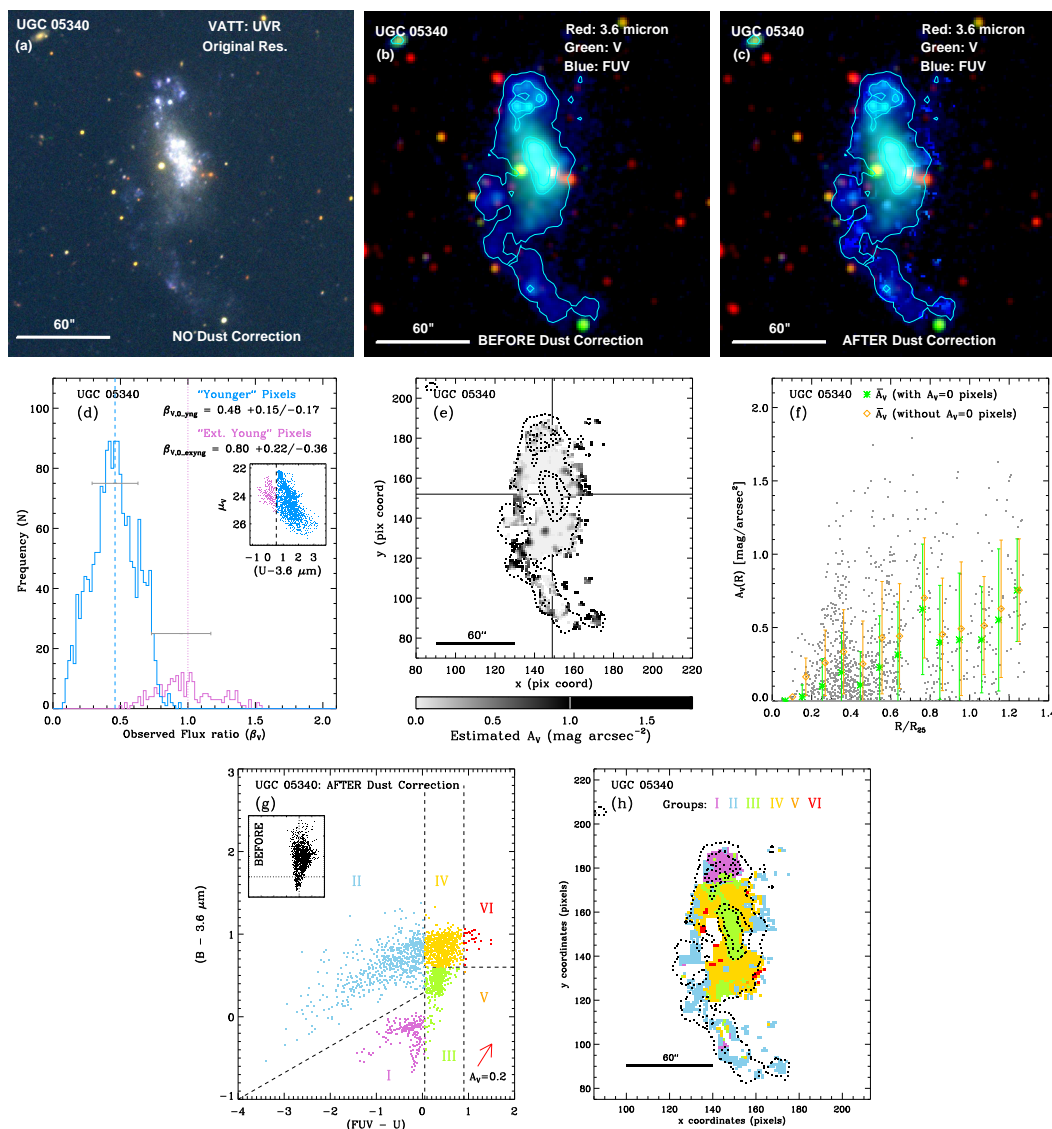


Figure 35. As Figure 25, for UGC05340. Blue contours trace the *GALEX* FUV emission. The red objects in panels (b) and (c) are foreground stars. (d) Pixels are separated into younger and extremely young groups: all of the extremely young pixels are located in the five SF regions at the northern end of the galaxy. (e) Dust extinction is mapped using the full range of gray-scales for $A_V \leq 1.0 \text{ mag arcsec}^{-2}$. (h) Most of SF-activity is going on at the northern end and in the tail extending toward the southern side of the galaxy.

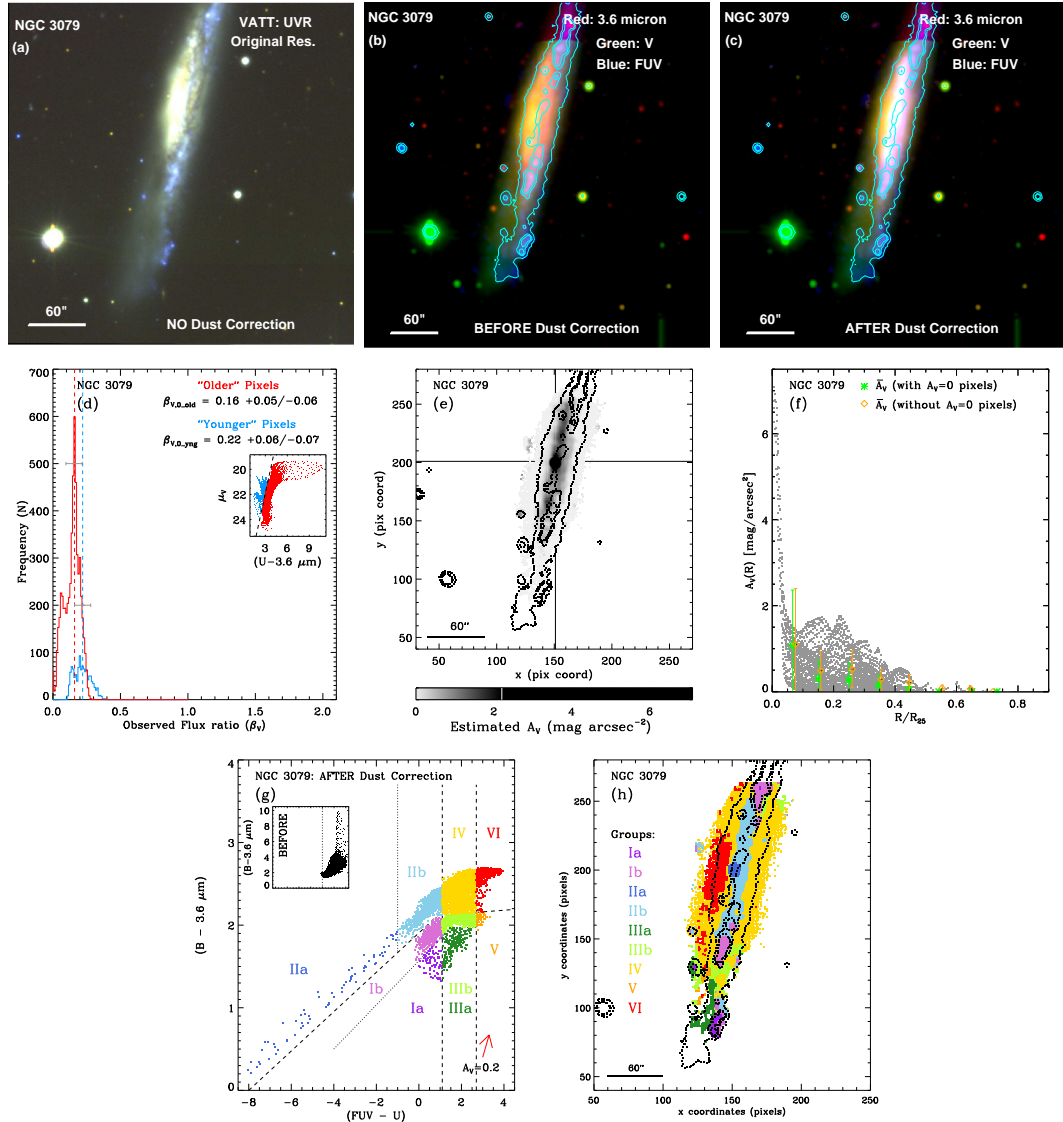


Figure 36. As Figure 25, for NGC 3079. Blue contours trace the *GALEX* FUV emission. While some dust lanes are visible in panel (a), these are hard to recognize in panel (b). (c) The significant change in apparent color of the galaxy bulge indicates that dust extinction is large in that region, as expected. (e) Dust extinction is mapped using the full range of gray-scales for $A_V \leq 2.2 \text{ mag arcsec}^{-2}$. (f) The dust extinction reaches $\sim 7 \text{ mag arcsec}^{-2}$ in the center of the galaxy, and amounts to $A_V \simeq 2.0$ at the inner radius (bulge) of the galaxy. (g) Each of Group I, II, and III pixels are separated further into two subgroups, based on their color-color distribution in the pCCD. Due to a plume extending to $(B - 3.6 \mu\text{m}) \simeq 10 \text{ mag}$, the the y -axis of inset is plotted with larger range, to cover all of the pixel distribution in the pCCD. (h) Group IIa pixels with extremely blue intrinsic $(FUV - U)$ colors are located only in the core of the galaxy.

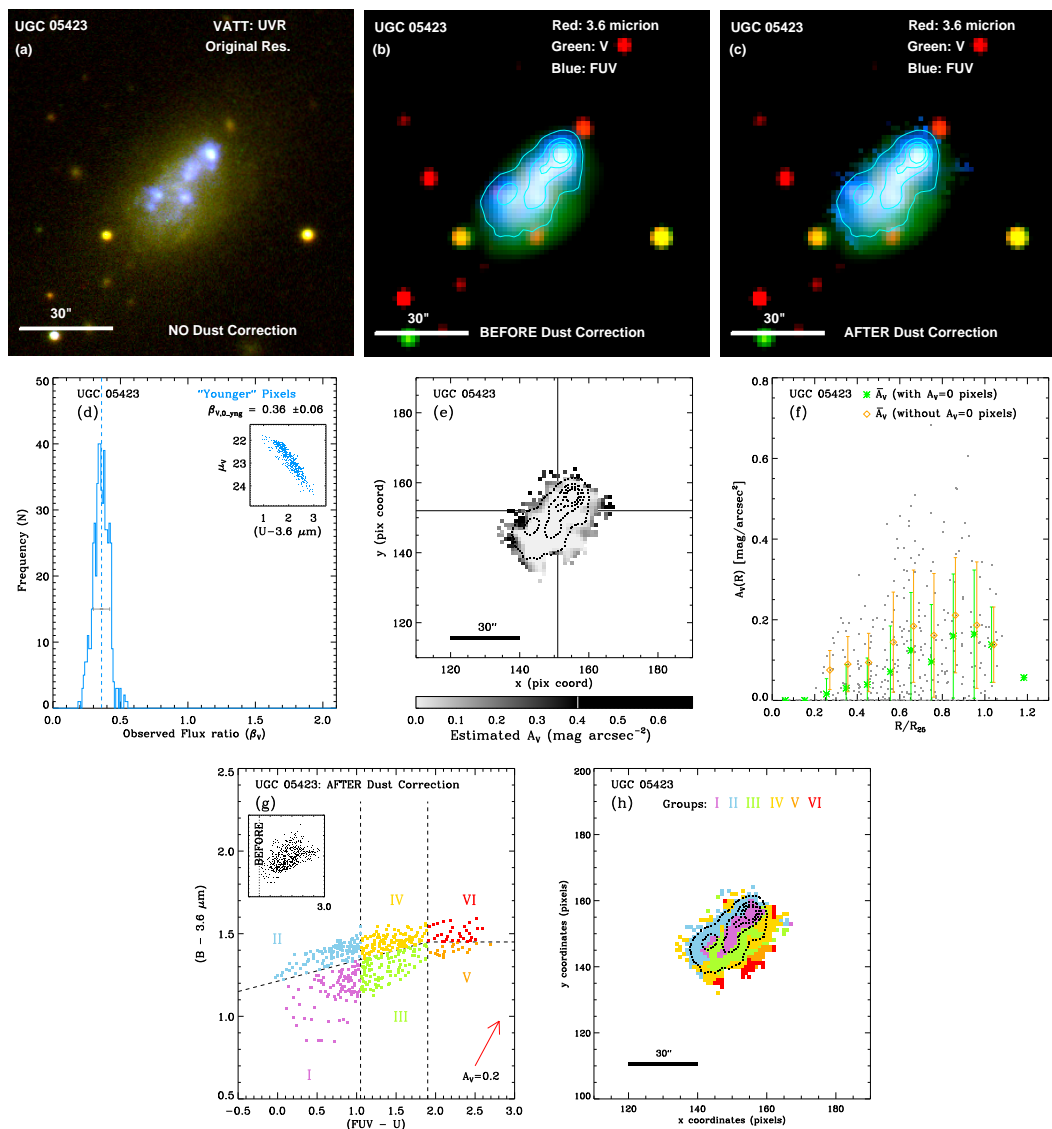


Figure 37. As Figure 25, for UGC05423. Blue contours trace the *GALEX* FUV emission. Red and yellow objects appear in panels (a)–(c) are mostly foreground stars. (d) All pixels are treated as younger pixels for this galaxy. (e) Dust extinction is mapped using the full range of gray-scales for $A_V \leq 0.4 \text{ mag arcsec}^{-2}$. (f) There is no measurable dust extinction at the center, and A_V increases toward outer radii, as can be seen in panel (e).

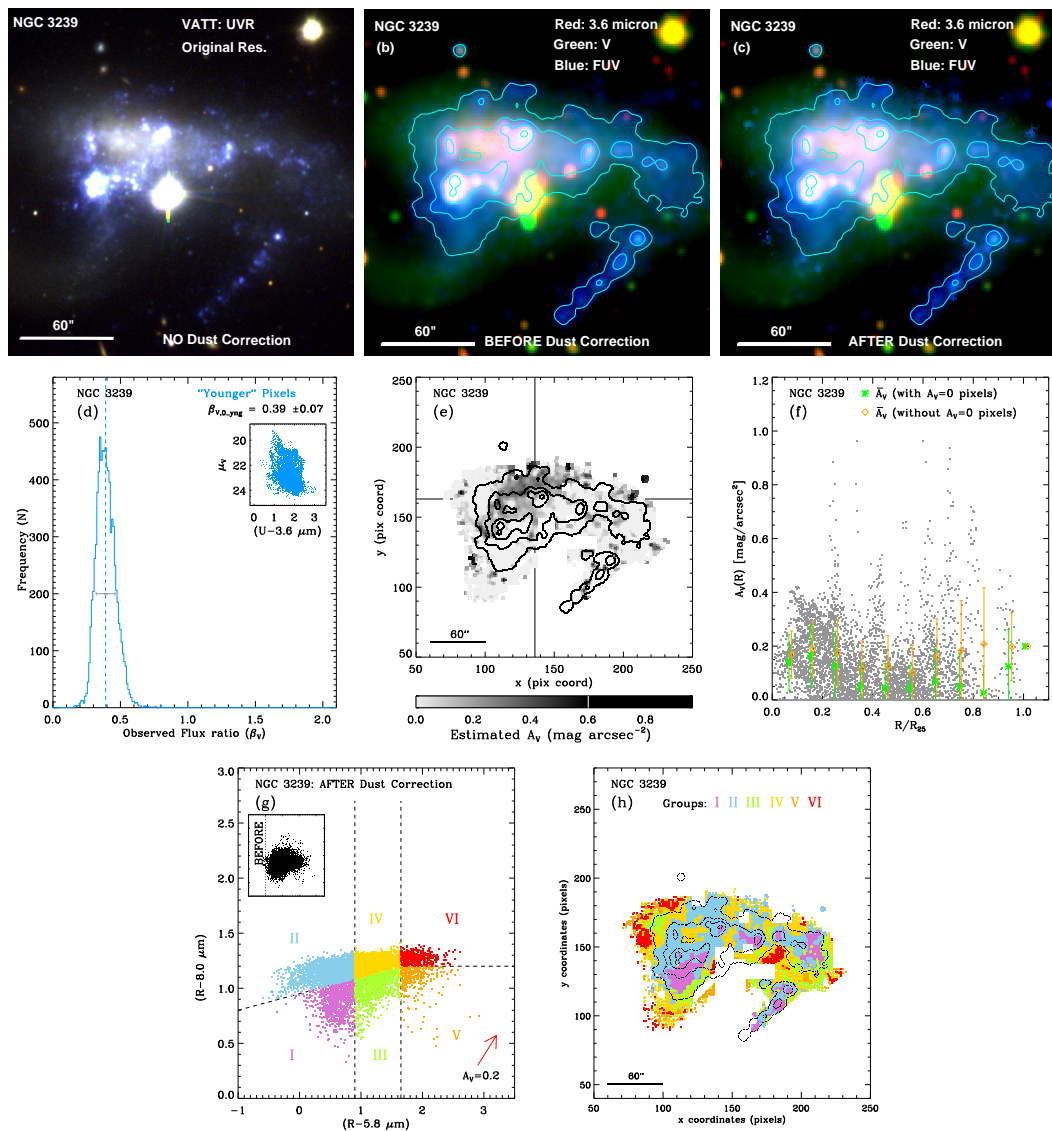


Figure 38. As Figure 25, for NGC 3239. Blue contours trace the *GALEX* FUV emission. Pixels affected by the bright foreground star at the SW edge of the galaxy center has been removed from the analysis. (d) All pixels are treated as younger pixels for this galaxy. (e) Dust extinction is mapped using the full range of gray-scales for $A_V \leq 0.6 \text{ mag arcsec}^{-2}$.

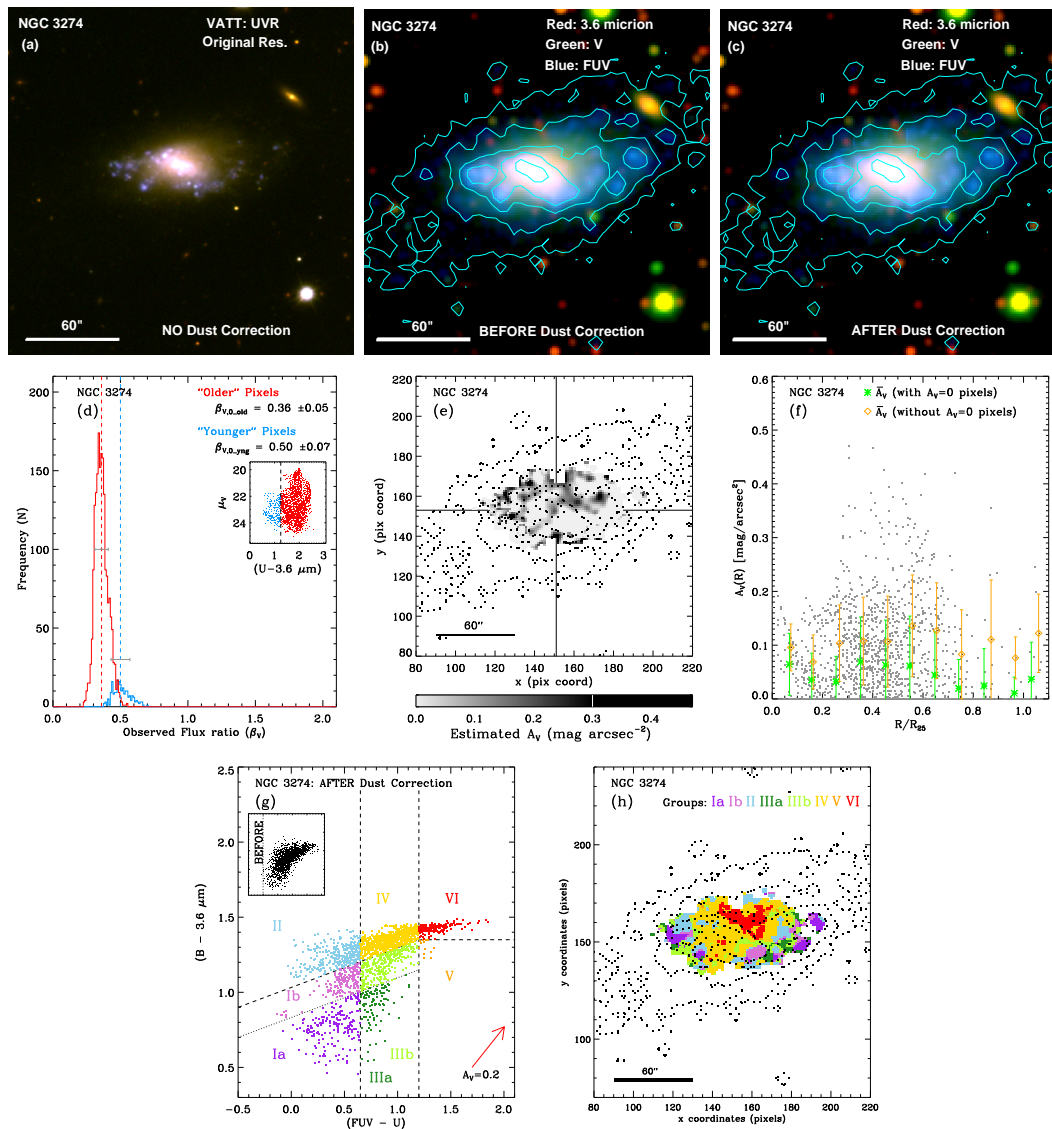


Figure 39. As Figure 25, for NGC 3274. Blue contours trace the *GALEX* FUV emission. The FUV light extends to much larger radii than the visible portion of the galaxy disk. (e) Dust extinction is mapped using the full range of gray-scales for $A_V \leq 0.3 \text{ mag arcsec}^{-2}$. (g) Group I and III pixels are separated into two subgroups, due to their distribution in pCCD. (h)

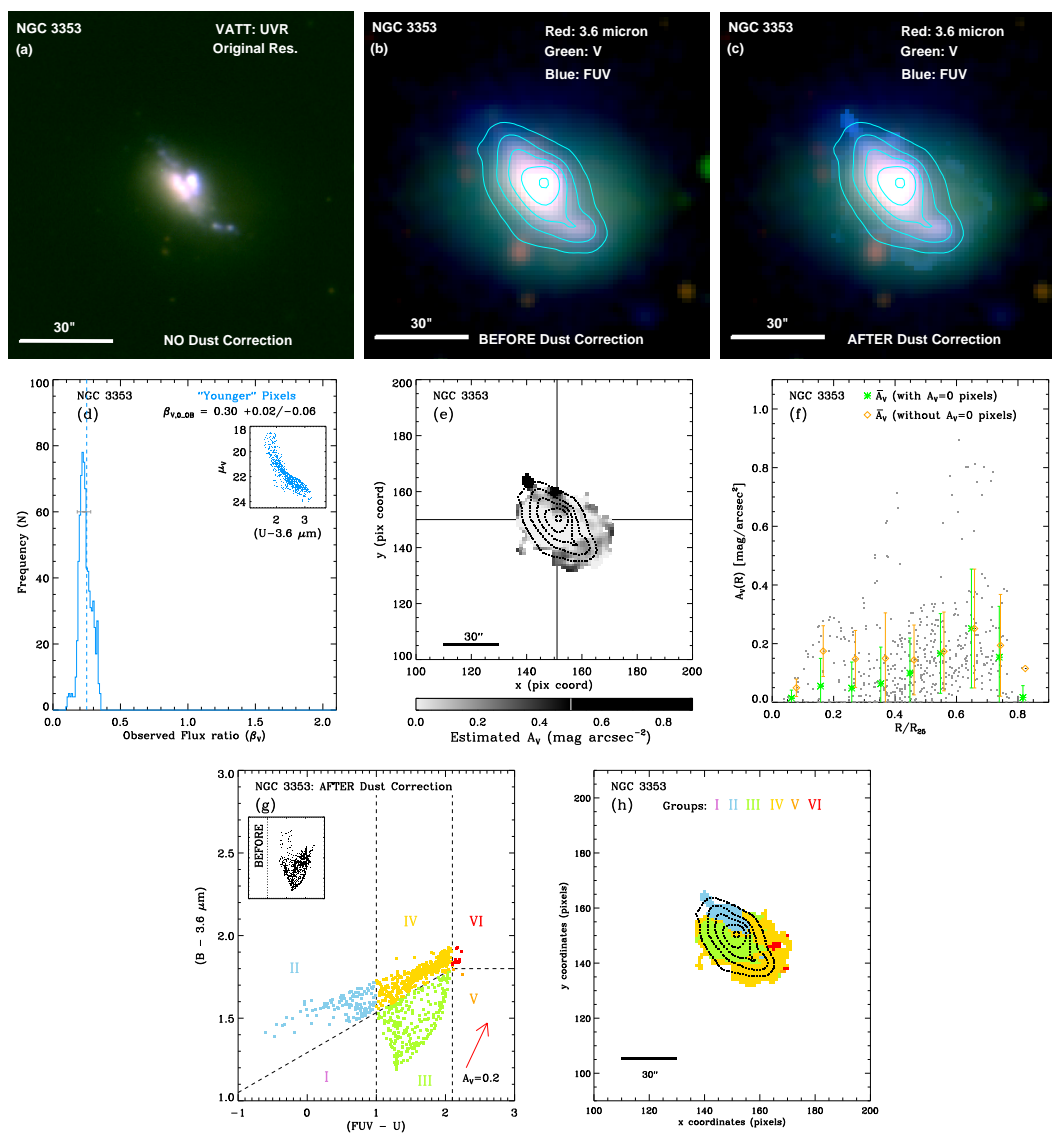


Figure 40. As Figure 25, for NGC 3353. Blue contours trace the *GALEX* FUV emission. (d) All pixels is treated as younger pixels in this galaxy. (e) Dust extinction is mapped using the full range of gray-scales for $A_V \leq 0.5 \text{ mag arcsec}^{-2}$.

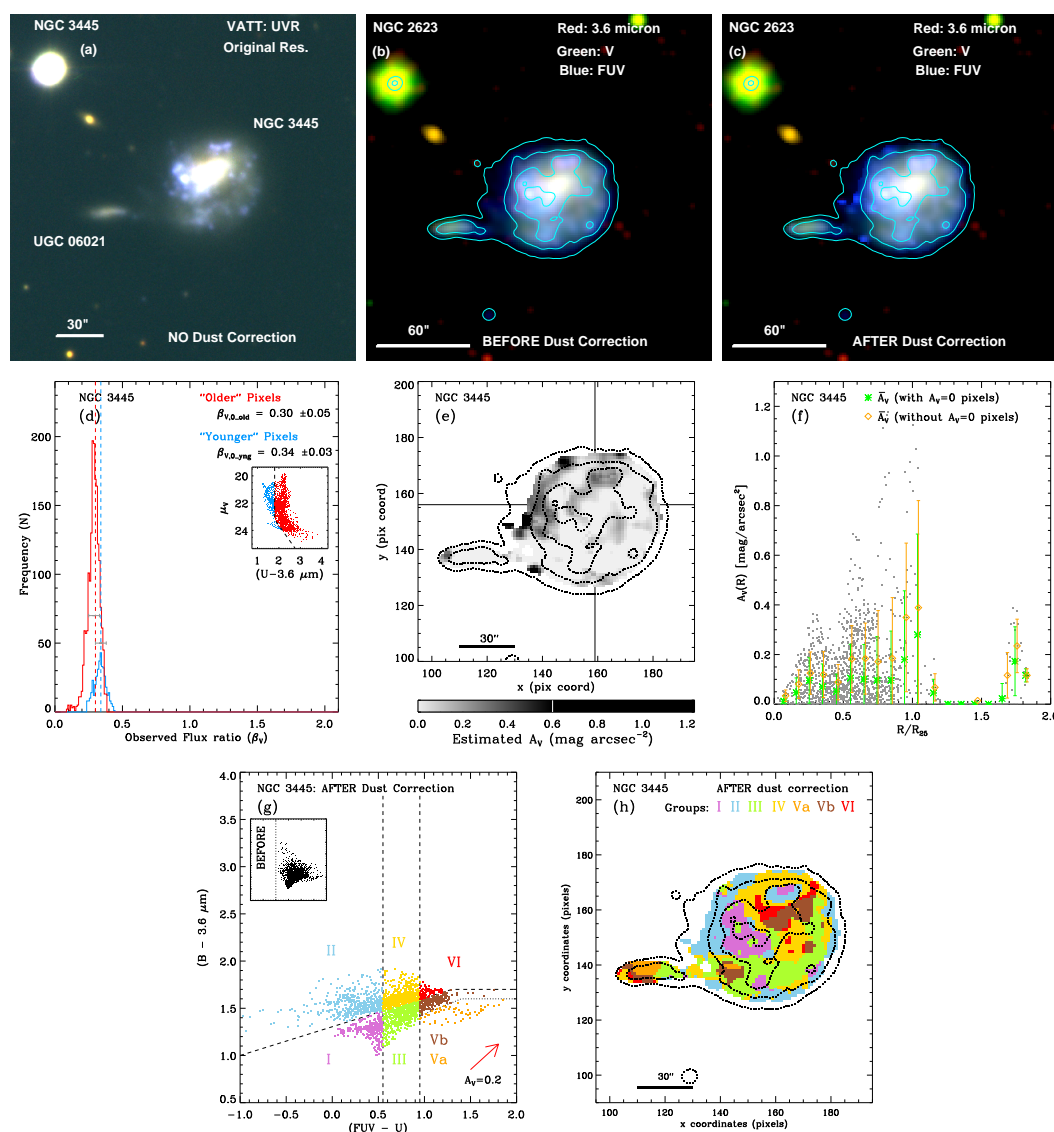


Figure 41. As Figure 25, for NGC3445. Blue contours trace the *GALEX* FUV emission. The smaller galaxy SE of NGC 3445—connected by contours in panels (b) and (c)—is UGC06021, whose pixels are analyzed together with NGC3445. (e) Dust extinction is mapped using the full range of gray-scales for $A_V \leq 0.6$ mag arcsec $^{-2}$. (f) The group of pixel-based dust extinction, $A_{V,i}$ at $R/R_{25} \gtrsim 1.2$ belongs to UGC06021, which is located at the eastern (left) end of the UGC06021, as indicated in panel (e). (g) Group V pixels are separated into Va and Vb, where most of Group Va (orange) pixels belong to UGC06021 and the SE corner of NGC 3445, as can be seen in panel (h).

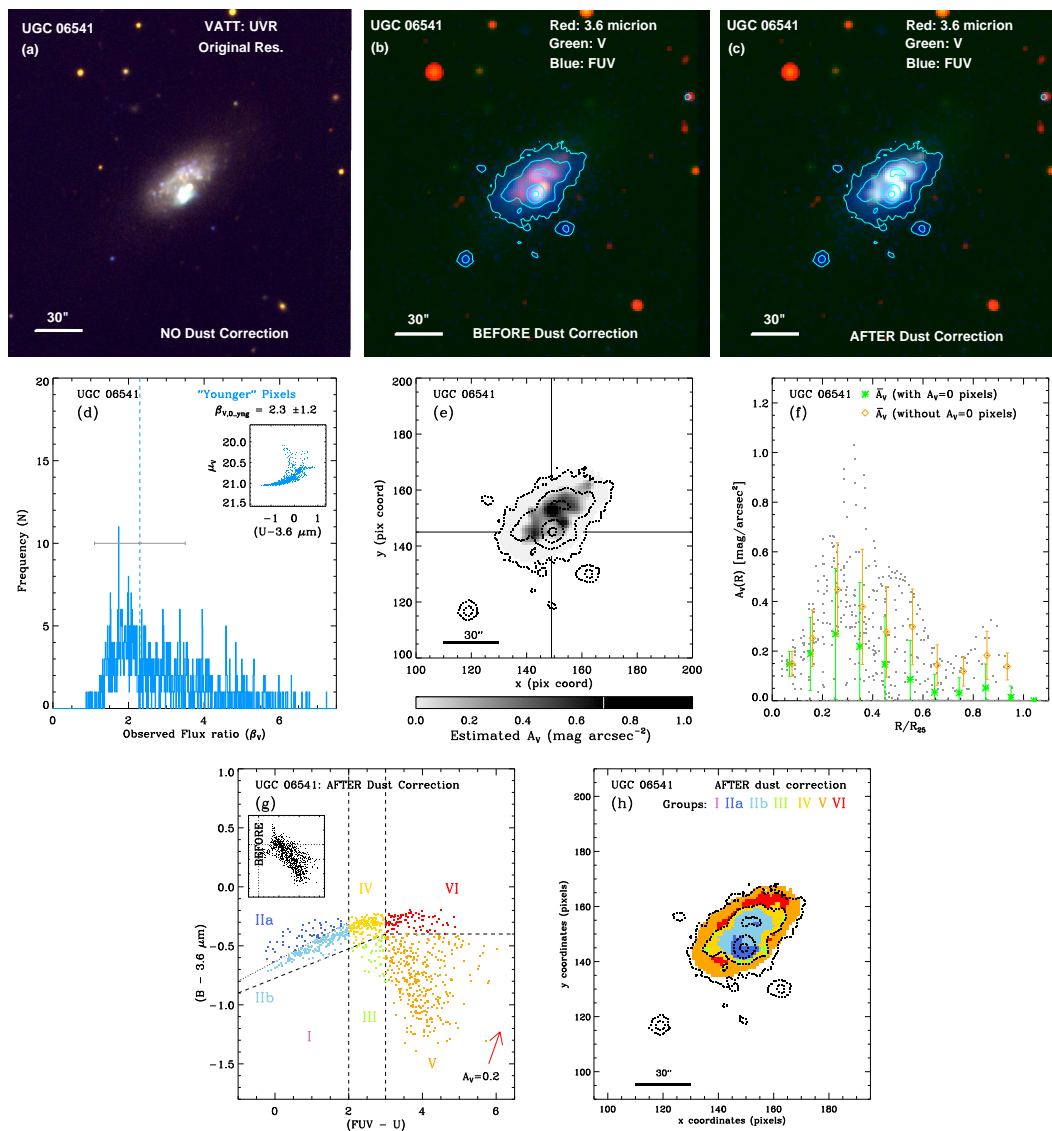


Figure 42. As Figure 25, for UGC06541. Blue contours trace the *GALEX* FUV emission. According to NED, this galaxy has a strong H II region. Therefore all pixels are treated as younger pixels in panel (d). (e) Dust extinction is mapped using the full range of gray-scales for $A_V \leq 0.7 \text{ mag arcsec}^{-2}$. (g) Group II pixels are separated into IIa and IIb, which is not based on $(\text{FUV} - U)$ color as for some other galaxies, but based on $(B - 3.6 \mu\text{m})$ color, due to their distribution pattern seen in the pCCD.

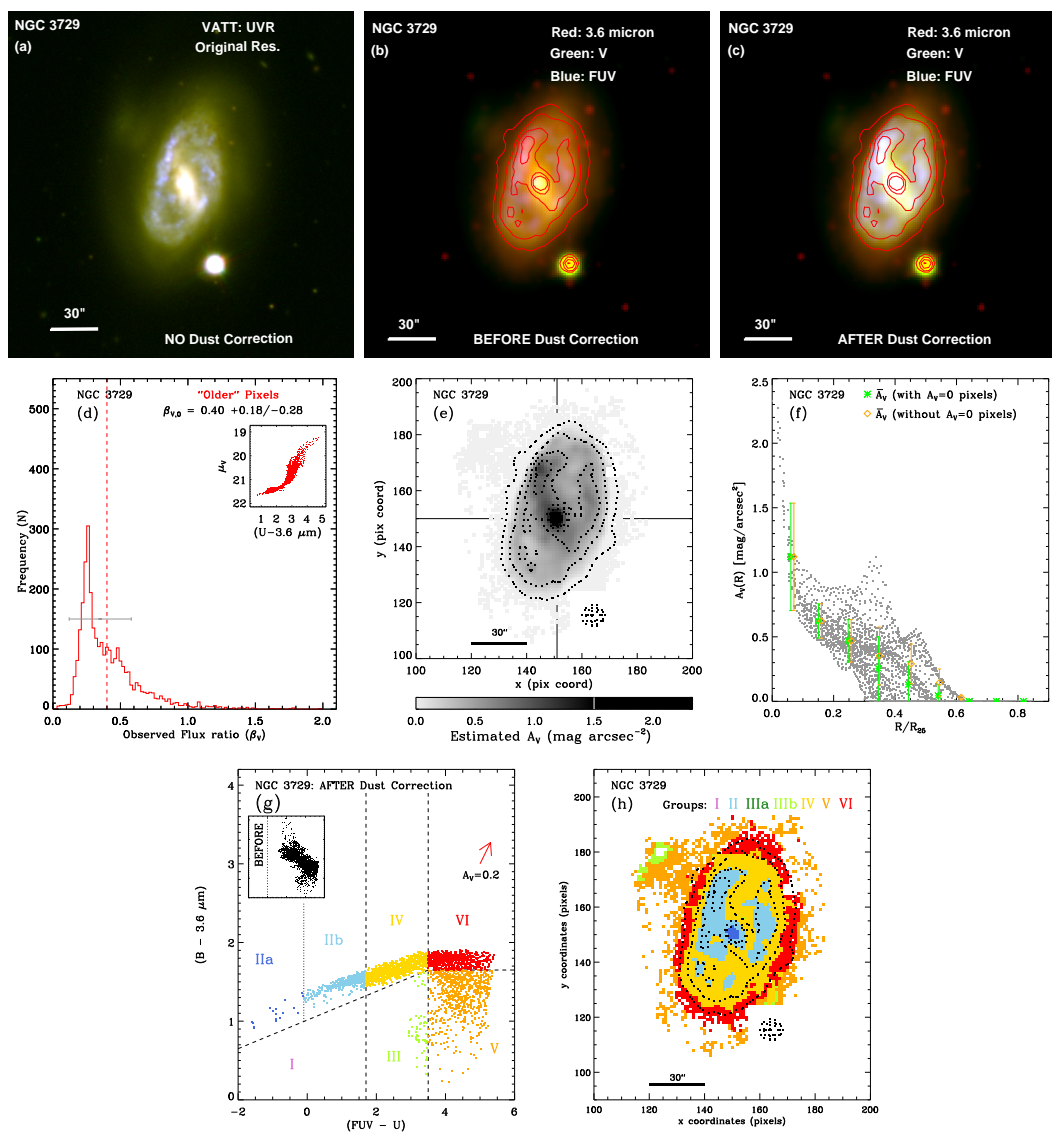


Figure 43. As Figure 25, for NGC 3729. Red contours trace the IRAC $8.0\mu\text{m}$ emission. (d) All pixels are treated as older pixels in this galaxy. (e) Dust extinction is mapped using the full range of gray-scales for $A_V \leq 1.5 \text{ mag arcsec}^{-2}$. (f) Even though this galaxy is not classified as a Seyfert galaxy, the radial dust extinction profile shows similar characteristics as seen in the other Seyfert galaxies at the galaxy centers. (g) Group II pixels are separated into IIa and IIb. While Group IIb pixels are located in the bar and ring of the galaxy, Group IIa pixels are located only in the nucleus of the galaxy.

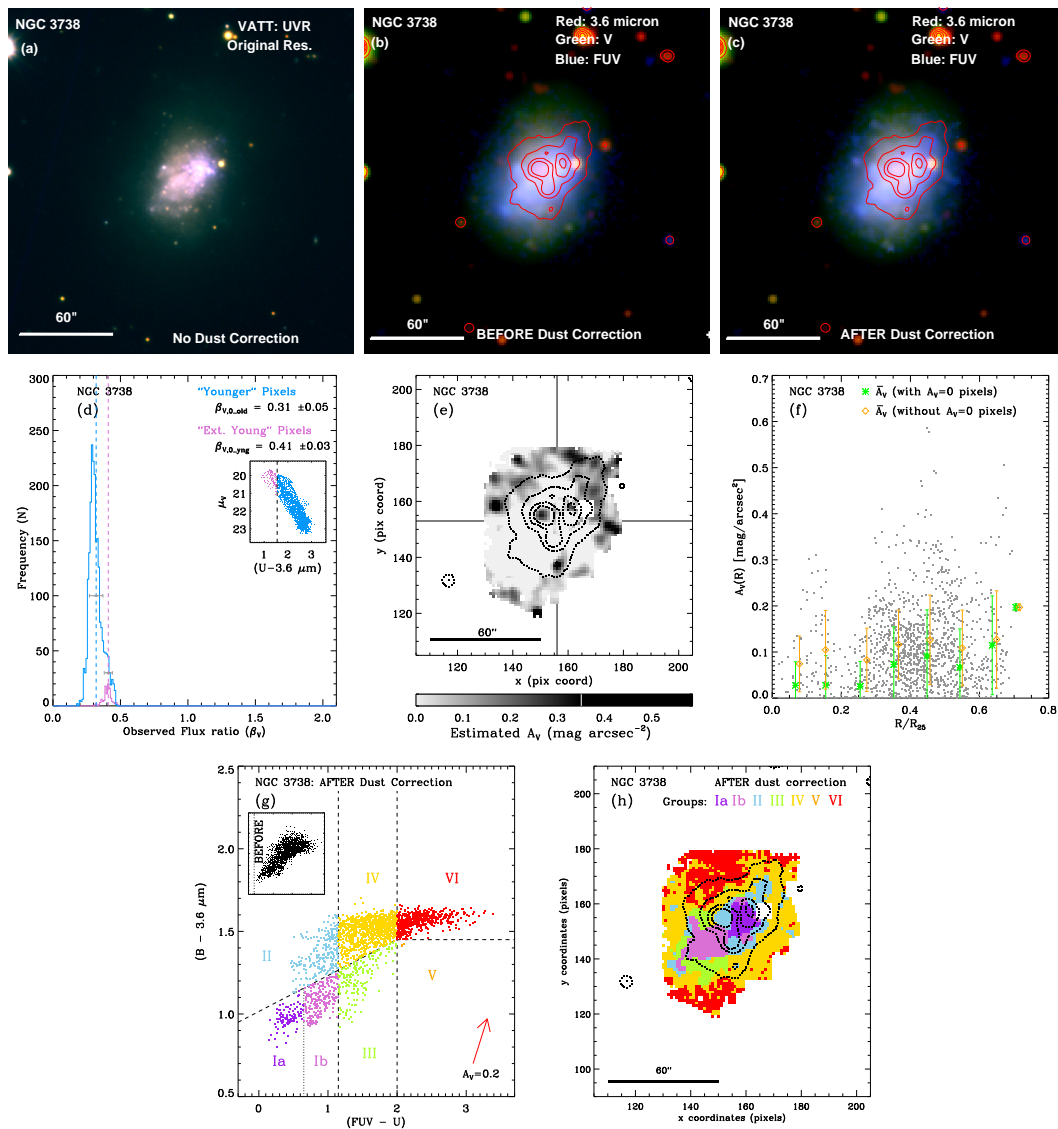


Figure 44. As Figure 25, for NGC 3738. Red contours trace the IRAC 8.0 μm emission. The foreground star to the NW of the galaxy center is removed from the analysis. (d) A group of pixels that extends out from the main body of the pixel distribution toward blue ($U - 3.6 \mu\text{m}$) color in the pCMD (inset) are treated as extremely young pixels. (e) Dust extinction is mapped using the full range of gray-scale for $A_V \leq 0.35 \text{ mag arcsec}^{-2}$. (g) Group I pixels are separated into Ia and Ib.

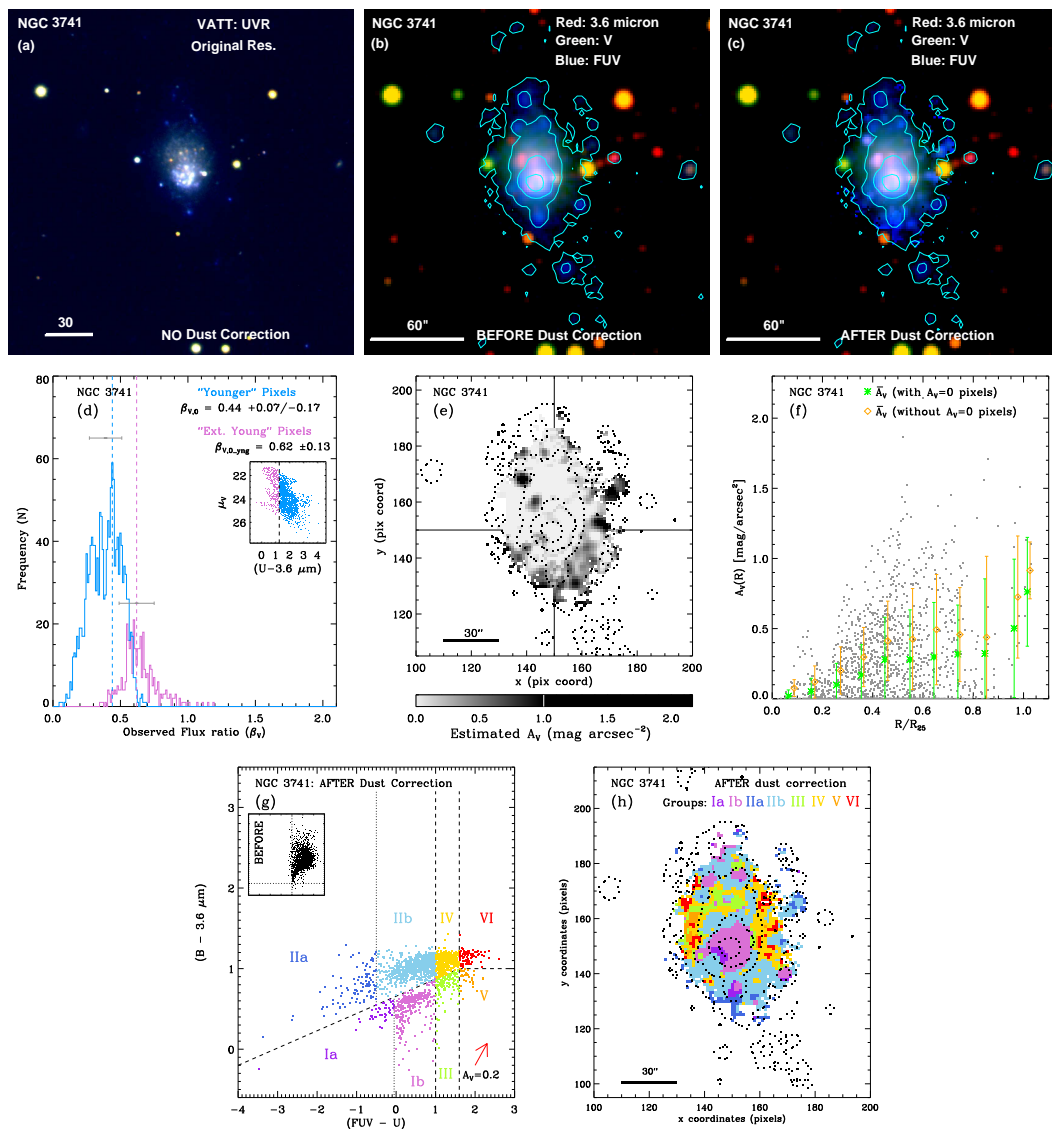


Figure 45. As Figure 25, for NGC 3741. Blue contours trace the *GALEX* FUV emission. (d) Pixels are separated into younger and extremely young groups for this galaxy. (e) Dust extinction is mapped using the full range of gray-scales for $A_V \leq 1.0 \text{ mag arcsec}^{-2}$. Group I and II pixels are separated into two subgroups, based on their distribution in panel (g). Yet two subgroups, Group Ia and Ib and Group IIa and IIb, are not significantly different in distribution as in some other galaxies.

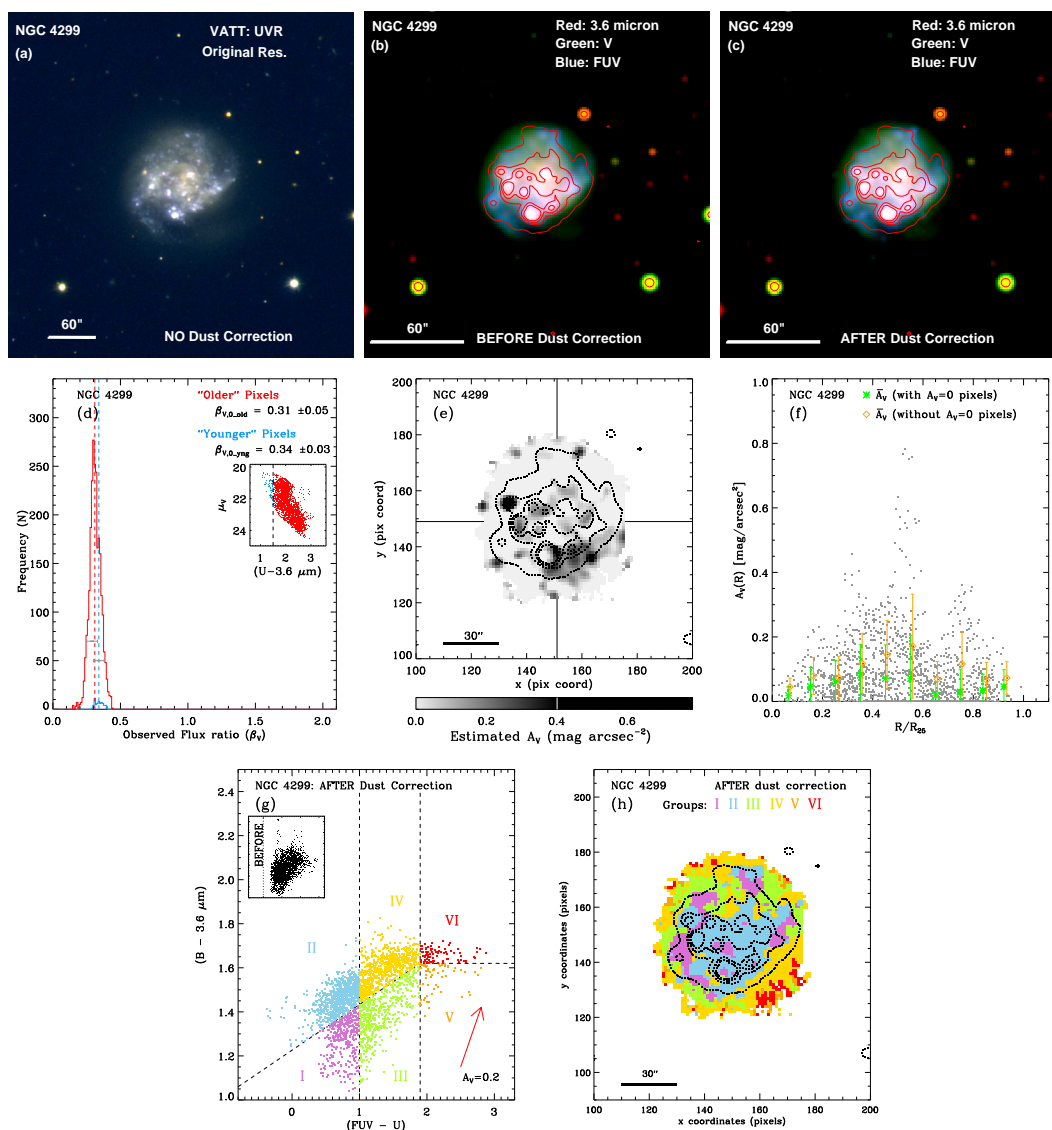


Figure 46. As Figure 25, for NGC 4299. Red contours trace the IRAC $8.0 \mu m$ emission. (e) Dust extinction is mapped using the full range of gray-scales for $A_V \leq 0.4 \text{ mag arcsec}^{-2}$. (h) The distribution of Group I and III pixels shows spiral structure in the galaxy disk.

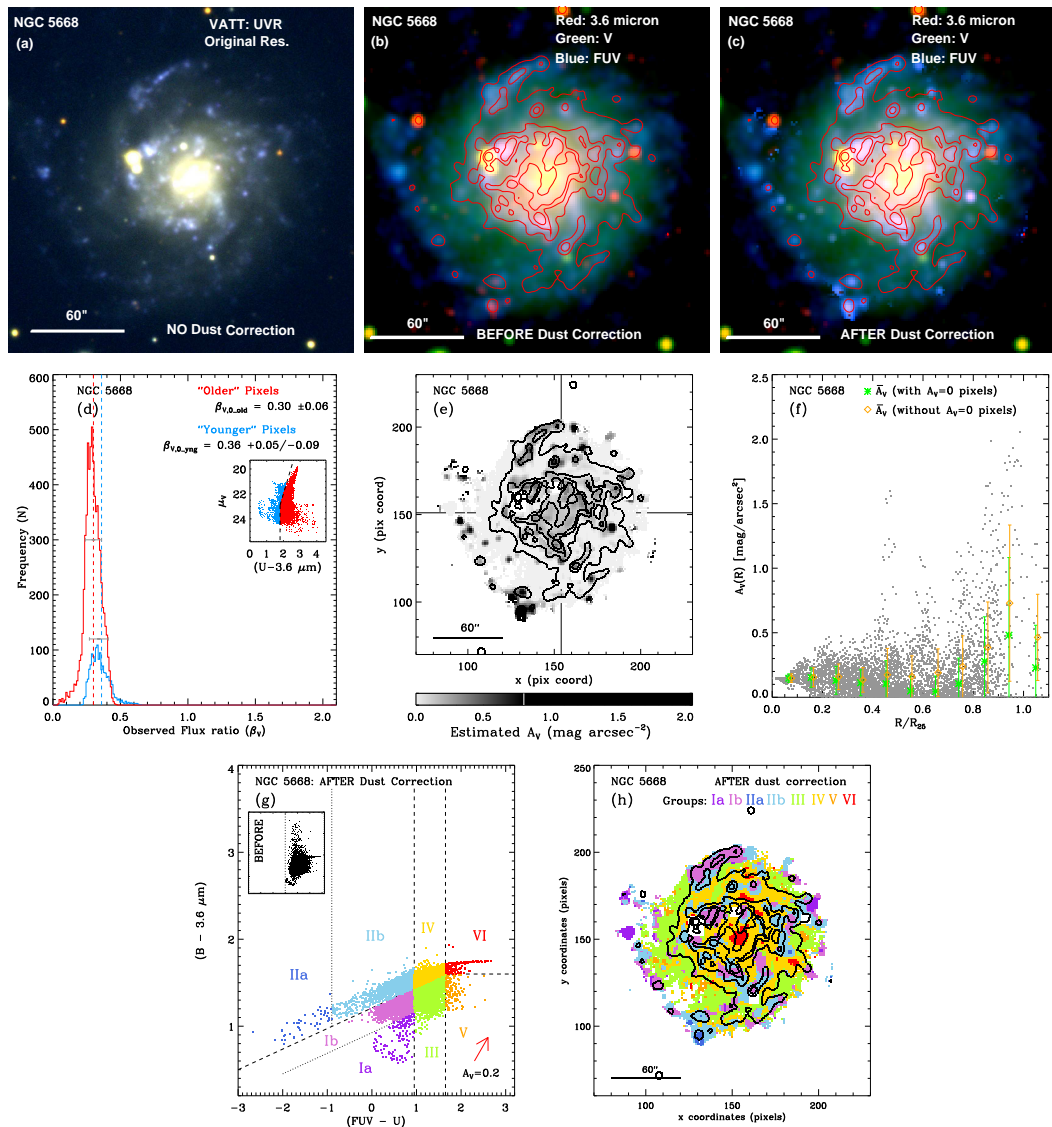


Figure 47. As Figure 25, for NGC 5668. Red contours trace the IRAC $8.0 \mu\text{m}$ emission. (e) Dust extinction is mapped using the full range of gray-scales for $A_V \leq 0.8 \text{ mag arcsec}^{-2}$. (g) Group I and II pixels are separated into two subgroups. (h) Distribution of the different pixel-groups clearly trace the spiral structure of the galaxy.

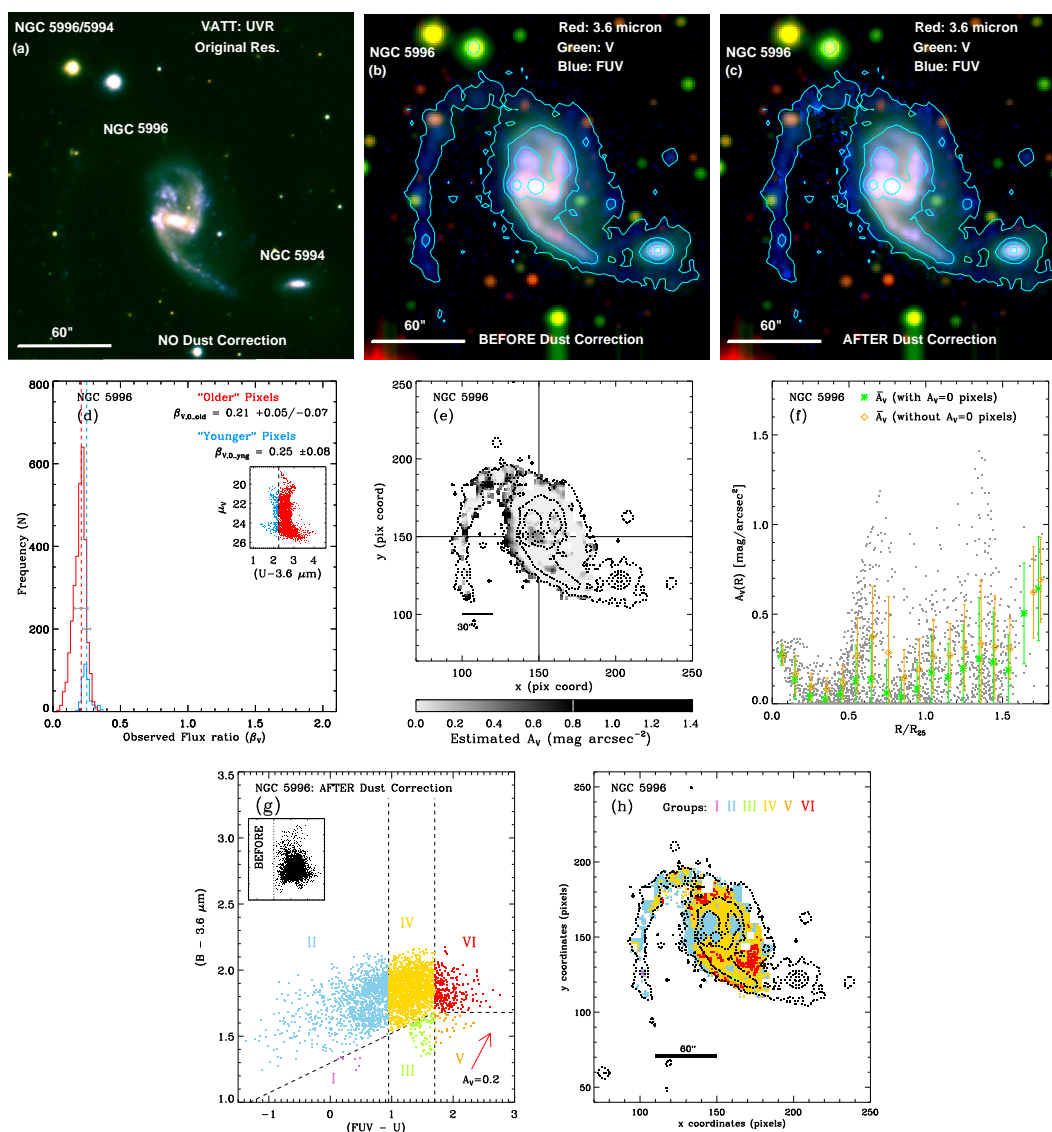


Figure 48. As Figure 25, for NGC 5996. Blue contours trace the *GALEX* FUV emission. Green and red objects in panels (b) and (c) are foreground objects. NGC 5996 and 5994 are a merging pair, but we only analyzed NGC 5996, since most of the pixel in NGC 5994 did not satisfy our minimum S/N ratio in some filters. For the same reason, a limited number of pixels are analyzed in the spiral arm on the east side of NGC 5996. (e) Dust extinction is mapped using the full range of gray-scales for $A_V \leq 0.8 \text{ mag arcsec}^{-2}$. (g) Due to the larger distance to the galaxy ($D \simeq 53 \text{ Mpc}$), light blending is significant, and as a result, Group I and II pixels form one single distribution in the pCCD.

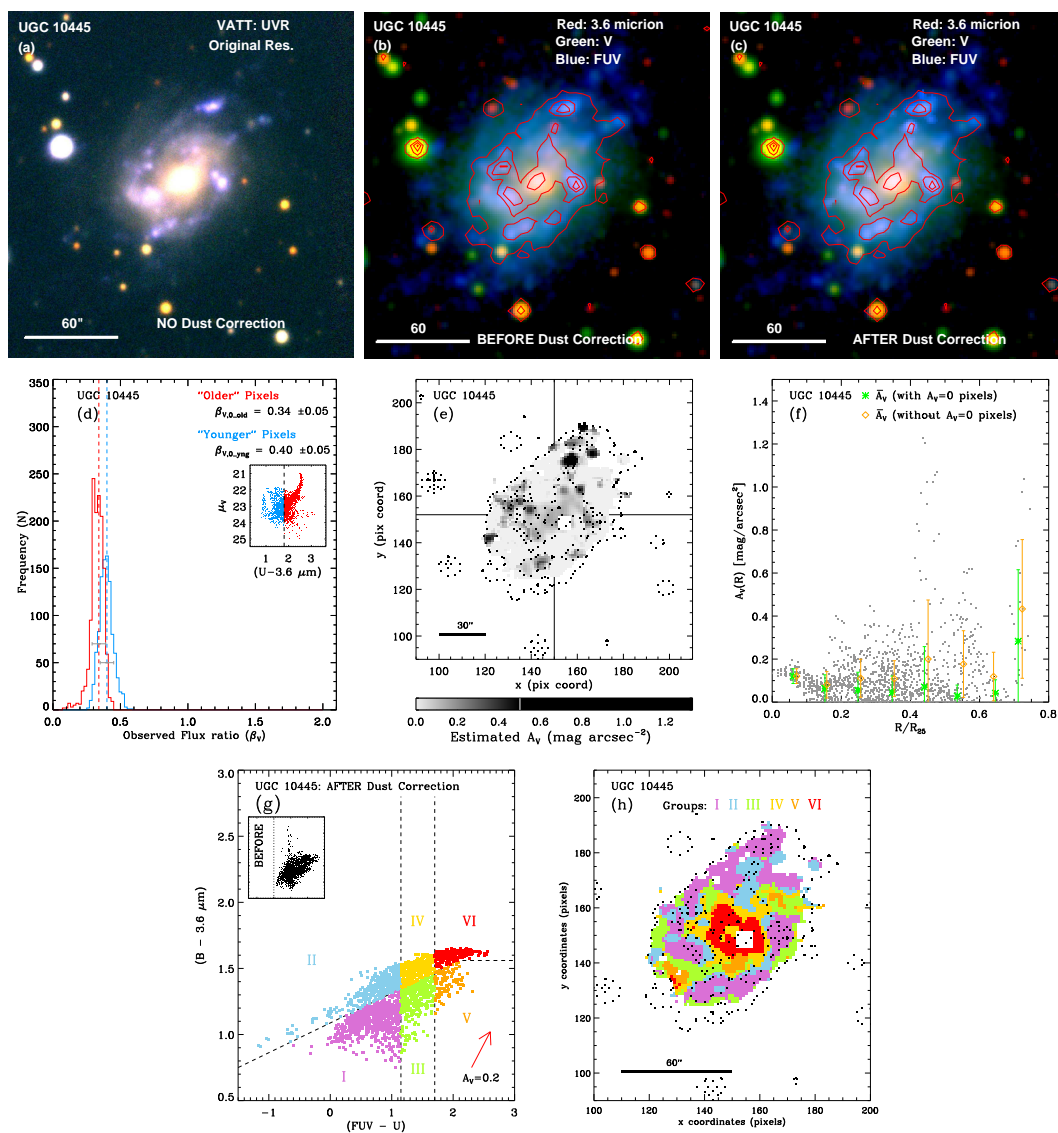


Figure 49. As Figure 25, for UGC 10445. Red contours trace the IRAC $8.0\ \mu\text{m}$ emission. Red and green objects are foreground stars. (e) Dust extinction is mapped using the full range of gray-scales for $A_V \leq 0.5\ \text{mag arcsec}^{-2}$. (h) Distribution of different pixel-groups clearly trace the spiral structure of the galaxy.

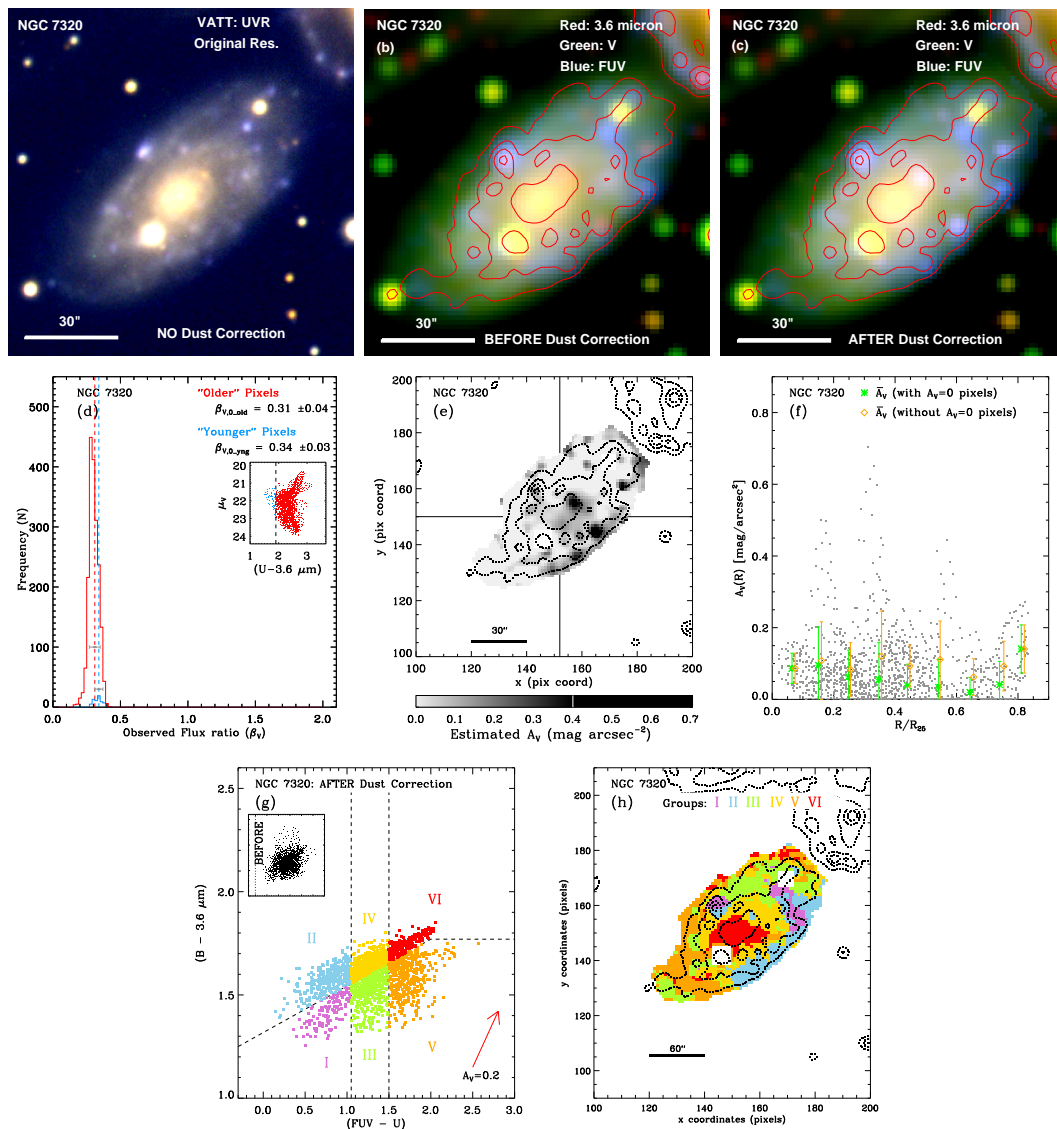


Figure 50. As Figure 25, for NGC 7320. Red contours trace the IRAC $8.0\ \mu\text{m}$ emission. A galaxy visible at the top right corner of panels (a)–(c) is one of Stephan’s Quintet galaxies, whose distance is much further than NGC 7320, and hence removed from our analysis of NGC 7320. (d) Some pixels—branching from the main distribution of the pixels—with bluer (FUV – U) color are treated as younger pixels. (e) Dust extinction is mapped using the full range of gray-scales for $A_V \leq 0.4\ \text{mag arcsec}^{-2}$.

4.2.3. Comments on Individual Galaxies

UGC 01104 (Figure 26): The red objects at the southern edge of the galaxy in panels (b) and (c) are background/foreground objects, as can be seen in panel (a). Panels (g) and (h) indicate that strong SF-activity is going on in the center of the galaxy, where OB-associations dominate the light. Panels (e) and (f) shows that there is no measurable dust extinction at the center of this galaxy, but that A_V increases quite steeply as the radius increases compared to most of the other galaxies.

NGC 1156 (Figure 27): Three bright foreground stars are visible in panels (a)–(c). The pixels covered by these foreground stars were removed from the analysis. Panels (g) and (h) show that strong SF-activity is going on both in the center and the NE part of the galaxy. Most of the dust is distributed in localized clumps, and is especially concentrated at the NE side of the galaxy. Panels (e) and (f) show that dust extinction is relatively low in the center, and gradually increases outward. The narrow and relatively high peaks in A_V seen in panel (f) correspond to dust clumps distributed throughout the galaxy. Panels (g) and (h) show that star-formation is indeed active in the galaxy center, and on the NE side of the galaxy, while the SW edge of the galaxy contains older and more quiescent stellar populations.

UGC 04459 (Figure 28): The brighter green and fainter red objects that appear all over panels (b) and (c) are foreground stars due to the relatively low galactic latitude ($b \simeq 35^\circ$) of this galaxy. The two brightest knots in the galaxy—one at the northern end and the other at the southern end—in panels (a)–(c) are also likely foreground stars. These objects are masked out, and their pixels are not used in the

analysis, as can be seen as empty (white) boxes in panel (h). Panels (g) and (h) show that this galaxy is actively star-forming throughout. Panel (e) shows that a moderate amount of extinction is pervasive, especially toward the northern half of the galaxy, but that most of the dust extinction is distributed in localized clumps, and generally found at larger radii within this galaxy.

UGC 04483 (Figure 29): As for UGC 04459, due to its relatively low galactic latitude ($b \simeq 34^\circ$), many foreground stars appear in panels (b) and (c), that are particularly evident in the IRAC $3.6 \mu\text{m}$ image. The orange colored blob—visible in panel (a), and also appears in panels (b) and (c) on the NW side of redder colored region—seems to be located outside of current actively star-forming regions, and the region appears dominated by older stellar populations. We therefore assume that this is a part of the galaxy. For the region of pixels that appears bright red at the southern side of the galaxy in panel (b), since there is no indication that it is associated with a distinct feature in the pixel distribution of the pCMD (inset of panel (d)) or pCCDs (panel (g)), we treat this region as a part of the galaxy. Panel (f) shows that the azimuthally averaged radial dust-extinction profile, $\overline{A_V}(R)$, is relatively flat, but our dust map (panel (e)) shows that the dust extinction in individual pixels, $A_{V,i}$, at the northern edge of the detected galaxy is much larger than elsewhere.

NGC 2623 (Figure 30): This galaxy is classified as a major merger (e.g., Toomre 1977; Taylor et al. 2005), and is listed as a Low-Ionization Nuclear Emission-Line Region (LINER), Luminous Infrared Galaxy (LIRG), and Seyfert galaxy in the NASA/IPAC Extragalactic Database (NED). Panels (e) and (f) show a much larger

A_V value in the galaxy center than in any other part of the galaxy, and panels (g) and (h) indicate that the galaxy has strong SF-activity at or very near its nucleus, which confirms that this galaxy contains an Active Galactic Nucleus (AGN). In the color-composite image after dust-extinction correction (panel (c)), the central region of the galaxy becomes much brighter, visually revealing the strong nuclear SF-activity. While the disk of the galaxy is mostly composed of Group VI pixels, its tidal tails and a knot at the southern end of the disk mostly consist of Group III pixels. Even though this galaxy is a major merger with a strong AGN, the lack of Group I pixels is most likely due to the galaxy's rather large distance ($D \simeq 80$ Mpc). Since the physical area covered by a single pixel at this distance is $\sim 600 \times 600$ pc², and the PDF FWHM corresponds to ~ 2.1 kpc, the light from any OB-associations is blended with that from older stellar populations.

NGC 2719/2719A (Figure 31): NGC 2719 and its physical companion NGC 2719A (with recessional velocity based distance estimates of $D_{\text{NGC2719}} = 46.4$ Mpc and $D_{\text{NGC2719A}} = 47.0$ Mpc) are classified as merging galaxies (e.g., Karachentsev 1972; Taylor et al. 2005). The color-composite images (panels (a)–(c)) do not show a clear physical connection (e.g., a bridge) between the galaxies, but panels (e) and (h) show a continuous extinction feature and a continuous distribution of Group II pixels between the two galaxies, indicating that some SF-activity may be present in the low-surface brightness area between them, perhaps in an unresolved tidal tail or distorted spiral arm. The extinction map (panel (e)) and radial A_V profiles (panels (f)) show that dust extinction is more concentrated in the outskirts of both galaxies.

UGC 04998 (Figure 32): The color-composites (panels (a)–(c)) show that this galaxy is relatively red in appearance compared to other galaxies, with a hint of some SF-activity in its northern and western part. There is a foreground star on the west side of the galaxy center. Panel (e) shows that its dust is mostly distributed toward the north to NE side of the galaxy. The stellar population analysis in panel (h) shows that there may be an arm-like or ring-like structure at the NW side of the galaxy disk. Therefore, this galaxy may actually be a spiral galaxy, rather than an irregular as currently classified.

UGC 05101 (Figure 33): This galaxy is the most distant galaxy in our sample at $D \simeq 164$ Mpc. While most part of the galaxy is too faint to meet our minimum S/N ratio criteria, the central area of the galaxy is bright, indicative of strong nuclear activity, as confirmed by panels (g) and (h). Panels (e) and (f) show that the galaxy center suffers far more dust extinction ($A_V \simeq 0.5\text{--}2.5$ mag arcsec $^{-2}$) than the remainder of the galaxy ($A_V \lesssim 0.5$ mag arcsec $^{-2}$), which are similar characteristics as seen in NGC 2623. This galaxy is classified as a LIRG (Scoville et al. 2000), as well as a combination of LINER and Seyfert galaxy (e.g., Zink et al. 2000; Farrah et al. 2003), consistent with the large A_V and strong SF-activity in its nucleus found here.

UGC 05189 (Figure 34): This is one of the most chaotic galaxies in our sample, with an arc-like or crescent shape, and with strong ongoing SF-activity in its NW and SE knots (see panel (h)). Panel (e) shows that while there is a thin layer of dust extinction throughout the galaxy, the A_V at SF regions—bright white regions in panel (a)—tend to have smaller extinction than some fainter region of the galaxy.

UGC 05340 (Figure 35): The red objects visible in panels (b) and (c) are likely foreground stars. There are also two green/yellow foreground stars in panels (b) and (c), one near the galaxy’s central SF region, and the other at the southern end of its tail-like structure. The pixels occupied by foreground stars that overlap with the galaxy are removed from our analysis. Combined with the low S/N ratio in galaxy’s southern tail, removal of pixels affected by foreground stars resulted in many blank spots, especially in its southern tail (see panel (h)). Since the galaxy appears blue in the color-composites (panels (a)–(c)), and is known as a young galaxy (e.g., Pustilnik et al. 2005), the pixels are separated into “younger” and “extreme young” pixels in panel (d). Panel (h) shows that the northern end of the galaxy is vigorously forming stars, but panel (e) shows there is almost no measurable dust extinction in this region. Panel (h) also shows that while the central region is the brightest, this region has a large fraction of underlying older stellar population.

NGC 3079 (Figure 36): This galaxy is a large edge-on galaxy with an morphological classification of SB(s)c in NED. Thick dust lanes are clearly visible in the color-composite from the original VATT *UVR* images at its native resolution (panel (a)). Before the extinction correction, pCMD (inset of panel (d)) and pCCD (inset of panel (g)) show that some groups of pixels are significantly affected by dust extinction. Panels (g) and (h) show that these pixels correspond to the nucleus of the galaxy, and its extinction map (panel (e)) and radial dust-extinction profile (panel (f)) confirm that the nucleus of the galaxy indeed has a significantly high A_V value ($A_{V,i}$ up to ~ 7 mag arcsec $^{-2}$!). As for NGC 2623 and UGC 05101, this galaxy is

also classified as LINER (Heckman 1980) and Seyfert galaxy (Sosa-Brito et al. 2001). Panel (g) shows that before extinction correction, there is no recognizable branching or grouping of pixels, other than the branch extending out toward red ($B - 3.6 \mu\text{m}$) colors. After applying our extinction correction, multiple groups and branches of the pixels becomes clearly discernible. Distribution of pixel-groups in panel (h) follows the *GALEX* FUV contours, and the visible features in panels (a) and (c). As in some of our previous galaxies, most of the Group I pixels with dominant OB-associations have relatively small dust extinction, while Group II pixels are associated with much larger dust extinction. These results (panels (e)–(h)) for NGC 3079, therefore, show that our dust extinction measurement method works, not only for a thin layer of dust, but also for a thick dust lanes and dust clumps. This also indicates that the small clumps of dust extinction seen in other galaxies in our sample are likely real features.

UGC 05423 (Figure 37): Panel (a) shows several bright blue knots in the inner part of the galaxy, indicating some strong SF-activity in this region. In panels (b) and (c), red and yellow objects are foreground stars and background objects. Among these foreground stars, the ones overlapping with the galaxy at the NW edge and at the southern end of the galaxy are excluded from the analysis. Panel (e) shows that most of its dust is located in the outskirts of the galaxy. It also shows that there is no measurable dust extinction in its central region, where panel (h) shows that most of the dominant OB-associations (bright blue knots in panel (a)) are located. Panel (f) confirms that the radial extinction profile increases as radius increases.

NGC 3239 (Figure 38): This galaxy appears blue in all three color-composites (panels (a)–(c)), indicating that the stellar populations in this galaxy are young and actively star-forming. In panels (b) and (c), some faint, green stellar light surrounds these SF regions of the galaxy. Panel (g) shows larger number of Group I and II pixels in both $(B - 3.6 \mu\text{m})$ and $(\text{FUV} - \text{U})$ colors than redder Group V and VI pixels. Panel (h) shows that the central region of the galaxy is indeed mostly filled with Group I and II pixels, and that the redder pixels are distributed in the outer regions of the galaxy. The narrow peaks of A_V in panel (f) are due to small clumps of high- A_V and the large apparent size (major diameter, $a = 5''.0$) of the galaxy.

NGC 3274 (Figure 39): Panels (b) and (c) show that the galaxy disk traced by the *GALEX* FUV contours extends out to much larger radii than the visible distribution of stellar light. This galaxy is indeed classified as a low surface brightness galaxy (e.g., Capozziello et al. 2007). Panel (e) shows that its dust extinction is distributed more toward the NE half of the galaxy, and as dust filaments rather than as small localized clumps. The radial A_V profiles in panel (f) show some ups and downs, but stays relatively flat out to $R \simeq 0.5 R_{25}$. Panel (h) shows that star-formation is going on, not at the center, but in the outskirts of its visible disk, as defined by our minimum S/N ratio requirement. The bulge of the galaxy is actually dominated by older stellar populations.

NGC 3353 (Figure 40): While panel (a) clearly shows a bluer knot on the northern side of the slightly redder, extended distribution of its stellar populations, these features are blended together in panels (b) and (c). Panel (e) shows that

relatively high values of A_V are distributed at the northern end of the galaxy, and lower A_V values over larger areas in the SW part of the galaxy. However, there appears to be no dust-lane between these two separate stellar populations seen in panel (a). Panel (f) shows that the radial extinction profiles have increasing trends, as expected from the A_V distribution in panel (e). Our stellar population analysis (panel (h)) shows that, even though the light is blended together, the northern and southern halves of the galaxy consists of different stellar populations.

NGC 3445 (Figure 41): This galaxy and the smaller companion galaxy at its SE side (UGC 06021) are at the initial stage of merging. Panels (a)–(c) show that the eastern half of the galaxy is somewhat bluer (due to its SF-activity), than the western half. In panel (f), $A_{V,i}$ at $R \lesssim 1.2 R_{25}$ belongs to NGC 3445, and the ones at $R \gtrsim 1.2 R_{25}$ belongs to the companion galaxy UGC 06021. The extinction distribution in panel (e) shows that dust extinction is highly concentrated on the NE side of the galaxy. Panel (f) shows that the average radial extinction profile increases, while the error bars are also progressively become larger, due to the asymmetric distribution of dust in NGC 3445. This is a good example of how important a two-dimensional pixel-based dust-extinction measurement is. The extinction-corrected pCCD (panel (g)) and pixel-coordinate map (panel (h)) show that the younger stellar populations with OB-associations are distributed more toward the eastern half of the galaxy, where dust extinction is more prevalent. While Group I pixels at its outer radii coincide with distribution of high- A_V , the pixels at the inner radii contain much less dust extinction.

UGC 06541 (Figure 42): Visually, this galaxy looks very similar to NGC 3353. However, its distribution of dust extinction (panels (e) and (f)) and our stellar population analysis (panels (g) and (h)) indicate that the two galaxies are completely different. Panels (e) and (f) show that, even though A_V is low in the bright blue knot at the galaxy center, extinction increases just outside of this knot and decreases toward the outer radii. Panels (g) and (h) show that the bright blue knot at the center actually contains some light from its underlying older stellar population (since there are no Group I pixels). The stellar population at its outer radii, where the surface brightness is low, mostly consists of relatively old stars (Group V and VI pixels).

NGC 3729 (Figure 43): This is a particularly dusty galaxy. Panel (e) shows that this galaxy has very smooth distribution of dust from its center outward, which can also be seen in the radial dust extinction profile in panel (f). Along the bar and its ring structure, where the PAH $8.0\mu\text{m}$ contours are strong, the amount of extinction increases as well. Panels (b) and (c)—which were created with the *same* color stretch—show that the effect of dust extinction is significant. By correcting for dust extinction, we are able to reveal that NGC 3729 has a blue (strong FUV) nucleus, indicating vigorous SF-activity. Even though this galaxy is currently *not* classified as a galaxy with an AGN (e.g., Ryan et al. 2007), its radial A_V profile (panel (f)), pCCD (panel (g)), and the distribution of its Group Ia pixels on the pixel-coordinate map (panel (h)) indicate that this galaxy may well contain an AGN.

NGC 3738 (Figure 44): Panels (a)–(c) show that while the galaxy itself extends out to much larger radii than its $8.0\mu\text{m}$ contours, most of its star-formation

(appearing as purple and blue light in each panel) is concentrated in the central region of the galaxy. The foreground stars on the western and northern side of the galaxy have been masked out. Panel (e) shows that a high concentration of dust extinction is located as clumps more toward its outer radii, as an arc from the east to west through the northern end of the galaxy. The distributions of Group Ia, Ib, II, and III pixels are clearly separated in different branches in panel (g), and they map onto distinct regions, following different stellar populations that is visible in panel (a). Group Ia pixels are concentrated in the center of galaxy, where bright blue-white stellar population is visible in panel (a). Group Ib pixels follow the purple-colored, higher density of stellar populations, which is located on the SE side of the galaxy center in panel (a). Group II pixels are located around the Group Ia pixels (galaxy center), and mostly distributed toward the NW side of the galaxy, where it appears dark in panel (a), but clearly has some blue (FUV) light in panel (c) after applying our extinction correction. Group III pixels surround the Group Ib pixels on the SE side of the galaxy, where a purple colored, faint stellar population is visible in panel (a). Panel (h) shows that the outermost radii—on the northern and southern edge of the galaxy—are dominated by quiescent old-and-dead stellar populations.

NGC 3741 (Figure 45): Panel (a) shows a large association of bright star clusters at the galaxy center. This region is filled with Group Ia and Ib pixels in panel (h). Panel (e) shows that dust extinction is mostly distributed along the southern rim of the galaxy, from its east to west side. While somewhat continuous, dust extinction is mostly grouped as small clumps in different SF regions. As in some other actively

star-forming galaxies, most of Group Ib pixels have much smaller dust extinction than Group II pixels. The averaged radial dust-extinction profiles (panel (f)) show a continuous increase in the A_V values with increasing error bars, which indicate the 1σ distribution of $A_{V,i}$. Again, this galaxy is a good example of why a pixel-based two-dimensional extinction correction is important. It is interesting to see that to the north of the galaxy center, there is a group of pixels that is dominated by intermediate and old age stellar populations (Group III and IV pixels), somewhat resembling a spiral arm-like distribution pattern in panel (h).

NGC 4299 (Figure 46): There seems to be some spiral structure in the color-composite of panel (a). Yet, the distribution of dust extinction in panel (e) does *not* follow the spiral structure at all, but instead follows the $8.0\ \mu\text{m}$ PAH emission contours. Dust extinction is especially concentrated on the south side of the galaxy, which appears visually darker in panel (a). When the extinction-corrected stellar populations are analyzed, panel (h) clearly shows spiral structure, with pixels that are dominated by OB-associations (Group I pixels), as well as Group III pixels.

NGC 5668 (Figure 47): This galaxy has a very bright bulge, and faint but clear spiral arms, as can be seen in panels (a)–(c). Panel (e) shows that low dust extinction values ($A_V \simeq 0.15\ \text{mag arcsec}^{-2}$) are distributed smoothly at the galaxy center, and small clumps of high A_V values are located in spiral arms. While there are large areas with low or no measurable dust-extinction in the inter-arm region of the disk of the galaxy, the radial A_V extinction profiles in panel (f) show a rather flat dust-extinction profile throughout the galaxy. While there are only a few features that

can be recognized in our pCCD before the extinction correction was applied, multiple groups of pixels are apparent, and are classified after the extinction correction. These pixel-groups are then plotted on the pixel-coordinate map (panel (h)), which shows that each pixel-group clearly follows its inner and outer spiral structure (by Group I and II), as well as the inter-arm regions of the galaxy disk (by Group III and IV). The center of the galaxy is dominated by older stellar populations (Group VI pixels), indicating that not much SF-activity is going on in this region.

NGC 5996 (Figure 48): This galaxy and its companion, NGC 5994 (on the SW side of NGC 5996), is a merging pair. It is hard to see in panel (a), but there is a faint and long spiral arm at eastern side of NGC 5996, which is traced by the *GALEX* FUV contours in panels (b) and (c). Panel (e) shows that most of its dust extinction is distributed on the eastern rim of the detected galaxy disk and in the faint spiral arm on the eastern side of the galaxy, where panel (h) indicates that star-formation is going on. Even though not clearly visible in panels (a)–(c), the pixel-based radial extinction profile, $A_{V,i}$, clearly indicates that large A_V values at the radii corresponding to these regions. However, the amplitude of radial dust extinction profile reduces significantly, when azimuthally averaged. An interesting aspect to note is that pixels with high A_V values are located on the far side from the merging NGC 5994, which is the opposite situation from the extinction distribution in the merging pair of NGC 3445 and UGC 06021. Small amounts of dust extinction can also be located along the bar and the bulge of the galaxy.

UGC 10445 (Figure 49): This galaxy is a nice face-on spiral (SBc) with a bar that runs from SE to NW across the galaxy. Panel (e) shows that a thin layer of dust extinction is distributed along the bar, and several clumps of extinction can be located at its outer radii. However, there is no clear indication that dust extinction is distributed along its spiral structures. Panel (f) shows that the averaged radial extinction is very low throughout the galaxy, while some clumps have $A_V \geq 1.0 \text{ mag arcsec}^{-2}$. Panels (g) and (h) clearly show that stellar population analysis after applying our dust-extinction correction is able to reveal the spiral structure of the galaxy. Our stellar population analysis also reveals that there is not much SF-activity going on at the center of the galaxy.

NGC 7320 (Figure 50): This galaxy is one of the five belonging to Stephan's Quintet. Yet, this particular galaxy is not a merging pair, but a single foreground galaxy located much closer ($cz \simeq 800 \text{ km s}^{-1}$) than the other four galaxies ($cz \simeq 5700\text{--}6700 \text{ km s}^{-1}$; Moles et al. 1997). Panel (e) shows that its dust extinction is distributed as a thin layer around the center, and extends mostly toward the SW rim of the detected galaxy disk. Some clumps of extinction are also distributed in the outskirts of the galaxy where some SF-activity is visible in the color-composites in panels (a) and (c). The azimuthally averaged radial profile of dust extinction is relatively flat, with a decreasing slope for the most radii, while high- A_V clumps are clearly visible as narrow spikes of individual pixel measurements at several distinct radii. Panel (h) shows that most of its star-formation is taking place at the SW edge of detected galaxy disk, as well as in a bright blue knot seen on the NE side of the galaxy disk

(see panel (a)). The bulge, and most of its inter-arm regions, are dominated by older stellar populations, as shown in panel (h).

4.3. Discussion of the Pixel-based Dust Extinction Measurement

In this chapter, we measured and mapped the two-dimensional distribution of dust extinction in 27 galaxies with different morphological types (spirals, irregulars, and mergers) and distances (~ 1.3 Mpc to ~ 164 Mpc). These extinction maps (all panels (e) in Figures 25–50) clearly show that dust is *not* distributed uniformly or symmetrically in these galaxies. In fact, the dust is more commonly distributed as clumps, and distributed more on one side of galaxy than on the other side for many galaxies. Some examples of the asymmetric distribution of the resulting extinction, A_V , can be seen in NGC 1156, UGC 04998, NGC 3445, NGC 3741, NGC 4299, and NGC 7320. If this asymmetric extinction distribution is due to a combination of a gradient in the sky background and inappropriate sky subtraction—especially in the IRAC $3.6\ \mu\text{m}$ images—the result would be a gradual increase of A_V from one side to the other side of the galaxy. Since the one-sided A_V distribution is mostly due to a larger number of clumps with high extinction values, an error in the sky subtraction or presence of an uncorrected gradient is unlikely to be the cause of the asymmetric extinction distribution. Higher resolution color composites constructed from VATT UBV images (panels (a) in Figures 25–50) also indicate that these regions with high inferred extinction, even when found at large distances from the center of a galaxy, are indeed affected by dust extinction and not an artifact.

Comparing to the earlier study of dust extinction distribution, the radial extinction profile that resembles the results of Boissier et al. (2004) best is that for NGC 3729 (Figure 43(e)), which has a high central A_V value and $\overline{A_V}$ values that decrease as the radius increases. Yet at any given radius, the range of the pixel-based extinction values, $A_{V,i}$, is more than $\sim 0.5 \text{ mag arcsec}^{-2}$. Studying the pixel-based radial dust-extinction profiles (all panels (f) of Figures 25–50), one important result is the radial distribution of $A_{V,i}$, which indicates different structures at different radii in a galaxy. A good example can be seen in NGC 3729 (Figure 43(f)), where one such feature can be identified at radii between $0.25 R_{25} \lesssim R \lesssim 0.4 R_{25}$. At this range of radii, pixels with higher extinction values—appearing as a triangular shape for $A_V \gtrsim 0.5 \text{ mag arcsec}^{-2}$ in Figure 43(f)—correspond to the section of ring at the NE side of the galaxy (see Figure 43(e)). Similar features can be seen in other galaxies, such as NGC 0959 (Figure 25(f)), NGC 1156 (Figure 27(f)), NGC 3079 (Figure 36(f)), NGC 3239 (Figure 38(f)), and NGC 5668 (Figure 47(f)). When the azimuthally averaged extinction is calculated for other galaxies, however, regardless of whether pixels with $A_V = 0 \text{ mag arcsec}^{-2}$ are included, these small-scale features are washed away, resulting in a radial extinction profile ($\overline{A_V}(R)$) that is smooth from the center out to the detection edge of the galaxy. As discussed in Chapter 3, for NGC 0959, while $\overline{A_V}(R)$ usually does not reach $0 \text{ mag arcsec}^{-2}$ (see Figure 18 and panels (f) of Figures 25–50), the 27 galaxies studied here have on average 40–60% of the analyzed pixels best fit with $A_{V,i} = 0.0 \text{ mag arcsec}^{-2}$. An azimuthally averaged one-dimensional (radial) extinction profile will therefore *undercorrect* the dust extinction in many re-

gions within a galaxy, while *overcorrecting* the emission from regions that suffered little or no extinction.

In Figures 26–50, all panels (g) show the comparison of the pixel-distribution in the same pCCD of the $(B - 3.6 \mu\text{m})$ versus $(\text{FUV} - U)$ color *before* (inset) and *after* (main panel) the extinction correction was applied to each galaxy. Due to many different factors (e.g., different distances, stellar contents, and the effects of light blending), the distribution of pixels in this pCCD shifts slightly from galaxy to galaxy. Even though the $(B - 3.6 \mu\text{m})$ and $(\text{FUV} - U)$ color-ranges are different for some galaxies, all galaxies show distinct groupings of pixels in their color-color distribution after applying our extinction correction. For each galaxy, pixels in this pCCD are separated into different pixel-groups with somewhat arbitrary criteria, but based on distinct separations in the apparent color-color distribution of pixels. Some galaxies, e.g., NGC 2623 (Figure 30), UGC 05101 (Figure 33), NGC 3079 (Figure 36), and NGC 3274 (Figure 39), even have pixel-groups that are separated into sub-groups, based on an apparent further separation in their distribution in color-color space.

Plotting these pixel-groups onto a pixel-coordinate map for each galaxy (all panels (h) in Figures 26–50) reveals that *all* of these pixel-groups follow the galactic structures, such as spiral arms and bulge of the galaxies. Other than NGC 0959, galaxies that clearly show these structures are, NGC 2623 (Figure 30(h)), UGC 04998 (Figure 32(h)), NGC 3079 (Figure 36(h)), NGC 3274 (Figure 39(h)), NGC 5668 (Figure 47(h)), and UGC 10445 (Figure 49(h)). The pixel-map of NGC 2623 indicates that this galaxy has an active nucleus, while the surrounding disk consists mostly of old

stellar populations. The two extended spiral arms or tidal tails show some mixture of relatively recent star-formation and of intermediate-age and older stellar populations. UGC 04998 shows that, while most of the galaxy is relatively old, there is some possible recent SF-activity in the western to northern region of the galaxy, where some Group II (blue), III (green), and IV (yellow) pixels are located. NGC 3079 is especially interesting, since the pCCD after extinction correction clearly shows multiple groupings of pixels, none of which were recognizable in the pCCD before the extinction correction (except the highly extinguished Group IIa pixels). NGC 3274, NGC 5688, and UGC 10445 show that—while their bulges mostly consist of Group VI pixels (older stellar populations)—their spiral arms along the outskirts of the galaxy disks consists mostly of Group I and II pixels, indicating strong SF-activity in their spiral arms.

These results reveal the intrinsic galactic structures in panel (h), that are hidden behind the complicated distribution of dust extinction. Especially, the appearance of different branching and groupings of pixels that are dominated by different stellar populations in panel (g) after the application of our extinction correction proves that our method is working correctly to first order. This is only possible, if the dust extinction in each pixel is corrected for appropriately. Therefore, we conclude that—even though our method of estimating dust extinction is simply based on the flux ratio of the V -to- $3.6\ \mu\text{m}$ images—our method is robust, and applicable to a wide range of spiral and irregular galaxies located relatively nearby to well beyond the Local Group and Virgo Cluster.

4.4. Dust Distribution Pattern and Galaxy Parameters

We will now compare the radial distribution pattern of dust extinction (all panels (f) in Figures 25–50) as a function of different parameters of the galaxies. For easy comparison of the following figures, the plotting range of radius (R/R_{25}) and dust extinction ($A_V(R)$) are fixed to $0.0 \leq R/R_{25} \leq 2.1$ and $0 \leq A_V(R) \leq 1.8 \text{ mag arcsec}^{-2}$, respectively, for all galaxies.

4.4.1. *The Dust Distribution in Spiral Galaxies*

In this section, we plot the radial dust-extinction profile as a function of the morphological type of galaxies. In Figure 51, 12 spiral galaxies are arranged from earlier (Sa/b) to later (Sm) morphological type. The classification of NGC 0959, originally Sdm in the RC3, was changed to SBcd following the discovery of a stellar bar in Chapter 3. Two galaxies, UGC 04998 and UGC 05101, without RC3 classifications, but possibly spiral galaxies, are added at the end of this figure.

Comparing these galaxies, we find an interesting trend going from early (Sa/b) to late (Sm) type morphology. In the inner parts ($R \lesssim 0.3 R_{25}$) of a galaxy, the slope of the azimuthally averaged radial dust extinction profile ($\overline{A_V}(R)$, represented by green asterisks) decreases from earlier toward later morphological type. This is especially clear when the Sc, (NGC 3079, NGC 5996, UGC 10445, and NGC 0959), Sd (NGC 7320, NGC 5668, and NGC 3274), and Sm (NGC 4299 and NGC 3445) types are compared. The $\overline{A_V}(R)$ slopes at inner radii are: (1) negative for Sc (and earlier) galaxies; (2) relatively flat for Sd galaxies; and (3) positive for Sm galaxies. The sample size for the earlier (Sa–Sc) is very small, with only one Sa/b and three Sc’s.

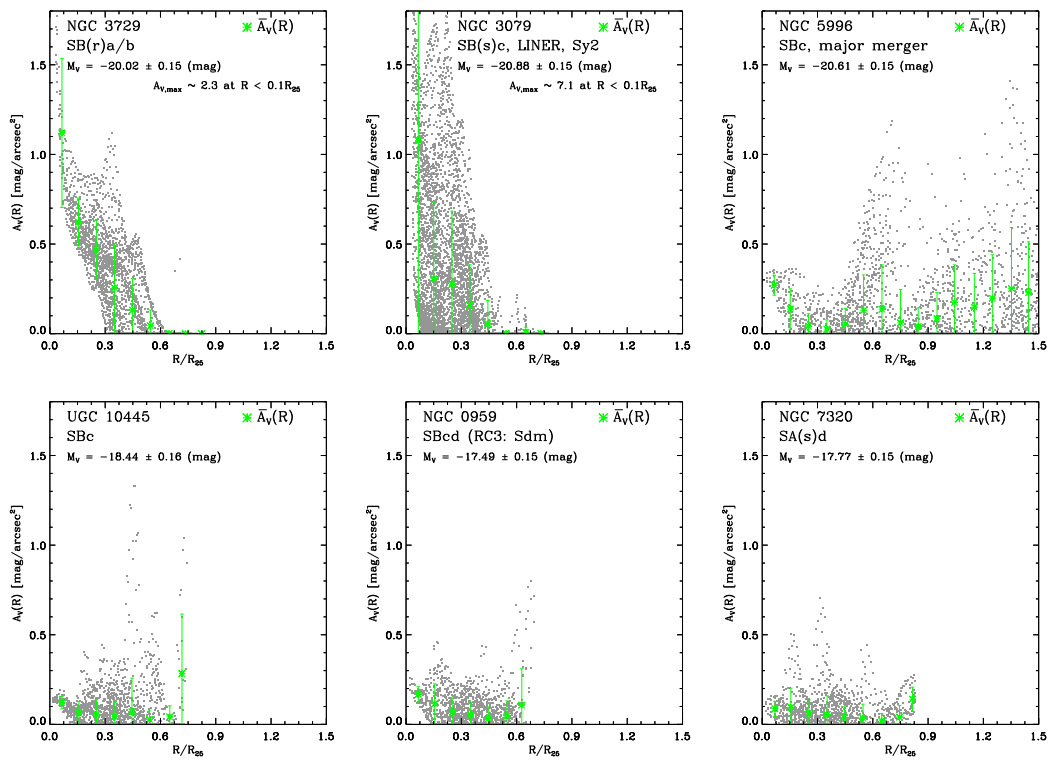


Figure 51. Radial A_V profile for spiral galaxies, as a function of morphological type.

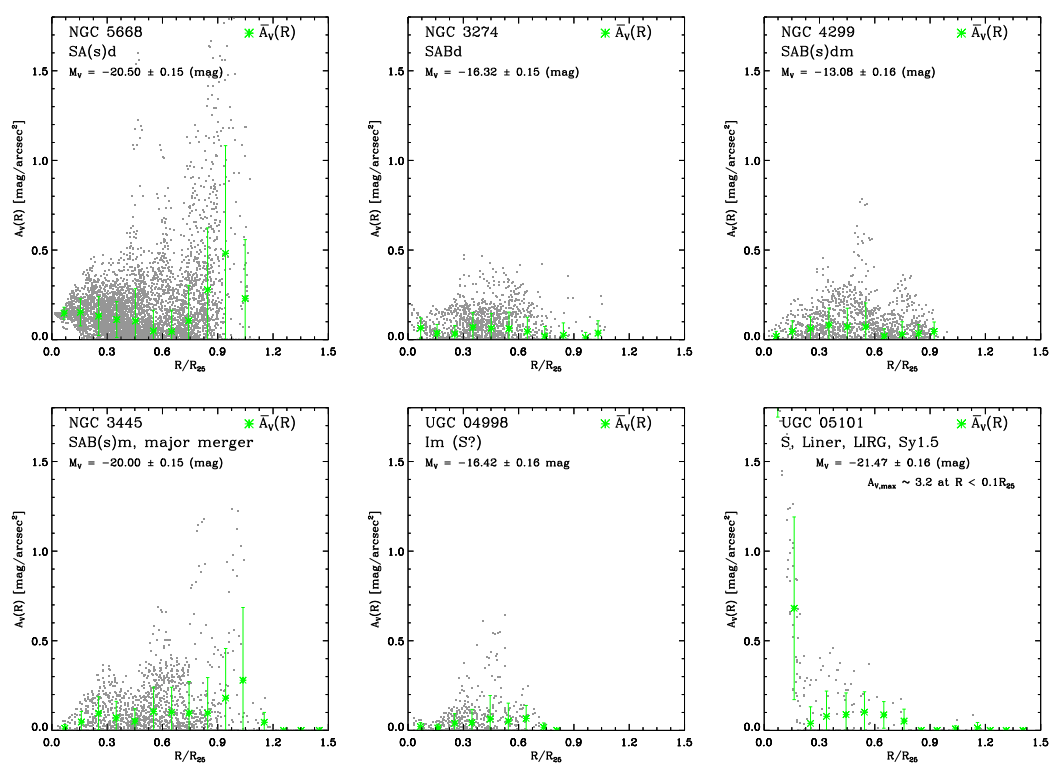


Figure 51. Continued.

Yet, observing the similar trend in multiple late-type spirals (Sc–Sm) indicates that this decreasing $\overline{A_V}(R)$ slope, and the trend of $\overline{A_V}(R)$ slope to turn up for Sm galaxies, is most likely a true feature of the dust distribution in spiral galaxies and their assembly history.

UGC 04998, classified as irregular (Im), but shows a spiral arm like structure in Figure 32(h), shows a slightly increasing radial extinction profile at its inner radius. Also, the measurements of dust extinction for each individual pixel, $A_{V,i}$, in this galaxy show a similar radial distribution as NGC 4299 and NGC 3445, which are two Sm type galaxies. Therefore, the morphological classification for this galaxy may be more like an Sm rather than an Im.

The unique characteristic of radial dust extinction profiles for the galaxies NGC 3729, NGC 3079, and UGC 05101 is the strong central peak in dust extinction. Among these three galaxies, NGC 3079 and UGC 05101 are known Seyfert galaxies (type-1.5 and 2, respectively; e.g., Zink et al. 2000; Sosa-Brito et al. 2001). A Seyfert galaxy has a supermassive black hole at its center. This black hole is surrounded by a torus of thick dust, where vigorous star-formation is believed to be going on. Depending on the viewing angle of this AGN, it is classified either as type-1 (observed from top, with strong broad-band emission lines) or type-2 (observed from side, without broad-band emission), or some fraction as type-1.5 depending on how much of each characteristics is visible. The successful detection of high- A_V values at the center for both NGC 3079 and UGC 05101 suggests that NGC 3279 may also be a galaxy with an AGN.

While the assumption for our method is that the observed light is coming from “normal” stellar populations, the SEDs from AGN are characterized by a significant contribution from non-thermal (synchrotron) emission. Therefore, the dust extinction measured for the regions dominated by the light from AGN may be underestimated or overestimated. To examine the measured values of dust extinction for AGN, we first derive the theoretical V -to- $3.6\ \mu\text{m}$ flux ratio for AGN. Figure 52 shows the broken power law model for AGN SEDs in blue lines, based on the mean quasar spectrum of Vanden Berk et al. (2001), which represents the mean of over 2200 quasars—including Seyfert type 1 and 2 AGN—identified in the Sloan Digital Sky Survey (SDSS; York et al. 2000). Shortward of $\sim 5000\ \text{\AA}$, the power-law slope is $\alpha_{\text{UV}} = -1.54$, while at $5000 \lesssim \lambda \lesssim 9000\ \text{\AA}$, that slope becomes $\alpha_{\text{VIS}} = -0.42$. The purple and red SEDs are the youngest (4 Myr), most metal poor ($Z = 0.0004$), and the oldest (13.5 Gyr), most metal rich ($Z = 0.04$) SSPs from Figure 1 (from the SED library of Anders & Fritze-von Alvensleben (2003)). The theoretical intrinsic V -to- $3.6\ \mu\text{m}$ flux ratio for a typical AGN is calculated to be $\beta_{\text{AGN},0} = 0.051$, which is significantly smaller than the $\beta_{V,0}$ for SSP models (Figure 2). This means that our method is most likely *overestimating* the amount of dust extinction at the center of the galaxy if an AGN is present. The actual intrinsic flux ratio—and hence the extinction value in the central resolution element—remains uncertain, depending on the relative contributions of non-thermal and stellar light, but will likely be between the adopted $\beta_{V,0}$ and theoretical $\beta_{\text{AGN},0}$.

For UGC 05101, the empirically selected flux ratio for older pixels, which are distributed in the central region of the galaxy, is $\beta_{V,0} = 0.09$. If the light at the

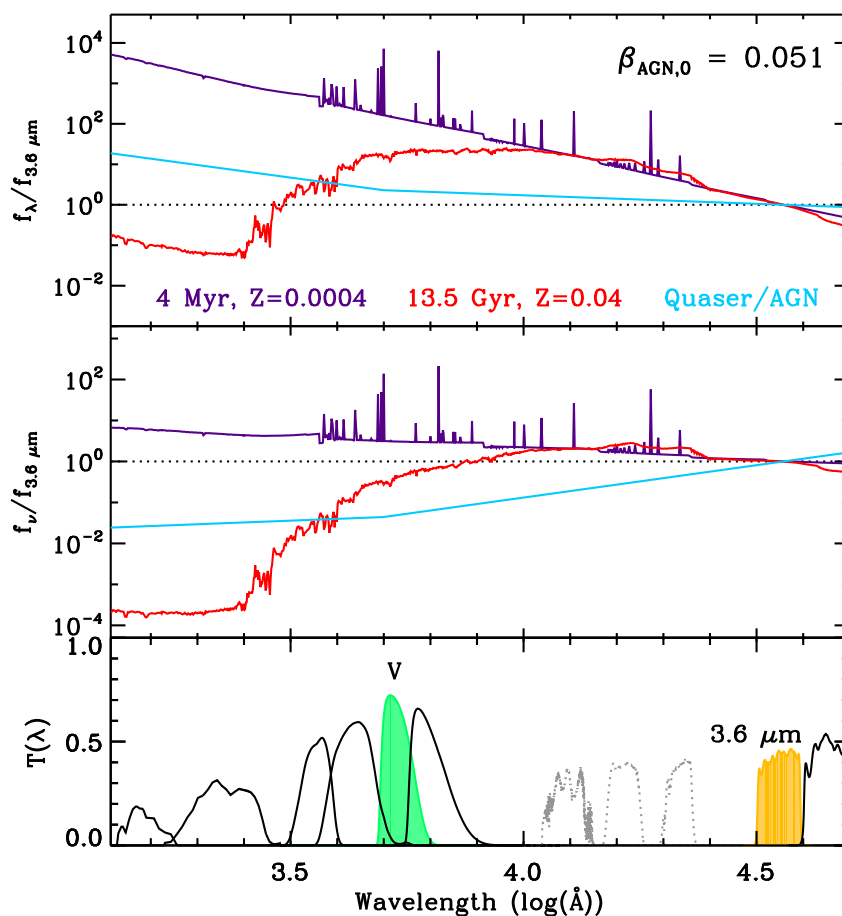


Figure 52. Comparison of SSP and AGN SEDs. Top and middle panels show the $f_\lambda/f_{3.6\mu\text{m}}$ and $f_\nu/f_{3.6\mu\text{m}}$ as a function of wavelength. Purple and red lines in both panels are SEDs of a SSP at 4 Myr with a metallicity $Z=0.0004$ and a SSP at 13.5 Gyr with $Z=0.04$, respectively, from Anders & Fritze-von Alvensleben (2003). The blue line is a broken power law model spectrum based on the mean quasar spectrum of Vanden Berk et al. (2001). The SED slope longward of $\sim 9000\text{ \AA}$ is assumed to remain the same as that for $5000 \lesssim \lambda \lesssim 9000\text{ \AA}$. The bottom panel shows the throughput curves of *GALEX* FUV and NUV, VATT *UBVR*, 2MASS *JHK_s* (in gray dotted curves), and *Spitzer*/IRAC 3.6 and 4.5 μm passbands. The inferred intrinsic *V*-to-3.6 μm flux ratios for AGN, $\beta_{\text{AGN},0}$, is indicated in the top panel.

center of the galaxy is purely from an AGN, the A_V for the pixels in this region is overestimated by $\Delta A_V = 0.62 \text{ mag arcsec}^{-2}$. Similarly, the amounts of visual extinction overestimated for NGC 3079 ($\beta_{V,0} = 0.19$) and NGC 3729 ($\beta_{V,0} = 0.40$) are $\Delta A_v = 1.24 \text{ mag arcsec}^{-2}$ and $2.24 \text{ mag arcsec}^{-2}$, respectively. However, these are the worst-case values, were *all* of the light observed in these pixels emitted by the AGN. In reality, the AGN is embedded in the central stellar core, where large amount of normal stellar populations are also found. Moreover, light blending due to a finite PSF will typically result in significant mixture of light from surrounding stellar populations, reducing the fraction of non-thermal light due to the AGN in even the central pixels. Since we do not know the relative contributions of the AGN and the surrounding stellar populations, we cannot accurately infer the actual amount of visual extinction for AGN. Therefore, when studying the central regions of galaxies hosting an AGN, we have to be careful not to overinterpret the results in terms of the properties of their stellar populations. Even though the A_V is overestimated when an AGN is present, the fact that all the galaxies in our sample that host an AGN show a distinct central peak in their radial dust extinction profile can still be a valuable tool to detect (hidden) AGN in galaxies.

4.4.2. *The Dust Distribution in Irregular Galaxies*

Let us now take a look at our 16 irregular galaxies. In Figure 53, such galaxies of similar morphology are plotted together. Unlike spiral galaxies, there is no particular systematic trend in slope of the azimuthally averaged radial A_V profiles: some galaxies show a $\overline{A_V}(R)$ profile with a positive slope, while others have flat or negative,

or even mixed $\overline{A_V}(R)$ profiles. Yet, some interesting characteristics are visible in the radial distribution of our pixel-based dust extinction measurements.

First, we find multiple narrow A_V peaks in NGC 3239 and NGC 1156 that are spiking up over the full range of radii studied. These spikes correspond to individual clumps of dust located in these galaxies. Similar, but wider peaks in A_V can be seen in the $\overline{A_V}(R)$ profiles of other galaxies. NGC 1156 and NGC 3239 happen to be relatively nearby ($D \simeq 9.8$ and 6.5 Mpc) and large on the sky (major diameter, $a \simeq 5''0$ and $3''3$, respectively). Therefore, the appearance of narrow peaks may be a result of the fine spatial sampling.

Second, we find a strong rise in A_V toward larger radii in NGC 2719A and UGC 01104, both classified as irregular (Im) galaxies, and a somewhat similar feature in UGC 05340 (Im/BCD), NGC 3741 (ImIII/BCD), and NGC 3353 (BCD/Irr). All of these galaxies show strong current and recent SF-activity at their centers (see panels (h) in Figures 35, 45, and 40). Therefore, dust at the center of these galaxies is most likely blown away or destroyed by, e.g., stellar winds (e.g., Murray et al. 2005) and/or starburst heating (e.g., Mihos & Hernquist 1994, 1996).

Finally, the peculiar galaxy NGC 2623, classified as a major merger (e.g., Toomre 1977; Taylor et al. 2005), shows a strong extinction peak in its galaxy center. Like NGC 3079 and UGC 05101, this galaxy is indeed known to exhibit AGN activity (LINER, LIRG, and Seyfert type 2). As in the case for the other Seyfert galaxies in the previous section, the measured A_V can be overestimated as much as $\Delta A_V = 1.43$ mag arcsec⁻². Yet assuming the distance to this galaxy ($D \simeq 80$ Mpc),

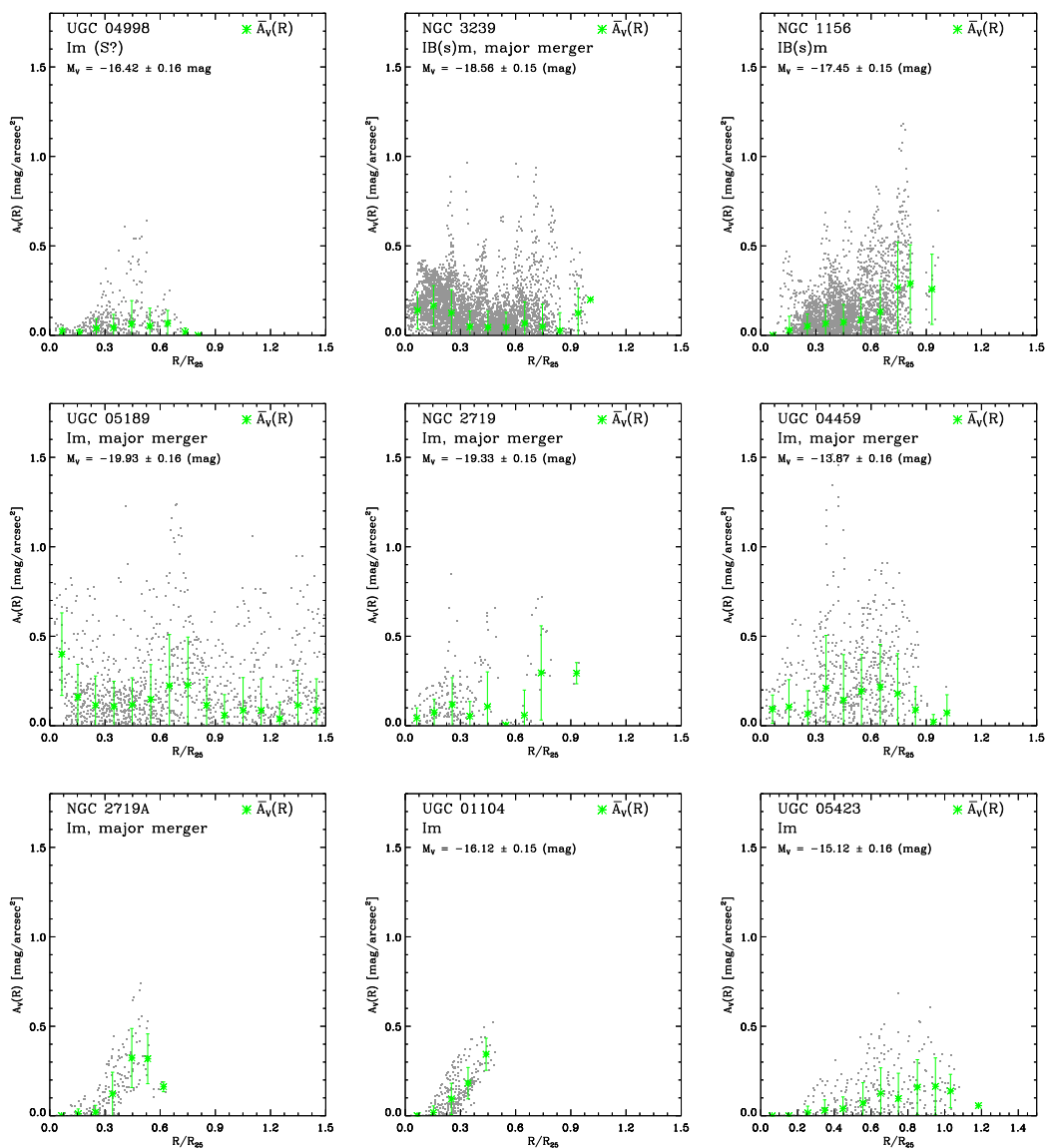


Figure 53. Radial A_V profile for irregular galaxies, as a function of morphological typ.

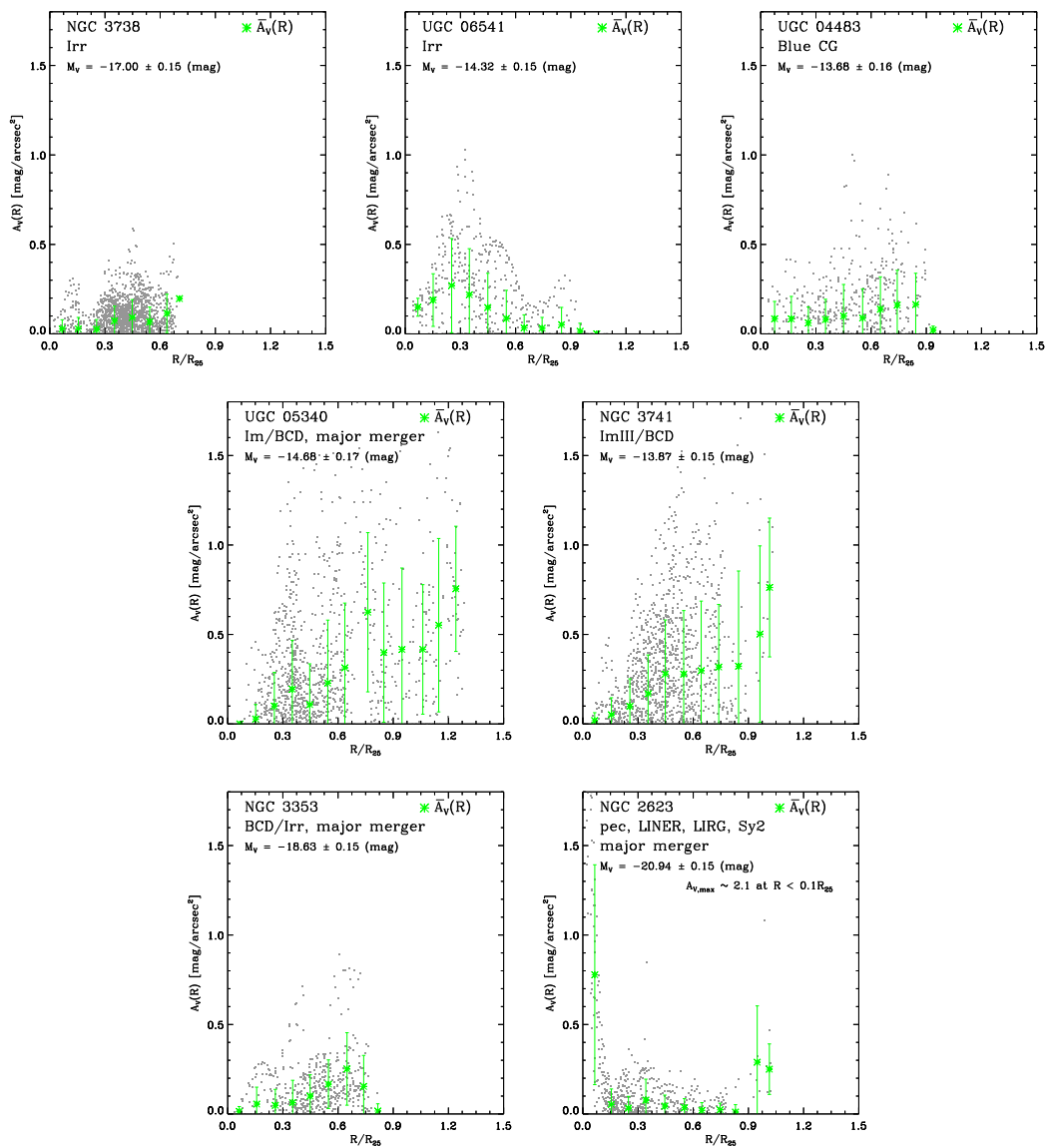


Figure 53. Continued.

the light blending from underlying and surrounding stellar populations are significantly large, and therefore the measured extinctions should not be as different from the actual extinction.

4.4.3. *The Dust Distribution as a Function of Absolute Magnitude: All Galaxies*

Next, we rearrange the order of the radial dust extinction profile plots as a function of the absolute magnitude, M_V , of the galaxies. The apparent magnitude, adopted distance modulus, and absolute magnitude of each galaxy are summarized in Table 6. Figure 54 shows again all 27 galaxies, but now arranged from the most luminous (UGC 05101, $M_V = -21.47$ mag) to the least luminous (NGC 4299, $M_V = -13.08$ mag), with the companion galaxy NGC 2719A plotted at last.

When all galaxies are ordered by their absolute magnitude, galaxies with AGN come to the top of the list, as expected. The first three galaxies, UGC 05101, NGC 2623, and NGC 3079 are all known Seyfert galaxies. NGC 3729 is not at the top of the list, but about one magnitude dimmer than these other three Seyfert galaxies. Therefore, the AGN of NGC 3729 may be slightly weaker than in the three galaxies officially noted as Seyfert galaxies.

Table 6
Apparent and Absolute Magnitudes

ID	Galaxy	m_V^a (mag)	Dist. Mod. ^b (mag)	M_V (mag)
1	UGC 01104	13.97 ± 0.03	30.09 ± 0.15	-16.12 ± 0.15
2	NGC 0959	12.48 ± 0.02	29.97 ± 0.15	-17.49 ± 0.15
3	NGC 1156	11.63 ± 0.02	29.08 ± 0.15	-17.45 ± 0.15
4	UGC 04459	13.13 ± 0.05	27.00 ± 0.15	-13.87 ± 0.16
5	UGC 04483	14.87 ± 0.04	28.55 ± 0.15	-13.68 ± 0.16
6	NGC 2623	13.56 ± 0.02	35.50 ± 0.15	-20.94 ± 0.15
7	NGC 2719	14.00 ± 0.02	33.33 ± 0.15	-19.33 ± 0.15
8	NGC 2719A	...	33.36 ± 0.15	...
9	UGC 04998	14.16 ± 0.04	30.58 ± 0.16	-16.42 ± 0.16
10	UGC 05101	14.61 ± 0.03	36.08 ± 0.15	-21.47 ± 0.16
11	UGC 05189	13.52 ± 0.05	33.45 ± 0.15	-19.93 ± 0.16
12	UGC 05340	14.50 ± 0.07	29.18 ± 0.15	-14.68 ± 0.17
13	NGC 3079	10.70 ± 0.02	31.58 ± 0.15	-20.88 ± 0.15
14	UGC 05423	14.54 ± 0.04	29.66 ± 0.15	-15.12 ± 0.16
15	NGC 3239	11.40 ± 0.02	29.96 ± 0.15	-18.56 ± 0.15
16	NGC 3274	12.84 ± 0.01	29.16 ± 0.15	-16.32 ± 0.15
17	NGC 3353	12.70 ± 0.01	31.33 ± 0.15	-18.63 ± 0.15
18	NGC 3445	12.67 ± 0.01	32.67 ± 0.15	-20.00 ± 0.15
19	UGC 06541	13.99 ± 0.03	28.31 ± 0.15	-14.32 ± 0.15
20	NGC 3729	11.57 ± 0.01	31.59 ± 0.15	-20.02 ± 0.15
21	NGC 3738	11.45 ± 0.02	28.45 ± 0.15	-17.00 ± 0.15
22	NGC 3741	14.02 ± 0.03	27.89 ± 0.15	-13.87 ± 0.15
23	NGC 4299	12.47 ± 0.01	25.55 ± 0.16	-13.08 ± 0.16
24	NGC 5668	11.71 ± 0.01	32.21 ± 0.15	-20.50 ± 0.15
25	NGC 5996	$13.03^c \pm 0.05$	33.64 ± 0.15	-20.61 ± 0.15
26	UGC 10445	13.07 ± 0.04	31.51 ± 0.15	-18.44 ± 0.16
27	NGC 7320	12.96 ± 0.02	30.73 ± 0.15	-17.77 ± 0.15

Notes.

^a Measured by Taylor et al. (2005) unless specified otherwise

^b Adopted values listed in NED. Parameters used for distance calculation are: $H_0 = 70.5$, $\Omega = 0.27$, and $\Lambda = 0.73$ from Wilkinson Microwave Anisotropy Probe (WMAP) 5-year results (Komatsu et al. 2009).

^c Measured by Huchra (1977).

However, the radial extinction profiles of the other galaxies in Figure 54 does not show any systematic change as a function of their absolute magnitude. When the galaxies with $M_V \lesssim -19.0$ mag are compared (on the first page of Figure 54), NGC 5996 ($M_V = -20.61$ mag) and UGC 05189 ($M_V = -19.93$ mag) have a decreasing $\overline{A_V}(R)$ profile at their inner radii ($R < 0.3 R_{25}$). NGC 5668 ($M_V = -20.50$ mag) has a flat $\overline{A_V}(R)$ profile, and NGC 3445 and NGC 2719 have an increasing $\overline{A_V}(R)$ profile at $R < 0.3 R_{25}$. The same is true for the galaxies in the middle range of the sampled absolute visual magnitudes (on the second page of Figure 54, or $-19.0 \lesssim M_V \lesssim -16.0$ mag). The slopes of the averaged radial A_V profiles varies without any systematic pattern. For the faintest group of galaxies (on the third page of Figure 54, or $-16.0 \lesssim M_V$), some increasing $\overline{A_V}(R)$ trend can be seen at inner radii, but the $\overline{A_V}(R)$ slopes and profile beyond $0.3 R_{25}$ varies significantly.

4.4.4. *The Dust Distribution as a Function of Absolute Magnitude: Spirals*

Since spiral and irregular galaxies are fundamentally different in their structure (i.e., existence of bars and/or spiral arms, and surface brightness distribution), it may be better to arrange them separately when the averaged radial dust extinction profile ($\overline{A_V}(R)$) and pixel-based extinction measurements ($A_{V,i}$) are studied, as a function of their absolute magnitude. Figure 55 shows only spiral galaxies (with UGC 04998 included) arranged from the brightest to the faintest M_V value.

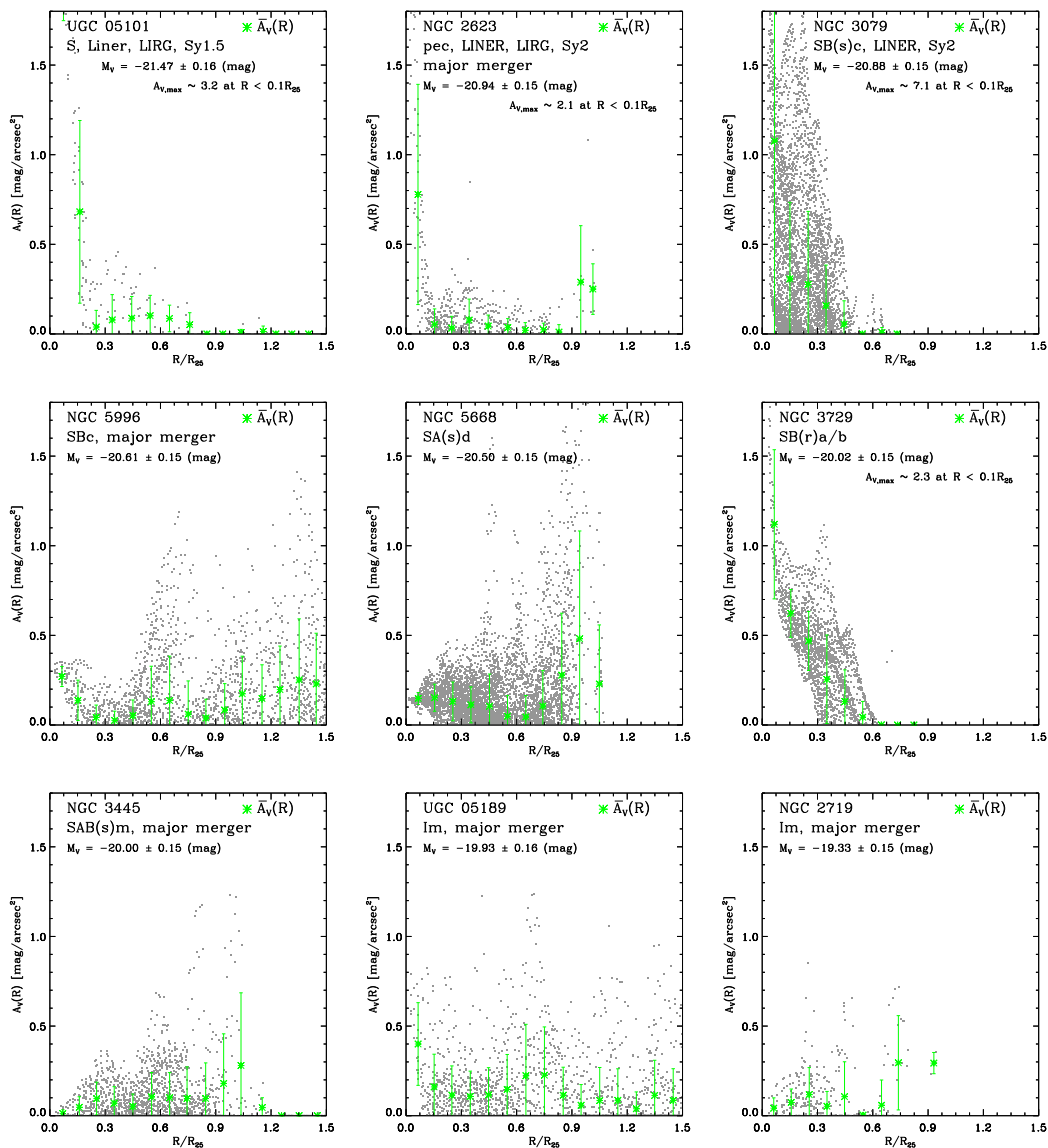


Figure 54. Radial A_V profile of all galaxies as a function of their absolute visual magnitude, M_V . Both spirals and irregulars are plotted together in this figure.

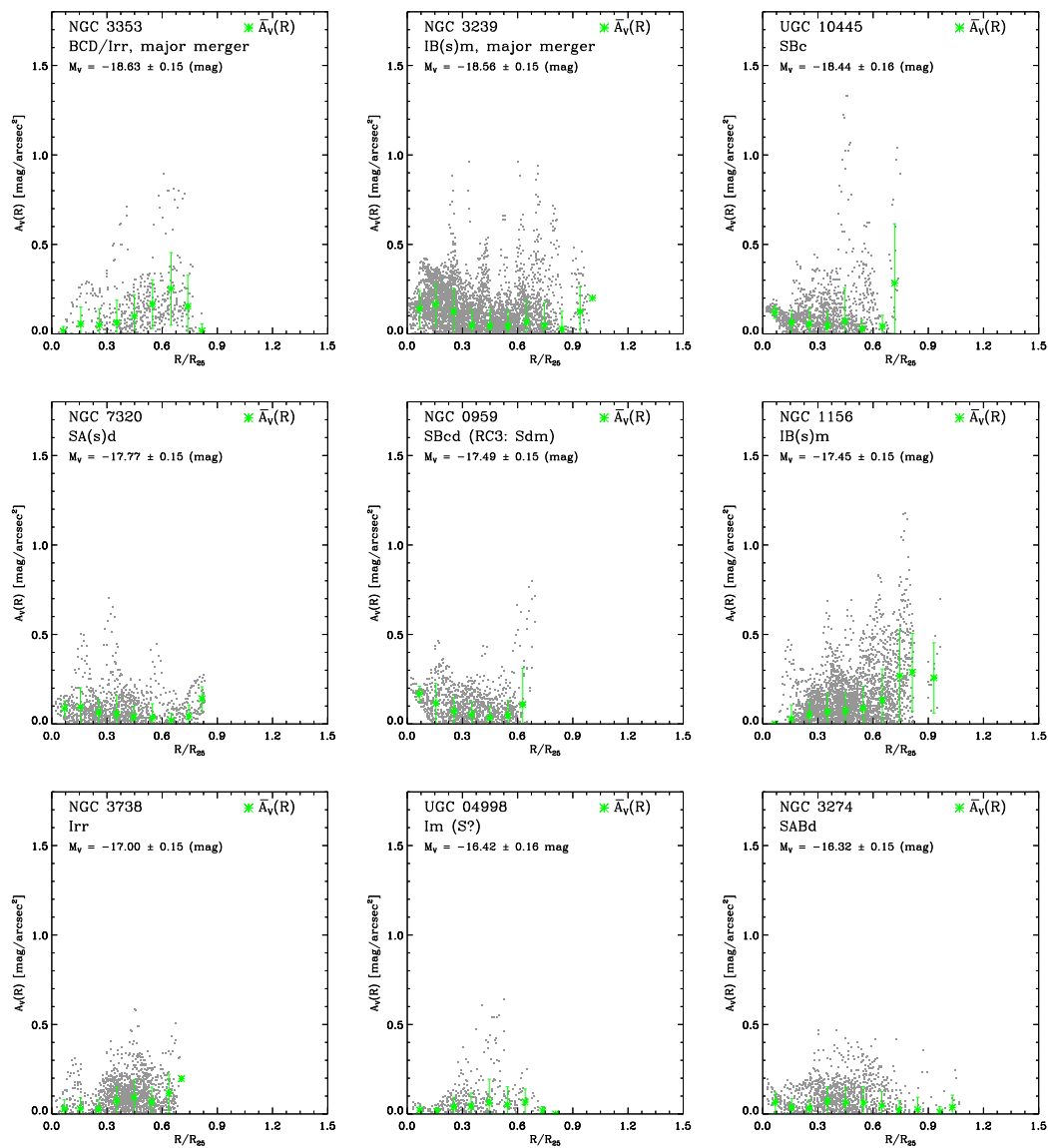


Figure 54. Continued.

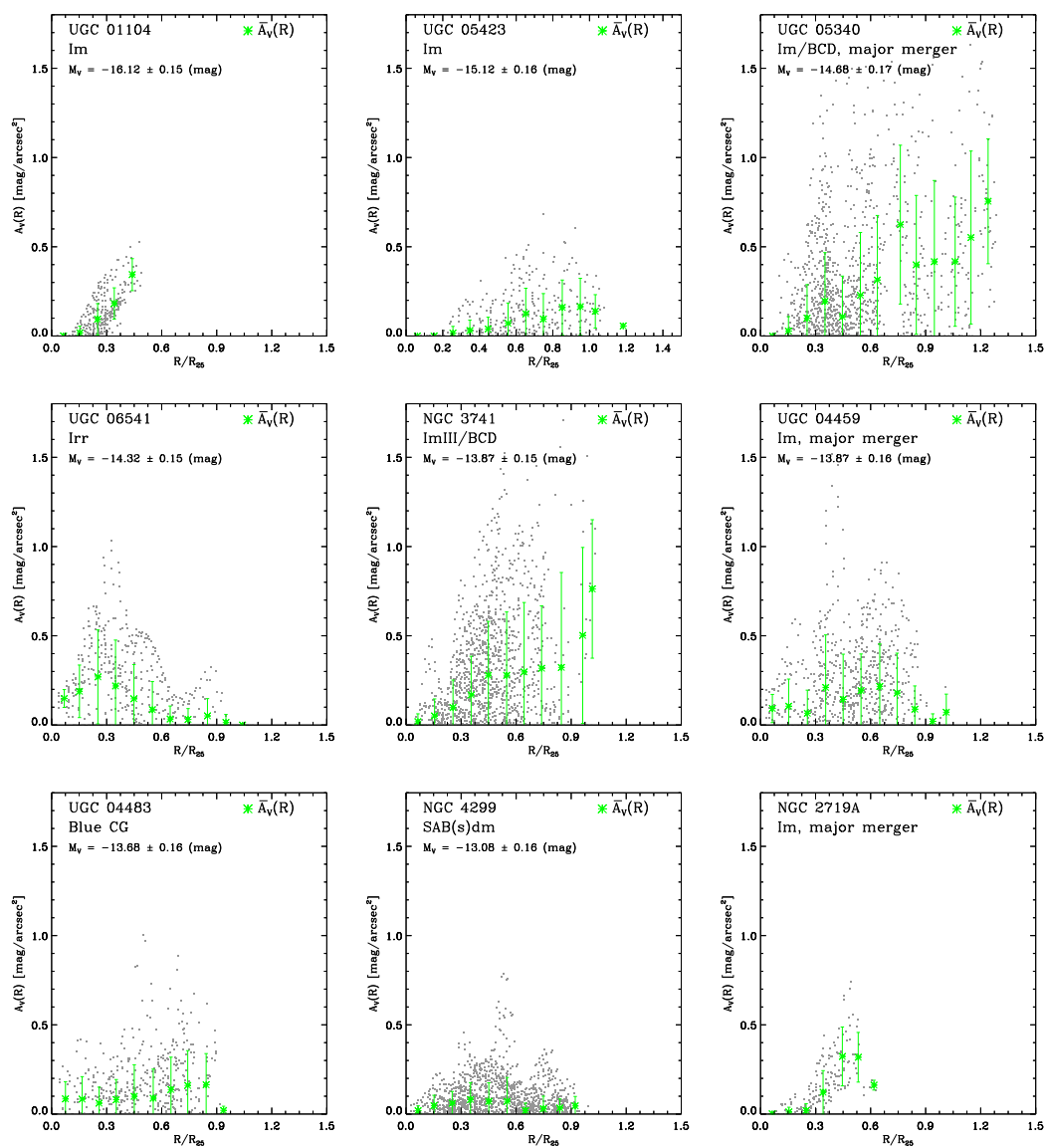


Figure 54. Continued.

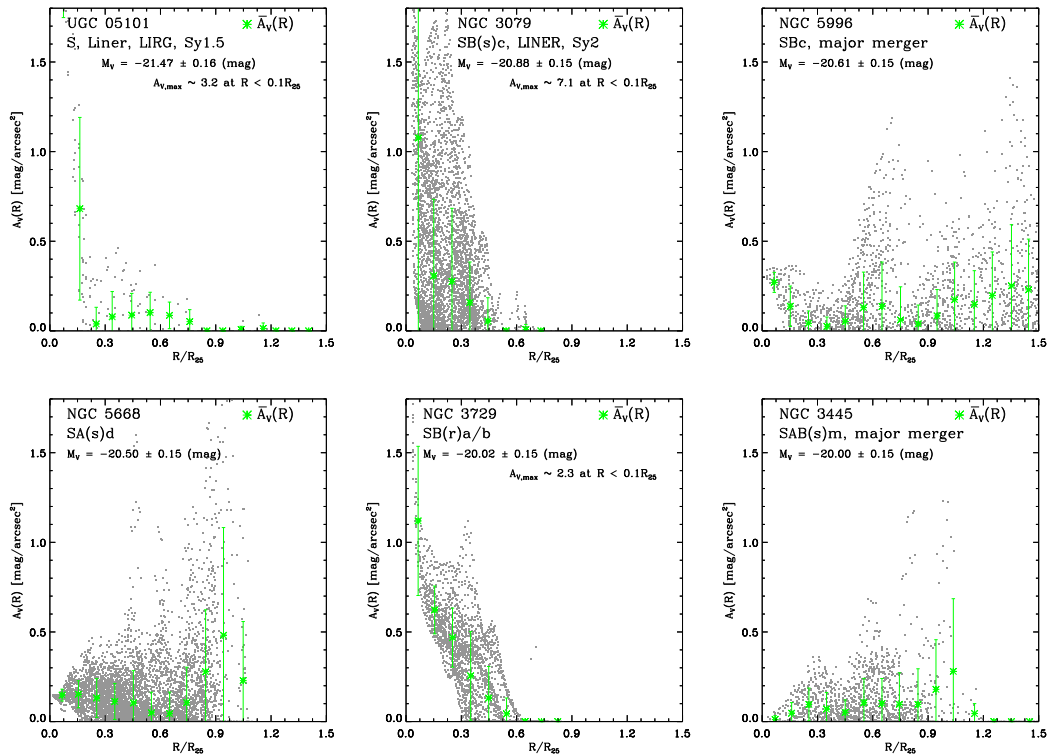


Figure 55. Radial A_V profile of spiral galaxies as a function of their absolute visual magnitude, M_V .

As in previous section, when all the galaxies are compared, the slope of $\overline{A_V}(R)$ for $R \lesssim 0.3 R_{25}$ shows no specific pattern in its ordering. Positive, negative, and flat $\overline{A_V}(R)$ profiles are all mixed together in this sample. Instead, we note that the level of azimuthally averaged $\overline{A_V}(R)$ value decreases as M_V becomes fainter. Since the $A_{V,i}$ spikes at different radii are still visible, with sometime high- A_V , an $\overline{A_V}(R)$ profile with smaller averaged extinction value does not mean that there is no SF-activity in the galaxy, but simply that these galaxies may have a really localized distribution of dust extinction.

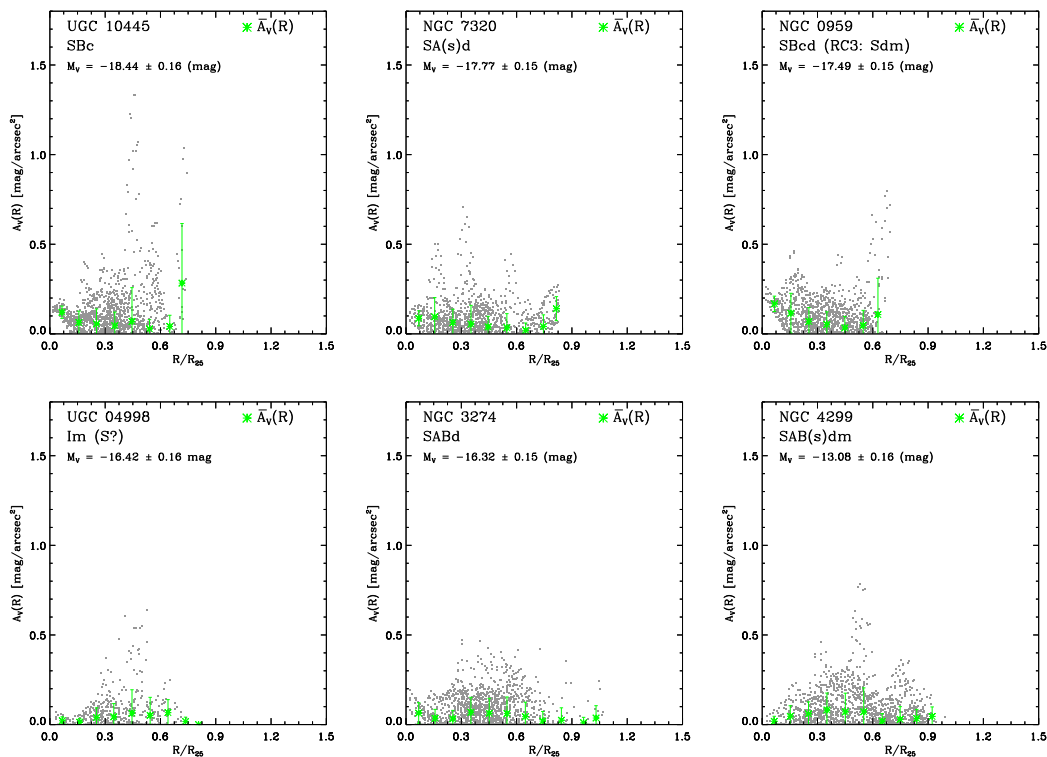


Figure 55. Continued.

4.4.5. The Dust Distribution as a Function of Absolute Magnitude: Irregulars

Figure 56 shows the radial dust extinction profile for irregular galaxies, arranged in order of absolute magnitude. As for spirals, irregular galaxies do not show any systematic trend in inner slope of $\overline{A_V}(R)$ profile as a function of their absolute magnitude. The distribution of individual pixel measurements, $A_{V,i}$ also varies, establishing no particular pattern in this figure. Therefore, we conclude that for irregular galaxies, there is no special pattern or trend for the radial dust extinction profile, regardless of whether they are arranged by morphological type or absolute magnitude. This result is somewhat expected since—as the name “irregular” indicates—these galaxies *cannot* be grouped together based on their observed structure.

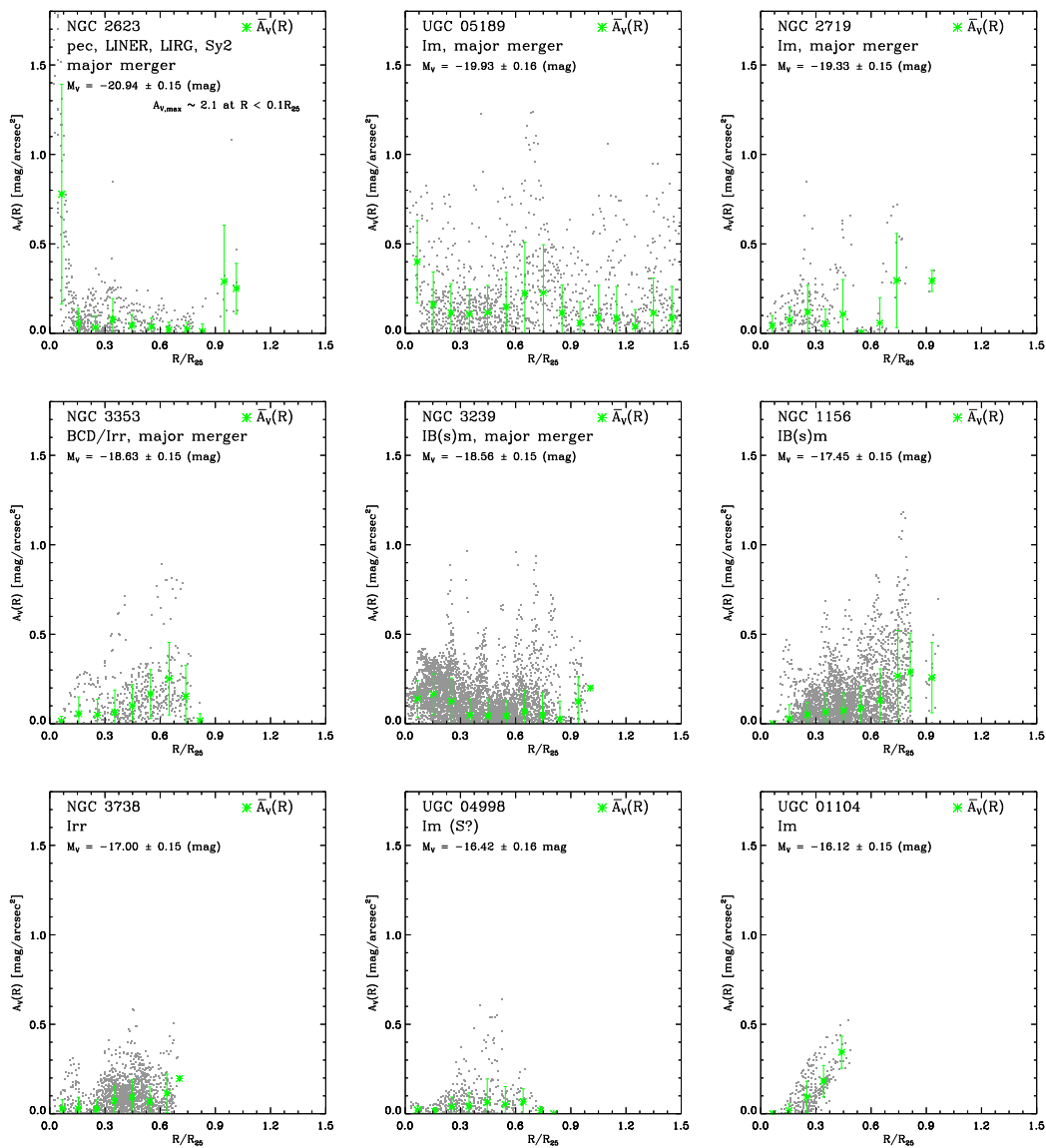


Figure 56. Radial A_V profile for irregular galaxies as a function of their absolute magnitude, M_V .

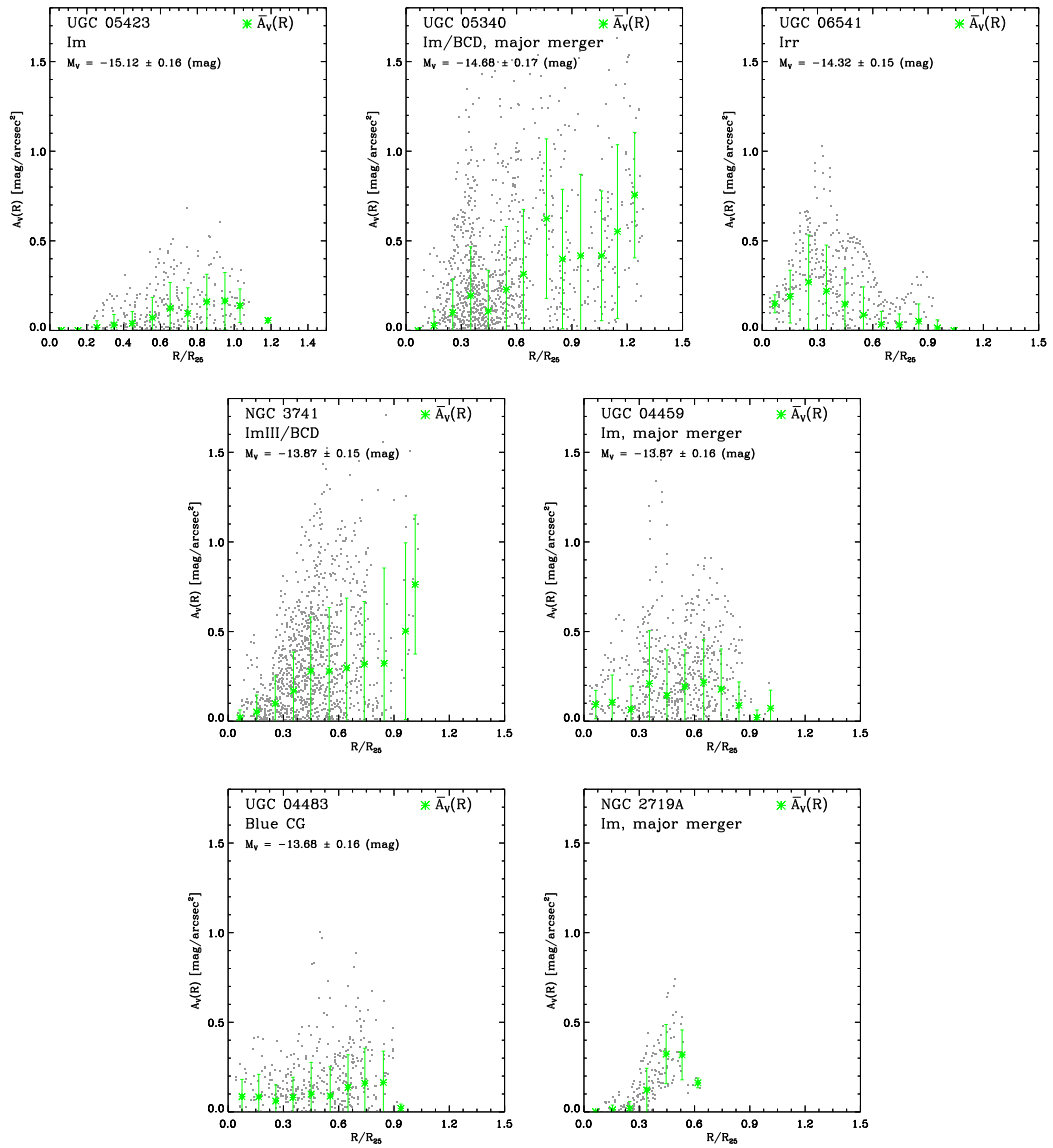


Figure 56. Continued.

4.5. Summary and Conclusion

In this chapter, we applied the pixel-based dust-extinction measurement (Chapter 2) and our pixel-based stellar population analysis (Chapter 3) to a total of 27 galaxies, that spans from early spiral (SB(s)a/b) to irregular types, and to compact galaxies. While some galaxies do not have useful *Spitzer*/IRAC 8.0 μm images to trace their PAH emission, all galaxies have deep enough ground-based (VATT) optical V and IRAC 3.6 μm images, as well as *GALEX* FUV and VATT U and B images, to apply our pixel-based dust-extinction measurement/correction and stellar population analysis.

Applying our pixel-based dust-extinction measurement based on observed V -to-3.6 μm flux ratio, β_V , to each galaxy, we successfully mapped the two-dimensional distribution of dust extinction in galaxies of different morphologies and absolute magnitudes. From their two-dimensional extinction maps, we found that in all galaxies—regardless of their morphology—dust extinction is distributed more frequently in small clumps, rather than in a smooth, large-scale distribution. These small clumps of dust extinction are not distributed symmetrically, but are randomly distributed throughout the galaxy. Moreover, even in spiral galaxies with a face-on disk, dust extinction is often distributed more heavily on one side of the galaxy than the other side. This asymmetric distribution of dust extinction is especially evident in, e.g., NGC 0959, NGC 3445, and NGC 7320.

Plotting the pixel-based dust extinction ($A_{V,i}$) as a function of radius shows that each small dust clump appears as a narrow extinction spike at different radii.

Some good examples are NGC 1156 and NGC 3239. Larger galactic structures, such as spiral arms, bars, and rings, appear as similar but broader peaks in the $A_V(R)$ profile. Such radial A_V distribution patterns can be seen in, e.g., NGC 0959, NGC 3079, and NGC 3729. Once the dust extinction is azimuthally averaged, all these features are smoothed out, and no longer recognizable in the averaged radial profile of the dust extinction, $\overline{A_V}(R)$. The application of such averaged extinction correction therefore results in under-correction of dust extinction in regions where the actual A_V is much higher, and in over-correction in regions that suffered less extinction. Therefore, pixel-based two-dimensional extinction mapping is critical to faithfully reveal both small- and large-scale structures of a galaxy.

While studying the distribution of $\overline{A_V}(R)$ and $A_{V,i}$ as a function of morphology and absolute magnitude, we find that the only trend is the decrease and sign-change of the inner slopes of $\overline{A_V}(R)$ for spiral galaxies. However, since we have only 12 spiral galaxies in our sample, with more emphasis toward later (Sc–Sm) morphological types, this trend may simply be due to small number statistics. In the future, we will expand our sample to a much larger number of galaxies per type and luminosity bin, to study the trends of the radial A_V profile in spiral and irregular galaxies.

A serendipitous discovery from our two-dimensional dust-extinction map and the radial A_V profiles is that our method may become a useful tool in searching for galaxies with (hidden) AGN. There are three known Seyferts (UGC 05101 (Type-1.5), NGC 2623 (Type-2), and NGC 3079 (Type-2)) in our sample of 27 galaxies, and all three show much higher A_V values in their galaxy centers than in the surrounding

galaxy disk. Other than these three galaxies, we observed that NGC 3729 shows a similar central dust-extinction peak. Currently, this galaxy is classified as SB(r)a in NED with a note that this galaxy is also peculiar, and as Sb by Taylor et al. (2005), but not as a galaxy with an AGN. Indeed, this galaxy is treated as a nonactive galaxy by Ryan et al. (2007). Since we do not see a similar feature in the radial A_V distribution other than in Seyfert (Type-1.5–2) galaxies, we suggest that NGC 3729 may also host an AGN, or at least a weak one.

Using our extinction-corrected images, we analyzed the stellar populations in each galaxy through a pCCD of $(B - 3.6 \mu\text{m})$ versus $(FUV - U)$ color. While the color-ranges vary for different galaxies due to a combination of various causes (e.g., light blending and the physical area covered by a single pixel), all galaxies show some degree of separation and branching of pixels in their pCCD, that are not recognizable before our extinction correction is applied. Separating these stellar populations into six (or more) groups, and plotting them on a pixel-coordinate map for each galaxy, reveals that these pixel-groups are not distributed randomly, but trace genuine galaxy structures (e.g., SF regions, spiral arms, bars, and bulges). Each resolution element corresponds to the *GALEX* NUV PSF, and is $\sim 3 \times 3$ pixels. Since the size of these small- and large-scale galaxy structures visible in pixel-coordinate maps is generally larger than this, we conclude that these pixel-groups indeed indicate the different properties of their dominant stellar population. The only way to reveal the branchings and groupings of pixels in the pCCD is to apply an appropriate dust extinction correction to each pixel. We therefore conclude that *our method of measuring the dust*

extinction through the V -to- $3.6\mu\text{m}$ flux ratio, β_V , while simple and crude, appears to be a robust approach to map the two-dimensional variations in the dust extinction within galaxies. More importantly, applying the pixel-based two-dimensional extinction correction is crucial to study the nature of the stellar populations hidden behind the complicated distribution of dust extinction in nearby galaxies.

High redshift galaxies (at $z \simeq 1$ and beyond), many of which are merging and vigorously forming stars (e.g., Zepf & Koo 1989; Burkey et al. 1994; Conselice 2006; Ryan et al. 2008), are important to understand the history of galaxy formation and evolution. To date, dust extinction of these galaxies are usually still treated with a single averaged value for each galaxy to correct for the observed light. The results of our study, with a sample of 27 nearby spiral and irregular galaxies, proves that our pixel-based extinction correction and analysis with a pCCD can be a powerful tool to study the intrinsic stellar populations underlying the complicated distribution of dust extinction. The combination of *HST*/WFC3 and *JWST* with their superb angular resolution (FWHM $\simeq 0''.06$ – $0''.16$) and the method described in this dissertation would allow one to study more detailed intrinsic properties of the stellar populations in these distant galaxies. Revealing a more accurate picture of galaxy formation and evolution at $z \gtrsim 1$ is thus an important ingredient to better understand the process of galaxy assembly throughout the history of the Universe.

CHAPTER 5

CONCLUSION

5.1. Summary of Current Work

This dissertation presents the results of a multi-wavelengths pixel-based study of nearby late-type galaxies. The primary goal of this study is to explore a new pixel-based approach of measuring and mapping the radial distribution of dust extinction. Using panchromatic data from *GALEX* FUV and NUV, ground-based VATT *UBVR*, and *Spitzer*/IRAC 3.6, 4.5, 5.8, and 8.0 μm images, we performed stellar population analysis through a pCCD of $(B - 3.6 \mu\text{m})$ versus $(\text{FUV} - U)$ color to show how well our new extinction correction method reveals the true nature of the underlying stellar populations, which is significantly hidden behind the complicated distribution of dust extinction in nearby late-type galaxies.

In the first half of Chapter 2, we perform a conceptual study using the SED library for different ages and metallicities of SSPs. We explore different combinations of filters to select the best possible filters to study the effect of dust. Shorter wavelengths show a larger effect from dust extinction, but at the same time, metallicity and age of the stellar population affect the amount of observed flux more as well. On the other hand, longer wavelengths (i.e., near-IR) have much less age and metallicity dependence, but the dust extinction at these wavelengths also becomes significantly smaller. The restframe optical *V*-band, which has relatively small effects from age and metallicity, but still suffers from dust extinction, is selected at the short wavelength side. To trace the stellar light distribution, and hence use it as a base for estimating the intrinsic *V*-band flux, the *Spitzer*/IRAC 3.6 μm (mid-IR) passband is selected. The advantages of using the IRAC 3.6 μm filter are: (1) the effect of

dust extinction reaches a minimum at this wavelength, and becomes essentially non-measurable within the photometric uncertainties; and (2) no PAH emission—which becomes strong at wavelengths $\gtrsim 5 \mu\text{m}$ —is contaminating the observed flux. Using these two filters, we also find that for different metallicities, the ratio of V -to- $3.6 \mu\text{m}$ flux, β_V , is relatively flat for older ($t \gtrsim 500 \text{ Myr}$), younger ($10\text{--}100 \lesssim t \lesssim 500 \text{ Myr}$), and extremely young ($t \lesssim 10\text{--}100 \text{ Myr}$) stellar populations (at least for sub-solar metallicities). This allows us to simply separate the ages of observed stellar populations into two groups (or three groups, if extremely young stellar populations are individually separable), and apply the same calculation to estimate the dust extinction within each group of such pixels.

In the second half of Chapter 2, we apply our method to the actual data of the late-type spiral galaxy NGC 0959 as a case study. Due to light-blending, as a result of its large PSF (FWHM $\simeq 5''.3$) and large pixel scale ($1''.5 \text{ pixel}^{-1}$), the light from neighboring stellar populations are heavily mixed together. Even though the flux observed in a single pixel comes no longer from a *single* stellar population as in the case of a theoretical study, we assume that the light in a given pixel is dominated by the youngest stellar populations, since it usually has the strongest contribution to the total emitted light. Using the pCMD of μ_V versus $(U - 3.6 \mu\text{m})$ color, we first separate the pixels dominated by younger and older stellar populations. Then using the histogram of V -to- $3.6 \mu\text{m}$ flux ratio β_V —where we assumed that about half of the pixels are not affected by dust extinction to within the photometric uncertainties—we empirically selected the intrinsic flux ratio, $\beta_{V,0}$, that is used to

estimate the *extinction-free* V -band flux from the *observed* $3.6\ \mu\text{m}$ flux. Comparing this empirically estimated intrinsic flux to the observed V -band flux, we estimated the visual dust extinction, A_V . The pixels with an excess of *observed* V -band flux are treated as extinction free. Mapping the *measured* dust extinction onto a pixel coordinate map clearly shows the small- and large-scale distribution of dust extinction throughout the galaxy. The distribution of moderate A_V follows the IRAC $8.0\ \mu\text{m}$ (PAH) emission contours, and is also distributed as small clumps in other regions of the galaxy disk. The main discovery from this study is that—while dust is commonly treated as a smooth distribution with a simple azimuthally averaged radial profile—our result shows that the actual extinction distribution is much more complicated, and in general not smooth at all.

In Chapter 3, we demonstrate the importance of our pixel-based dust-extinction correction, by analyzing the stellar populations of NGC 0959. Using the images from the *GALEX* FUV through *Spitzer*/IRAC $8.0\ \mu\text{m}$ passbands, we examined various combinations of pCMDs and pCCDs to see how our extinction correction changes the distribution of pixels in color-magnitude and color-color space. Among various combinations of colors and magnitudes, we select a pCCD of $(B - 3.6\ \mu\text{m})$ versus $(\text{FUV} - U)$ color that shows a significant change in the color-color distribution of the pixels *before* and *after* application of our extinction correction. This color combination traces some of the important properties (i.e., star formation history and age) of the stellar populations *averaged* over each pixel. While there is no grouping, branching, or separation of the pixel distribution *prior* to applying our extinction

correction, a clear separation—as blue and red sequences—and grouping of pixels appear *after* the application of extinction correction. These pixels are separated into six different pixel-groups, based on their color-color distribution, and then charted onto a pixel-coordinate map. The spatial distribution of these pixel groups shows that pixels belonging to the same group are distributed in contiguous regions within the galaxy, which traces the visible galaxy structures as well as IRAC $8.0\ \mu\text{m}$ contours. This confirms that our selection of pixel groups are indeed based on the different properties of the dominant stellar populations for individual pixels, and that the selection of these pixel-groups is *only accomplishable, if dust extinction in each pixel is corrected appropriately*. These results confirm that our pixel-based dust-extinction mapping, even though it is simple and crude, is measuring proper dust-extinction in the galaxy to first order. We also discovered that NGC 0959 harbors a *previously unrecognized* bar-like structure, and we therefore suggest the classification for this galaxy be changed from Sdm to SBcd.

In Chapter 4, we apply our method of pixel-based extinction correction to other 26 nearby late-type galaxies, ranging from SB(s)a to irregulars (Irr and Im), and to compact galaxies. Regardless of morphology, our method is successful in revealing the separate distribution of pixel-groups in the pCCD of $(B - 3.6\ \mu\text{m})$ versus $(\text{FUV} - U)$ color for all galaxies in our sample. This confirms that our method works not only for NGC 0959, but can be applicable to a wide range of galaxies. By studying the dust-extinction map and radial dust-extinction profile for each galaxy, we find that dust extinction is not distributed in a simple one-dimensional radial pro-

file, nor in an averaged or smoothed distribution. Instead, *dust extinction is highly localized, and generally distributed asymmetrically within each galaxy.* Studying the radial distribution map of individual pixel-based dust-extinction measurements ($A_{V,i}$) and the azimuthally averaged radial extinction profile ($\overline{A_V}(R)$), we find that—while $A_{V,i}$ shows individual clumps of localized dust extinction at different radii—the azimuthally averaged $\overline{A_V}(R)$ profile completely smooths out the small-scale distribution of dust. Another important difference between $\overline{A_V}(R)$ and $A_{V,i}$ is that while $\overline{A_V}(R)$ usually does not reach $0 \text{ mag arcsec}^{-2}$ at any radius, about half of pixels analyzed with our method have no measurable dust extinction (i.e., $A_{V,i} = 0 \text{ mag arcsec}^{-2}$) to within the photometric uncertainties. This suggests that—when dust extinction is corrected with a simple averaged value for an entire galaxy or a radial profile at different radii—most regions within a galaxy are either over-corrected or under-corrected for dust extinction, which may lead to an incorrect stellar population analysis. Therefore, *the only way to properly measure and correct for dust extinction is to measure it with small enough physical scale and two-dimensionally (e.g., using a pixel-based dust-extinction mapping).*

We also studied the trend in the (azimuthally averaged) radial A_V profile as a function of the morphology and absolute V -band magnitude, M_V , of the galaxies. Even though our sample size is small, we find that the radial extinction profile of spiral galaxies shows a morphology dependence, at least at their inner radii ($R \lesssim 0.3 R_{25}$), where earlier type spiral galaxies have a steeper decrease in $\overline{A_V}(R)$, while, as the morphology change to later-types, the slope becomes flat, and then starts to increase.

Since irregular galaxies are classified as such due to the lack of any structural features, there is no clear pattern in their radial dust extinction profile. The $\overline{A_V}(R)$ is also studied as a function of the absolute V -band magnitude, M_V . There might be a slight trend of decreasing level of average extinction value in the radial profile for spiral galaxies as the galaxy have lower luminosity. However, both spiral and irregular galaxies do not show any recognizable systematic pattern in the change in slope of $\overline{A_V}(R)$ profile for their inner radii. Therefore, we conclude that the radial A_V profile shows some trend as a function of the morphology of spiral galaxies, yet this needs to be confirmed with a much larger sample of galaxies, to fully quantify the observed trend.

A serendipitous discovery from studying the radial A_V distribution is that our method may be used to detect (hidden) AGN in Seyfert galaxies. These galaxies have extremely high A_V values at their nucleus compared to the extinction values measured in their disk. Our method is able to select out all three galaxies that are classified as a Seyfert (Type-1.5–2) in our sample. We also find one other galaxy, NGC 3729 (SB(s)a with a note of being peculiar in NED), that has a similar radial extinction profile as the three Seyferts, but is not classified as a Seyfert galaxy. Therefore, we assume there is an AGN, or at least a weak one, at the center of this galaxy.

5.2. Future Work

This study was made possible especially thanks to the successful launch of the *Spitzer* Space Telescope in 2003, and its smooth operation since then. On 2009 May 15, the *Spitzer* cryogen was depleted, and currently the observation with *Spitzer* is

shifted into the *Spitzer* Warm Mission phase, where only the two channels at shorter wavelengths (3.6 and 4.5 μm) of IRAC are used. One of the missions recently approved is the Spitzer Survey of Stellar Structure in Galaxies (S4G, K. Sheth PID: 60007). This project aims to image ~ 2000 galaxies within a distance of 40 Mpc using the IRAC 3.6 and 4.5 μm channels to study the stellar structure within nearby galaxies. Since our current sample size is small, especially for spiral galaxies, the additional data obtained by S4G program will be critical to study the relationship between the radial dust extinction profiles (azimuthally averaged $\overline{A_V}(R)$ and pixel-based $A_{V,i}$) and other galaxy properties (e.g., morphology, absolute magnitude, and mass) with much better statistical significance.

In the current study, the missing morphological groups of galaxies from our sample are the ellipticals and lenticulars. Elliptical galaxies are thought to be mostly dust free, but recent studies show that some ellipticals contain a large amount of dust (e.g., Goudfrooij et al. 1994a,b; Van Dokkum & Franx 1995; Kaviraj et al. 2007a; Oosterloo et al. 2007a,b; Emonts et al. 2008). Since the amount of SF-activity in ellipticals and lenticulars is in general much less than that in spiral and irregular galaxies, commonly used methods that are based on the FIR/UV flux ratio or on Hydrogen recombination line ratio are not as useful as they are in star-forming spirals. Our method, which only depends on images observed in the optical V and mid-IR 3.6 μm passbands—with an additional filter of UV wavelengths (ground-based U , in our study) for age separation—is ideal for a study of dust distribution within these early-type galaxies.

Another application of our dust-extinction measuring and mapping technique is to investigate the dust distribution in the disks of galaxies. Taylor et al. (2005) finds that some galaxies have redder colors at their outer regions. This reddening may be caused either by a change in stellar populations, or due to the presence of dust. Holwerda et al. (2009), using the occulting pair of galaxies, shows that some spiral galaxies contain significant amount of dust at their outer radii. Our current multi-color (panchromatic) study is limited to the high surface brightness regions in galaxy disks, due to minimum S/N ratio requirement *across all filters* from the *GALEX* FUV through IRAC mid-IR wavelengths. In the future, we can study the distribution of dust extinction and underlying stellar populations with much deeper images in the optical and mid-IR filters, at much higher spatial resolution.

In this dissertation, our method has been applied and studied using nearby galaxies. To fully understand the formation and evolution of galaxies, studying higher redshift galaxies at $z \simeq 0.5-2$ becomes important, where the merger rate of galaxies is much higher than in the current universe at $z=0$ (e.g., Zepf & Koo 1989; Burkey et al. 1994; Conselice 2006; Ryan et al. 2008). In summer of 2009, Wide Field Camera 3 (WFC3) that is newly installed on the *Hubble Space Telescope HST* has shown that it can image galaxies with a superb UV–near-IR resolution. WFC3 has two imaging channels: the Ultraviolet and Visual (UVIS) channel covers 0.2–1.0 μm wavelengths with a pixel scale of $0''.04 \text{ pixel}^{-1}$, and the IR channel covers 0.9–1.7 μm wavelengths with a pixel scale of $0''.13 \text{ pixel}^{-1}$ at point spread function (PSF) of full width at half maximum (FWHM) $\lesssim 0''.16$. *James Webb Space Telescope (JWST)* will also have two

imaging cameras: the Near Infrared Camera (NIRCam) covers $0.6\text{--}5\ \mu\text{m}$ wavelengths at $0''.032$ and $0''.065\ \text{pixel}^{-1}$ in two channels, and the Mid Infrared Instrument (MIRI) covers $5\text{--}27\ \mu\text{m}$ wavelengths at $\sim 0''.11\ \text{pixel}^{-1}$. These instruments will thus allow us to study and map the distribution of dust extinction, and the stellar populations hidden behind the dust, at high precision and at much finer spatial resolution within galaxies at these high redshifts. Studying the stellar content and star-formation history in galaxies at $z \gtrsim 1$ with these facilities is therefore of significant importance to reveal the precise nature of galaxy assembly and evolution.

CHAPTER 6

APPLICATION OF ASTRONOMICAL IMAGE ANALYSIS TOOLS: DETECTION OF SMALL SENSORY NERVE FIBERS IN TYPE-II DIABETES DIAGNOSIS

6.1. Overview

Computerized Detection Method (CDM) software programs have been extensively developed in the field of astronomy to process and analyze images from nearby bright stars to tiny galaxies at the edge of the Universe. These object-recognition algorithms have potentially broader applications, including the detection and quantification of cutaneous Small Sensory Nerve Fibers (SSNFs) found in the dermal and epidermal layers, and in the intervening basement membrane of a skin punch biopsy. Here, we report the use of astronomical software adapted as a semi-automated method to perform density measurements of SSNFs in skin-biopsies imaged by Laser Scanning Confocal Microscopy. Comparison between the normalized CDM and the visual classification results on identical images demonstrates that the two density measurements are comparable. The CDM therefore can be used—at a relatively low cost—as a quick (*a few hours for entire processing of a single biopsy with 8–10 scans*) and reliable (*high-repeatability with minimum user-dependence*) method to determine the densities of SSNFs.

6.2. Background

Damage to the peripheral nervous system can be idiopathic, or can occur as a result of known causes, such as of pre- and post-diabetic disorder (e.g., Lacomis 2002; Smith & Singleton 2006). This damage can be characterized by pathology of SSNFs (e.g., Dyck et al. 1981; Periquet et al. 1999; Vergheze et al. 2001; Sumner et al. 2003; Malik et al. 2005; Smith & Singleton 2006), which are difficult to assess functionally,

and may be variable in symptoms (e.g., pain and tingle), signs (e.g., sensory loss), or disabilities.

The difficulty in diagnosing an SSNF neuropathy has led to the development of histological analysis of skin punch biopsy tissue, utilizing morphological surrogate markers and confocal, or conventional microscopy (e.g., Dalsgaard et al. 1989; Karanth et al. 1991; Kennedy & Wendelschafer-Crabb 1993). This technique is a safe, reliable, and reproducible method of quantifying SSNF pathology. It also has been advocated for diagnosing SSNF neuropathy from a variety of causes (Holland et al. 1997, 1998), and for assessing the degree of neuropathy from none to severe (Quattrini et al. 2007). A basis for such diagnostic procedure is that these biopsy tissues are rich in SSNFs (often referred to as C-fibers), that can be labeled by immunostaining with a pan-neuronal marker (e.g., Protein Gene-Product (PGP) 9.5; Dalsgaard et al. 1989; Karanth et al. 1991), and quantified as density values (e.g., fibers mm^{-1}) of epidermal length, or as in this presentation, of basement membrane length where fibers are counted in the basement membrane.

Under normal clinical conditions, the key issue in visually measuring the density of SSNFs is the reliability. The use of multiple blind-study classifiers is usually used to improve the reliability of the analysis. Statistical studies show the correlation coefficient for repeated observations by the same classifier is 0.80 ± 0.06 (McArthur et al. 1998), and for observations between different classifiers is 0.90 ± 0.04 (Hirai et al. 2000). Smith et al. (2005) shows that the interobserver variability is $9.6\% \pm 9.4$ (in the form of relative intertrial variability (RIV) \pm standard deviation (SD)), and

intraobserver variability is $9.6\% \pm 8.9$ for each biopsy, where a RIV value of less than 10% indicates a high degree of repeatability. Detailed descriptions of how to calculate the RIV and SD are provided by Smith et al. (2005). To improve the reliability, a number of computerized programs have been adopted (e.g., Kennedy et al. 1996). One practical issue with these programs is the cost of the software. We therefore propose here: (1) a *low-cost*, novel, and semi-automated computerized detection method, which can determine the density of SSNFs in immunostained tissue images; and (2) that this method, with some adaptation, can be readily used to detect SSNFs, and to determine the presence of SSNF neuropathy in any kind of tissue.

In this chapter, we present a quantitative semi-automated method of measuring the SSNF densities within the basement membrane, using parts of existing computer codes. These codes have been successfully used for decades to analyze images of tiny galaxies in the field of extragalactic astronomy (e.g., Driver et al. 1995; Odewahn et al. 1996; Arnouts et al. 1997). Since the 1960's, astronomers have developed many techniques for detection of those tiny objects. As a result, current technology allows us to detect and analyze from the surface of the Sun to objects 10^{22} times fainter than the Sun, and up to 10 million times smaller than the angular size of the full Moon (e.g., Tyson 1988; Neuschafer & Windhorst 1995; Pascarella et al. 1996; Windhorst et al. 1998, 2008). Astronomers also have developed numerical techniques to obtain the best possible resolution through deconvolution and other methods such as the Maximum Entropy Method (MEM: Gull & Daniell 1978, 1979), CLEAN (Högbom 1974), and Pixon methods (Pina & Puetter 1993; Puetter 1997). Some of these (e.g.,

MEM and Pixon methods) have been adapted for use in the medical field, such as the detection of breast cancer from X-ray mammograms. For these reasons, we employ the rich expertise of astronomical image analysis software to detect SSNFs in the basement membrane of skin punch biopsies of volunteer subjects.

6.3. Materials and Methods

All human studies have been approved by the Institutional Review Boards of two institutions: Banner Good Samaritan Medical Center, Phoenix, AZ and Arizona State University, Tempe, AZ. They have been performed in accordance with the ethical standards laid down in the Declaration of Helsinki. All persons gave their informed consent prior to the investigation. A group of 27 subjects were recruited yielding 52 biopsies. Skin punch biopsies were obtained from the proximal forearm and/or distal thigh of these subjects.

The intent of this work is to demonstrate that SSNF density values attained by computer analysis compares favorably to the visually-monitored density counts within the same subject. Thus, in any one subject, a healthy or unhealthy pool of subjects is not specifically relevant to the research question. Nevertheless, in this study, we chose to examine SSNF densities in a representative cohort of obese subjects with no neuropathic symptoms with the purpose to conduct a later study, which would examine the present cohort with another obese population with diabetes.

6.3.1. *Sample Preparation*

6.3.1.1. *Biopsy Technique*

A 2 cm circle was drawn around the hairy skin sites of the proximo-lateral forearm and the disto-medial aspect thigh. Each skin site was then sterilized with an alcohol swab and anesthetized with 1% lidocaine. Once the subject reported complete numbness in the area, a skin punch biopsy was performed (3 mm diameter by 3 mm depth). The sample was placed in fixative, and a small sample of gelfoam was placed on top of the wound to expedite healing. Bacitracin[®] (a topical antibiotic) was swabbed on a bandage and placed on top of the site. There were no reports of adverse events as a consequence of these procedures.

6.3.1.2. *Sectioning and Staining*

Skin punch biopsies were fixed overnight in modified Zamboni's fixative (2% formaldehyde, 15% Picric acid in 0.1M Phosphate buffered saline (PBS), pH 7.5); biopsies were equilibrated in 50% sucrose in 0.01M PBS for 12 hours at 4°C, and mounted in Tissue Tek Optimum Cutting Temperature (OCT) Compound (Miles Inc., Elkhart, IN); 0.06 mm (60 μm) thick sections were obtained by cryostat sectioning. Biopsy sections were then blocked in blocking solution (0.1M PBS, 0.05% Tween-20, 0.1% Triton X-100, 5% bovine serum albumin frac V) at 4°C for 12 hours, then washed twice by solution replacement with washing solution (0.1M PBS, 0.05% Tween-20, 2% Bovine Serum Albumin (BSA), pH 7.5). Primary antibodies to collagen IV (mouse anti-human collagen IV monoclonal, Cat. # MAB1910, Chemicon International, Temecula, CA) and PGP 9.5 (rabbit anti-human PGP 9.5 IgG purified

polyclonal, Cat. # 7863-0507, BioGenesis, Kingston, NH) were diluted 1:50 with antibody dilution buffer (0.1M PBS, 1% BSA, pH 7.5). Sections were immunolabeled for 24 hours at 4°C in the primary antibody solution. Sections were then washed twice in washing solution. Secondary antibodies (Alexa Fluor 488 goat anti-mouse IgG (H+L); Cat. # A11001, and Alexa Fluor 633 goat anti-rabbit IgG (H+L), Cat. # A21070, Molecular Probes, Eugene, OR) were diluted 1:100 in antibody dilution buffer. Sections were incubated in this solution for 24 hours at 4°C, and washed twice with washing buffer.

6.3.1.3. *Visualization and Image Acquisition*

Immunofluorescently labeled sections were dehydrated in a graded ethanol series, transferred to methyl salicylate, and wet mounted for visualization using a Leica TCS-NT Laser Scanning Confocal Microscope (LSCM) at the W. M. Keck Bioimaging Facility (Keck Lab) at the Arizona State University using Ar and He/Ne lasers. For each sample, 32 z -plane optical sections were imaged every 0.00125 mm (1.25 μm) through a 0.040 mm (40 μm) region with 0.16 mm \times 0.16 mm (160 μm \times 160 μm) in the x - y dimensions (see Figure 57). Serial sections of these images were obtained using Leica TCS-NT image software. Images were obtained at 63 \times magnification with an image resolution of 1024 \times 1024 pixels to increase the visibility of small diameter fibers to facilitate quantification of their density.

6.3.1.4. *Intraepidermal Nerve Fiber Density Quantification*

For each biopsy, up to 12 scans were observed manually, and by up to four different observers. The number of fibers embedded into or penetrating the basement

Confocal Data Set of Tissue Biopsies

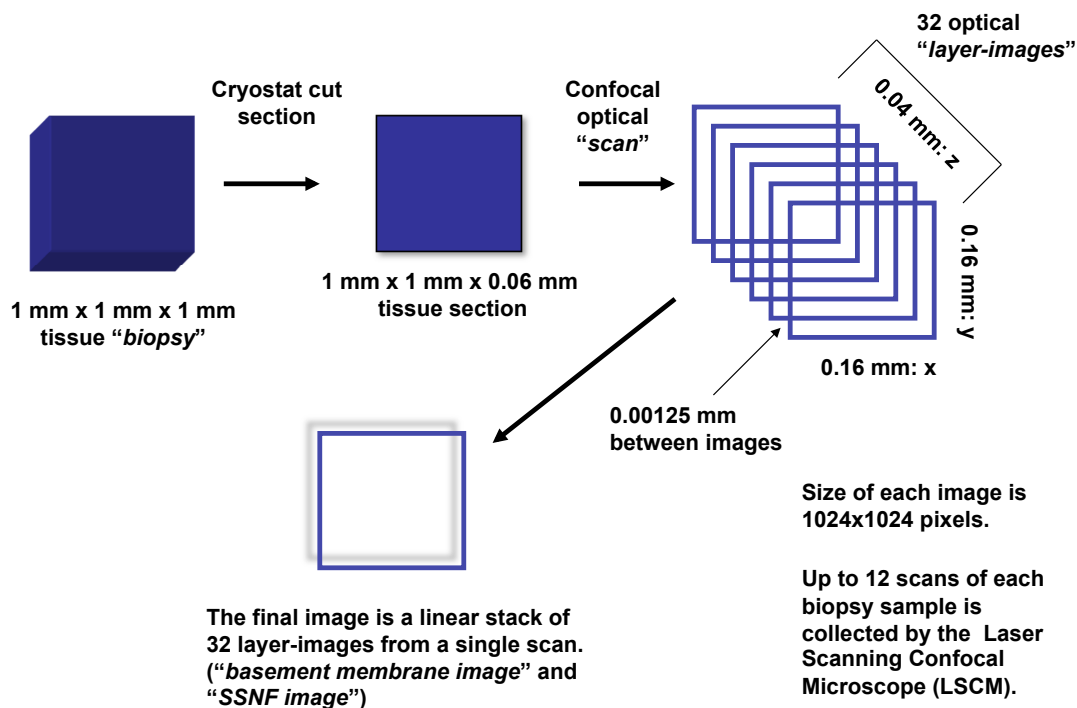


Figure 57. A diagrammatical illustration at different stages of the image preparation and analysis. From a single "biopsy" sample, a thin tissue section is prepared by immunostaining, then the LSCM takes up to 12 "scans" of image-sets, each with a $63\times$ magnification. A single "scan" consists of two sets of 32 "layer-images"—one for the basement membrane and the other for the SSNFs—with a spacing of 0.00125 mm between layers. Only one set is illustrated here for simplicity. These two sets of 32 "layer-images" are then distributed to individual CDM and visual classifiers. Once distributed, each classifiers stacks these "layer-images" linearly to create a single projected "basement membrane image" and a single "SSNF image" for further analysis.

membrane was visually assessed by examination of the scans. Mean density for each biopsy were then determined, based on the densities for each series of images, and recorded as a number of intraepidermal nerve fibers per mm of basement membrane length, yielding a mean density value for the scans of a single biopsy.

Although the conventional method is to report epidermal length as the reference for calculating the density value, when *the purpose is to examine only the density of intraepidermal nerve fibers, which are terminating into or penetrating the basement membrane*, we use basement membrane length as the reference.

6.3.2. Data and Tools

6.3.2.1. Definition and Terminology

Throughout our analysis, the data—in a form of digital images—are undergoing multiple processing steps. The images at different steps, and at different levels of grouping, therefore need to have specific names to be identified. The structure of our dataset is diagrammatically illustrated in Figure 57, and is defined as follows: (1) there are a total of 52 skin punch biopsies, or “*biopsies*”; (2) each *biopsy* has up to 12 LSCM “*scans*” at different locations along the basement membrane section(s); and (3) a single LSCM *scan* creates a set of 32 “*layer-images*” of basement membrane images and 32 “*layer-images*” of SSNF images. These *layer-images* are then distributed to, and “stacked” into a single “*basement membrane image*” and a single “*SSNF image*” by individual classifiers for analysis.

6.3.2.2. *Steps of Computerized Detection Method*

In this specific study, we use a Computerized Detection Method (CDM), derived from the field of astronomy, to measure SSNF densities in skin punch biopsies of our volunteer subjects. In the following sections, we describe the steps in the semi-automated CDM analysis, which include: (1) preparation of digitized images by: (a) converting the image format; (b) stacking two sets of *layer-images*; (c) smoothing the stacked *basement membrane image*; and (d) adding a small Gaussian noise-field to the stacked *SSNF image*, and similarly smoothing it; (2) determination of the location and length of the basement membrane in a *basement membrane image*; (3) detection of SSNF segments in an *SSNF image*; and (4) calculation of the median “*Source Extractor (SExtractor) detection rate*” for each biopsy. Upon completion of these steps, the CDM results are compared to the visual classification results for normalization and proper intercomparison—by converting from *SExtractor detection rate* to estimated *fiber density*—and for the assessment of the reliability of our method.

6.3.2.3. *Astronomical Tools*

In our CDM, we use analysis tools, such as software and computer languages, that are commonly used in the field of astronomy. These tools have been developed and optimized over time for image analysis, especially for detecting stars and small distant galaxies in a large field of view, which somewhat resemble the appearance of SSNF segments in a basement membrane. Since the majority of astronomical tools are developed primarily under the UNIX/Linux operating systems, all processes for this study are performed using Red Hat Linux[®] or the freely available Community

ENTerprise Operating System[®] (CentOS[®]). The astronomical tools used in this study are distributed with *no* or *at low cost*, and most of them can also be used with other operating systems, such as Microsoft Windows[®] or Macintosh[®]. Other tools, software, and computer languages could be substituted, given the preference of a CDM user.

Astronomical image-processing tools have been developed in the last three or four decades by the National Astronomical Observatories¹, and astronomers all over the world. New and improved astronomical software packages and tools are continuously under development as well. These image-processing tools currently consist of many large software packages, each with 2–4 million lines of code, and many hundreds of person-years of software development. The main tools and software used in this project are, amongst others, the Smithsonian Astrophysical Observatory Image DS9 (SAOImage DS9: Joye & Mandel 2003), the Flexible Image Transport System (FITS: Wells et al. 1981), the National Optical Astronomy Observatory (NOAO) Image Reduction and Analysis Facility (IRAF: Stefl 1990, and references therein), the Interactive Data Language (IDL[®]), the Source Extractor (SExtractor: Bertin & Arnouts 1996), SuperMongo (SM²), and FORTRAN 77 (F77). Most of these software packages and languages are distributed on the internet with low or no cost. Since these tools could be substituted by many other free software packages and languages, all of the CDM steps can be in principle constructed *without any major software cost*

¹National Optical Astronomy Observatory (NOAO): <http://www.noao.edu/>
 National Radio Astronomy Observatory (NRAO): <http://www.nrao.edu/>
 Space Telescope Science Institute (STScI): <http://www.stsci.edu/>

²The SM Reference Manual. Robert H. Lupton and Patricia Monger (1977):
<http://www.astro.princeton.edu/~rhl/sm/sm.html>
<http://www.supermongo.net/>

to the user. In this chapter, we present one well tested implementation of this CDM for detection of SSNFs in the human basement membranes..

6.3.3. *Post-Digitized Image Preparation*

In this section, we give a high level review of all the necessary steps of the CDM. Readers not interested in the high level steps may directly proceed to Section 6.3.4, or even to Section 6.4.

6.3.3.1. *Image Format Conversion*

The first step in the image preparation is converting the image file format as it arrives from the LSCM. While the original layer-images obtained with the LSCM are saved in the Tagged Image File Format (TIFF), the image-displaying software, DS9, and *all* subsequent software requires the FITS image format. To convert the file format, a pre-written F77 program with a sequence of various Linux commands and IRAF tasks is used. Once an original TIFF image is read in by this program, the signal (original image data) is recorded in one of the Red–Green–Blue (RGB) channels of the portable anymap (PNM) format image, which are then separated into three independent PNM image files. Using IRAF tasks, the image file containing the data is saved into a FITS image. As a result of this file format conversion, originally green- and red-colored TIFF images for the basement membrane and SSNFs are converted into gray-scale images as shown in Figures 58–60. During this format conversion, the original signals are rounded into integer values in units of Data Numbers (DNs), with the lowest value set to zero. To avoid a systematic error due to this zero-signal, a value of 1.0 DN is added to all pixels. Since the immunostained basement membrane

and the SSNFs have large signal values ($\gtrsim 1000$ DN), adding 1.0 DN does not affect the final results.

While it would take a long time if all of these processes are performed manually, this pre-programed image conversion only takes a fraction of a second for an image on modern computers.

6.3.3.2. *Stacking Layer-Images and Smoothing the Basement Membrane Image*

The SSNFs are running through a basement membrane and surrounding tissue not two-dimensionally, but three-dimensionally. A single layer-image therefore cannot capture an entire SSNF, unless it happens to exactly line up with the scanning focal plane of the LSCM. By imaging at 32 different depths of a biopsy section for a single scan, and by stacking these layer-images, we ensure that SSNFs are imaged. Stacking these 32 layer-images also helps the CDM detection software by enhancing the total signal-to-noise (S/N) level of the basement membrane and of SSNFs. The second step in the preparation therefore includes: (1) stacking all the basement membrane and SSNF layer-images from a single scan; and (2) smoothing the stacked basement membrane image (see Figure 58). The stacked SSNF image requires several more steps in this preparation, and hence they are treated separately in the following steps (Section 6.3.3.3).

The first process is to stack all of the layer-images into a single image using an F77 program. Once a computer disk path to a single scan is provided, this program creates a new sub-folder and the necessary files for subsequent analysis. The number of layer-images to be combined is set to 32 for our CDM, but this number can be

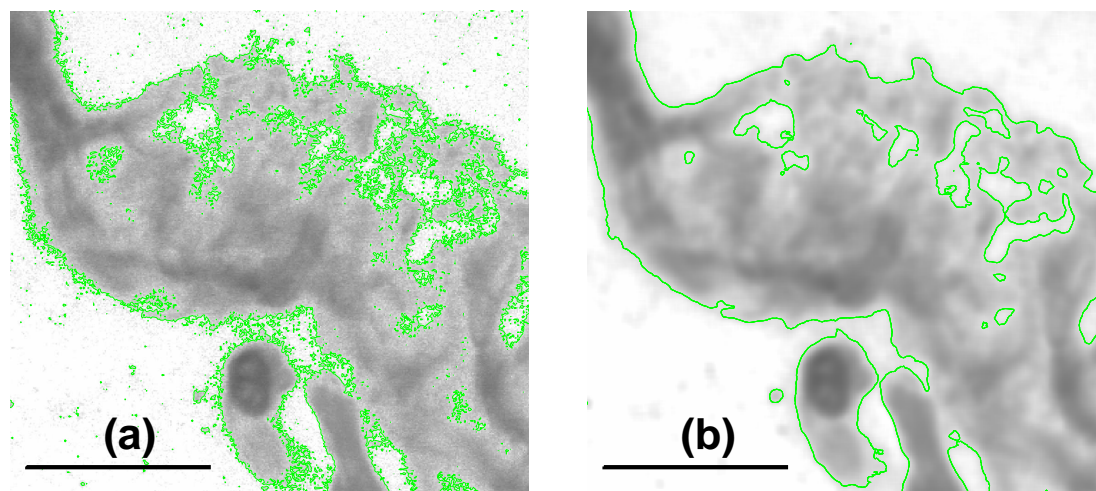


Figure 58. Zoomed-in images of an example basement membrane: (a) without smoothing (i.e., an untreated stack of 32 layer-images of a single scan of a biopsy); and (b) with smoothing applied. In the visualization software (DS9), the darker gray indicates the stronger signal. In both panels, green-colored contours are drawn at the same signal level of 130 DN. While the edge of basement membrane is untraceable by the graininess of the original image (panel (a)), this effect is removed in the smoothed image (panel (b)), making the edges of basement membrane easily traceable. Scale bars at the bottom-left indicate 0.02 mm.

changed with a few easy modifications to the program if necessary. To actually stack the layer-images, the IRAF executable file created by the F77 program has to be run in the directory where the IRAF parameter file is stored (usually at the top working directory). Once this script has run, IRAF automatically starts up and stacks the 32 layer-images to create a single basement membrane image and a single SSNF image. During this process, 3σ -clipping—where σ stands for the standard deviation of the image noise—is applied to remove any hot or bad pixels. These pixels usually have extremely high or low values due to spontaneous electrical effects of a photodetector, e.g., photomultiplier tubes (PMTs) or Charge-Coupled Devices (CCDs), used in the LSCM, and would cause a systematic error in the subsequent analysis.

The next process is to outline the basement membrane in the stacked image. Figure 58(a) shows the stacked basement membrane image without any treatment (i.e., smoothing), with green-colored contours drawn at a signal level of 130.0 DN. Without smoothing, the perimeter contours outlining the basement membrane have jagged edges, which will cause errors in subsequent SSNF detection at the edges of the basement membrane. Since the inner and outer edges of the basement membrane should be ideally outlined by rather simple contours, we smooth the stacked basement membrane image to remove this graininess. Figure 58(b) shows the smoothed image of Figure 58(a), with the green-colored contours applied to the same signal level of 130.0 DN. While the original image (Figure 58(a)) has a slightly sharper appearance, the edges in the smoothed image (Figure 58(b)) are much easier to trace and visualize. Another important effect of smoothing is that it softens and removes, or shrink the regions of slightly lower signals within a basement membrane. Without any treatment, these low-signal regions appear as small “bubbles” along edges or inside of basement membrane (see Figure 58(a)), and would affect the final results. In the same IRAF script to stack layer-images, another IRAF task—BOXCAR with a box-size of 7 pixels—is therefore used to smooth the stacked basement membrane image.

As in the previous step, stacking multiple images, creating folders and files, and smoothing the stacked basement membrane image only take at most a few seconds on a ~ 2 GHz Linux box.

6.3.3.3. Preparation of the SSNF Images

The final step is to prepare the stacked SSNF image. This step involves: (1) the treatment of the large flat-signal regions; and (2) the application of *unsharp masking* to the SSNF image.

The critical issue with the original (untreated) stacked SSNF image (Figure 59(a)) is that the lightest gray-colored regions in the background have a noiseless, flat-signal level of 32.0 DN, due to the simple stacking of 32 layer-images with 1.0 DN in these regions. If an area with a flat-signal is relatively small, the subsequent processes will not be affected. In most of stacked SSNF images, however, these regions usually extend over a significant fraction of an image (e.g., see Figure 60). Since the SExtractor code uses the signal statistics of an entire image, a large region with a constant value has to be removed or modified. Without any treatment, these extended flat-signal regions would cause systematic errors in the automated object detection by SExtractor in the subsequent analysis. The optimal and easiest solution to this issue is to add a small Gaussian noise-field to the entire image, which simulates the regular electronic noise in CCD images.

To create a simulated noise image, the IDL random number generator function, `RANDOMN`, is used, which creates floating-point numbers in any specified multi-dimensional vector or matrix. In our study, we create a set of random values in a two-dimensional matrix, corresponding to the same size as LSCM scanned images. The values originally created have a Gaussian distribution with a mean of 0.0 and a standard deviation of 1.0. To simulate the low-level noise of a CCD image, this initial

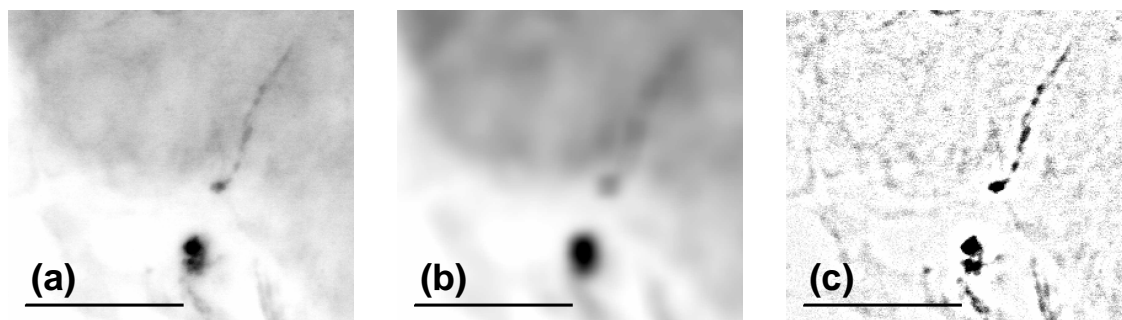


Figure 59. Zoomed-in images of an example SSNF: (a) without any treatment (i.e., no smoothing nor unsharp masking was applied); (b) with smoothing applied; and (c) with unsharp masking applied (i.e., smoothed image (panel (b)) is subtracted from the (noise-added) stacked image (panel (a))). As for the basement membrane images (Figure 58), the original red-immunostained images are converted into a gray-scale image. The technique of unsharp masking enhances the signals of SSNFs in small structures within an image (panel (c)). Scale bars at the bottom-left indicate 0.02 mm.

noise matrix is multiplied by a factor of 25.0, which is determined from the signal statistics of SSNF images to be about optimal. Once the noise matrix is saved as a FITS image, IRAF is used to linearly add this noise image to stacked SSNF images.

The SSNF images have another significant issue to be solved. The cause of this problem stems from the relatively strong signal regions of immunostained tissues other than SSNFs. These regions affect the image statistics, and may cause the under-detection of SSNF segments by SExtractor. Since these non-SSNF tissues usually have physically larger appearances than SSNFs, “*unsharp masking*” is used to remove these larger structures from the SSNF images. Removing these large-scale, high S/N structures ensures a much improved detection of the SSNF segments. *Unsharp masking* is a technique commonly used to sharpen digital images in many different fields. In signal processing jargon, it optimally separates the high spatial-resolution structures from the low resolution ones. For the current project, this technique is used

to bring out higher contrast of the small-scale structures, specifically the SSNFs. The Gaussian noise-added SSNF image is smoothed with the same IRAF task applied to the basement membrane images earlier, with a box-size of 9 pixels. Figure 59(b) shows the smoothed version of Figure 59(a), where large-scale structures remain, and small-scale structures are diluted or faded away. The smoothed image is then subtracted from the noise-added, unsmoothed image. The final image (Figure 59(c)) shows that after the *unsharp masking* process, the small-scale structures are now much more clearly recognizable. One caution about unsharp masking is that the smoothing box-size has to be adjusted, based on the apparent size of SSNFs and other non-SSNF structures. The SSNFs will be subtracted out if the smoothing box-size is too small. On the other hand, some non-SSNF structures will remain if the box-size is too large.

Since all the steps described above are pre-determined, and all the necessary parameter values are already written inside the programs and codes, using the CDM does not only reduce the time for processing, but also significantly reduces the chance of making mistakes.

6.3.4. Analysis

6.3.4.1. Determining the Basement Membrane

The first step in the analysis is identifying the basement membrane using the smoothed basement membrane image (Figure 58(b)). DS9 is used to display and interact with the image. The contour level is adjusted manually, and DS9 automatically fits the contours to the entire image. Figures 58(b) and 60(a) show how nice smooth contours are fitted to the basement membrane, as well as to some regions

other than the basement membrane. While the green-colored contours are saved as a DS9 formatted contour-file (with a file extension “.con”), the actual contour level, indicated by a single value, is saved in a separate file to be read in by the subsequent program. At this point, if we do not distinguish the basement membrane from other regions marked by spurious contours, the subsequent program will detect any high S/N features (e.g., blood vessels) that still exist within the corresponding regions in the SSNF image. To exclude these spurious contours from subsequent analysis, black rectangular boxes are drawn around them as seen in Figure 60(a), and saved into a DS9 formatted region-file (with a file extension “.reg”).

Once the basement membrane is identified, blue line segments are fitted along the ridge of the basement membrane (see Figure 60(a)), and saved into another region-file. These line segments are used to measure the length of a basement membrane, which is used later on to calculate the SExtractor detection rate. An important step before tracing the basement membrane with these line segments is that all of the previous markings (i.e., black boxes) must be deleted from the DS9 image. If any markings other than blue-colored line segments are left in the image, these will cause an error in subsequent analysis due to difference in the DS9 region-shape. Contours, which are treated differently from the box- or line-markings by DS9—and hence reside in a different file format—can be left overplotted in the basement membrane image during this process.

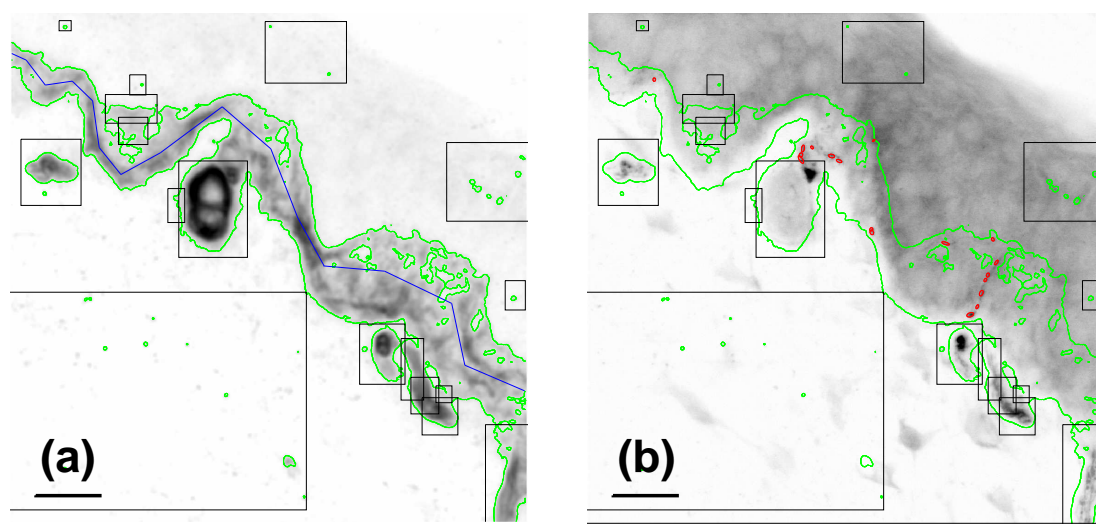


Figure 60. The final set of: (a) the basement membrane image; and (b) the SSNF image, with marked regions relevant to each image overlaid. In panel (a), green contours outline the basement membrane (and other strong signal regions), black rectangular boxes exclude the spurious contours, and blue line-segments are used to measure the length of the basement membrane. In panel (b), red ovals indicate SExtractor detections of SSNF segments, and green contours and black boxes are the same as in panel (a). Scale bars at the bottom-left indicate 0.02 mm.

6.3.4.2. *Detecting SSNF Segments*

SExtractor is used on the unsharp masked SSNF image (Figure 59(c)) to detect SSNF segments. The critical difference between the visual measurement and the CDM is how SSNFs are recognized in an image. While a single SSNF is observed as “*one SSNF*” by a visual observer, SExtractor usually detects “*multiple segments*” of an SSNF. This results in a chain of SExtractor detections for a single SSNF (e.g., red ovals in Figure 60(b)). A total number of SExtractor detections therefore not only depends on how many SSNFs are physically present in a basement membrane, but also depends on how long each SSNF is within a basement membrane. We will come back to this issue in a later section, where we compare the CDM results to the visual results, and apply the appropriate normalization to the CDM results.

Because SExtractor scans the entire image, SExtractor detections are generally distributed all over the image. An IDL program is therefore used to select the SExtractor detections inside the basement membrane. This program reads in: (1) the smoothed basement membrane image; (2) the saved contour level for the basement membrane; (3) the SExtractor detection results; and (4) the region-file of exclusion regions. The coordinates of the applied contours, exclusion regions, and SExtractor detections are compared, and the final SSNF segment candidates are saved into a new DS9 format region-file. A separate file with a simple numerical summary of the final SExtractor detections is also created. Figure 60 shows a final basement membrane image (Figure 60(a)) and a final SSNF image (Figure 60(b)), with all the related markings overplotted. Figure 60(b) shows the SExtractor detections as a

chain of small red-colored ovals, with green contours and black exclusion boxes from the basement membrane image (Figure 60(a)).

At this point in the CDM process, the selected SExtractor detections should be checked visually. It is possible that some spurious SExtractor detections are left inside a basement membrane, or visible SSNFs are significantly under-detected. In these cases, the CDM processes have to be repeated with adjusted SExtractor parameters and locations of exclusion boxes until a satisfactory result is achieved. It is also important to re-analyze all scans from the same biopsy previously processed with the new SExtractor parameters. Since all images from a single biopsy is scanned at a “fixed” LSCM settings, this helps to keep the personal bias by a CDM user to a minimum.

6.3.4.3. *Calculating the SExtractor Detection Rate*

After reasonable SExtractor detections are obtained for a set of SSNF images from a single biopsy, the final step in the CDM analysis is to calculate the SExtractor detection rate. The calculation program, written in F77, reads in files containing a number of SExtractor detections and the length—region-file of fitted blue line segments—of the basement membrane for each scan. Provided with the LSCM image scale of $0.0001551 \text{ mm pixel}^{-1}$, the SExtractor detection rate is calculated in units of “detections mm^{-1} ”, and the median value of all scans is selected as the representative detection rate of a given biopsy. While a “mean with σ -clipping” statistic could provide a slightly more accurate representative detection rate, this is better applicable if there exists a large number of scans for a single skin-biopsy, or if a scatter in measure-

ments is small. Since a typical biopsy has only ~ 6 – 8 scans, and with a large scatter in measured SExtractor detection rates, the median is a more sensible representative value than a σ -clipped mean. Especially in the early-phase (see Section 6.4.2), and in the pre-early project phase—when the CDM was in development—a systematic error due to the specific LSCM settings could cause a large scatter in the SExtractor detection rates among the scans for a single biopsy.

A file containing this result is then read by an SM script for plotting as shown in Figure 61(a). This figure—along with Figure 61(b)—is recreated in IDL for the consistency of figure styles. Figure 61(a) shows the results of all scans for a single biopsy. The black dashed-line indicates the median SExtractor detection rate ($\rho_{\text{median}} = 53.97$ detections mm^{-1}) for this particular biopsy. The error for the representative detection rate (± 13.30 detections mm^{-1}) is the standard error in the distribution for a median. The brown dotted-line—which is added at the time of re-creating this figure in IDL—indicates a σ -clipped mean at $\rho_{\text{mean}} = 50.06$ detections mm^{-1} with a standard deviation of 20.31 detections mm^{-1} . This σ -clipped mean value is currently not used as a part of the CDM. Since a σ -clipped mean does provide more accurate representative SSNF densities for visual classifiers, the σ -clipped mean of the SExtractor detection rate is added for comparison to the visual SSNF densities.

Finally, another SM script is used to plot the representative SExtractor detection rates for the analyzed biopsies. Figure 61(b), which is recreated by IDL, shows the median (black asterisks) and σ -clipped mean (brown diamonds) of the SExtractor detection rates for the 52 biopsies, which are used for the comparison to the visual

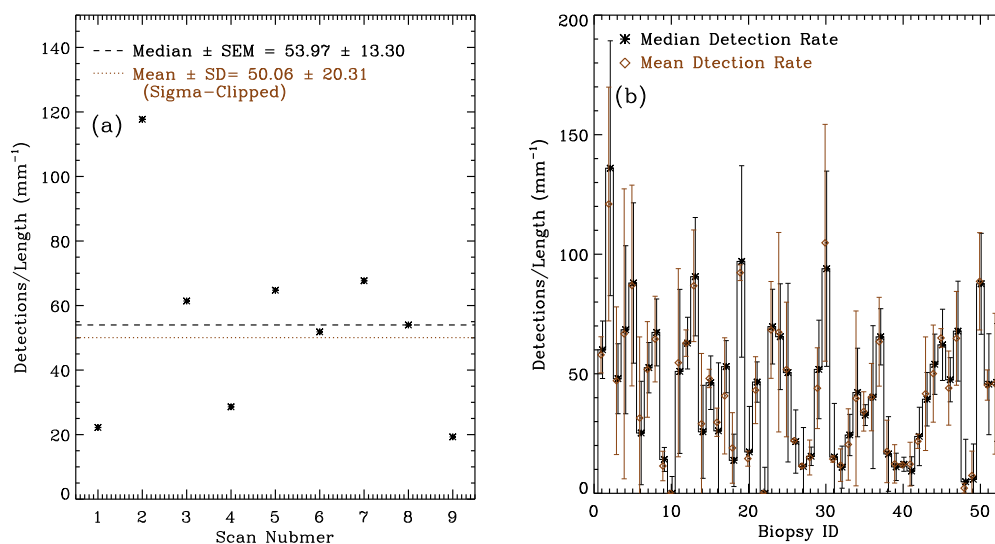


Figure 61. The pre-normalized results of the CDM are shown. Panel (a) shows the result for a single biopsy with a total of 9 scans. The horizontal black dashed-line indicates the *median* SExtractor detection rate, and the horizontal brown dotted-line indicates the σ -clipped mean SExtractor detection rate. The error for the median is the standard error of the median (SEM), and the error of the σ -clipped mean is the standard deviation (σ) over the 9 scans. Panel (b) shows the results of 52 biopsies. The black asterisks are the median detection rates, and the brown diamonds are σ -clipped mean detection rates, with corresponding errors as described in panel (a).

results in later section (Section 6.4). While a few SExtractor detection densities are different by ~ 15 detections mm^{-1} , most of the biopsy's median and σ -clipped mean values are very similar. Hence, the σ -clipped mean of SExtractor detection rates can be compared to the σ -clipped mean of the visual SSNF densities.

One difference from the original SM plot—as a part of the CDM technique—is that while the original SM plot differentiates the biopsies from forearm and from thigh, this differentiation is removed from the recreated IDL plot (Figure 61(b)). Since the main goal of this study is to examine the correlation between the CDM results and visual classification densities, studying any correlation between the SExtractor detection rates and these body parts is beyond the scope of this study. Also, to reduce the prejudice and personal bias by knowing the degree of disease of each volunteer subject (and hence of each biopsy), this information is not provided to the visual and CDM classifiers at this time. A detailed study of relationships among the SExtractor detection rates, the body parts, and the degree of disease are therefore deferred to a subsequent study.

The representative SExtractor detection rate ranges from 0.0 detection mm^{-1} up to ~ 140 detections mm^{-1} . Assuming that the segmentation by SExtractor is affecting all SSNFs equally, the SExtractor detection rate should in general increase as a physical SSNF density increases. Yet, without knowing the results from visual classifiers, we cannot assess how reasonable the CDM results are to the actual SSNF densities.

6.4. Results

While the CDM technique was developed and applied, no communication of the results between the CDM and visual classifiers was permitted to avoid any prejudice. To study how our CDM results are related to the actual SSNF density, we will now proceed to compare our results to those from the four expert visual classifiers. In this section, we first have to ensure that the results of visual classifiers are in agreement. Once this agreement is confirmed, the mean visual SSNF densities can be compared to the CDM results. A conversion factor, or formula, from the SExtractor detection rate to the estimated SSNF density are then determined to assess our results and the effect of the CDM on the measured SSNF densities.

6.4.1. *Visual Classification Results*

Figure 62(a) shows the results from four different visual classifiers. A σ -clipped mean and its standard deviation are used to show the measured visual SSNF densities. The results of the first visual classifier (blue asterisks) are also plotted as a light-blue bar-graph for easy visualization of which biopsy number is displayed. Except for a few biopsies, most visual classifiers agree with each other within the range of the rms errors. When calculating the representative density of all four visual classifiers for a single biopsy, we simply used the mean over all visual classifiers. These final representative visual densities are plotted with orange triangles in Figure 62(b), with orange shaded bar-graph for better visualization. The error bars for mean visual densities represent the mean standard deviations of all visual classifiers.

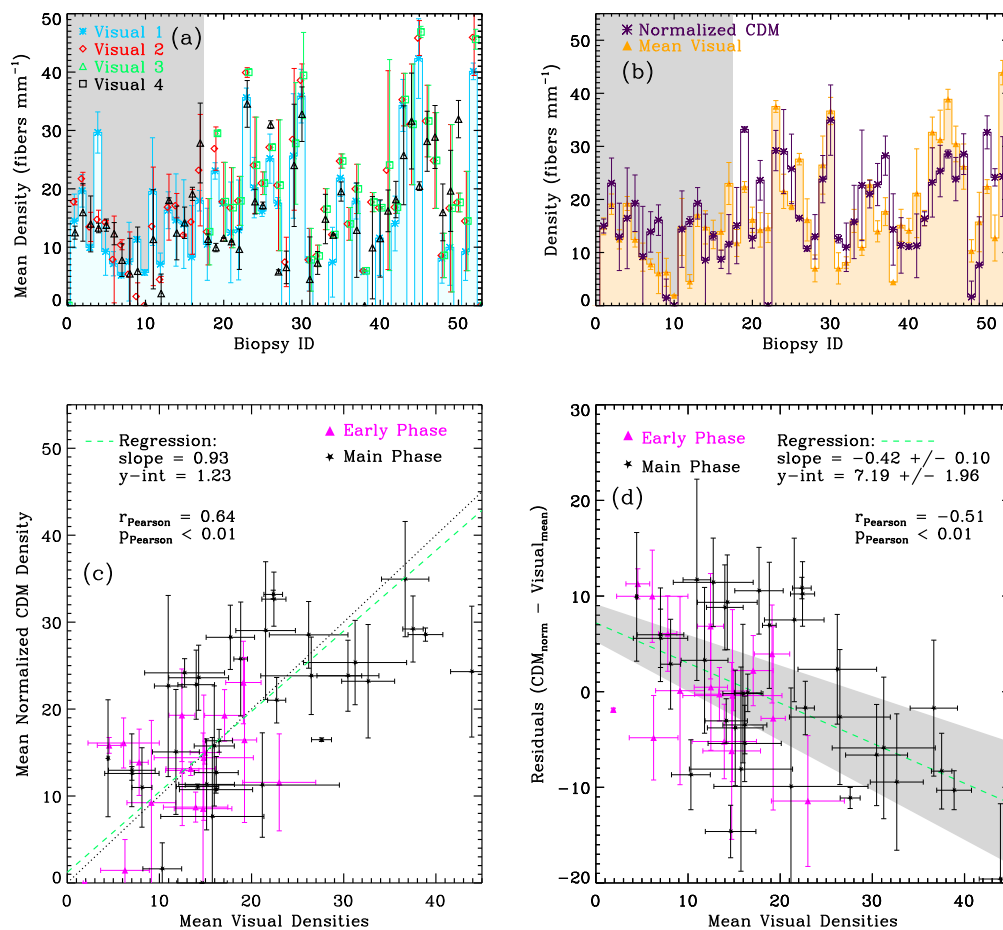


Figure 62. Comparisons of the measured SSNF densities between visual classifiers and the normalized CDM. (a) A comparison among visual classifiers. The first 17 biopsies (with a shaded background) are from the early-phase, and the other biopsies (without shaded background) are from the main-phase of this project. Different colors and symbols (blue asterisks, red diamonds, green triangles, and black squares) represent the four different visual classifiers. (b) A comparison between the *mean* visual densities (orange triangles) and the *normalized* mean CDM densities (purple asterisks). (c) A direct comparison between the *mean* visual and the *normalized* mean CDM densities. The black dotted-line represents the ideal one-to-one correlation ($x = y$) and the green dashed-line represents the best-fit regression. The pink triangles and black stars are from the early- and main-phase of the project, respectively. (d) The residuals between the normalized CDM and mean visual densities. The green dashed-line show the best-fit regression line, and the shaded region represents the 1σ distribution around the regression line through the residuals. Error bar in all panels represent the standard error of the mean.

6.4.2. Normalization of the CDM Results

To compare the SExtractor detection rates to the visual SSNF densities, a normalization has to be applied to the original CDM results. As mentioned earlier, there is no single constant, or a defined formula, to convert the segmented SExtractor detection rate into an SSNF density. Instead, the amount of segmentation increases as the length of a nerve fiber inside a basement membrane becomes longer. For a single SSNF, the number of SExtractor detections can be only equal to 1 if the apparent length of an SSNF is really short, or it can be up to $\gg 10$ if this length is much longer. In other words, the normalization of the SExtractor detection rate depends on the CDM result itself.

Before determining this normalization, there is one important issue that requires attention. In the course of this study, the settings of the LSCM has been changed in the Summer of 2005. Earlier biopsies with $ID \leq 17$ (indicated by a gray background shading in Figures 62(a) and (b)) were scanned with the LSCM before this date, and biopsies with $ID \geq 18$ (with no background shading in the same figures) were scanned after that date. We define these two groups as the “*early-phase*” and the “*main-phase*” of this study. In the *early-phase*, the images were scanned at lower PMT levels than during the *main-phase*. This effect is clearly visible when the CDM results in Figure 61(b) and the visual densities in Figures 62(a) and (b) are compared. The CDM results are relatively consistent over both phases in Figure 61(b), or the early-phase have somewhat larger average detection rate. On the other hand, Figures 62(a) and (b) show that the biopsies in the early-phase have, on

average, smaller visual densities than those in the main-phase biopsies. We therefore have to apply two different normalizations to each phase, since it is clear that the two different PMT settings caused this difference.

To determine a normalization formula, we plot another figure of (normalization-in-process) CDM densities vs. mean visual densities (not shown here but similar to Figure 62(c)), while various normalizations are being examined. The normalization is applied such that the SExtractor detection rate becomes an indicator of the SSNF density. The normalized CDM densities therefore should have one-to-one relation with the mean visual SSNF densities in the ideal case. We first plot regression lines—determined by the IDL function `ROBUST_LINEFIT` with the “bisect” option enabled—through datapoints for: (1) the early-phase biopsies (pink triangles in Figure 62(c)); (2) the main-phase biopsies (black stars in Figure 62(c)); and (3) all 52 biopsies. We then adjust the coefficient, power, and constant of each term in the normalization formula for both the early- and main-phases until all three regression slopes and y-intercepts become as close to 1.0 and 0.0 as possible, respectively. Figure 62(c) shows the final regression line (green dashed-line) for *all* biopsies with a slope of $m = 0.93$ and y-intercept of $b = 1.23$. The black dotted-line in Figure 62(c) shows the ideal one-to-one regression with a slope of 1.0 and y-intercept of 0.0. The two lines are within the statistical errors and indistinguishable.

The normalization formula applied for the main-phase is

$$\rho_{\text{CDM,norm}} = 1.4 \times [\ln(\rho_{\text{CDM,orig}})]^2 + \ln(\rho_{\text{CDM,orig}}), \quad (6.1)$$

and that for the early-phase is

$$\rho_{\text{CDM,norm}} = 1.1 \times [\ln(\rho_{\text{CDM,orig}})]^2 + 1.2 \times \ln(\rho_{\text{CDM,orig}}) - 8.0, \quad (6.2)$$

where $\rho_{\text{CDM,norm}}$ is the normalized SExtractor detection rate (a converted CDM SSNF density), $\rho_{\text{CDM,orig}}$ is the original SExtractor detection rate, and “ln” stands for the natural logarithm. Since a logarithm of 0.0 will cause an arithmetic error, any representative SExtractor detection rate of 0.0 is replaced with 1.0 detections mm^{-1} , which is not affecting the results given the statistical errors in Figure 62(c). Any resulting normalized $\rho_{\text{CDM,norm}}$ with the negative values ($\rho_{\text{CDM,norm}} < 0.0$)—which is unrealistic for any SSNF density, and due to the original SExtractor detection rate being equal to 0.0—are automatically replaced by 0.0 fibers mm^{-1} in the normalization process.

6.4.3. Comparison to the Visual Densities

Figures 62(b)–(d) shows the comparisons of normalized CDM densities to the mean of σ -clipped visual densities. Figure 62(b) shows the mean visual densities (orange triangle) and the normalized CDM densities (purple asterisks). Even though there are relatively large differences between the CDM and visual densities, a trend toward larger CDM densities for larger visual densities, and toward smaller CDM densities for smaller visual densities can be clearly recognized in this diagram. Figure 62(b) also shows that, even though the pre-normalized CDM results for the early-phase have larger SExtractor detection densities than the main-phase in general (see Figure 61(b)), the applied normalization (Equation 6.2) clearly reduces the normalized CDM densities to levels comparable with the visual SSNF densities.

To better visualize and analyze the correlation between the normalized CDM and the visual classification results, a direct comparison between these two quantities is plotted in Figure 62(c). Pink triangles represent the early-phase biopsies, and black stars represent the main-phase biopsies. Error bars are the standard deviations calculated from all scans for each biopsy.

The calculated Pearson correlation coefficient for the distribution in Figure 62(c) is $r_{\text{Pearson}} = 0.64$ with a p -value of $p_{\text{Pearson}} < 0.01$. In all of our statistics, we select $p = 0.05$ as the minimum threshold for significance. The $p_{\text{Pearson}} < 0.01$ therefore indicates that the mean visual densities and the normalized CDM densities are indeed correlated, yet as can be seen in Figure 62(c), with a large scatter. The cause of this scatter is discussed in detail in the following section. We also performed a two-tailed, paired, Student's t -test to see if their measurements are significantly different from each other. The calculated p -value for this t -test is $p_{t\text{-test}} > 0.05$, indicating that the two densities are non-significantly different. Combining these statistics, and the regression and y-intercept of 0.93 and 1.23, respectively, we conclude that the normalized CDM and the mean visual densities are not significantly different, and hence comparable to each other, as the best-fitted green dashed regression line and the black dotted $y = x$ line in Figure 62(c) already indicated.

Figure 62(d) shows the *residuals* between the normalized CDM and the mean visual classification densities, compared to the mean visual densities. The early-phase biopsies and the main-phase biopsies are represented using the same symbols and colors as in Figure 62(c). The best-fit regression line (green dashed-line) has

a slope of -0.42 ± 0.10 and y-intercept of 7.19 ± 1.96 , with the gray-shaded region represents the 1σ distribution around the regression line. The Pearson correlation coefficient is $r_{\text{Pearson}} = -0.51$, and the p -value associated with this Pearson correlation is $p_{\text{Pearson}} < 0.01$. Therefore, this negative correlation is a true feature. While the regression between the normalized CDM and the mean visual densities is ~ 1.0 (see Figure 62c), a negative correlation for these residuals (see Figure 62(d)) indicates that the CDM tends to somewhat over-estimate the SSNF density for low mean visual densities, and somewhat under-estimate the SSNF density for higher mean visual densities. Even though Figure 62(c) indicates that there is in general good agreement between the normalized CDM and mean visual densities, Figure 62(d) shows that there are still some systematic effects between the CDM detections and the visual classifications.

6.5. Discussion

Although the normalized CDM densities and the mean visual classification densities show a fair correlation, there is still a fairly large scatter in Figures 62(c) and (d). This scatter is caused by the different nature of the CDM detection method, i.e., the segmentation by SExtractor, as compared to the visual classification method, *and* due to several important factors of the images themselves. The object segmentation by SExtractor has already been described in Section 6.3.4.2. Another important cause for the discrepancy between the two methods is the visibility—the PMT or the S/N level—of the SSNFs in the stacked SSNF images, as described in Section 6.4.2. Detecting SSNFs by eye, as performed by the visual classifiers, requires SSNFs to

have much stronger signals than other tissue structures surrounding the SSNFs. In other words, the visual classification method requires an absolutely high-signal level. The CDM, on the other hand, uses the SSNF signal relative to the image noise, i.e., the S/N level, allowing SSNF segments to be detected even if the strongest signals are not available. The unsharp masking technique helps the CDM detection by enhancing the S/N ratio in the SSNFs, and therefore their detection levels. Even though some SSNFs are difficult to recognize by eye, the CDM is therefore able to detect SSNFs at a lower (absolute) signal level. The physical size of the image may also be an important factor in the visual classification method. The image size in the early-phase was half the size of that in the main-phase, making small and narrow SSNFs appear even smaller and narrower in an early-phase image. The CDM, on the other hand, is able to detect small SSNF segments—even though their apparent image size is small—as long as an SSNF segment is satisfying the SExtractor parameters.

Along with the segmented detection of SSNFs by SExtractor, another possible cause of scatter is the orientation of the SSNFs within a basement membrane relative to the plane of the scanned image. The image has physical dimensions of $\sim 0.16 \text{ mm} \times 0.16 \text{ mm}$, and a depth of $\sim 0.04 \text{ mm}$, which is converted to a two-dimensional image of $\sim 0.16 \text{ mm} \times 0.16 \text{ mm}$. An SSNF running along the plane of the image therefore appears as a long fiber, and is detected both by SExtractor and by eye without any problem. On the other hand, some SSNFs are running near-perpendicular, or in the z -direction of the biopsy section (see Figure 57). Such SSNFs appear short, or only as small oval shapes in extreme cases, and are most likely not

recognized by the visual classifiers. Since the SExtractor algorithm used by the CDM detects *any* small region, as long as it satisfies the provided minimum threshold parameters, these SSNFs running near-perpendicular to the plane of the image *are* in fact detected by SExtractor. These detections are shown in Figure 60(b), not as a chain of red ovals, but as isolated single or as a few connected red ovals.

Limitations to the measurement of the SSNF density not only occur with the visual classification method. Some SSNFs are not detected by the CDM, if they do not reach the required signal level by SExtractor. Furthermore, even though the CDM is semi-automated, its parameter values are still adjusted manually, and these parameters settings can be slightly different depending on a given CDM user. During this study, we observed that small differences ($\lesssim 10\%$) in the parameter values affect the final results only very slightly. This occurs, because the signal levels are generally much higher for the basement membrane and for the SSNFs, compared to other tissue structures after the smoothing and unsharp masking procedures.

The reduction of processing time, the significant independence of the user, and the nearly complete repeatability of the results are the significant advantages of the CDM, when compared to the visual classification method.

6.6. Conclusion

A computerized method of quantifying immunostained SSNF densities in the basement membrane of skin-biopsies is presented, using astronomical image-processing and object detection tools and software. The advantage of our method over other medical software is that the tools and software used in our CDM are distributed

without any cost, or at most with a minimum fee. There are also many other tools and software packages available to CDM users, which can be substituted, based on the preference of the user. The actual analysis using our specific implementation of the CDM involves: (1) preparation of the digitized skin-biopsy images; (2) determination of the location and length of the basement membrane; (3) automated detection of the SSNF segments; and (4) calculation of the segmented SSNF detection density in each biopsy.

The CDM also has significant advantages over the visual classification method. While some of the steps are time consuming if performed manually, using pre-written tasks and programs, most of the steps take only a fraction of a second on an average desktop computer. In addition to the reduction of the processing time, the CDM keeps the effects of personal prejudice, bias, and mistakes at a minimum level. Even though the CDM requires some manual input—such as determination of the contour level for a basement membrane and of the SExtractor parameters—small differences in these inputs have only a minimal effect on the final results. High repeatability, regardless of who or when the CDM is performed, is another major advantage. Other important aspects of the CDM are: (1) the CDM is based on the *relative* signal levels of SSNFs, instead of strong absolute signals required for the visual classification method; and (2) the CDM is capable of detecting visually hard-to-recognize SSNF, such as SSNFs running near-perpendicular to the plane of a skin-biopsy image.

Even though there is a fairly large scatter between the CDM and the visual classification results, this is due to the different nature of the two detection methods.

Considering these differences, we conclude that our CDM is detecting SSNFs in a reasonable manner. At this point, our CDM is not yet ready to fully replace the visual density measurements, but the CDM is at least able to support or confirm the visual classification results. With further studies and improvements to the CDM process—e.g., automated determination of whether two or more SExtractor detections are associated with the same SSNF—the CDM has the capability of eventually replacing the visual density measurement.

The current study shows that the CDM technique is dependable, and likely applicable to conventional studies of intraepidermal nerve fiber densities in normal and neuropathic populations. This topic will be addressed in more detail in a future study. Furthermore, our study proves that the CDM can effectively reduce the cost and time involved in detecting SSNFs, which are very important constraints when analyzing a very large number of medical images. In future, we will also pursue ways of reducing the systematic and random errors in the CDM, so as to further improve upon this method.

REFERENCES

- Abraham, R. G., Ellis, R. S., Fabian, A. C., Tanvir, N. R., & Glazebrook, K. 1999, MNRAS, 303, 641
- Anders, P., & Fritze-von Alvensleben, U. 2003, A&A, 401, 1063 (AF03)
- Arnouts, S., de Lapparent, V., Mathez, G., Mazure, A., Mellier, Y., Bertin, E., & Kruszewski, A. 1997, A&AS, 124, 163.
- Bachiller, R. C., & Cernicharo, J. 1986, A&A, 166, 283
- Barmby, P., et al. 2006, ApJ, 650, L45
- Bell, E. F. 2002a, ApJ, 577, 150
- Bell, E. F., Gordon, K. D., Kennicutt, R., C., & Zaritsky, D. 2002b, ApJ, 565, 994
- Bertelli, G., Bressan, A., Chiosi, C., Fagotto, F., & Nasi, E. 1994, A&AS, 106, 275
- Bertin, E., & Arnouts, S. 1996, A&AS, 117, 393
- Block, D. L., Buta, R., Knapen, J. H., Elmegreen, D. M., Elmegreen, B. G., & Puerari, I. 2004, AJ, 128, 183
- Block, D. L., & Purari, I. 1999, A&A, 342, 627
- Block, D. L., Puerari, I., Takamiya, M., Abraham, R., Stockton, A., Robson, I., & Holland, W. 2001, A&A, 371, 393
- Boissier, S., Boselli, A., Buat, V., Donas, J., Milliard, B. 2004, A&A, 424, 465
- Boissier, S., et al. 2005, ApJ, 619, L83
- Boissier, S., et al. 2007, ApJS, 173, 524
- Boselli, A., Gavazzi, G., & Sanvito, G. 2003, A&A, 402, 37
- Bothun, G. D. 1986, AJ, 91, 507
- Brown, R. L., Wild, W., & Cunningham, C. 2004, AdSpR, 34, 555
- Bruzual, G., & Charlot, S. 2003, MNRAS, 344, 1000
- Burstein, D., & Heiles, C. 1982, AJ, 87, 1165
- Buta, R., & Bock, D. L. 2001, ApJ, 550, 243
- Buat, V., & Xu, C. 1996, A&A, 306, 61
- Buat, V., et al. 2005, ApJ, 619, L51
- Burkey, J. M., Keel, W. C., Windhorst, R. A., & Franklin, B. E. 1994, ApJ, 429, L13

- Byun, Y.-I. 1992, Ph.D. thesis, Australian National University
- Calzetti, D., Armus, L., Bohlin, R. C., Kinney, A. L., Koornneef, J., & Storchi-Bergmann, T. 2000, *ApJ*, 533, 682
- Calzetti, D., Kinney, A., L., & Storchi-Bergmann, T. 1994, *ApJ*, 429, 582
- Calzetti, D., et al. 2005, *ApJ*, 633, 871
- Calzetti, D., et al. 2007, *ApJ*, 666, 870
- Caplan, J., & Deharveng, L. 1985, *A&AS*, 62, 63
- Caplan, J., & Deharveng, L. 1986, *A&A*, 155, 297
- Capozziello, S., Cardone, V. F., & Troisi, A. 2007, *MNRAS*, 375, 1423
- Cardelli, J. A., Clayton, G. C., & Mathis, J. 1989, *ApJ*, 345, 245
- Charlot, S., & Fall, S. M. 2000, *ApJ*, 539, 718
- Cohen, M., Wheaton, W., A., & Megeath, S., T. 2003, *AJ*, 126, 1090
- Conselice, C. J. 2006, *ApJ*, 638, 686
- Croton, D. J., et al. 2006, *MNRAS*, 365, 11
- Dale, D. A., Helou, G., Contursi, A. et al. 2001, *ApJ*, 549, 215
- Dalsgaard, C. J., Rydh, M., Haegerstrand, A. 1989, *Histochemistry*, 92, 385
- Deo, R. P., Crenshaw, D. M., & Kraemer, S. B. 2006, *AJ*, 132, 321
- de Vaucouleurs, G., de Vaucouleurs, A., Corwin, H. G., Buta, R. J., Paturel, G., & Fouque, P. 1991, *Third Reference Catalogue of Bright Galaxies* (Springer, New York)
- Dickman, R. L. 1978, *ApJS*, 37, 407
- Driver, S. P., Popescu, C. C., Tuffs, R. J., Graham, A. W., Liske, J., & Baldry, I. 2008, *ApJ*, 678, 101
- Driver, S. P., Windhorst, R. A., Ostrander, E. J., Keel, W. C., Griffiths, R. E., & Ratnatunga, K. U. 1995, *ApJ*, 449, L23
- Dyck, P. J., Oviatt, K. F., & Lambert, E. H. 1981, *Ann. Neurol.*, 10, 222
- Elmegreen, D. M. 1980, *ApJS*, 43, 37
- Elmegreen, D. M., Chromey, F. R., Bissell, B. A., & Corrado, K. 1999, *AJ*, 118, 2618

- Elvius, A. 1956, *StoAn*, 18, 9
- Emonts, B. H. C., Morganti, R., Oosterloo, T. A., Holt, J., Tadhunter, C. N., van der Hulst, J. M., Ojha, R., & Sadler, E. M. 2008, *MNRAS*, 387, 197
- Encrenaz, P. J., Falgarone, E., & Lucas, R. 1975, *A&A*, 44, 73
- Eskridge, P. B., et al. 2002, *ApJS*, 143, 73
- Eskridge, P. B., et al. 2003, *ApJ*, 586, 923
- Esipov, V. F., Kyazumov, G. A., & Dzhafarov, A. R. 1991, *SvA*, 35, 452
- Farrah, D., Afonso, J., Efstathiou, A., Rowan-Robinson, M., Fox, M., & Clements, D. 2003, *MNRAS*, 343, 585
- Fazio, G. G., et al. 2004, *ApJS*, 154, 10
- Fitzpatrick, E., L. 1999, *PASP*, 111, 63
- Frerking, M. A., Langer, W., D., & Wilson, R. W. 1982, *ApJ*, 262, 590
- Gil de Paz, A., et al. 2007, *ApJS*, 173, 185
- Gordon, K. D., Calzetti, D., & Witt, A., N. 1997, *ApJ*, 487, 625
- Gordon, K. D., Clayton, G. C., Misselt, K. A., Landolt, A. U., & Wolff, M. J. 2003, *ApJ*, 594, 279
- Goudfrooij, P., de Jong, T., Hansen, L., Norgaard-Nielsen, H. U. 1994a, *AJ*, 98, 538
- Goudfrooij, P., Hansen, L., Norgaard-Nielsen, H. U. 1994b, *MNRAS*, 271, 833
- Griffin, M., et al. 2007, *AdSpR*, 40, 612
- Gull, S. F., & Daniell, G. J. 1978, *Nature*, 272, 686
- Gull, S. F., & Daniell, G. J. 1979, *ASSL*, 76, 219
- Harjunpää, P., Lethinen, K., & Haikala, L. K. 2004, *A&A*, 421, 1087
- Harjunpää, P., & Mattila, K. 1996, *A&A*, 305, 920
- Hayakawa, T., Cambrésy, L., Onishi, T., Mizuno, A., & Fukui, Y. 2001, *PASJ*, 53, 1109
- Hayakawa, T., Mizuno, A., Onishi, T., Hara, A., Yamaguchi, R., & Fukui, Y. 1999, *PASJ*, 51, 919
- Heckman, T. M. 1980, *A&A*, 87, 152

- Helou, G., et al. 2004, *ApJS*, 154, 253
- Héraudeau, P., & Simien, F. 1996, *A&AS*, 118, 111
- Hirai, A., Yasuda, H., Joko, M., Maeda, T., Kikkawa, R. 2000, *J. Neurol. Sci.*, 172, 55
- Högbom, J. A. 1974, *A&AS*, 15, 417
- Holland, N. R., Crawford, T. O., Hauer, P., Cornblath, D. R., Griffin, J. W., & McArthur, J. C. 1998, *Ann. Neurol.*, 44, 47
- Holland, N. R., Stocks, A., Hauer, P., Cornblath, D. R., Griffin, J. W., & McArthur, J. C. 1997, *Neurology*, 48, 708
- Holwerda, B. W., Gonzalez, R. A., Allen, R. J., & van der Kruit, P. C. 2005, *AJ*, 129, 1396
- Holwerda, B. W., Keel, W. C., Williams, B., Dalcanton, J. J., & de Jong, R. S. 2009, *AJ*, 137, 3000
- Howarth, I. D. 1983, *MNRAS*, 203, 301
- Hubble, E. P. 1926, *ApJ*, 64, 321
- Huchra, J. P. 1977, *ApJS*, 35, 171
- Jansen, R. A., Knapen, J. H., Beckman, J. E., Peletier, R. F., & Hes, R. 1994, *MNRAS* 270, 373
- Joye, W. A., & Mandel, E. 2003, *Astronomical Data Analysis Software and Systems XII*, ASP Conf. Ser. 295. (Astronomical Society of the Pacific), 489
- Karachentsev, I. D. 1972, *Comm. Special Ap. Obs.*, 7, 1
- Karant, S. S., Springall, D. R., Kuhn, D. M., Levene, M. M., Polak, J. M. 1991, *Am. J. Anat.*, 191, 369
- Kaviraj, S., Rey, S.-C., Rich, R. M., Yoon, S.-J., & Yi, S. K. 2007a, *MNRAS*, 381, L74
- Kaviraj, S., et al. 2007b, *ApJS*, 173, 619
- Kennedy, W. R., & Wendelschafer-Crabb, G. 1993, *J. Neurol. Sci.*, 115, 184
- Kennedy, W. R., Wendelschafer-Crabb, G., Johnson, T. 1996, *Neurology*, 47, 1042
- Kennicutt, R. C., et al. 2003, *PASP*, 115, 928

- Kennicutt, R. C., et al. 2009, *ApJ*, 703,1672
- Knapen, J. H., Hes, R., Beckman, J. E., & Peletier, R. F. 1991, *A&A*, 241, 42
- Komatsu, E., et al. 2009, *ApJS*, 180, 330
- Komugi, S., Sofue, Y., Nakanishi, H., Onodera, S., & Egusa, F. 2005, *PASJ*, 57, 733
- Kong, X., Charlot, S., Brinchmann, C., & Fall, S. M. 2004, *MNRAS*, 349, 769
- Koornneef, J., & Code, A. D. 1981, *ApJ*, 247, 860
- Kotulla, R., Fritze, U., Weibacher, P., & Anders, P. 2009, *MNRAS*, 396, 462
- Kroupa, P. 2002, *Science*, 295, 82
- Lacomis, D. 2002, *Muscle and Nerve*, 26, 173
- Lanyon-Foster, M. M., Conselice, C. J., & Merrifield, M. R. 2007, *MNRAS*, 380, 571
- Leger, A., & Puget, J. L. 1984, *A&A*, 137, L5
- Lejeune, T., Cuisinier, F., & Buser, R. 1997, *A&AS*, 125, 229
- Lejeune, T., & Schaerer D. 2001, *A&A*, 366, 538
- Li, Z., & Han, Z. 2007, *A&A*, 471, 795
- Li, Z., & Han, Z. 2008, *MNRAS*, 385, 1270
- Lindblad, B. 1941, *StoAn*, 13, 8
- Maíz-Apellániz, J., Pérez, E., & Mas-Hesse, J. M. 2004, *AJ*, 128, 1196
- Malik, R. A., et al. 2005, *Diabetologia*, 48, 578
- Maraston, C. 2005, *MNRAS*, 362, 799
- Martin, D. C., et al. 2005, *ApJ*, 619, L1
- Martin, D. C., et al., 2007, *ApJS* 173, 356
- Martin, P. G., & Whittet, D. G. B. 1990, *ApJ*, 357, 113
- Mathis, J. S., Rumpl, W., & Nordsieck, K. H. 1977, *ApJ*, 217, 425
- McArthur, J. C., Stocks, E. A., Hauer, P., Cornblath, D. R., & Griffin, J. W. 1998, *Arch. Neurol.*, 55c 1513
- Meurer, G. R., Heckman, T. M., & Calzetti, D. 1999, *ApJ*, 521, 64

- Mihos, C. J., & Hernquist, L. 1994, *ApJ*, 427, 112
- Mihos, C. J., & Hernquist, L. 1996, *ApJ*, 464, 641
- Mill, J. D., et al. 1994, *J. of Spacecraft & Rockets*, 31, 900
- Moles, M., Sulentic, J. W., & Márquez, I. 1997, *ApJ*, 485, L69
- Morrissey, P., et al. 2005, *ApJ*, 619, L7
- Morrissey, P., et al. 2007, *ApJS*, 173, 682
- Mould, J. R., et al. 2000, *ApJ*, 529, 786
- Murray, N., Quataert, E., & Thompson, T. A. 2005, *ApJ*, 618, 569
- Neugebauer, G., et al. 1984, *ApJ*, 278, L1
- Neuschaefer, L. W., & Windhorst, R. A. 1995, *ApJS*, 96, 371
- Nilson, P. 1973, *Uppsala general catalogue of galaxies*, *Uppsala Obs. Ann.*, vol. 6
- Nitschelm, C. 1988, *A&AS*, 74, 67
- Odewahn, S. C., Windhorst, R. A., Driver, S. P., & Keel, W. C. 1996, *ApJ*, 472, L13
- Oke, J. B. 1974, *ApJS*, 27, 21
- Oke, J. B., & Gunn, J. E. 1983, *ApJ*, 266, 713
- Oosterloo, T. A., Morganti, R., Sadler, E. M., van der Hulst, T., & Serra, P. 2007a, *A&A*, 465, 787
- Oosterloo, T., Fraternali, F., & Sancisi, R. 2007b, *AJ*, 134, 1019
- Osterbrock, D. E. 1989, *Astrophysics of Gaseous Nebulae and Active Galactic Nuclei* (Mill Valley; University Science Books)
- Panuzzo, P., Bressan, A., Granato, G. L., Silva, L., & Danese, L. 2003, *A&A*, 409, 99
- Pascarelle, S. M., Windhorst, R. A., Keel, W. C., & Odewahn, S. C. 1996, *Nature*, 383, 45
- Periquet, M. I., et al. 1999, *Neurology*, 53, 1641
- Petersen, L., & Gammelgaard, P. 1997, *A&A*, 323, 697
- Pilbratt, G. L. 2004, *SPIE*, 5487, 401
- Pina, R. K., & Puetter, R. C. 1993, *PASP*, 105, 630

- Price, S. D., Carey, S. J., & Egan, M. P. 2002, *AdSpR*, 30, 2027
- Puetter, R. C. 1997, *Ann. N.Y. Acad. Sci.*, 808, 160
- Pustilnik, S. A., Kniazev, A. Y., & Pramskij, A. G 2005, *A&A*, 443, 91
- Quattrini, C., et al. 2007, *Diabetes*, 56, 2148
- Regan, M. W. 2000, *ApJ*, 541, 142
- Regan, M. W., & Mulchaey, J. S. 1999, *AJ*, 117, 2676
- Regan, M. W., et al. 2004, *ApJS*, 154, 204
- Relaño, M., Lisenfeld, U., Vilchez, J. M., & Battaner, E. 2006, *A&A*, 452, 413
- Rieke, G. H., & Lebofsky, M. J. 1985, *ApJ*, 288, 618
- Rieke, G. H., et al. 2004, *ApJS*, 154, 25
- Roussel, H., Gil de Paz, A., Seibert, M., Helou, G., Madore, B. F., & Martin, C. 2005, *ApJ*, 632, 227
- Rudy, R. J. 1984, *ApJ*, 284, 33
- Ryan, C. J., De Robertis, M. M., Virani, S., Laor, A., & Dawson, P. C. 2007, *ApJ*, 654, 799.
- Ryan, R. E., Cohen, S. H., Windhorst, R. A., & Silk, J. 2008, *ApJ*, 678, 751
- Salpeter, E. E. 1955, *ApJ*, 121, 161
- Scalo, J. M. 1986, *Fundam. Cosm. Phys.*, 11, 1
- Schlegel, D. J., Finkbeiner, D. P., & Davis, M. 1998, *ApJ*, 500, 525
- Scoville, N. Z., et al. 2000, *AJ*, 119, 991
- Scoville, N. Z., Polletta, M., Ewald, S., Stolovy, S. R., Thompson, R., & Rieke, M. 2001, *AJ*, 122, 3017
- Seaton, M. J. 1979, *MNRAS*, 187, 73
- Seiger, M. S., Block, D. L., Puerari, I., Chorney, N. E., & James, P. A. 2005, *MNRAS*, 359, 1065
- Sirianni, M., et al. 2005, *PASP*, 117, 1049
- Skrutskie, M. F., Cutri, R. M., Stiening, R., et al. 2006, *AJ*, 131, 1163

- Smith, A. G., Howard, J. R., Kroll, R., Hauer, P., Singleton, J. R., & McArthur, J. 2005, *J. Neurol. Sci.*, 228, 65
- Smith, A. G., & Singleton, J. R. 2006, *J. Neurol. Sci.*, 242, 9
- Sosa-Brito, R. M., Tacconi-Garman, L. E., Lehnert, M. D., & Gallimore, J. F. 2001, *ApJS*, 136, 61
- Steff S. CoSka, 1990, 20, 161
- Sumner, C. J., Sheth, S., Griffin, J. W., Cornblath, D. R., & Polydefkis, M. 2003, *Neurology*, 60, 108
- Tamura, K., Jansen, R. A., & Windhorst, R. A. 2009, *AJ*, in press, (arXiv:0909.4813)
- Taylor, V. A., Jansen, R. A., Windhorst, R. A., Odewahn, S. C., & Hibbard, J., E. 2005, *ApJ*, 630, 784
- Taylor-Mager, V. A., Conselice C. J., Windhorst, R. A., & Jansen, R. A. 2007, *ApJ*, 659, 162
- Toomre, A. 1977, in *The Evolution of Galaxies and Stellar Populations*, ed. B. M. Tinsley and R. B. Larson (New Haven: Yale University Observatory), p. 401
- Trauger, J. T., et al. 1994, *ApJ*, 435, L3
- Trewhella, M. 1998, *MNRAS*, 297, 807
- Trumpler, R. J. 1930, *PASP*, 42, 214
- Tyson, J. A. 1988, *AJ*, 96, 1
- Vanden Berk, D. E., et al. 2001, *AJ*, 122, 549
- Van Dokkum, P. G., & Franx, M. 1995, *AJ*, 110, 2027
- van Houten, C. J. 1961, *Bull. Astron. Inst. Neth.*, 16, 1
- Verghese, J., Bieri, P. L., Gellido, C., Schaumburg, H. H., & Herskovitz, S. 2001, *Muscle Nerve*, 24, 1476
- Viallefond, F., Goss, W. M., & Allen R. J. 1982, *A&A*, 115, 373
- Waller, W. H., Gurwell, M., & Tamura, M. 1992, *AJ*, 104, 63
- Walterbos, R. A. M., & Kennicutt, R. C. 1988, *A&A*, 198, 61
- Welikala, N., Connolly, A. J., Hopkins, A. M., Scranton, R., & Conti, A. 2008, *ApJ*, 677, 970

- Wells, D. C., Greisen, E. W., & Harten, R. H. 1981, *A&AS*, 44, 363
- Werner, M. W., et al. 2004, *ApJS*, 154, 1
- Whittet, D. C. B., Gerakines, P. A., Hough, J. H., & Shenoy, S. S. 2001, *ApJ*, 547, 872
- Whittet, D. C. B., Shenoy, S. S., Clayton, G. C., & Gordon, K. D. 2004, *ApJ*, 602, 291
- Willner, S. P., et al. 2004, *ApJS*, 154, 222
- Windhorst, R. A., Hathi, N. P., Cohen, S. H., Jansen, R. A., Kawata, D., Driver, S. P., & Gibson, B. 2008, *AdSpR*, 41, 1965
- Windhorst, R. A., Keel, W. C., & Pascarella, S. M. 1998, *ApJ*, 494, L27
- Windhorst, R. A., et al. 2002, *ApJS*, 143, 113
- Witt, A. N., & Gordon, K. D. 2000, *ApJ*, 528, 799
- Witt, A. N., Thronson, H. A., & Capuano, J. M. 1992, *ApJ*, 393, 611
- Worthey, G. 1994, *ApJS*, 95, 107
- Wright, E. L. 2006, *PASP*, 118, 1711
- Wyder, T. K., et al. 2007, *ApJS*, 173, 314
- Xu, C., & Helou, G. 1996, *ApJ*, 456, 152
- York, D. G., et al. 2000, *AJ*, 120, 1579
- Zepf, S. E., & Koo, D. C. 1989, *ApJ*, 337, 34
- Zink, E. C., Lester, D. F., Doppmann, G., & Harvey, P. M. 2000, *ApJS*, 131, 413